Oceanologia

Official Journal of the Polish Academy of Sciences: Institute of Oceanology and Committee on Maritime Research

EDITOR-IN-CHIEF
Prof. Janusz Pempkowiak
Institute of Oceanology Polish Academy of Sciences, Sopot, Poland

MANAGING EDITOR
Agata Bielecka - abielecka@iopan.pl

Editorial Office Address
Institute of Oceanology Polish Academy of Sciences (IO PAN)
Powstańców Warszawy 55
81-712 Sopot, Poland
Mail:editor@iopan.pl

THEMATIC EDITORS

Prof. Małgorzata Stramska — Institute of Oceanology, Polish Academy of Sciences, Sopot, Poland

Prof. Tymon Zieliński — Institute of Oceanology, Polish Academy of Sciences, Sopot, Poland

ADVISORY BOARD

Prof. Xosé Antón Álvarez Salgado
Marine Research Institute, Spanish Research Council (CSIC), Vigo, Spain

Dr Boris Chubarenko
P.P. Shirshov Institute of Oceanology, Russian Academy of Sciences, Kaliningrad, Russia

Prof. Mirosław Darecki
Institute of Oceanology, Polish Academy of Sciences, Sopot, Poland

Prof. Jerzy Dera
Institute of Oceanology, Polish Academy of Sciences, Sopot, Poland

Prof. Agnieszka Herman
Institute of Oceanography, University of Gdańsk, Gdynia, Poland

Prof. Genrik Sergey Karabashev
P.P. Shirshov Institute of Oceanology, Russian Academy of Sciences, Moscow, Russia

Prof. Alicja Kosakowska
Institute of Oceanology, Polish Academy of Sciences, Sopot, Poland

Prof. Zygmunt Kowalik
Institute of Marine Science, University of Alaska Fairbanks (UAF), USA

Prof. Matti Leppäranta
Institute of Atmospheric and Earth Sciences, University of Helsinki, Finland

Prof. Ewa Łupikasza
Faculty of Earth Sciences, University of Silesia, Sosnowiec, Poland

Prof. Hanna Mazur-Marzec
Institute of Oceanography, University of Gdańsk, Gdynia, Poland

Prof. Dag Myrhaug
Norwegian University of Science and Technology (NTNU), Trondheim, Norway

Prof. Sergej Olenin
Coastal Research and Planning Institute, Klaipeda University CORPI, Klaipeda, Lithuania

Prof. Tarmo Soomere
Tallinn University of Technology, Estonia

Prof. Hans von Storch
Institute of Coastal Research, Helmholtz Center Geesthacht, Germany

Prof. Dariusz Stramski
Scripps Institution of Oceanography, University of California, San Diego, USA

Prof. Piotr Szefer
Department of Food Sciences, Medical University of Gdańsk, Poland

Prof. Antoni Śliwiński
Institute of Experimental Physics, University of Gdańsk, Poland

Prof. Muhammet Türkoğlu
Çanakkale Onsekiz Mart University, Turkey

Prof. Jan Marcin Węsławski
Institute of Oceanology, Polish Academy of Sciences, Sopot, Poland

This journal is supported by the Ministry of Science and Higher Education, Warsaw, Poland

Indexed in: ISI Journal Master List, Science Citation Index Expanded, Scopus, Current Contents, Zoological Record, Thomson Scientific SSCI, Aquatic Sciences and Fisheries Abstracts, DOAJ

IMPACT FACTOR ANNOUNCED FOR 2018 IN THE 'JOURNAL CITATION REPORTS' IS 1.988; 5-year IF is 2.112. CITESCORE ANNOUNCED FOR 2018 IS 2.16

Publisher
Elsevier Sp. z o.o.
22, Jana Pawła II Avenue
00-133 Warsaw, Poland

Associate Publisher
Chen Lin
c.lin@elsevier.com
+86-10-8520 8768

ISSN 0078-3234

Oceanologia (2020) 62, 1—11

Available online at www.sciencedirect.com

ScienceDirect

journal homepage: www.journals.elsevier.com/oceanologia

ORIGINAL RESEARCH ARTICLE

Hydrogeochemistry and magnitude of SGD in the Bay of Puck, southern Baltic Sea

Żaneta Kłostowska[a], **Beata Szymczycha**[a,*], **Monika Lengier**[a], **Dorota Zarzeczańska**[b], **Lidia Dzierzbicka-Głowacka**[a]

[a] *Institute of Oceanology, Polish Academy of Sciences, Sopot, Poland*
[b] *Faculty of Chemistry, University of Gdańsk, Gdańsk, Poland*

Received 2 July 2019; accepted 12 September 2019
Available online 26 September 2019

KEYWORDS
Subterranean estuary;
Groundwater discharge;
Macro ions

Summary This work reports the hydrogeochemistry of submarine groundwater discharge (SGD) in the Bay of Puck, southern Baltic Sea. To understand the seasonal and spatial variability of SGD, groundwater and seawater-based SGD samples were collected in several sites in November 2017, March 2018, May 2018 and July 2018. Additionally, a vertical, one-dimensional, advection-diffusion model was used to estimate SGD in each site. The obtained results ranged from to 1.8×10^{-7} L cm^{-2} s^{-1} to 2.8×10^{-7} L cm^{-2} s^{-1} and depended on both: short-timescale factors (wind direction and monthly precipitation) and long-timescale factors (total precipitation and large-scale sea level variations). The calculated rates were further extrapolated to the entire Bay of Puck and ranged from 16.0 m^3 s^{-1} to 127.7 m^3 s^{-1}. The estimated SGD fluxes were significantly higher than results including only the freshwater component of SGD. In the Baltic Sea the importance of SGD, as a source of water and accompanying chemical substances, is still neglected, however, the present findings indicate that locally SGD can be higher than rivers runoff.

1. Introduction

Submarine groundwater discharge (SGD) is defined as all flow of water coming from the seabed to the water column, regardless of the fluid composition or driving force (Burnett et al., 2003). It includes both fresh groundwater discharge derived from terrestrial recharge and recirculated seawater (Burnett et al., 2006). In ocean research, any subsurface water is considered to be groundwater, but traditional hydrogeologists reserve the term groundwater for the

---

* Corresponding author at: Institute of Oceanology, Polish Academy of Sciences, ul. Powstańców Warszawy 55, 81—712 Sopot, Poland, Tel.:+48587311738; fax +48585512130.
E-mail address: beat.sz@iopan.gda.pl (B. Szymczycha).

Peer review under the responsibility of Institute of Oceanology of the Polish Academy of Sciences.

Production and hosting by Elsevier

https://doi.org/10.1016/j.oceano.2019.09.001
0078-3234/

water that originates from a terrestrial aquifer, which excludes recirculated seawater (Jiao and Post, 2019). This difference in terminology has caused the misunderstanding when SGD is estimated by different methods. It is worth mentioning, that the total SGD (including fresh and recirculated water) tends to be much higher than fresh SGD and can be comparable to river flux (Moore, 2010). In this study, the term SGD is used for both fresh SGD and recirculated SGD.

For many decades SGD was neglected in the global hydrological cycles. The reason for that is the difficulty to identify and measure SGD. Generally, rivers have been recognized to be a key pathway for terrestrial water to the ocean. Since Moore (1996) showed that chemical mass flux via SGD can exhibit 40% of this coming from the river water the subject has been receiving increased attention. SGD can be an important source of chemical substances as aquifers in many areas become enriched with chemicals (organic and inorganic substances) from land sources. Consequently, SGD should be considered in analyzing the chemical substances' budgets of coastal ecosystems.

Recently, several geochemical processes occurring in the groundwater-seawater mixing zone, such as precipitation/dissolution of ion, speciation of trace metals, the removal of nutrients, and the production of dissolved inorganic carbon (DIC) have been identified as modifying the chemical substances' fluxes via SGD (Cai et al., 2003; Charette and Sholkovitz, 2002, 2006; Kroeger et al., 2007). Relatively less attention has been attributed to the macro ions' (Cl^-, $SO_4{}^{2-}$, Na^+, K^+, Mg^{2+}, Ca^{2+}, and $HCO_3{}^-$) cycling, even though major ion distributions due to groundwater discharge can exert a much control over the chemical functioning of the coastal area (Liu et al., 2017; Santos et al., 2008).

In the Bay of Puck, southern Baltic Sea preliminary studies indicated that locally SGD is an important component of chemical budgets (e.g., Bolałek, 1992; Pempkowiak et al., 2010; Piekarek-Jankowska, 1994; Szymczycha et al., 2012, 2014, 2016). However, little is known about the SGD hydrogeochemistry, its magnitude, and variability. In this study, we investigated the hydrogeochemical characteristics and related hydrogeochemical processes. We sampled both the shallow groundwater wells (piezometers) and offshore SGD (pore water) in order to understand the dynamic character in the transition zone (subterranean estuary). Moreover, a vertical, one-dimensional, advection-diffusion model was used to estimate SGD. The obtained results were extrapolated to the entire bay assuming similar SGD rates in the area of comparable pore water salinity and knowing the literature SGD coverage in the Bay of Puck (Piekarek-Jankowska, 1996, 1996; Kozerski (Ed.), 2007; Kryza and Kryza, 2006). Additionally, SGD was correlated to both the short-timescale factors (wind direction and precipitation) and the long-timescale factors (large-scale sea level variations).

2. Material and methods

2.1. Study area

The Bay of Puck is an inner part of the Bay of Gdańsk and is an example of an active groundwater discharge area (Bolałek, 1992; Pempkowiak et al., 2010; Piekarek-Jankowska, 1994; Szymczycha et al., 2012, 2014, 2016). It is divided into two parts, the outer part with an average depth of 21 m and the inner, shallower part reaching a depth of about 3 m (Urbański et al., 2007). Hence, the inner part of the bay has limited access to the open Baltic Sea waters due to a natural barrier called Rybitwia Mielizna (Urbański et al., 2007), while the whole bay is separated by a narrow spit, called Hel Peninsula, from the open Baltic Sea (Nowacki, 1993).

The bay's hydrological regime is controlled by the exchange of mass, energy, and outflow from its catchment area, while the outer part of the bay is further influenced by contact with the Gulf of Gdańsk and the Vistula River (Cyberski, 1993). Both bays, namely the Bay of Puck and the Gulf of Gdańsk, have complex, hydrological systems consisting of Cretaceous, Tertiary, and Quaternary aquifers (Kozerski (Ed.), 2007). The detailed hydrogeological characteristics and drainage zones of the fresh groundwater in the Bay of Puck were presented by Piekarek-Jankowska (1996). In the Supplementary Material Figure 1S, the cross-section presenting the hydrogeological conditions of the sediments of the Bay of Puck is presented while in the Supplementary Material Figure 2S the SGD discharge zones modified after Piekarek-Jankowska (1994) and Kryza et al. (2005) are indicated.

The lithological characteristic of the Bay of Puck is closely related to the lagoon bay type. Generally, the grain size increases with the distance from the shoreline, which correlates with the depth and morphology of the bay (Piekarek-Jankowska, 1994). In the inner part of the bay, a small diversity of bottom sediments is observed. They are mainly dominated by fine-grained sands; however the coastal zone, until the 1 m isobath, is formed by medium-grained sands. In the outer part of the bay, the proportion of mud and clay increases according to the lithological diversity of the sediments (Piekarek-Jankowska and Łęczyński, 1993; Uścinowicz and Kramarska, 2011). The coarse-grained sands dominate to a depth of about 20 m, while the fine-aurantite sands are the majority in the deepest parts. The bay also contains a variety of shore types (e.g., sandy beaches, gravel beds, stony outcrops, clay cliffs, and vegetated river mouths).

2.2. Sampling and analytical procedures

SGD, shallow groundwater and seawater samples were collected in November 2017, March 2018, May 2018 and July 2018. The coastal SGD sites were located off Hel Peninsula (Hel, Jastarnia, and Chałupy) and off the mainland (Swarzewo, Osłonino, and Puck). Two of them — Hel and Jastarnia — were located in the outer part of the bay, while the other sites were located in the inner part of the bay (Fig. 1).

SGD samples for macro ions composition were collected at 10 cm depths by means of push points (e.g., Szymczycha et al., 2012) every 1 m along a 5-m-long transect perpendicular to the shoreline at each study site. Additionally, pore water from several depths up to 30 cm was collected 3 m offshore for chloride analyses. In July 2018, at every coastal SGD site, salinity surveys were recorded along 10-m-long, parallel transects that extended 5 m seaward (Fig. 2). Pore

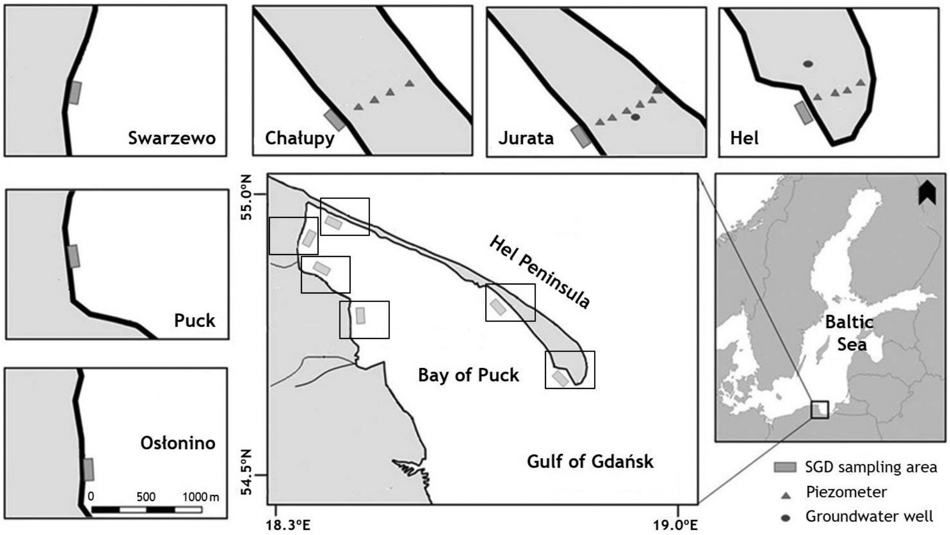

Figure 1 Map of the study sites located in the Bay of Puck, southern Baltic Sea. The submarine groundwater discharge (SGD) sites situated off Hel Peninsula (Hel, Jurata, Chałupy) and off the mainland (Puck, Swarzewo, and Osłonino) are marked as gray rectangles, while piezometers and groundwater wells are marked as triangles and circles, respectively.

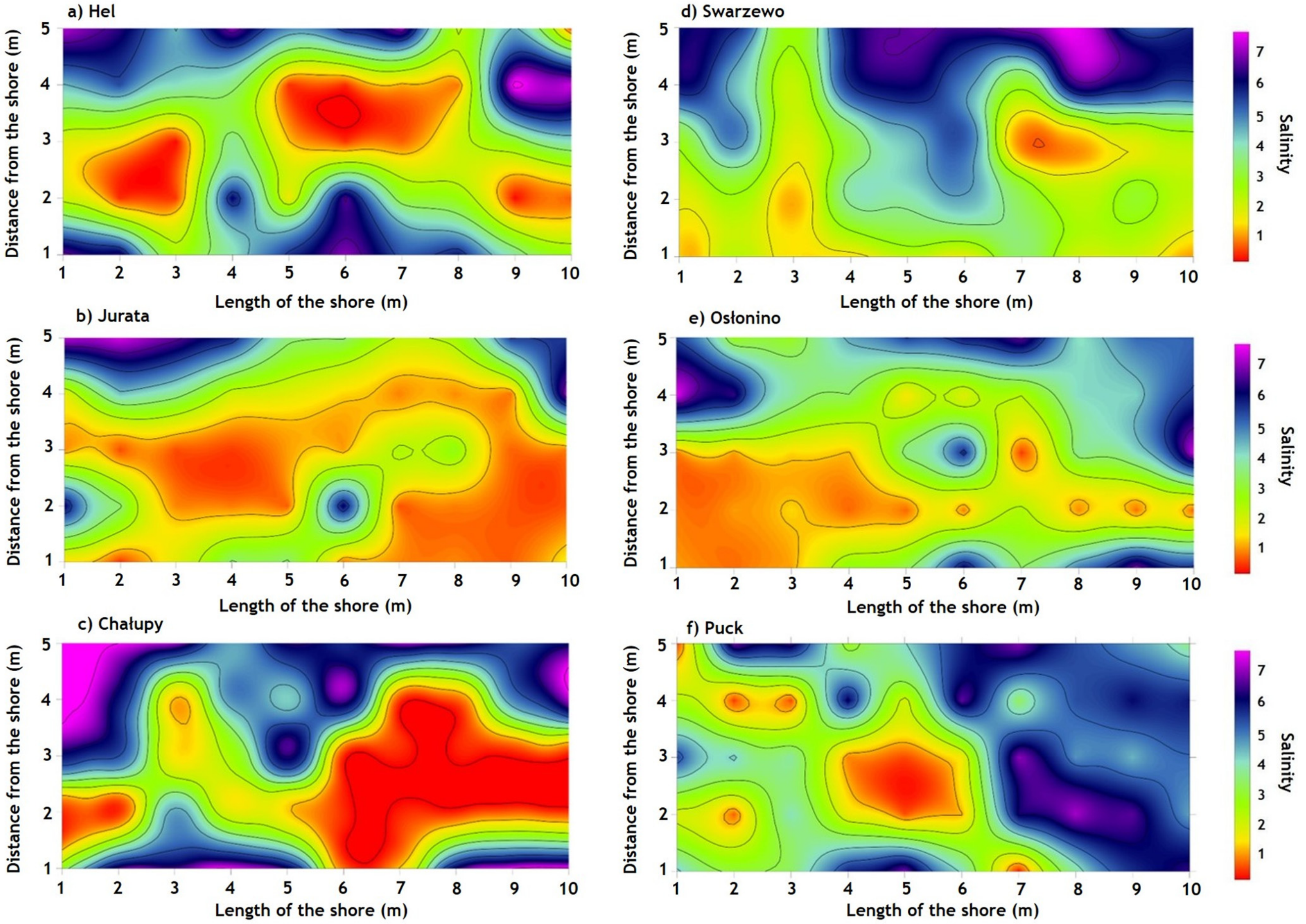

Figure 2 Porewater salinity distribution at 10 cm depth at six study sites located off Hel Peninsula — (a) Hel, (b) Jurata, (c) Chałupy — and off the mainland — (d) Swarzewo, (e) Osłonino, and (f) Puck — within the Bay of Puck, southern Baltic Sea.

water samples were collected every 1 m from 10 cm depth by means of push points. Data interpolation was performed in Surfer15 (Golden Software Partner).

Seawater samples were collected directly from the sea within the survey.

Shallow groundwater samples were collected from 14 piezometers situated at Hel Peninsula (Fig. 1). Water samples from the piezometers were collected using a peristaltic pump and a Teflon tube. The depths of the piezometers' mirrors were determined in situ using a hydrogeological whistle and meter, and they ranged from 1 m to 8.2 m.

Field parameters, such as oxygen concentration (O_2), pH, oxidation—reduction potential (ORP), and salinity, were measured in situ by means of a multimeter (Hach-Lange).

In all collected water samples, major ions (Ca^{2+}, Mg^{2+}, Na^+, K^+, Cl^-, $SO_4{}^{2-}$, and $HCO_3{}^-$) were analyzed. 10 ml of each water sample were collected for major metals (Na^+, Mg^{2+}, Ca^{2+}, and K^+) analyses. Samples were filtrated through cellulose acetate filters ($\varphi = 0.45\,\mu m$) into pre-prepared PE vials, preserved with 100 μL 3 M nitric acid (V) (HNO_3), and stored in the dark at 4C until analysis. The ion measurements were conducted by means of atomic absorption spectroscopy (SHIMADZU 6800). Background correction was applied with a deuterium lamp using a flame technique (flame: air — acetylene). Quality control was performed using certified reference material "ERM-CA-11b". The recovery was equal for Mg^{2+} to 96%, Ca^{2+} to 96%, K^+ to 103% and Na^+ to 105%, while the precision, described as the Relative Standard Deviation (RSD) of triplicate analyses, was not worse than 3%.

Water sample for Cl^- analysis was collected (with a volume of 40 ml) into polythene (PE) containers and stored in the dark at 4°C until analysis. The analyses were carried out via the potentiometric titration method, using the syringe microtitrator Cerko Lab System with an ion-selective chloride electrode (Schott Ag 6280). A standard solution of silver nitrate (0.1 M and 0.01 M) was used as a titrant, and portions $V = 0.041$ ml were dosed automatically. Quality control was performed using the standard curves. The precision, described as (RSD) of triplicate analyses, was not larger than 3%. The obtained concentrations of the procedural blank samples never exceeded 4% of concentrations measured in the actual samples.

Water samples (40 ml) for the analysis of $HCO_3{}^-$ were collected into vials made of borosilicate glass, conserved with 150 μl of saturated $HgCl_2$ solution, and stored in the dark at 4°C until analysis. The analyses were carried out using the potentiometric method, by means of a pH electrode (Cerko Lab System potentiometric microtitrator). As the titrant, a standard solution of hydrochloric acid (HCl) (0.1 M and 0.01 M) was used, and portions $V = 0.041\ cm^3$ were dosed automatically. Quality control was performed using the standard curves. The precision, described as the RSD of triplicate analyses, was not worse than 3%. The obtained concentrations of the procedural blank samples never exceeded 4% of the concentrations measured in the actual samples.

Around 40 ml of sample was collected for $SO_4{}^{2-}$ analysis into PE containers and stored in the dark at 4°C until analysis. The analyses were carried out with a conductometric precipitation titration method, using a conductivity cell probe (Schott LF413T-id) with a multi-parameter ProLab2000 meter (Schott Instruments). As the titrant, a standard barium acetate $Ba(CH_3COO)_2$ solution (0.005 M) was used. The titrant was added to the test sample in portions of 0.1 cm^3 in continuous measurement of conductivity, as well as pH and temperature control. For each sample, curves were plotted in a $\kappa' = f(VBa(CH_3COO)_2)$. Quality control for sulfate analysis was performed using standard curves. The precision, described as the RSD of triplicate analyses, was not worse than 3%. The obtained concentrations of the procedural blank never exceeded 5% of concentrations measured in the actual samples.

2.3. Ionic deltas

The ionic delta is an important indicator determining the nature of the geochemical reactions between the solid phase and the liquid phase in the coastal zone. The ionic delta is used mainly in studies of both SGD and seawater intrusion (Bolałek, 1992; Liu et al., 2017). It describes the difference between the measured concentration ($m_{i,sample}$) of ion (i) and its theoretical concentration ($m_{i,mix}$) when freshwater and seawater mix conservatively (Appelo and Postma, 2005; Liu et al., 2017) and can be described as:

$$\Delta m_i = m_{i,sample} - m_{i,mix}. \tag{1}$$

The theoretical concentration ($m_{i,mix}$) can be expressed as:

$$m_{i,mix} = f_{sea} - m_{i,sea} + (1 - f_{sea})m_{i,fresh}, \tag{2}$$

where $m_{i,sea}$ and $m_{i,fresh}$ are the concentrations of the seawater endmember and freshwater endmember, respectively, and f_{sea} is the fraction of seawater, which is usually calculated from Cl^- concentration in the water sample because of the conservative properties of the chloride ion. The fraction, based on Cl^-, is described as:

$$f_{sea} = \frac{m_{Cl^-,sample} - m_{Cl^-,fresh}}{m_{Cl^-,sea} - m_{Cl^-,fresh}}, \tag{3}$$

where $m_{Cl^-,sample}$ is the concentration of Cl^- in the sample; $m_{Cl^-,fresh}$ is the concentration of Cl^- in the freshwater endmember; and $m_{Cl^-,sea}$ is the Cl^- concentration in the seawater endmember.

2.4. Piper diagram

The Piper diagram is widely used in hydrochemical studies concerning the composition of groundwater — specifically its graphical classification and selection of the source of origin (Hounslow, 1995; Piper, 1994). In the Piper diagram, major ions are plotted as cation and anion percentages of milliequivalents in two base triangles. The total cations in meq dm^{-3}, and the total anions in meq dm^{-3} are set equal to 100%. The data points in the two triangles are then projected onto the diamond grid. The projection reveals certain useful properties of the total ion relationships. Every sample is represented by three data points — one in each triangle and one in the projection diamond grid. In this study, the Piper diagram was performed in the RockWare Software: AqQA.

2.5. Calculation of SGD rates

Chloride is used as an SGD tracer in marine environments, as it does not undergo either adsorption or chemical reactions.

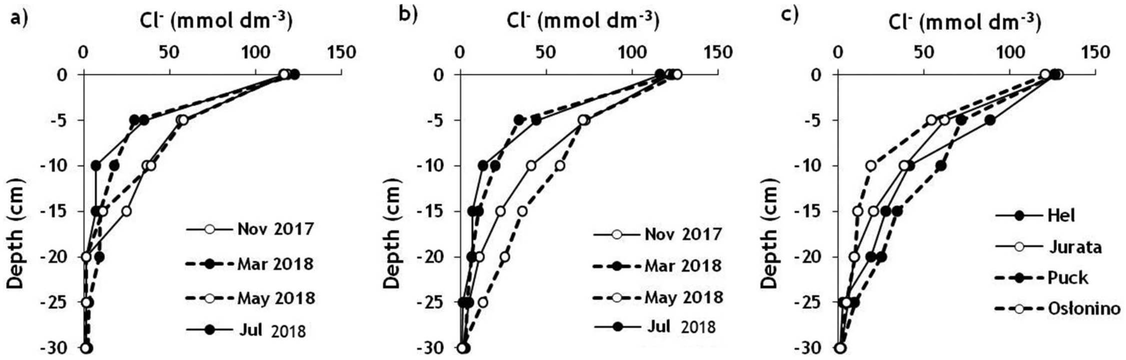

Figure 3 Seasonal pore water chloride (Cl^-) depth profiles for (a) Swarzewo, (b) Chałupy and (c) Hel, Jurata, Puck, and Osłonino collected in July 2018.

Therefore, pore water profiles of Cl^- solely reflect transport processes, such as advection and diffusion (Schlüter et al., 2004). The Cl^- pore water distribution can be described by a vertical, one-dimensional, advection-diffusion model (Schlüter et al., 2004), as shown in Eq. (4):

$$v\frac{\partial(\Phi C)}{\partial x} - D\frac{\partial^2(\Phi C)}{\partial x^2} = 0, \qquad (4)$$

where C is the concentration of Cl^-, Φ is the porosity; D is the molecular diffusion coefficient of Cl^- in the sediment, x is depth, and v is the velocity. The Cl^- diffusion coefficient for sediment (D) was based on Boudreau (1997). The calculation included the measure of the average bottom-water temperature of each season: summer (17°C), autumn (7°C), spring (5.1°C), and winter (0.1°C). The obtained molecular diffusion coefficient was corrected for the effect of tortuosity (θ) according to Boudreau (1997), as shown in Eq. (5):

$$\theta^2 = 1 - \ln(\Phi^2). \qquad (5)$$

The porosity was determined according to Bolałek (1992).

For Cl^- interpolation, the least-squares method was used, and the best function was obtained (Eq. (4)). The SGD velocity was then calculated as Eq. (6):

$$v = \frac{D\frac{\partial^2(\Phi C)}{\partial x^2}}{\frac{\partial(\Phi C)}{\partial x}}. \qquad (6)$$

The SGD rate was calculated based on measures in every site and included: seasonal sampling in Swarzewo (4 pore water chloride profiles) and Chałupy (4 pore water chloride profiles); and single measure (1 pore water profile collected in July 2018) for each study site located in Hel, Jurata, Osłonino, and Puck.

The shallow sediments of the Bay of Puck are rapidly becoming hypoxic or anoxic with increasing sediment depth. Usually, there is no oxygen at approximately 2 cm below water-sediment interface (Szymczycha et al., 2012). Therefore in model assumptions, we neglected the bioturbation effect.

Salinity at the depth of 10 cm below water-sediment interface was measured in every sampling site (Fig. 2) while at the selected station within each site the pore water chloride profiles were taken (Fig. 3). These profiles enable to determine the SGD flux using the vertical, one-dimensional, advection-diffusion model. The calculated water flow was further extrapolated to the area where similar salinity was observed. To assign the area with similar salinity, the salinity surveys (Fig. 3) and CorelDRAW software were used. The portion of the area ranged from 5% to 25% (chapter 3.1). The literature denotes that approximately half of the Bay of Puck is under direct SGD influence (Kozerski (Ed.), 2007; Kryza and Kryza, 2006). Therefore, we assumed that SGD enters to the half of the Bay of Puck however the SGD fluxes obtained in this study are characteristic only of the assigned in this study area (from 5% to 25%). We simply extrapolated the obtained minimum and maximum flux to the area ranging from 9.1 km^2 to 45.5 km^2. Moreover, we did similar calculation and extrapolated the obtained results to the inner Bay of Puck.

2.6. Monitoring data

The wind speed and wind direction data were obtained from the Maritime Office in Gdynia, from automatic stations. The daily atmospheric precipitation data and mean sea level were obtained from the Institute of Meteorology and Water Management (IMGW) database (https://dane.imgw.pl/data) from land-based stations (IMGW, 2019). The data are presented in the supplementary material (Supplementary Material Tab. 1S and 2S). Data characterizing deep groundwater wells located at Hel, Jurata, and Puck (Fig. 1) and the Reda River were obtained from the Regional Inspectorate for Environmental Protection, 2019.

3. Results

3.1. Salinity and chloride distribution

Generally, average seawater salinity in the Bay of Puck oscillates around 7, and, usually, significantly lower surface water salinities indicate freshwater influence, such as that of rivers and/or precipitation. In terms of the pore water vertical distribution of salinity, the profiles are generally constant or increase slightly with depth (Carman and Rahm, 1997). The consistent presence of low salinity pore water designates SGD (Kotwicki et al., 2014; Pempkowiak et al., 2010; Schlüter et al., 2004; Szymczycha et al., 2012). Figure 2 presents the pore water salinity distributions at 10 cm depth in six sites within the Bay of Puck. Three of

Table 1 The macro ion concentrations in submarine groundwater discharge (SGD), shallow groundwater (piezometers), deep groundwater (groundwater wells), river (Reda River) and seawater.

Sample type		Average ($mmol\ dm^{-3}$) Range: min-max						
		Cl^-	HCO_3^-	SO_4^{2-}	Na^+	K^+	Ca^{2+}	Mg^{2+}
SGD	Nov 2017	39.8	0.88	0.12	31.5	1.54	2.3	5.9
		1.1—126.1	0.01—1.96	0.12—1.60	0.2—123.3	0.10—2.70	0.3—3.5	0.3—13.1
	Mar 2018	22.3	4.22	0.51	19.5	0.62	1.6	2.1
		1.1—116.8	2.17—9.11	0.10—1.60	0.2—81.6	0.10—2.40	0.3—2.6	0.3—9.9
	May 2018	25.4	0.47	0.13	30.1	1.19	2.0	4.1
		2.3—123.0	0.20—1.12	0.03—0.18	3.1—141.2	0.10—4.20	1.0—3.3	0.6—13.0
	Jul 2018	30.7	0.58	0.14	30.0	0.53	1.9	1.8
		1.4—109.0	0.04—1.33	0.03—0.35	1.9—127.0	0.20—1.20	1.0—3.7	0.4—6.2
Shallow groundwater		13.3	1.56	0.24	33.3	0.35	1.8	1.0
		1.1—58.4	0.04—9.11	0.03—1.24	0.2—99.3	0.10—0.80	0.3—3.3	0.3—3.9
Deep groundwater		1.0	2.60	0.30	1.2	0.10	0.8	0.25
		0.3—1.4	2.40—3.20	0.20—0.50	0.4—1.7	0.08—0.13	0.6—1.4	0.2—0.3
Seawater		143.2	1.12	0.14	128.6	2.50	2.7	7.9
		123.2—159.6	0.34—2.34	0.10—0.18	82.5—151.0	2.40—2.60	1.9—3.5	0.7—13.0
River		0.6	2.90	0.50	0.5	0.07	2.0	0.35
		0.4—0.9	2.50—3.30	0.40—0.60	0.4—0.6	0.06—0.08	1.9—2.1	0.3—0.4

the sites are located offHel Peninsula (a) Hel, (b) Jurata, (c) Chałupy, and the other three sites are situated offthe mainland (d) Swarzewo, (e) Puck, and (f) Osłonino (Fig. 1). All surveys indicate the high spatial variability of salinity distribution within each site, indicating that, in each case, a certain portion of sediment is influenced by direct SGD (salinity below 1 at 10 cm depth) at the time of sampling. The portion of the area with direct SGD impact ranged from 5% to 25%. However, in each case, only small portions of pore water (less than 10%) had salinities characteristic of seawater. The spatial variability of the pore water salinity distribution can be attributed to the movement of the groundwater-seawater mixing zone and, therefore, to variations in groundwater discharge rates and/or increase of freshwater salinity (Kaleris, 2018). The increase of freshwater salinity can be also caused by chloride aerosols derived from sea spray that enter the shallow groundwater with recharge (Pietrucień, 1983).

Figure 3 presents the seasonal pore water chloride profiles in (a) Swarzewo and (b) Chałupy. Additionally, the chloride vertical distribution obtained in July 2018 is presented for (c) all remaining sites. Chloride concentration decreased with increasing depth at every season and site. This pattern is typical of the Baltic Sea coast, which is influenced by fresh groundwater (Schlüter et al., 2004; Szymczycha et al., 2012). The presence of a seawater-dominated zone in the upper first 5 cm of the sediment was evidenced by high chloride concentrations, comparable to those of bottom-water (~143.2 mmol dm^{-3}). Below that layer, an occurrence of freshwater is indicated by chloride concentrations significantly decreasing, reaching 1.0 mmol dm^{-3}. A small spatial variability among chloride vertical distribution is visible. Interestingly, there was higher variability among seasons.

3.2. Macro ion composition

The macro ion compositions of SGD, shallow and deep groundwater, river water, and seawater in samples collected in 2017 and 2018 are listed in Table 1. Additionally, SGD samples are divided according to the time of sampling, while the other types of water represent the average, minimum, and maximum values obtained over the course of the study. The macro ion concentrations in SGD differ across seasons. Similar to SGD, high ranges of minimum and maximum concentrations of macro ions were also observed in seawater and shallow groundwater. The compositions of the Reda River and deep groundwater are stable, and no seasonal changes were observed.

The Piper diagram depicts the relative proportions of major ions on a charge-equivalent basis for comparison and classification of water samples independent of total analyte concentrations, and it is a graphical illustration of water chemistry. It is widely used in studies concerning the composition and origin of groundwater (Hounslow, 1995; Piper, 1994). Based on the major ion data, the chemical composition of collected water samples can be classified into several groups (Fig. 4). Seawater is a sodium-chloride (Na-Cl) type of water. River water is a calcium-bicarbonate type (Ca-HCO_3), and deep groundwater reflects a similar composition. Shallow groundwater (samples from piezometers), depending on the season, is a Ca-HCO_3 type of water (in the summer (July 2018) and winter (March 2018)) or a Na-Cl type of water (in autumn (November 2017) and spring (May 2018)). SGD samples are generally Na-Cl types, showing the great influence of seawater intrusion.

Transformations in water chemistry can be reflected by flow paths presented as a series of points along trend lines in Fig. 4. Samples near the straight line (F-S) represent

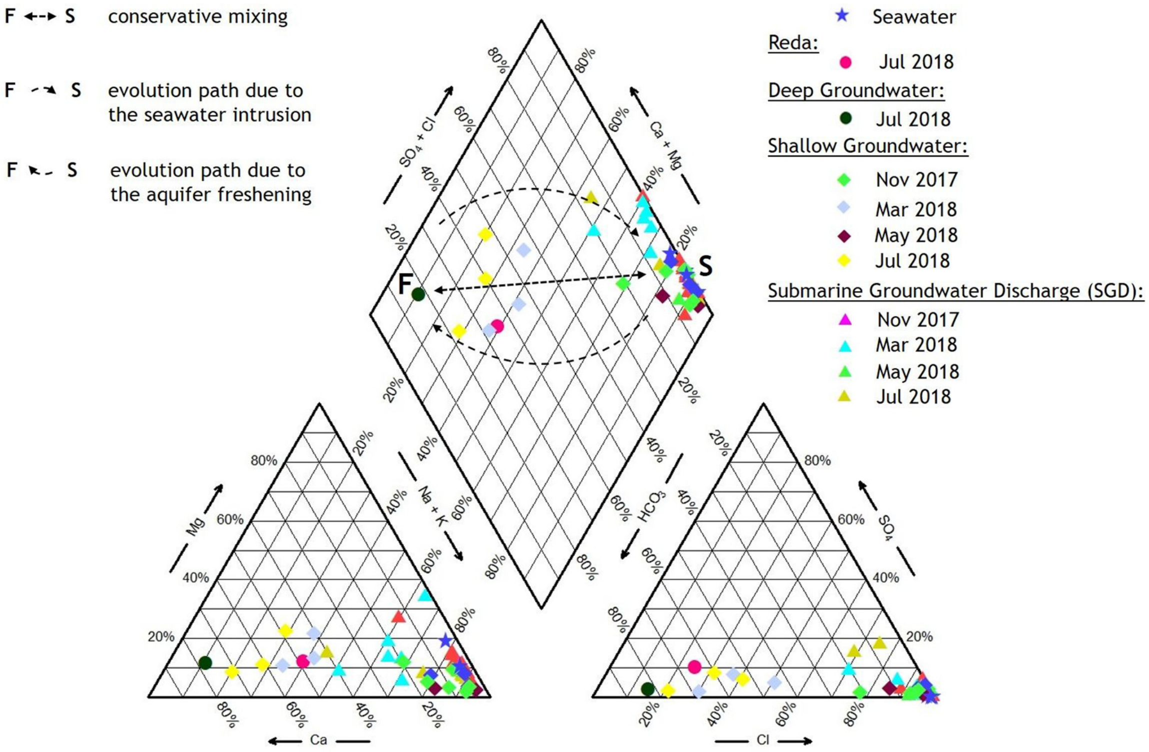

Figure 4 Piper diagram showing the ionic composition (% meq dm^{-3}) of seawater (seawater endmember), river water (Reda River, monitoring data), deep (monitoring data) and shallow groundwater, and submarine groundwater discharge (SGD). Samples of shallow groundwater and SGD were collected seasonally. The conservative (straight broken line) and nonconservative (concave and convex broken line) mixing between freshwater (F) and seawater (S) end-members are shown.

a mixture between the seawater (S) and freshwater (F) end-members. The upper path shows the direction along which the freshwater is replaced by seawater while the upward paths present the opposite process. In our data sets, no clear trends were observed. Samples from groundwater wells and the river were located generally closer to the upward evolution path denoting the aquifer freshening while SGD samples depending on the season showed both trends. It seems that in March and November the composition of most of the SGD samples was under higher seawater influence while in May and July the composition moved towards freshwater.

Groundwater often contains dissolved calcium, or magnesium, which originate from the weathering of surface rocks as well as dissolved organic compounds such as detritus, animal waste, or human contaminants. Since this water percolates through an aquifer, it may be modified and changed. Groundwater and accompanied dissolved calcium or magnesium moves towards the sea. Eventually, these ions may be exchanged for sodium in groundwater-seawater mixing zone and might form salts (Liu et al., 2017; Salem et al., 2016). The relationship between ΔMg^{2+}, ΔCa^{2+}, and $(\Delta Na^{+} + \Delta K^{+})$ is presented in Fig. 5. The collected water samples characterizing the coastal area can be divided into several zones according to the ionic deltas of cations (Liu et al., 2017). Each zone is represented as a quadrant from I to IV. At the direction from dissolution (I) to precipitation (III), the external sources or sinks play a key role in controlling the concentration of ions in the water. The other direction represents the cation exchange (II and IV). In quadrant II, Mg^{2+} or Ca^{2+} is exchanged with Na^{+} and K^{+}, and, in quadrant IV, the process is the opposite (Liu et al., 2017). The ionic deltas (ΔMg^{2+}, ΔCa^{2+}, and $(\Delta Na^{+} + \Delta K^{+})$) of collected samples mainly indicate the dissolution and cation exchange processes. The possible precipitation of magnesium and calcium was observed in only few samples collected in Mar and May 2018. Both positive ΔMg^{2+} and ΔCa^{2+} concentrations and positive $(\Delta Na^{+} + \Delta K^{+})$ and the Mg^{2+}/Ca^{2+} ratio lower than 0.5, show a possible dissolution of calcite mainly in Nov 2017 and Jul 2018. The possible cation exchange process was most pronounced in May 2017. Both processes namely the dissolution and cation exchange imply the dynamic processes that occur in the groundwater seawater mixing zone.

4. Discussion

4.1. SGD flux to study sites

The obtained chloride pore water profiles can deliver information about fluid transport in sediments (Schlüter et al., 2004). Hence, diffusion is indicated by a linear decrease in the Cl^{-} concentration, while the freshwater flow is indicated by a concave-shaped curve (Oehler et al., 2017; Schlüter et al., 2004). In this study, the pore water chloride profiles had the concave shape indicative of freshwater flow. Therefore, to estimate the SGD rate, we used a

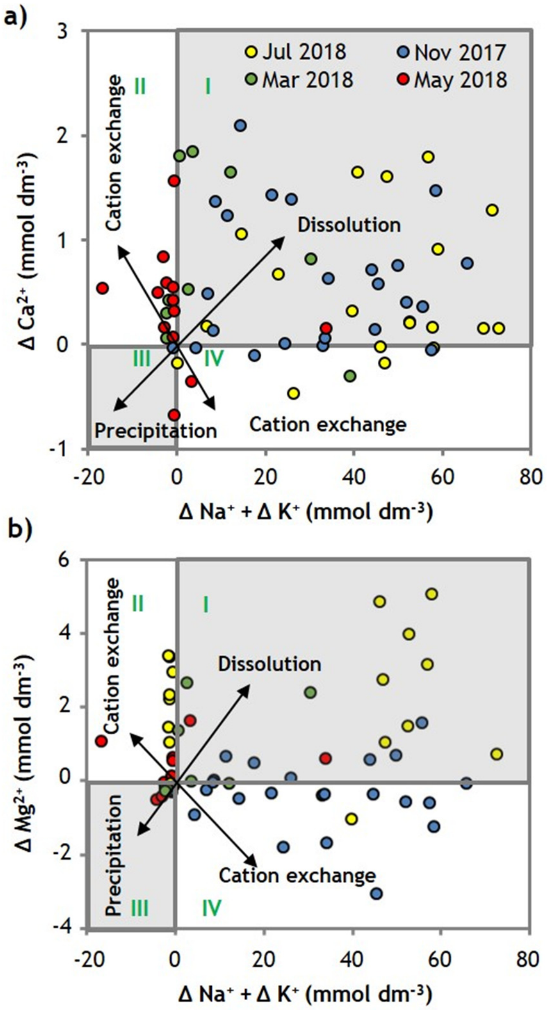

Figure 5 The ΔMg^{2+} and ΔCa^{2+} (mmol dm^{-3}) are plotted vs. ($\Delta Na^{+}+\Delta K^{+}$) (mmol dm^{-3}) for each sample to reveal the mechanism of enrichment or depletion of major cations in the mixing zone (transition zone = subterranean estuary) of the Bay of Puck. The quadrants from I to IV indicate several processes such as: dissolution (I), cation exchange (II and IV), and precipitation (III).

one-dimensional, advection-diffusion model based on the vertical chloride distribution (12 chloride pore water profiles presented at Fig. 3). The functions used for calculations are listed in the Supplementary Material Tab. 1S while the obtained fluxes are shown in Table 2. Surprisingly there was no significant spatial variability among sites in calculated SGD rates. The pronounced seasonal changes are visible, with the highest flux observed in July 2018 and the lowest in November 2017 and May 2018. The seasonal SGD flux variability was also observed in previous studies located off Hel (Szymczycha et al., 2012). The SGD flux to the Bay of Puck obtained in this study was comparable with seepage rates (Szymczycha et al., 2012) but was significantly lower (several orders of magnitude) than groundwater flux estimated by means of gradient meter method (Bublijewska et al., 2017). In the Eckernförde Bay, Western Baltic Sea SGD flux was estimated using similar to this study approach and the calculated flux was two orders of magnitude lower than submarine groundwater discharge to the Bay of Puck. One reason for that can be difference in hydrogeological characteristics of both bays.

Table 2 The SGD flux measured in Chałupy, Swarzewo, Jurata, Hel, Swarzewo, Puck, and Osłonino.

Date	SGD in each study area (x 10^{-7} L cm^{-2} s^{-1})					
	Chałupy	Jurata	Hel	Swarzewo	Puck	Osłonino
Nov 2017	1.8	nd	nd	1.8	nd	nd
Mar 2018	2.3	nd	nd	2.2	nd	nd
May 2018	1.8	nd	nd	1.8	nd	nd
Jul 2018	2.7	2.6	2.7	2.8	2.0	2.8

nd — no data.

SGD is influenced by the components of the short-timescale (minutes, hours, days) which are due to wave actions, tides, and precipitation as well as the components of the long-timescale — which result from the seasonal movement of the mixing zone and large-scale, sea level variations (Kaleris, 2018). SGD was correlated with average speed, the direction of the wind, and the total precipitation within 72 h prior sampling (Supplementary Material Tab. 2S) and with the total monthly precipitation and sea level change (Supplementary Material Tab. 3S). The 72 h (h) time interval was based on Kozerski (Ed.) (2007), who estimated the shallow groundwater residence time to be 72 h in the Bay of Gdańsk region. In this study, the wind speed ranged from 2.9 m s^{-1} to 4.6 m s^{-1} and did not correlate with increased or decreased SGD fluxes (Tab. 2S). Reversely, a correlation of increased SGD flux and increased total precipitation within 72 h prior sampling was observed (Supplementary Material Tab. 2S). Generally, in November 2017 the total precipitation (Supplementary Material Tab. 3S) was highly similar to the sea level. In March 2018, the sea level significantly decreased, while the precipitation rate was at an average magnitude. In May 2018, the wind changed direction to the northeast (Supplementary Material Tab. 3S), and the sea level started to increase while the average monthly precipitation and total precipitation stayed at an average rate. In July 2018, the south wind direction was observed, total precipitation slightly increased while no significant increase in sea level was observed. It seems that increased precipitation increases SGD rate if there is no rise in sea level. In addition, south wind can move the seawater from the southern coast further seaward and can enable groundwater to discharge more even if the precipitation is at an average rate. The wind direction at the time before and during sampling, average monthly precipitation, and sea level conditions significantly influenced the SGD rate, while wind speed several hours prior to sampling was less important. It seems that all three drivers (wind direction at the time before and during sampling, precipitation, and sea level conditions) can be used as parameters enabling the estimation of the SGD rate change.

4.2. SGD flux to the Bay of Puck

Several studies have concentrated on SGD along the coastal areas of the Baltic Sea (e.g., Kozerski (Ed.), 2007; Kryza

Table 3 Extrapolated SGD fluxes.

Date	Extrapolated SGD to the Bay of Puck based on salinity distribution and assuming that half of the bay is under SGD influence min—max ($m^3\ s^{-1}$)	Extrapolated SGD to the inner Bay of Puck based on salinity distribution and assuming half of the bay is under SGD influence min—max ($m^3\ s^{-1}$)
Nov 2017	16.4—82.1	9.2—47.3
Mar 2018	20.2—101.1	11.7—58.7
May 2018	16.3—80.1	9.4—46.1
Jul 2018	24.8—127.7	14.3—73.5
Annually	16.3—127.7	9.2—73.5

and Kryza, 2006; Peltonen 2002; Piekarek-Jankowska 1994; Viventsowa and Voronow, 2003) mostly addressing the fresh component of SGD. The magnitude of SGD was negligible in comparison to river runoff. Consequently, the scientific community has recognized SGD (both fresh SGD and recirculated SGD) as an insignificant factor affecting the ecosystem of the Baltic Sea. It is worth noticing that in the global literature, we can find results indicating that seawater circulation caused by tide and wave set-up may contribute 96% of the total SGD compared to 4% of fresh SGD (Li et al., 1999). Interestingly, Krall et al. (2017) indicated that SGD rates at Forsmark, Gulf of Bothnia, Baltic Sea are significantly higher than results obtained from local hydrological models, which consider only the fresh component of SGD.

Given the absence of SGD flux to the Bay of Puck including the fresh and recirculated SGD we extrapolated the results obtained in each study site to the entire bay. The details related to the extrapolation methodology are given in the materials and methods chapter. The obtained SGD flux to the entire Bay of Puck ranged from 16.0 $m^3\ s^{-1}$ to 127.7 $m^3\ s^{-1}$ while to the inner Bay of Puck ranged from 9.2 $m^3\ s^{-1}$ to 73.5 $m^3\ s^{-1}$ (Table 3). The wide range of obtained flux can be due to the seasonal variability of SGD. The obtained result is significantly higher than the fresh SGD flux calculated by Piekarek-Jankowska (1994). Moreover, it is from 2.5 to 25 times more than the annual discharge of the biggest river entering the Bay of Puck — the Reda River (5 $m^3\ s^{-1}$). Matciak et al. (2015) seem to confirm our results. They observed salinity anomalies in the bottom-water of the Bay of Puck and suggested that less saline water appeared and changed the seawater salinity. The volume of freshwater must have been significant to reduce the bottom-water salinity. In comparison to other sites located in the Baltic Sea, the SGD fluxes to the Bay of Puck are notably higher (Schlüter et al., 2004). Recently, Krall et al. (2017) indicated, on the basis of a ^{224}Ra mass balance, that SGD rate at Forsmark, Gulf of Bothnia, Baltic Sea ranges from $(5.5 \pm 3.0) \times 10^3\ m^3\ d^{-1}$ to $(950 \pm 520) \times 10^3 m^3\ d^{-1}$. These rates are up to three orders of magnitude lower than those obtained during this study. The significant differences in estimated SGD rates can be related to both (1) different hydrogeological characteristics of both sites and (2) different method used to calculated SGD flux.

We are aware that the extrapolated SGD involves errors and uncertainties. However, we wanted to show the order of magnitude rather than the actual numbers. SGD is a source of chemical substances globally (Cai et al., 2003; Charette and Sholkovitz, 2002, 2006; Kroeger et al., 2007), and, certainly, it supplies the Bay of Puck with nutrients or dissolved carbon (Szymczycha et al., 2012, 2014). Therefore, it should be considered as a driver for ecosystem change, such as algae blooms and eutrophication. We would like to encourage the scientific community to acknowledge SGD as a significant source of water and, most probably, an important source of chemical substances. The future SGD studies in the Baltic Sea region should include the similar approach to estimate SGD, and, additionally, include several different methods such as analytical or numerical modeling; direct measurements; and environmental tracer techniques.

5. Conclusions

SGD in the Bay of Puck ranged from 16.0 $m^3\ s^{-1}$ to 127.7 $m^3\ s^{-1}$, which is significantly higher than previously obtained results by Piekarek-Jankowska (1994) that excluded the recirculated seawater component of SGD. The flux obtained in this study correlates well with the observations of the bottom water salinity anomalies in the Bay of Puck (Matciak et al., 2015). The SGD rate and its' composition correlated with both short-time scale factors (wind direction and precipitation) and long-timescale factors (seasonal movement of the mixing zone and large-scale sea level variations).

This study demonstrates a need to include SGD as a source of water and, most probably, chemical substances in studies characterizing the functioning of the coastal areas of the Baltic Sea. In order to better understand the generation and fate of SGD in the Bay of Puck and other Baltic Sea coastal areas, further studies are needed.

Acknowledgments

The results reported herein were obtained within the framework of the statutory activities of the Institute of Oceanology Polish Academy of Sciences and the following research projects: PharmSeepage 2016/21/B/ST10/01213, funded by the Polish National Science Center, and WaterPUCK BIOSTRATEG3/343927/3/NCBR/2017, financed by the National

Center for Research and Development (NCBiR) within the BIOSTRATEG III program.

We thank Leszek Łęczyński, Emilia Bublijewska, and Marcin Stokowski for their help in installing piezometers. We are also grateful to Tadeusz Ossowski for help in enabling the laboratory facilities in order to analyze chloride, bicarbonates, and sulphates in water samples. We thank Jolanta Walkusz-Miotk for help in major cations analyses. We thank the anonymous reviewers for their careful reading of our manuscript and their many insightful comments and suggestions.

Supplementary materials

Supplementary material associated with this article can be found, in the online version, at doi:10.1016/j.oceano.2019.09.001.

References

Appelo, C., Postma, D., 2005. Geochemistry, Groundwater and Pollution, 2nd edn. Balkema, Rotterdam, 683 pp., http://dx.doi.org/10.1201/9781439833544.

Bolałek, J., 1992. Ionic macrocomponents of the interstitial waters of Puck Bay sediments. Oceanologia 33, 131—158.

Boudreau, B.P., 1997. Diagenetic Models and Their implementation: Modelling Transport and Reactions in Aquatic Sediments. Springer—Verlag, Berlin, Heidelberg, New York, 414 pp.

Bublijewska, E., Łęczyński, L., Marciniak, M., Chudziak, Ł., Kłostowska, Ż., Zarzeczańska, D., 2017. In situ measurements of submarine groundwater supply from the Puck Lagoon. Prz. Geol. 65 (11—2), 1173—1178.

Burnett, W.C., Bokuniewicz, H., Huettel, M., Moore, W.S., Taniguchi, M., 2003. Groundwater and pore water inputs to the coastal zone. Biogeochemistry 66 (1—2), 3—33, https://doi.org/10.1023/B:BIOG.0000006066.21240.53.

Burnett, W.C., Aggarwal, P.K., Aureli, A., Bokuniewicz, H., Cable, J.E., Charette, M.A., Kontar, E., Krupa, S., Kulkarni, K.M., Loveless, A., Moore, W.S., Oberdorfer, J.A., Oliveira, J., Ozyurt, N., Povinec, P., Privitera, A.M.G., Rajar, R., Ramessur, R.T., Scholten, J., Stieglitz, T., Taniguchi, M., Turner, J.V., 2006. Quantifying submarine groundwater discharge in the coastal zone via multiple methods. Sci. Total Environ. 367 (2—3), 498—543, https://doi.org/10.1016/j.scitotenv.2006.05.009.

Cai, W.—J., Wang, Y.—C., Krest, J., Moore, W.S., 2003. The geochemistry of dissolved inorganic carbon in a surficial groundwater aquifer in North Inlet, South Carolina, and the carbon fluxes to the coastal ocean. Geochim. Cosmochim. Ac. 67 (4), 631—639, https://doi.org/10.1016/S0016-7037(02)01167-5.

Carman, R., Rahm, L., 1997. Early diagenesis and chemical characteristics of interstitial water and sediments in the deep deposition bottoms of the Baltic proper. J. Sea Res. 37 (1—2), 25—47, https://doi.org/10.1016/S1385—1101(96)00003—2.

Charette, M.A., Sholkovitz, E.R., 2002. Oxidative precipitation of groundwater—derived ferrous iron in the subterranean estuary of a coastal bay. Geophys. Res. Lett. 29 (10), 85—1—85—4, https://doi.org/10.1029/2001GL014512.

Charette, M.A., Sholkovitz, E.R., 2006. Trace element cycling in a subterranean estuary: part 2. Geochemistry of the pore water. Geochim. Cosmochim. Ac. 70 (40), 811—826, https://doi.org/10.1016/j.gca.2005.10.019.

Cyberski, J., 1993. Hydrologia zlewiska. In: Korzeniewski, K. (Ed.), Zatoka Pucka. Fundacja Rozwoju Uniwersytetu Gdańskiego, Gdańsk, 40—70.

Hounslow, A.W., 1995. Water Quality Data: Analysis and Interpretation. CRC Press LLC, Lewis Publishers, Boca Raton, 416 pp., https://doi.org/10.1201/9780203734117.

Institute of Meteorology and Water Management (IMGW) database, https://dane.imgw.pl/data, (accessed on 21.08.2019).

Jiao, J., Post, V., 2019. Coastal Hydrogeology. Cambridge University Press, Cambridge, 404 pp., https://doi.org/10.1017/9781139344142.

Kaleris, V., 2018. Submarine groundwater discharge and its influence on the coastal environment. Available from: http://www.coastalwiki.org/wiki/Submarine_groundwater_discharge_and_its_influence_on_the_coastal_environment, (accessed on 20—08—2019).

Kotwicki, L., Grzelak, K., Czub, M., Dellwig, O., Gentz, T., Szymczycha, B., Böttcher, M.E., 2014. Submarine groundwater discharge to the Baltic coastal zone: impacts on the meiofaunal community. J. Marine Syst. 129, 118—126, https://doi.org/10.1016/j.jmarsys.2013.06.009.

Kozerski, B., 2007. In: Jaworska—Szulc, B., Piekarek—Jankowska, H., Pruszkowska, M., Przewłócka, M. (Eds.), Gdański System Wodonośny. Wydawnictwo Politechniki Gdańskiej, Gdańsk, 113 pp.

Krall, L., Trezzi, G., Garcia—Orellana, J., Rodellas, V., Morth, C.—M., Andersson, M., 2017. Submarine groundwater discharge at Forsmark, Gulf of Bothnia, provided by Ra isotopes. Mar. Chem. 196, 162—172, https://doi.org/10.1016/j.marchem.2017.09.003.

Kroeger, K.D., Swarzenski, P.W., Greenwood, J.Wm., Reich, C., 2007. Submarine groundwater discharge to Tampa Bay: nutrient fluxes and biogeochemistry of the coastal aquifer. Mar. Chem. 104 (1—2), 85—97, https://doi.org/10.1016/j.marchem.2006.10.012.

Kryza, J., Kryza, H., Pruszkowska, M., Szczepiński, J., Szlufik, A., Tomaszewski, B., 2005. Dokumentacja hydrogeologiczna określająca warunki bezpośredniego odpływu podziemnego do akwenu bałtyckiego z analizą możliwości zagospodarowania i ochrony wód podziemnych. Integrated Management Services, Wrocław, 138 pp.

Kryza, J., Kryza, H., 2006. The analytic and model estimation of the direct groundwater flow to Baltic sea on the territory of Poland. Geologos 10, 153—166.

Li, L., Barry, D.A., Stagnitti, F., Parlange, J.—Y., 1999. Submarine groundwater discharge and associated chemical input to a coastal sea. Water Resour. Res. 35 (11), 3253—3259, https://doi.org/10.1029/1999WR900189.

Liu, Y., Jiao, J.J., Liang, W., Kuang, X., 2017. Hydrogeochemical characteristics in coastal groundwater mixing zone. Appl. Geochem. 85 (Pt. A), 49—60, https://doi.org/10.1016/j.apgeochem.2017.09.002.

Matciak, M., Bieleninik, S., Botur, A., Podgórski, M., Trzcińska, K., Dragańska, K., Jaśniewicz, D., Kurszewska, A., Wenta, M., 2015. Observations of presumable groundwater seepage occurrence in Puck Bay (the Baltic sea). Oceanol. Hydrobiol. St. 44 (2), 267—272, https://doi.org/10.1515/ohs—2015—0025.

Moore, W.S., 1996. Large groundwater inputs to coastal waters revealed by 226Ra enrichments. Nature 380, 612—614, https://doi.org/10.1038/380612a0.

Moore, W.S., 2010. The effect of submarine groundwater discharge on the ocean. Annu. Rev. Mar. Sci. 2 (1), 59—88, https://doi.org/10.1146/annurev—marine—120308—081019.

Nowacki, J., 1993. Morfometria zatoki. In: Korzeniewski, K. (Ed.), Zatoka Pucka. Inst. Oceanogr., UG, Gdańsk, 71—78.

Oehler, T., Mogollón, J.M., Moosdorf, N., Winkler, A., Kopf, A., Pichler, T., 2017. Submarine groundwater discharge within a landslide scar at the French Mediterranean coast. Estuar. Coast. Shelf Sci. 198, 128—137, http://dx.doi.org/10.1016/j.ecss.2017.09.006.

Peltonen, K., 2002. Direct Groundwater Inflow to the Baltic Sea. TemaNord, Nordic Councils of Ministers, Copenhagen, Netherlands, 79 pp.

Pempkowiak, J., Szymczycha, B., Kotwicki, L., 2010. Submarine groundwater discharge (SGD) to the Baltic Sea. Rocz. Ochr. Środ. 12 (1), 17—32.

Piekarek—Jankowska, H., Łęczyński, L., 1993. Morfologia dna. In: Korzeniewski, K. (Ed.), Zatoka Pucka. Fundacja Rozwoju UG, Gdańsk, 222—281.

Piekarek—Jankowska, H., 1994. Zatoka Pucka jako Obszar Drenażu Wód Podziemnych. Rozp. Monogr. 204, Wyd., UG, Gdańsk, 31—32.

Piekarek—Jankowska, H., 1996. Hydrochemical effects of submarine groundwater discharge to the Puck Bay (southern Baltic Sea, Poland). Geographica Polonica 67, 103—119.

Pietrucień, Cz., 1983. Regionalne Zróżnicowanie Warunków Dynamicznych i Hydrochemicznych Wód Podziemnych w Strefie Brzegowej Południowego i Wschodniego Bałtyku. Wyd. UMK, Toruń, 269 pp.

Piper, A.M., 1994. A graphic procedure in the geochemical interpretation of water analysis. Am. Geophys. Union Trans. 25, 914—923.

Regional Inspectorate for Environmental Protection (http://www.gios.gov.pl/pl/, (accessed on 21.08.2019).

Salem, Z.E., Al Temamy, A.M., Salah, M.K., Kassab, M., 2016. Origin and characteristics of brackish groundwater in Abu Madi coastal area, Northern Nile Delta, Egypt. Estuar. Coast. Shelf Sci. 178, 21—35, https://doi.org/10.1016/j.ecss.2016.05.015.

Santos, I.R., Burnett, W.C., Chanton, J., Mwashote, B., Suryaputra, I.G.N.A., Dittmar, T., 2008. Nutrient biogeochemistry in a Gulf of Mexico subterranean estuary and groundwater—derived fluxes to the coastal ocean. Limnol. Oceanogr. 53 (2), 705—718, https://doi.org/10.4319/lo.2008.53.2.0705.

Schlüter, M., Sauter, E.J., Andersen, C.E., Dahlgaard, H., Dando, P.R., 2004. Spatial distribution and budget for submarine groundwater discharge in Eckernförde Bay (Western Baltic Sea). Limnol. Oceanogr. 49 (1), 157—167, https://doi.org/10.4319/lo.2004.49.1.0157.

Szymczycha, B., Vogler, S., Pempkowiak, J., 2012. Nutrient fluxes via submarine groundwater discharge to the Bay of Puck, southern Baltic Sea. Sci. Total Environ. 438, 86—93, https://doi.org/10.1016/j.scitotenv.2012.08.058.

Szymczycha, B., Maciejewska, A., Winogradow, A., Pempkowiak, J., 2014. Could submarine groundwater discharge be a significant carbon source to the southern Baltic Sea? Oceanologia 56 (2), 327—347, https://doi.org/10.5697/oc.56—2.327.

Szymczycha, B., Kroeger, K.D., Pempkowiak, J., 2016. Significance of groundwater discharge along the coast of Poland as a source of dissolved metals to the southern Baltic Sea. Mar. Pollut. Bull. 109 (1), 151—162, https://doi.org/10.1016/j.marpolbul.2016.06.008.

Urbański, J., Grusza, G., Chlebus, N., 2007. Fizyczna Typologia Dna Zatoki Gdańskiej. Pracownia Geoinformacji Zakładu Oceanografii Fizycznej. Instytut Oceanografii UG, Gdynia, 8 pp.

Uścinowicz, S., Kramarska, R., 2011. Geological setting and bottom sediments in the Baltic Sea. The quaternary basement. In: Uścinowicz, S. (Ed.), Geochemistry of Baltic Sea Surface Sediments. Pol. Geol. Inst. — Nat. Res. Inst., 66—70.

Viventsowa, E.A., Voronow, A.N., 2003. Groundwater discharge to the Gulf of Finland (Baltic Sea): ecological aspects. Environ. Ecol. 45, 221—225.

Oceanologia (2020) 62, 12—22

Available online at www.sciencedirect.com

ScienceDirect

journal homepage: www.journals.elsevier.com/oceanologia/

ORIGINAL RESEARCH ARTICLE

Grain-size characteristics and net transport patterns of surficial sediments in the Zhejiang nearshore area, East China Sea

Juan Liang [a,b,*], **Jian Liu** [c,d], **Gang Xu** [c,d], **Bin Chen** [c,d]

[a] *School of Earth Sciences, China University of Geosciences, Wuhan, China*
[b] *School of Marine Science and Technology, Zhejiang Ocean University, Zhoushan, China*
[c] *Key Laboratory of Marine Hydrocarbon Resources and Environmental Geology, Ministry of Land and Resources, Qingdao, China*
[d] *Qingdao Institute of Marine Geology, Qingdao, China*

Received 11 January 2019; accepted 20 June 2019
Available online 10 July 2019

KEYWORDS
Grain-size trend analysis;
Sediment transport;
Sedimentary rate;
Zhejiang nearshore area

Summary Spatial variations in grain-size parameters can reflect sediment transport patterns and depositional dynamic environments. Therefore, 616 surficial sediment samples taken from the Zhejiang nearshore area in the East China Sea were analyzed to better understand the net sediment transport pattern in this region. The study area is generally dominated by clayey silt and has relatively coarse mud sediment in the southeast. The sorting coefficient of surface sediment is higher than 1.4, and sediment is poorly sorted throughout the study area. The skewness has a strong correlation with the mean grain-size diameter. The net sediment transport pathways obtained by the grain-size trend analysis indicate several distinct characteristics of the surficial sediment transport. The sediment is transported southward under the action of the stronger southward Zhejiang—Fujian Coastal Current (ZMCC) in winter in the upper part of the nearshore area. Influenced by the obstruction of the Taiwan Warm Current (TWC) and the tidal current, surficial sediment transport vectors display two areas of grain-size trend convergence and indicate the net deposition environment has a high sedimentation rate. However, the transport is mainly toward the north under the control of the prevailing northward ZMCC and the strong TWC in the summer. The sedimentary rate is closely related to the processes of the sediment transport. On the one hand, sediment transportation affects the depositional rate in a different

---

* Corresponding author at: School of Marine Science and Technology, Zhejiang Ocean University, 1 Haida South Road, Lincheng Changzhi Island, Zhoushan, Zhejiang, 316022, China. Tel.: +86 580 8186297.
E-mail address: ljzjou@163.com (J. Liang).

Peer review under the responsibility of Institute of Oceanology of the Polish Academy of Sciences.

Production and hosting by Elsevier

https://doi.org/10.1016/j.oceano.2019.06.002

environment. On the other hand, the modern sedimentary rate can reflect indirectly the sediment source and sediment transportation.

1. Introduction

The spatial variations in grain-size parameters are the natural result of the comprehensive effect of sedimentary dynamics processes in the marine environment. Grain-size parameters can intensively reflect local sedimentary environments, such as hydrodynamic conditions, sediment transport, subsidence, and redistribution processes (Folk, 1966; Passega, 1964; Pejrup, 1988). In particular, abundant information about sediment transport is contained in the sediment grain-size data. Therefore, grain-size analysis is extensively applied to distinguish sediment types, recover sediment mechanisms, and discuss sediment environmental evolution (Asselman, 1999; Cartier and Héquette, 2015; Ma et al., 2014; Pedreros et al., 1996; Rosenberger et al., 2016; Roux, 1994). Many geoscientists are trying to identify sedimentary transport directions according to the spatial variation trends in grain-size parameters. The spatial difference in grain-size parameters is defined as the grain size trends analysis and could be regarded as the results of sediment transport and accumulation (McCave, 1978). Three grain-size parameters (mean size, sorting, and skewness) were utilized to develop a one-dimensional trend model, which could identify the net surficial sediment transport pathways (McLaren, 1981; McLaren and Bowles, 1985). Based on an in-depth study of the McLaren model, a two-dimensional trend method was developed to define net sediment transport patterns: the Grain-Size Trend Analysis (Gao, 1996; Gao and Collins, 1991). The results showed that this pattern could mainly reflect actual sediment transport in areas like estuaries, coasts, and continental shelves (Balsinha et al., 2014; Cheng et al., 2004; Yamashita et al., 2018; Zhang et al., 2013).

The East China Sea (ECS) is a marginal sea with a wide, flat continental shelf in the western Pacific Ocean, which is surrounded by the continent of Asia, China's Taiwan Island, the Korean peninsula, the Kyushu of Japan, and Ryukyu Island. The East China Sea Continental Shelf (ECSCS) is one of the best examples of a river-dominated ocean margin, and its sediment mainly comes from the continental river in surrounding areas. The Yangtze River has long been considered the dominant contributor to the inner-shelf mud area in the ECSCS, which is mainly derived from finer suspended sediments and transported southward by the Zhejiang-Fujian Coastal Current (ZMCC) (Guo et al., 2003; Milliman and Meade, 1983). Researchers have carried out many studies considering sedimentation along the ECSCS, obtaining many beneficial findings. Studies have shown that nearly 47% of the Yangtze River-derived sediment has accumulated in the ECSCS, of which approximately 32% has been deposited in the inner shelf along the Zhejiang—Fujian coasts (Dai et al., 2016; Liu et al., 2007; Saito et al., 2001). Due to the continuous input of the terrigenous and sea sediments, the basic distribution pattern of surface sediments in the ECSCS indicated fine-grained sediments in the nearshore shallow sea and middle continental shelf areas, with coarse sediments in the outer continental shelf area (Li et al., 2012). Moreover, by using ^{210}Pb and ^{137}Cs dating methods, studies on centennial deposition rates indicated that the modern sedimentation rate in the coastal area was higher than that offshore (Su and Huh, 2002; Xu et al., 2012). Ultimately, the mud areas are gradually formed and become depositional centers for the modern continental shelf in the ECS (Liu et al., 2007; Xu et al., 2016).

Many previous studies have investigated the relationship between the sediment distribution in the ECSCS and the corresponding ocean dynamical environment. Some researchers have proposed that the position and deposition rate of the muddy deposits in the continental shelf depend on the sediment supply and the transport ability of the marine dynamics (McKee et al., 1983; Xu et al., 2016). The control of eddy dynamics in the region plays an important role for the formation of mud areas (Hu, 1984). A numerical simulation was applied to analyze the mechanisms that control upwelling on the mud sediment, and it is found that the upwelling can increase the depositional process of fine-particle sediments (Qu and Hu, 1993; Zhang et al., 2011). The sediment transport in the ECSCS is strongly influenced by the Taiwan Warm Current (TWC) and the coastal current in the ECS. Moreover, the coastal currents in the ECS are necessary for the formation of the coastal mud area in the inner shelf (Liu et al., 2007; Xu et al., 2009). Based on the sedimentary velocity and granularity of the sediment, the possible generating process of mud areas was better elaborated (Demaster et al., 1985). After analyzing the seasonal variation of suspension sources and vortex dynamics in the mud area to the north of the ECSCS, the results showed that there are obvious seasonal differences in the sedimentation dynamics of the mud area (Wang et al., 2014). According to the in situ observations of the ocean temperature, salinity, flow, and suspension turbidity, the results indicate that the major force driving the sediment to suspend and transport is the tidal current, and the sediment supplied by the Yangtze River is transported southwards along the coast (Sternberg et al., 1985). Satellite remote sensing image data and numerical simulations were also used to study the seasonal differences of the sedimentary processes of the mud areas in the ECSCS, and the results indicated that the inner mechanism has a close relationship with the seasonal variations of the supply from river sediments, marine dynamic factors, and the ocean current system (Moon et al., 2009; Yanagi et al., 1996; Yuan et al., 2008). However, previous studies mostly focused on the relationship between the sedimentation processes with a single influencing factor, especially when sediment transport was analyzed. These previous studies have primarily emphasized the influence of the marine environment on the sediment transport pathway, providing somewhat superficial insight into the effects of sediment transport on the sedimentary environment. Therefore, the objectives of this paper are to (1) clarify the changes in the surficial sediment distributions in the Zhejiang nearshore area; (2) illuminate the sediment transport patterns by grain-size trend analysis; and (3) expound on explicating the interaction between surficial sediment transport patterns and the marine deposition environment. In addition, combining the results with long-term accumulation rates based on ^{210}Pb dating helps improve understanding of erosion and deposition in the nearshore mud area.

2. Regional setting

This study area lies in the southwest of the ECSCS between 28°N—31°N and 121°30′E—123°E (Fig. 1). The northern coast of the Zhejiang Province is located in the southern wing of the Yangtze River Delta and Qiantang River Estuary Plain, while southern regions are the low hilly shoreline of volcanic rock (Fig. 2). The terrain of the nearshore area slopes downward from northwest to southeast and until plunges down to the East China Sea, with some mountains becoming islands. The Zhoushan Archipelago, adjacent to the Yangtze Estuary and Hangzhou Bay, is northwest of the study area. Islands are scattered in the Zhoushan sea area, where fjords are plentiful between the islands and the water depth is greater. There are large and small mountainous river dispersal systems, such as the Qiantang River. Large amounts of sediment from these rivers are transported to the nearshore area, with a part of sediment originating from the Yangtze Estuary. The twists and turns of the nearshore area create a coastline of more than 6000 km, distributed with bays like the Hangzhou, Xiangshan, Sanmen, Taizhou, and Yueqing Bays. The coastal types of Zhejiang Province could be generalized into the muddy (about 50% of total length), bedrock (40%), and sand coast (4%). Under the influence of the hydrodynamic condition and sediment source, these coasts have obvious seasonal variations: erosion in summer and deposition in winter.

The climate factors, such as heat, temperature, precipitation, and evapotranspiration, vary obviously with seasonal and latitudinal changes. The annual temperature increases from the north to the south, varying from 16 to 21°C. The annual rainfall is between 900 and 1300 mm, with a tendency to be higher in the south and lower in the north in coastal regions. The main tidal characteristics are mixed semidiurnal tides with medium tide ranges and high current velocities. The flood currents come from the outer shelf and flow toward the nearshore area, while the ebb currents have the opposite behavior. Moreover, this area is often threatened by typhoons and strong tropical storms. Surge waves are more frequent

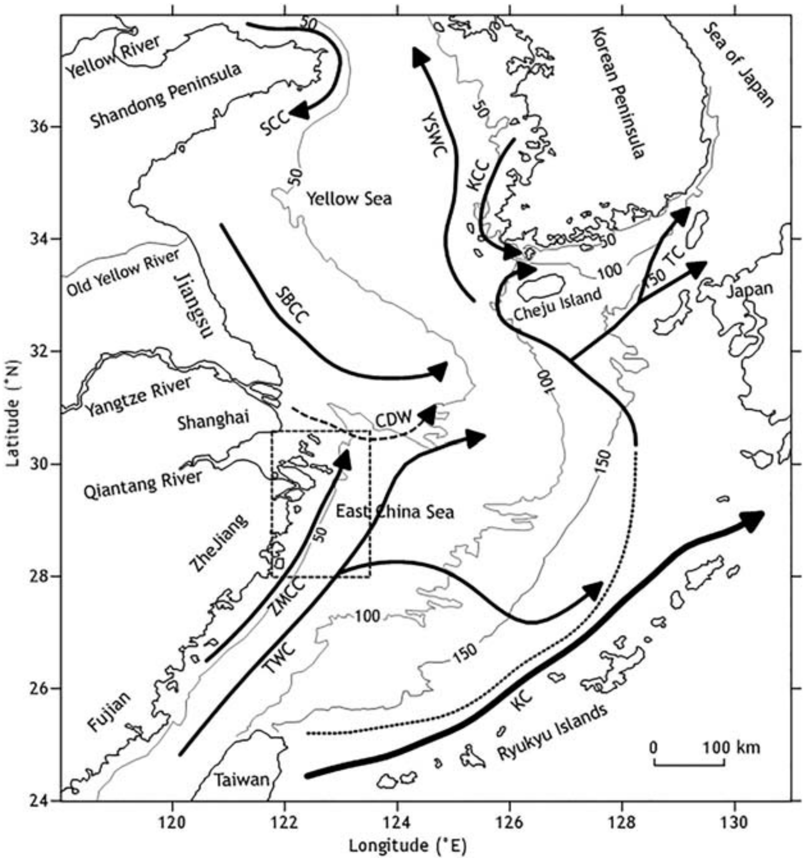

Figure 1 Schematic map of the bathymetry and regional circulation pattern in the ECSCS and adjacent areas during summertime (modified after Liu et al., 2010). Water depth in meters. The dashed square indicates the study area. SSCC, South Shandong Coastal Current; YSWC, Yellow Sea Warm Current; KCC, Korean Coastal Current; NJCC, North Jiangsu Coastal Current; CDW, Changjiang (Yangtze River) Diluted Water; ZMCC, Zhejiang—Fujian Coastal Current; TWC, Taiwan Warm Current; KC, Kuroshio Current; TC, Tsushima Current.

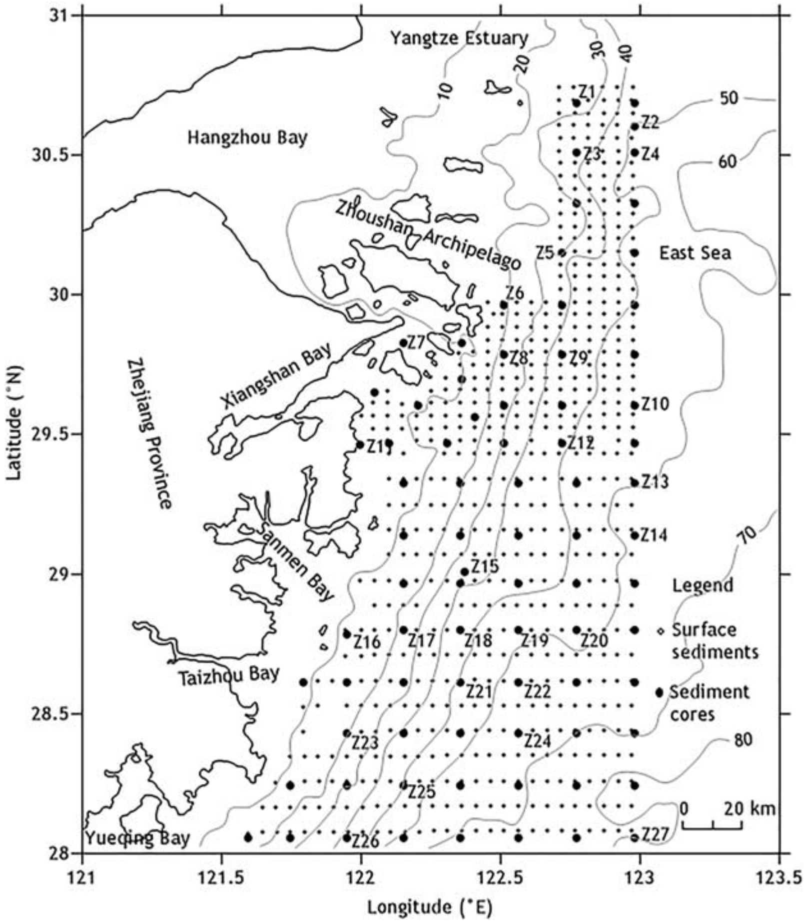

Figure 2 Location of the surface sediment and columnar core samples in the Zhejiang nearshore area. Water depth in meters. (The numbered core samples were chosen for ^{210}Pb and ^{137}Cs experiments.)

than wind waves affected by the southeasterly winds (Liu et al., 2006; Zhang et al., 2014).

The general current circulation system in the study area is dominated by the KC, TWC, and coastal current (Fig. 1). The KC, which originates from the north equatorial warm current, intrudes onto the ECSCS on the large scale and flows northeast along the edge of the continental shelf (Andres et al., 2008; Li et al., 2013; Zheng and Huang, 1993). The TWC is parallel to the KC and is characterized by a high temperature, high salinity, and low turbidity, and it flows northward all year round along the coast, with stronger currents in the summer than in the winter (Fang et al., 1991). The ZMCC is formed in a seashore environment and flows northward in the summer and southward in the winter due to monsoons (Su, 2001). The circulation patterns mentioned above control the sediment transport processes and affect the sediment framework in the study area.

3. Material and methods

3.1. Field sampling

616 surficial sediment samples were collected with box core from the Zhejiang nearshore area on board of the R/V *Yezhizheng* in June 2013 (Fig. 2). The positions of the samples were determined using a differential GPS system. The samples were about 3 cm thick and were taken from the superficial layer of each box core, and 10 g samples were chosen for the grain-size analytical experiment. Meanwhile, 80 columnar cores (2.2—3.5 m long each) were collected with a vibrocorer. According to the geological and topographic features of the study area, 27 columnar cores were chosen for ^{210}Pb and ^{137}Cs experiments.

3.2. Grain size experiment

The samples were pretreated with 10% H_2O_2 and 0.1 N HCl to remove organic matter and biogenic carbonate, respectively. Then, the samples were dispersed with 0.5% $(NaPO_3)_6$ and subsequent ultrasonic dispersion. The grain size was measured with a Malvern Mastersizer 2000 Laser particle size analyzer (Malvern Instruments Ltd., UK), with a measuring range from 0.02 to 2000 μm, a particle resolution of 0.01 ϕ, and relative error of $<2\%$. Three main grain-size parameters, including mean diameter (μ), sorting coefficient (σ), and skewness (Sk), were calculated using the statistic moment method (McManus, 1988):

$$\mu = \sum_{1}^{n} P_i S_i, \tag{1}$$

$$\sigma = \left[\sum_{1}^{n} P_i (S_i - \mu)^2\right]^{1/2}, \tag{2}$$

$$Sk = \left[\sum_{1}^{n} P_i (S_i - \mu)^3\right]^{1/3}, \tag{3}$$

where S_i is the size class, P_i is the percentage of size S_i (in ϕ units), and n is the total number of size classes. The Shepard classification scheme (Shepard, 1954) was adopted in this study to describe the sediment types of surficial sediment samples.

3.3. Columnar cores and ^{201}Pb dating

The subsamples of 27 columnar cores for ^{210}Pb, ^{226}Ra, and ^{137}Cs analysis were selected at 5—10 cm intervals to calculate sediment accumulation rates for the sample sites. ^{210}Pb activities were determined by a BE3830 gamma-ray spectrometer (CANBERRA Ltd., USA) following a standard operation procedure (Xia et al., 2011), and the uncertainties associated with sample measurements were typically less than 10%. Supported ^{210}Pb activities were assumed to be equal to the measured ^{226}Ra activities, and excess ^{210}Pb activities were calculated by subtracting the supported ^{210}Pb activities from the total ^{210}Pb activities measured (Pfitzner et al., 2004). The influence of grain-size variations on the ^{210}Pb activities was eliminated by normalizing the ^{210}Pb activities to the corresponding clay (<4 μm) content of each sample (Palinkas et al., 2006). The sediment accumulation rates were calculated by means of a Constant Initial Concentration model (Oldfield et al., 1978). Analyses of grain size and ^{210}Pb dating experiments were carried out at the Center of Testing, Qingdao Institute of Marine Geology, China Geological Survey.

3.4. Grain-size trend analysis

Grain-size trends were calculated in this study by operating the two-dimensional model that can describe net sediment transport patterns (Gao and Collins, 1994). This method is based on the assumption that the trend used for the analysis has a significantly higher probability of occurrence in the direction of net transport than in any other directions (Gao, 1996). It tries to identify the possible net transport paths by comparing two neighboring sampling sites. By employing the three most frequently used grain-size parameters (μ, σ, and Sk), the most appropriate grain-size trends for trend analysis can be found (Gao and Collins, 1994). Then, by comparing the three grain-size parameters between the two nearest neighboring stations within a characteristic distance, a dimensionless trend vector is defined. The vector has a unit length and points from the station with the higher sorting coefficient toward that with the lower sorting value. Each of the two neighboring stations are compared in a grid of surficial sediment samples, and all of the grain-size trend vectors are generated. A single resultant vector is produced after summing the identified trend vector at each sampling station and its neighboring stations. This resultant vector represents the tendency of the sediment transport at the station. Finally, a smoothing operation is performed to remove background noise by averaging the resultant vector at any sampling station and the resultant vectors of its neighboring stations to produce a residual vector. The transport vector maps can successfully reflect the net sediment transport trend via this sequence of steps.

4. Results and discussion

4.1. Sediment compositions and distributions patterns

Surface sediments were classified and plotted in a ternary diagram of sand ($>$0.063 mm), silt (0.004—0.063 mm), and clay ($<$0.004 mm) contents (Fig. 3). Five primary sediment types occur in the Zhejiang nearshore area: clayey silt (YT), sand-silt-clay (STY), silty sand (TS), silt (T), and fine sand (FS) (Fig. 4). YT is the dominant sediment type (74% of all 616 surficial sediment samples) and is primarily deposited in the center of the nearshore area with a NE—SW banding distribution, which is also known as the mud area in shallow sea water. T (2%) is scattered along the coastline and mainly originates from the Yangtze River and some mountain rivers. From the center to the eastern deep water more than 50 m, STY (16%), TS (6%), and FS (2%) gradually become present, and sediments become gradually coarser in grain size. Overall, there are coarse-fine-coarse gradations in the grain sizes of the sediments from the nearshore to the offshore.

The distributions of size fraction components (sand, silt, and clay) correspond well with those of the surficial sediment types (Fig. 4). The sand component is distributed much less widely, mainly in the offshore area, compared with the silt and clay in the study area (Fig. 5a). The high content of the sand component benefits from the contributions of residual sand sediment from the ECSCS (Niino and Emery, 1961; Shen, 1986). The silt component is distributed in the western nearshore area and presents a zonal distribution, ranging from 50% to 70%. A relatively high silt component appears near the Zhejiang coast, which is abundant in terrigenous sediment supply transported by the ZMCC and some mountain rivers (Fig. 5b). The clay component (average 28%) is generally distributed in the middle of the Zhejiang nearshore

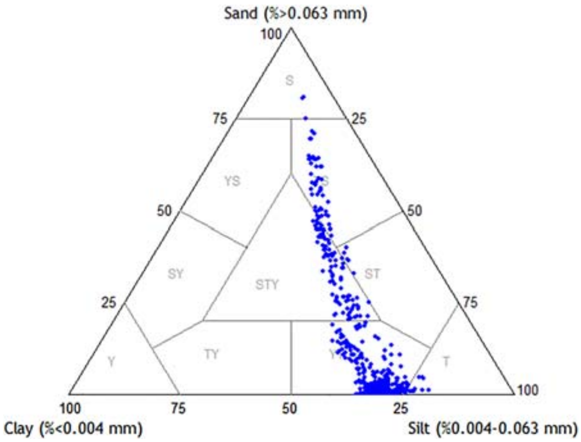

Figure 3 Ternary diagram of sand/silt/clay proportions of samples in the Zhejiang nearshore area (S, sand; T, silt; Y, clay; YS, clayey sand; TS, silty sand; SY, sandy clay; S-T-Y, sand-silt-clay; ST, sandy silt; TY, silty clay; YT, clayey silt).

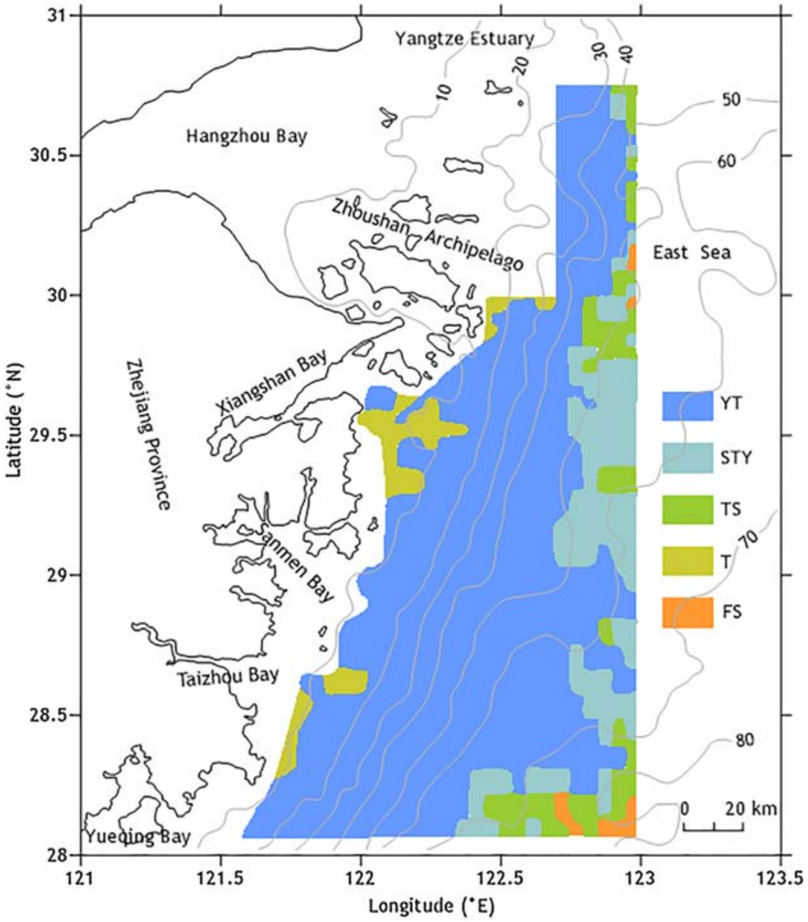

Figure 4 Spatial distribution of the surficial sediment types in the Zhejiang nearshore area. Water depth in meters.

area, known as the mud area in the inner shelf (Fig. 5c) (Liu et al., 2007; Xu et al., 2016). The clay content gradually diminishes toward the edges of the center area.

4.2. Log-ratio and correlation analysis of grain-size parameters

The spatial distribution of the mean diameter of the surface sediments shows a clear coarse-fine-coarse trend from the shallow water to the deep water of the nearshore area (Fig. 6a). The mean diameters of the surface sediments vary generally from 2.9 ϕ to 7.5 ϕ and reach their peaks at the center region, which is the mud area in the nearshore area. The surface sediment becomes coarser with increasing distance from the nearshore region. Finally, the coarsest sediments (<3 ϕ) occur in the southeastern regions of the nearshore area. The sorting coefficients of surface sediment are generally larger than 1.3, indicating relatively poor

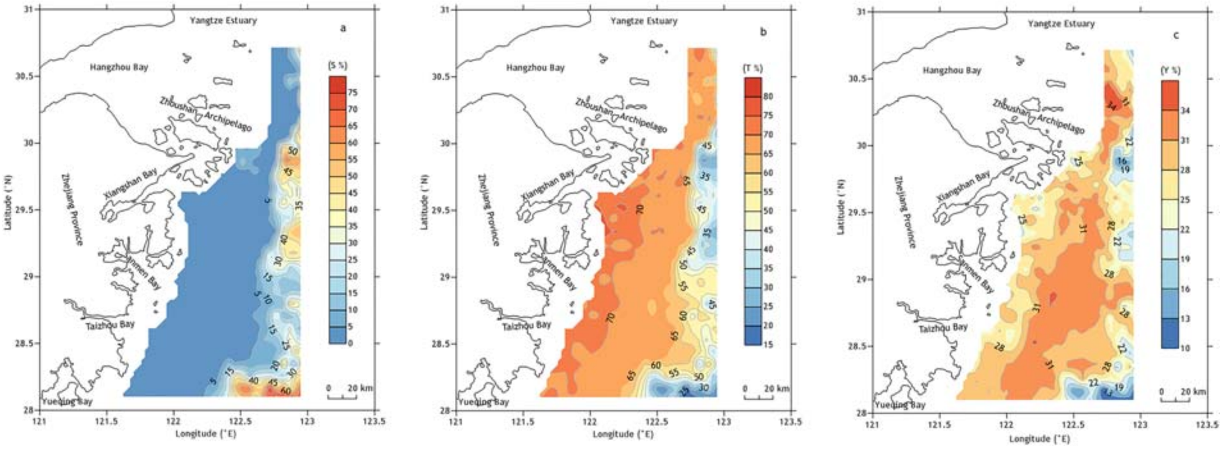

Figure 5 Spatial distributions of the contents of the sand (a), silt (b), and clay (c) in the Zhejiang nearshore area.

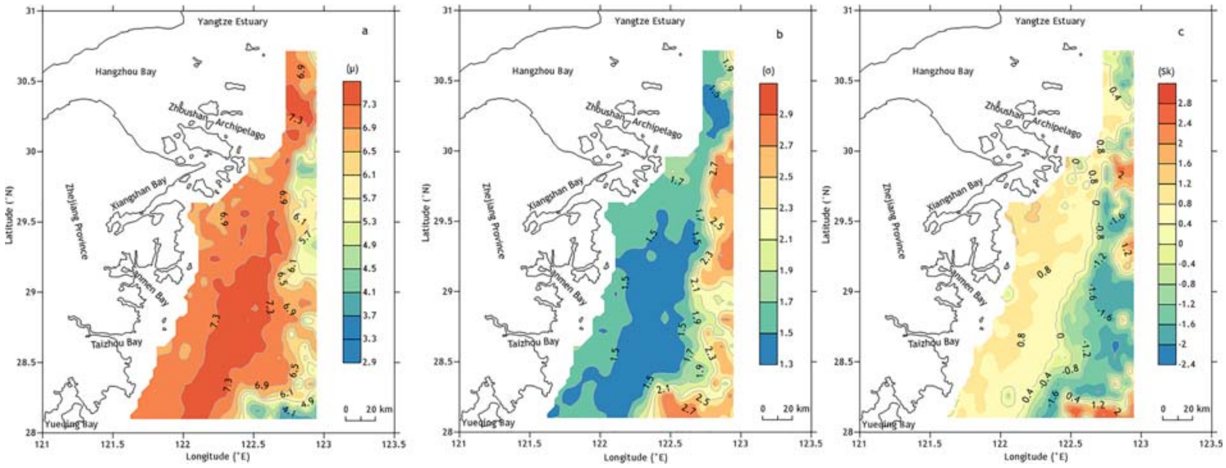

Figure 6 Spatial distributions of the mean diameter of the surface sediment (a), the sorting coefficient (b), and the skewness (c) in the Zhejiang nearshore area.

sorting in the study area (Fig. 6b). However, the sorting is relatively better in the southeastern regions with the distribution of the coarser sediments. The spatial distribution of the sorting coefficient is similar to that of the mean size. Size distributions in the study area are almost symmetrical, with values of skewness varying from −2.4 to 2.8 (Fig. 6c). Higher values are generally located at the two sides of the center mud area. And lower values occur over the central eastern parts. The main factors affecting the spatial distribution of grain-size parameters are sediment sources and characteristics, hydrodynamic conditions, and topography features.

The correlativity between the sorting coefficient, skewness, and mean diameter is presented in Fig. 7. As the mean diameter decreases from 3 ϕ to 6 ϕ, the sorting coefficient of surface sediments keeps the high value from 2.4 to 2.8 and generally does not change obviously (Fig. 7a). However, with the further decrease in mean diameter from 6 ϕ to 8 ϕ, it seems a sorting improves. The skewness has a strong correlation with the mean grain diameter. For surface sediments with a median diameter of 3—5.5 ϕ, their skewnesses are positively skewed (Fig. 7b). When the median grain diameter is higher than 6 ϕ, the sediment size distributions become more negatively skewed, with part cases of positive skewness. Overall, it shows that the skewness changes from positive to symmetrical and then to negative with the decrease in median grain diameter. These tendencies of

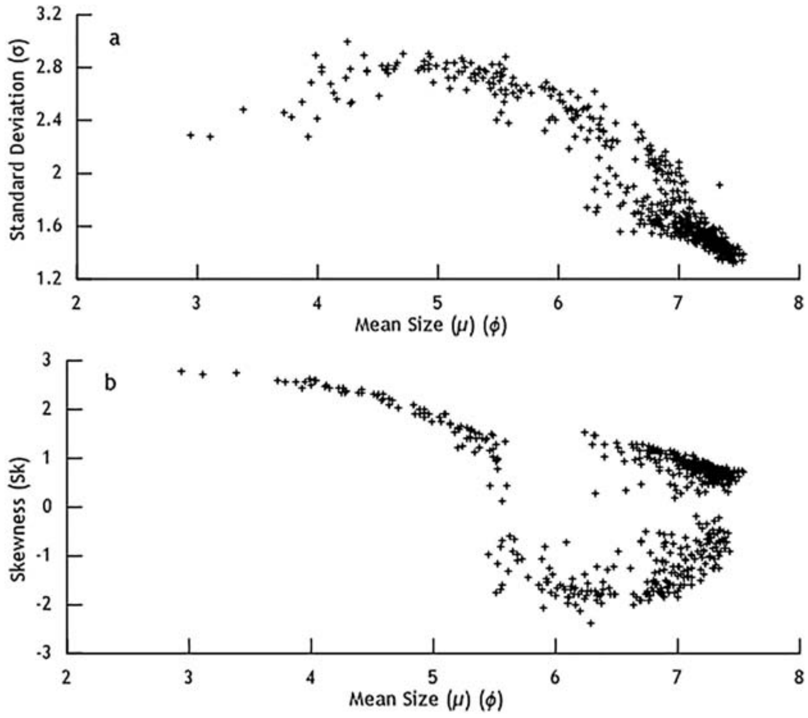

Figure 7 Relationship between mean size (ϕ) and sorting (a), and mean size (ϕ) and skewness (b) in the Zhejiang nearshore area.

the skewness change are probably related to the accumulation and erosion of the sedimentary environment in the study area.

4.3. Net sediment transport pathways

The net sediment transport patterns, obtained by the grain-size trend analysis, reveal several distinct characteristics in the Zhejiang nearshore area (Fig. 8). The arrows indicate the direction of sediment transport. The lengths of the resultant vectors do not represent the intensity of sediment transport but rather the significance of transport trends (Gao and Collins, 1994). The surficial sediment transport seems relatively complicated due to the comprehensive influence of the topographical conditions, hydrodynamic characteristics, and sediment sources in the study area.

In the northeastern Zhoushan Archipelago area, the sediment is clearly transported southward due to the stronger southward ZMCC prevailing in winter. Meanwhile, both the velocity and duration of the flood-tide are larger than those of the ebb-tide under the influence of the funnel shape topography of Hangzhou Bay. This can be seen from the distribution trends of the bathymetric contour (Fig. 2). Affected by the transportation function of the tidal current flowing from the outer shelf to Hangzhou Bay, the accumulation of sediment supplied mainly from the Yangtze River occurs in this region. Transport trends in this region also show that there is a depositional environment with a convergence of the transport vectors. Likewise, in the southern Zhoushan Archipelago area, the sediments are transported southeastward through some fjords between these islands. There is also a significant convergence, counter-balanced by the TWC and the coastward flood current.

To the south of Sanmen Bay, the residual vector pattern shows northeastward transport along the coast because the surficial sediment transport is a comprehensive and long-term system process. The ZMCC is dominant northward in the summer (Su, 2001). Moreover, the powerful TWC flows northward through the Taiwan Strait, preventing the sediments transported by the ZMCC from continuing seaward transport. The seasonality of these currents helps to determine the paths of transport. Therefore, the sediments are transported toward the northeast along the coast in this region. However, it can clearly be seen that the vectors display a northwestern trend in the eastern part of this area. Surficial sediment transport is controlled by the combined effects of the TWC and a tidal current flowing from the sea, which results in the surface sediment being transported northwestward. Thus, transport trends in this region also indicate a smaller convergence.

In addition, it is worth mentioning that the nearshore upwelling plays a significant role in intensifying the sediment transportation pattern toward the coast in some periods. Some studies have shown that the sea-bottom upwelling can prompt the fine particles from the outer shelf to be transported and deposited toward the coast (Hu, 1984; Qu and Hu, 1993; Wang et al., 2014). Under the control of the sediment transport process mentioned above, the sediments from the Yangtze River and other sources are accumulated along the coast in the study area, with enormous thickness deposition (referred to as mud belt deposit) on the inner shelf of the ECS (Liu et al., 2014).

4.4. Spatial distributions of sedimentation rate

The spatial distribution of ^{210}Pb sediment accumulation rates in the study area is shown in Fig. 9. Generally, the sedimentation rate gradually decreases from north to south. The highest rates are seen in the Zhoushan Archipelago area, dominantly varying from 2.4 to 3.9 cm/a, and the lowest are

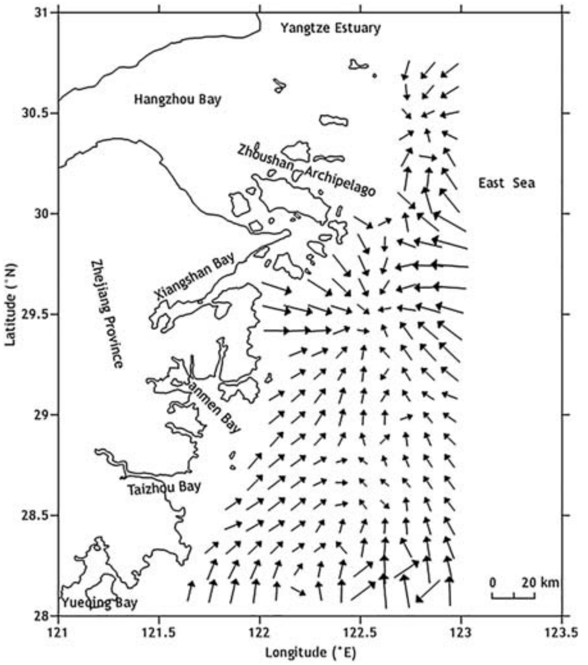

Figure 8 Distribution of residual transport vectors in the Zhejiang nearshore area.

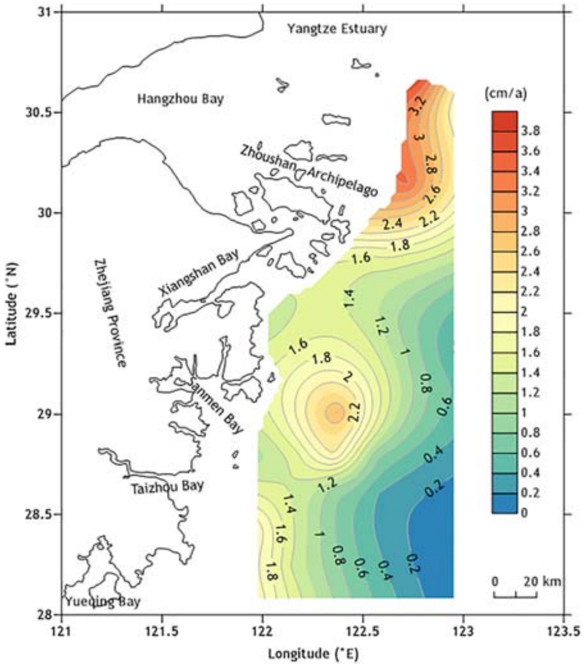

Figure 9 Spatial distribution variation in the modern sedimentary rate in the Zhejiang nearshore area.

seen at the southeastern outer shelf at less than 0.2 cm/a. Then the sedimentation rate declines from nearshore to offshore, both in the northern and southern regions. However, the deposition rate is relatively high (2.8 cm/a) in the central part of the study area and gradually declines from the center to the coast and offshore areas. Some previous studies have shown similar results along the coast of the ECS (Chen et al., 2004; Demaster et al., 1985; Liu et al., 2006; Su and Huh, 2002). Overall, the shoreward shallow area is a high modern sedimentary rate area in water less than 40 m deep (Figs. 9 and 2). From nearshore to offshore, the depositional rate is gradually reduced with increasing water depth. Finally, the sedimentary rate is almost zero with a depth of more than 70 m, which is presumably associated with erosion.

The sediment transport pathway is important because it determines the topography of the nearshore area. However, the sedimentation rate is a key parameter for the evolution of erosion and deposition in marine topography. The spatial distributions of sedimentation rate are closely related to the sediment sources, hydrodynamic conditions, and sediment transport. In the waters adjacent to the Zhoushan Archipelago and Xiangshan Bay, a large amount of sediment from the Yangtze River is transported southward under the control of the ZMCC and deposited rapidly, which leads to high sedimentation rates. Accordingly, the transport trends in the high modern sedimentation rate area also show that there is a depositional environment with the convergence of the transport vectors (Fig. 8).

In the southern area of Sanmen Bay, the TWC prevents the suspended sediment from being further transported to the outer shelf in the ECS. The thick, finer sedimentary layers occur in the nearshore area, which are known as the mud area in the inner shelf. Previous studies have revealed that mud areas are the depositional center during high sea levels since the last deglaciation period (Li et al., 2012; Liu et al., 2007; Xu et al., 2012). When it comes to the sand composition deposited in the southeastern Zhejiang nearshore area, the lowest sedimentation rate appears and approaches zero (Figs. 4 and 9). This is influenced by the residual sand in the middle and outer shelves of the ECS (Wang et al., 2012). The residual sediments belong to the marine sedimentary environment in the last stage of the late Pleistocene and are reformed by modern marine dynamics. Ultimately, a coarser reconstructive deposition called the residual sand is left in place, and the suspended finer sediment is carried by the flood current to the nearshore area (Liu, 1987; Xu et al., 2009).

5. Conclusions

Surface sediments of the Zhejiang nearshore area were analyzed in this study in order to better understand the sediment transport process. Grain-size distributions of the surface sediment show a mud area and the domination of clayey silt. Generally, the mean diameters of the surface sediments display an apparent coarse-fine-coarse trend from the shallow water to the deep water of the nearshore area. However, the sorting coefficient of surface sediments is relatively high, and sediment is poorly sorted over the study area. There is no significant correlation between the sorting coefficient and the medium grain diameter. Nevertheless, the skewness has a strong correlation with the mean grain diameter. Coarse sediment is associated with higher skewness of the corresponding size distribution, while the size distribution of finer sediment shows a relatively lower skewness.

The grain-size trend analysis was employed to ascertain the net surficial sediment transport pattern in the Zhejiang nearshore area. The results reveal that the sediment transport is closely related to the sediment sources, hydrodynamic conditions, and topographical features in the ECSCS. There are several distinct characteristics of the surficial sediment transport. In the northern part of the study area, sediments are transported southward under the action of the stronger southward ZMCC in the winter. Simultaneously being affected by the obstruction of the TWC and the tidal current, surficial sediment transport vectors display two grain-size trend convergences and indicate a high-speed sedimentation environment. Accordingly, there is a high modern sedimentation rate in this region. In the southern part, however, the transport is mainly toward the north under the control of the prevailing northward ZMCC and the strong TWC in summer. The surficial sediment transport trends agree well with the sedimentation rate distribution pattern on the basis of the ^{210}Pb dating data, which implies that the sedimentation rate validates the results of the grain-size trend analysis and makes up for the disadvantages of the grain trend size analysis in predicting erosion and deposition of the topography. The results of this study only represent long-term average sediment transport. Further studies should pay attention to the specific exchange process between surface sediment and suspended sediment.

Acknowledgments

This research was financially supported by the National Basic Research Program of China (Grant No. GZH201200506), the China-ASEAN maritime cooperation fund: Comparative study of Holocene Sedimentary Evolution of the Yangtze River Delta and the Red River Delta. We thank the fieldwork group and laboratory staff of the program for this contribution. This manuscript benefited from comments and suggestions from Prof. Janusz Pempkowiak and two anonymous reviewers.

References

Andres, M., Wimbush, M., Park, J.H., Chang, K.I., Lim, B.H., Watts, D.R., Ichikawa, H., Teague, W.J., 2008. Observations of Kuroshio flow variations in the East China Sea. J. Geophys. Res. 113 (C5) C05013, 14 pp., http://dx.doi.org/10.1029/2007JC004200.

Asselman, N.E.M., 1999. Grain-size trends used to assess the effective discharge for floodplain sedimentation, River Waal, the Netherlands. J. Sediment. Res. A 69 (1), 51—61, http://dx.doi.org/10.2110/jsr.69.51.

Balsinha, M., Fernandes, C., Oliveira, A., Rodrigues, A., Taborda, R., 2014. Sediment transport patterns on the Estremadura Spur continental shelf: insights from grain-size trend analysis. J. Sea Res. 93, 28—32, http://dx.doi.org/10.1016/j.seares.2014.04.001.

Cartier, A., Héquette, A., 2015. Vertical distribution of longshore sediment transport on barred macrotidal beaches, northern France. Cont. Shelf Res. 93, 1—16, http://dx.doi.org/10.1016/j.csr.2014.11.009.

Chen, Z., Saito, Y., Kanai, Y., Wei, T., Li, L., Yao, H., Wang, Z., 2004. Low concentration of heavy metals in the Yangtze estuarine sediments, China: a diluting setting. Estuar. Coast. Shelf Sci. 60 (1), 91—100, http://dx.doi.org/10.1016/j.ecss.2003.11.021.

Cheng, P., Gao, S., Bokuniewicz, H., 2004. Net sediment transport patterns over the Bohai Strait based on grain size trend analysis. Estuar. Coast. Shelf Sci. 60 (2), 203—212, http://dx.doi.org/10.1016/j.ecss.2003.12.009.

Dai, Z., Fagherazzi, S., Mei, X., Gao, J., 2016. Decline in suspended sediment concentration delivered by the Changjiang (Yangtze) River into the East China Sea between 1956 and 2013. Geomorphology 268, 123—132, http://dx.doi.org/10.1016/j.geomorph.2016.06.009.

Demaster, D.J., Mckee, B.A., Nittrouer, C.A., Qian, J., Cheng, G., 1985. Rates of sediment accumulation and particle reworking based on radiochemical measurements from continental shelf deposits in the East China Sea. Cont. Shelf Res. 4 (1), 143—158, http://dx.doi.org/10.1016/0278-4343(85)90026-3.

Fang, G., Zhao, B., Zhu, Y., 1991. Water volume transport through the Taiwan Strait and the continental shelf of the East China Sea measured with current meters. Elsev. Oceanogr. Ser. 54, 345—358, http://dx.doi.org/10.1016/S0422-9894(08)70107-7.

Folk, R.L., 1966. A review of grain-size parameters. Sedimentology 6 (2), 73—93, http://dx.doi.org/10.1111/j.1365-3091.1966.tb01572.x.

Gao, S., 1996. A FORTRAN program for grain-size trend analysis to define net sediment transport pathways. Comput. Geosci. 22 (4), 449—452, http://dx.doi.org/10.1016/0098-3004(95)00100-X.

Gao, S., Collins, M., 1991. A critique of the “McLaren Method” for defining sediment transport paths. J. Sediment. Petrol. 61 (1), 143—146, http://dx.doi.org/10.1306/D42676A9-2B26-11D7-8648000102C1865D.

Gao, S., Collins, M., 1994. Net sediment transport patterns inferred from grain-size trends, based upon definition of “transport vectors” — reply. Sediment. Geol. 90 (1—2), 157—159, http://dx.doi.org/10.1016/0037-0738(94)90023-X.

Guo, Z., Yang, Z., Fan, D., Pan, Y., 2003. Seasonal variation of sedimentation in the Changjiang Estuary mud area. J. Geogr. Sci. 13 (3), 348—354, http://dx.doi.org/10.1007/bf02837510.

Hu, D., 1984. Upwelling and sedimentation dynamics: I. The role of upwelling in sedimentation in the Huanghai Sea and East China Sea — a description of general features. Chin. J. Oceanol. Limnol. 2 (1), 12—19, http://dx.doi.org/10.1007/BF02888388.

Li, J., Wei, H., Zhang, Z., Lu, Y., 2013. A modelling study of interannual variation of Kuroshio intrusion on the shelf of East China Sea. J. Ocean Univ. China 12 (4), 537—548, http://dx.doi.org/10.1007/s11802-013-2203-z.

Li, P., Yang, S.L., Milliman, J.D., Xu, K.H., Qin, W.H., Wu, C.S., Chen, Y.P., Shi, B.W., 2012. Spatial, temporal, and human-induced variations in suspended sediment concentration in the surface waters of the Yangtze Estuary and adjacent coastal areas. Estuar. Coast. 35 (5), 1316—1327, http://dx.doi.org/10.1007/s12237-012-9523-x.

Liu, J., Saito, Y., Kong, X., Wang, H., Xiang, L., Wen, C., Nakashima, R., 2010. Sedimentary record of environmental evolution off the Yangtze River estuary, East China Sea, during the last $\sim$13,000 years, with special reference to the influence of the Yellow River on the Yangtze River delta during the last 600 years. Quaternary Sci. Rev. 29 (17—18), 2424—2438, http://dx.doi.org/10.1016/j.quascirev.2010.06.016.

Liu, J.P., Li, A.C., Xu, K.H., Velozzi, D.M., Yang, Z.S., Milliman, J.D., DeMaster, D.J., 2006. Sedimentary features of the Yangtze River-derived along-shelf clinoform deposit in the East China Sea. Cont. Shelf Res. 26 (17—18), 2141—2156, http://dx.doi.org/10.1016/j.csr.2006.07.013.

Liu, J.P., Xu, K.H., Li, A.C., Milliman, J.D., Velozzi, D.M., Xiao, S.B., Yang, Z.S., 2007. Flux and fate of Yangtze River sediment delivered to the East China Sea. Geomorphology 85 (3—4), 208—224, http://dx.doi.org/10.1016/j.geomorph.2006.03.023.

Liu, S., Shi, X., Fang, X., Dou, Y., Liu, Y., Wang, X., 2014. Spatial and temporal distributions of clay minerals in mud deposits on the inner shelf of the East China Sea: implications for paleoenvironmental changes in the Holocene. Quatern. Int. 349, 270—279, http://dx.doi.org/10.1016/j.quaint.2014.07.016.

Liu, X., 1987. Relict sediments in China continental shelf. Mar. Geol. Quat. Geol. 7 (1), 1—14, http://en.cnki.com.cn/Article_en/CJFDTOTAL-HYDZ198701000.

Ma, X., Yan, J., Fan, F., 2014. Morphology of submarine barchans and sediment transport in barchans fields off the Dongfang coast in Beibu Gulf. Geomorphology 213 (10), 213—224, http://dx.doi.org/10.1016/j.geomorph.2014.01.010.

McCave, I.N., 1978. Grain-size trends and transport along beaches; example from eastern England. Mar. Geol. 28 (1—2), 43—51, http://dx.doi.org/10.1016/0025-3227(78)90092-0.

McKee, B.A., Nittrouer, C.A., Demaster, D.J., 1983. Concepts of sediment deposition and accumulation applied to the continental shelf near the mouth of the Yangtze River. Geology 11 (11), 631—633, http://dx.doi.org/10.1130/0091-7613(1983)11<631:COSDAA>2.0.CO;2.

McLaren, P., 1981. An interpretation of trends in grain size measures. J. Sediment. Res. 51 (2), 0611—0624, http://dx.doi.org/10.1306/212F7CF2-2B24-11D7-8648000102C1865D.

McLaren, P., Bowles, D., 1985. The effects of sediment transport on grain-size distributions. J. Sediment. Res. 55 (4), 0457—0470, http://dx.doi.org/10.1306/212F86FC-2B24-11D7-8648000102C1865D.

McManus, J., 1988. Grain size determination and interpretation. In: Tucker, M. (Ed.), Techniques in Sedimentology. Blackwell, Oxford, 63—85, https://ci.nii.ac.jp/naid/10004029583/en.

Milliman, J.D., Meade, R.H., 1983. World-wide delivery of river sediment to the oceans. J. Geol. 91 (1), 1—21, http://dx.doi.org/10.1086/628741.

Moon, J.-H., Pang, I.-C., Yoon, J.-H., 2009. Response of the Changjiang diluted water around Jeju Island to external forcings: a modeling study of 2002 and 2006. Cont. Shelf Res. 29 (13), 1549—1564, http://dx.doi.org/10.1016/j.csr.2009.04.007.

Niino, H., Emery, K.O., 1961. Sediments of shallow portions of East China Sea and South China Sea. Geol. Soc. Am. Bull. 72 (5), 731—762, http://dx.doi.org/10.1130/0016-7606(1961)72[731:SOSPOE]2.0.CO;2.

Oldfield, F., Appleby, P.G., Battarbee, R.W., 1978. Alternative ^{210}Pb dating: results from the New Guinea Highlands and Lough Erne. Nature 271 (5643), 339—342, http://dx.doi.org/10.1038/271339a0.

Palinkas, C.M., Nittrouer, C.A., Walsh, J.P., 2006. Inner-shelf sedimentation in the Gulf of Papua, New Guinea: a mud-rich shallow shelf setting. J. Coastal Res. 224 (4), 760—772, http://dx.doi.org/10.2112/03-0086.1.

Passega, R., 1964. Grain size representation by CM patterns as a geologic tool. J. Sediment. Res. 34 (4), 830—847, http://dx.doi.org/10.1306/74D711A4-2B21-11D7-8648000102C1865D.

Pedreros, R., Howa, H.L., Michel, D., 1996. Application of grain size trend analysis for the determination of sediment transport pathways in intertidal areas. Mar. Geol. 135 (1—4), 35—49, http://dx.doi.org/10.1016/S0025-3227(96)00042-4.

Pejrup, M., 1988. The triangular diagram used for classification of estuarine sediments: a new approach. In: de Boer, P.L., van Gelder, A., Nio, S.D. (Eds.), Tide-Influenced Sedimentary Environments and Facies. Reidel, Dordrecht, 289—300, http://dx.doi.org/10.1007/978-94-015-7762-5_21.

Pfitzner, J., Brunskill, G., Zagorskis, I., 2004. ^{137}Cs and excess ^{210}Pb deposition patterns in estuarine and marine sediment in the central region of the Great Barrier Reef Lagoon, north-eastern Australia. J. Environ. Radioactiv. 76 (1—2), 81—102, http://dx.doi.org/10.1016/j.jenvrad.2004.03.020.

Qu, T., Hu, D., 1993. Upwelling and sedimentation dynamics II. A simple model. Chin. J. Oceanol. Limnol. 11 (14), 289—384, http://dx.doi.org/10.1007/BF02850633.

Rosenberger, K.J., Storlazzi, C.D., Cheriton, O.M., McPhee-Shaw, E. E., 2016. Variability of the internal tide on the southern Monterey Bay continental shelf and associated bottom boundary layer sediment transport. Cont. Shelf Res. 120, 68—81, http://dx.doi.org/10.1016/j.csr.2016.03.016.

Roux, J.P.l., 1994. Net sediment transport patterns inferred from grain-size trends, based upon definition of "transport vectors" — comment. Sediment. Geol. 90 (1—2), 153—156, http://dx.doi.org/10.1016/0037-0738(94)90022-1.

Saito, Y., Yang, Z., Hori, K., 2001. The Huanghe (Yellow River) and Changjiang (Yangtze River) deltas: a review on their characteristics, evolution and sediment discharge during the Holocene. Geomorphology 41 (2—3), 219—231, http://dx.doi.org/10.1016/S0169-555X(01)00118-0.

Shen, H., 1986. A model of genesis of the relict sediment on the East China Sea shelf. Acta Oceanol. Sin. 5 (3), 437—446, http://www.cnki.com.cn/Article/CJFDTotal-SEAE198603013.htm.

Shepard, F.P., 1954. Nomenclature based on sand-silt-clay ratios. J. Sediment. Res. 24 (3), 151—158, http://dx.doi.org/10.1306/D4269774-2B26-11D7-8648000102C1865D.

Sternberg, R.W., Larsen, L.H., Miao, Y.T., 1985. Tidally driven sediment transport on the East China Sea continental shelf. Cont. Shelf Res. 4 (1—2), 105—120, http://dx.doi.org/10.1016/0278-4343(85)90024-X.

Su, C.-C., Huh, C.-A., 2002. ^{210}Pb, ^{137}Cs and ^{239,240}Pu in East China Sea sediments: sources, pathways and budgets of sediments and radionuclides. Mar. Geol. 183 (1—4), 163—178, http://dx.doi.org/10.1016/S0025-3227(02)00165-2.

Su, J.L., 2001. A review of circulation dynamics of the coastal oceans near China. Acta Oceanol. Sin. 23 (4), 1—16, (in Chinese), http://dx.doi.org/10.3321/j.issn:0253-4193.2001.04.001.

Wang, L., Li, G., Gao, F., Liu, L., Liu, Y., Dada, O.A., 2014. Sediment records of environmental changes in the south end of the Zhejiang-Fujian coastal mud area during the past 100 years. Chin. J. Oceanol. Limnol. 32 (4), 899—908.

Wang, Z.-B., Yang, S.-Y., Zhang, Z.-X., Ri-Hui, L.I., Wang, H., Lan, X.-H., 2012. The grain size compositions of the surface sediments in the East China Sea: indication for sedimentary environments. Oceanol. Limnol. Sin. 43 (6), 1039—1049, http://dx.doi.org/10.1007/s11783-011-0280-z.

Xia, P., Meng, X., Yin, P., Cao, Z., Wang, X., 2011. Eighty-year sedimentary record of heavy metal inputs in the intertidal sediments from the Nanliu River estuary, Beibu Gulf of South China Sea. Environ. Pollut. 159 (1), 92—99, http://dx.doi.org/10.1016/j.envpol.2010.09.014.

Xu, G., Liu, J., Liu, S., Wang, Z., Hu, G., Kong, X., 2016. Modern muddy deposit along the Zhejiang coast in the East China Sea: response to large-scale human projects. Cont. Shelf Res. 130, 68—78, http://dx.doi.org/10.1016/j.csr.2016.10.007.

Xu, K., Li, A., Liu, J.P., Milliman, J.D., Yang, Z., Liu, C.-S., Kao, S.-J., Wan, S., Xu, F., 2012. Provenance, structure, and formation of the mud wedge along inner continental shelf of the East China Sea: a synthesis of the Yangtze dispersal system. Mar. Geol. 291—294, 176—191, http://dx.doi.org/10.1016/j.margeo.2011.06.003.

Xu, K., Milliman, J.D., Li, A., Liu, J.P., Kao, S.-J., Wan, S., 2009. Yangtze- and Taiwan-derived sediments on the inner shelf of East China Sea. Cont. Shelf Res. 29 (18), 2240—2256, http://dx.doi.org/10.1016/j.csr.2009.08.017.

Yamashita, S., Naruse, H., Nakajo, T., 2018. Reconstruction of sediment-transport pathways on a modern microtidal coast by a new grain-size trend analysis method. Prog. Earth Planetary Sci. 5 (1), 18 pp., http://dx.doi.org/10.1186/s40645-018-0166-9.

Yanagi, T., Takahashi, S., Hoshika, A., Tanimoto, T., 1996. Seasonal variation in the transport of suspended matter in the East China Sea. J. Oceanogr. 52 (5), 539—552, http://dx.doi.org/10.1007/bf02238320.

Yuan, D., Zhu, J., Li, C., Hu, D., 2008. Cross-shelf circulation in the Yellow and East China Seas indicated by MODIS satellite observations. J. Mar. Syst. 70 (1—2), 134—149, http://dx.doi.org/10.1016/j.jmarsys.2007.04.002.

Zhang, C., Hong, H., Hu, C., Shang, S., 2011. Evolution of a coastal upwelling event during summer 2004 in the southern Taiwan Strait. Acta Oceanol. Sin. 30 (1), 1—6, http://dx.doi.org/10.1007/s13131-011-0084-9.

Zhang, Q., Liu, H., Qin, S., Yang, D., Liu, Z., 2014. The study on seasonal characteristics of water masses in the western East China Sea shelf area. Acta Oceanol. Sin. 33 (11), 64—74, http://dx.doi.org/10.1007/s13131-014-0556-9.

Zhang, W., Zheng, J., Ji, X., Hoitink, A.J.F., van der Vegt, M., Zhu, Y., 2013. Surficial sediment distribution and the associated net sediment transport pattern in the Pearl River Estuary, South China. Cont. Shelf Res. 61—62, 41—51, http://dx.doi.org/10.1016/j.csr.2013.04.011.

Zheng, Y., Huang, W., 1993. A preliminary analysis on the characteristics of the Kuroshio Frontal Eddy in the East China Sea in spring. Chin. J. Oceanol. Limnol. 11 (3), 276—284, http://dx.doi.org/10.1007/BF02850861.

Oceanologia (2020) 62, 23—30

Available online at www.sciencedirect.com

ScienceDirect

journal homepage: www.journals.elsevier.com/oceanologia/

ORIGINAL RESEARCH ARTICLE

Extreme wind waves in the Black Sea

Boris V. Divinsky [a,*], Vladimir V. Fomin [b], Ruben D. Kosyan [a], Yuri D. Ratner [b]

[a] *Shirshov Institute of Oceanology, Russian Academy of Sciences, Moscow, Russia*
[b] *Marine Hydrophysical Institute, Russian Academy of Sciences, Sevastopol, Russia*

Received 9 January 2019; accepted 28 June 2019
Available online 7 December 2019

KEYWORDS
Wind waves;
Swell;
Wave climate;
Black Sea;
Numerical modeling;
Return period

Summary Results of the analysis of a long-term data set, including fields of significant wave heights of the surface wave components, and mixed (total) wave field in the Black Sea are presented. The data set was collected on the basis of retrospective calculations using the MIKE 21 SW spectral wave model with the atmospheric forcing based on the ERA-Interim data in the period from 1979 to 2017. A criterion is used to isolate the swell waves from the initial wave data set that takes into account the wave age. We used the experimental data to develop a regression relationship showing that the maximum possible wave height can exceed the significant wave height approximately one and a half times. Analysis of the spatial distribution of wave heights in the Black Sea suggests that a possibility exists that significant wave height of storm waves can be as high as ~12 m. This result indicates that the actual heights of maximum waves in the Black Sea can reach 18—19 m. Three regions are distinguished on the basis of the wave potential. The times of manifestation of extreme situations in these regions are different: in the southwestern part of the sea, extreme storm situations occur, as a rule, in December—January; in the region south of the Crimea Peninsula this happens in February; in the northeastern part of the sea they occur in November. It was also found that the south-southeastern and eastern parts of the sea are most affected by swell.

1. Introduction

Application of sea transport routes, hydraulic engineering construction, planning and production of offshore works, study of hydrodynamic processes and the structure of sea water require information about the regimes of wind waves. Climatic characteristics of wind waves can be divided into two parts: operational, reflecting events of frequent recurrence, and extreme, possible once in a given number of years. The greatest interest is the study of the destructive

---

* Corresponding author at: Shirshov Institute of Oceanology, Russian Academy of Sciences, 36 Nahimovskiy pr., Moscow, 117997, Russia. Tel.: +7 918 4567922; fax: +7 86141 28281.
E-mail address: divin@ocean.ru (B.V. Divinsky).

Peer review under the responsibility of Institute of Oceanology of the Polish Academy of Sciences.

Production and hosting by Elsevier

https://doi.org/10.1016/j.oceano.2019.06.003

extreme waves. A simple question is put forward: what maximum waves are generally possible in the Black Sea?

The first publications about this problem were apparently the works of Matushevsky (1978, 1979). The author provides an estimate of the height of maximum waves based on the analysis of the regime functions of the distribution of wave heights, possible once every 50 years; their height is 14.4 m. According to Matushevsky, the maximum ever possible wave height in the Black Sea is 15.0 m.

Unfortunately, verification of such assessments is restricted by a strong lack of experimental data. However, we can cite several examples of successful experiments on recording wind wave parameters in the offshore zone. In 1996—2003 wave characteristics were measured on the northeastern shelf of the sea near the city of Gelendzhik using a Datawell Waverider wave recorder (Kos'yan et al., 1998). The maximum recorded wave height in the entire experiment was 12.43 m (over the 80 m depth of the sea). In the northwestern part of the sea, a significant wave height of 11 m was recorded on the Gloria platform using a string wave recorder (Rusu et al., 2006). Since this height (11 m) is presented in the widely accepted common terms of significant wave heights let us find the relationship between the significant and maximum wave heights. We possess about 14 thousand 20-min records of the displacements of the Datawell Waverider buoy in the horizontal and vertical planes. Each record contains wave profiles at the intersection of the zero surface, and we can determine the maximum wave height in each record; then, we construct the frequency spectrum and find the significant wave height. Regression of significant and maximum wave heights based on the experimental data is shown in Fig. 1.

Fig. 1 also contains a box-whisker plot, describing statistics of the ratio of maximum wave heights to significant heights (location of the average value of the ratio and also the values of 10, 25, 75, and 90% distribution quantiles). It follows from Fig. 1, that the maximum wave heights exceed the significant waves approximately by a factor of 1.54. Returning to the observations on the Gloria platform, we state that if the significant wave height is 11 m as reported in Rusu et al. (2006), the maximum wave height should be as high as about 17 m.

Instrumental measurements of wind wave parameters in the open part of the Black Sea (in the context of the possibility of using them for climate analysis) are almost absent. Among the available observation tools, we distinguish visual assessments (from the passing ships), satellite altimetry, and numerical simulation. The visual method of determining the characteristics of waves is associated with significant subjectivity. Satellite observations are characterized by obvious advantages (unchanging tracks, in particular), and by the disadvantages of uncertainties in the interpretation of signals. Mathematical modeling for studying wind waves is a modern method, which in some sense has no alternative. The spectral wave models of the last generation fully describe the physical nature of generation, transformation, and decay of the surface waves. Since we are interested in the manifestation of extreme waves in the Black Sea, we cite several works devoted to this approach. In the publication by Rusu (2016), the author describes the constructed predictive wave system based on the SWAN model, and provides some results of the calculation of wind-wave fields. We cite the author: "... *there are areas in the sea where the significant wave height is greater than 10 m, which means*

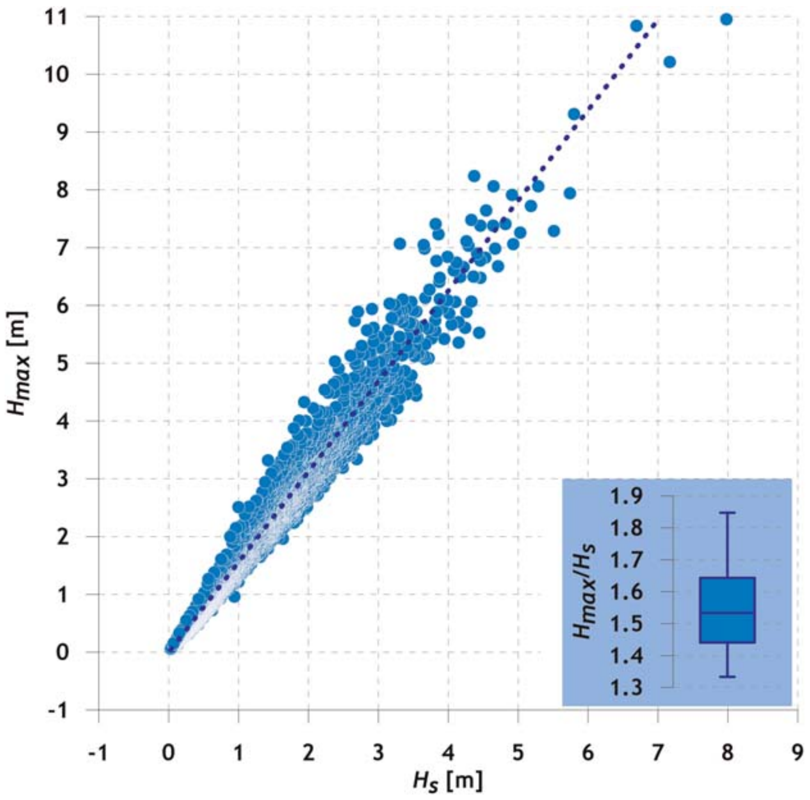

Figure 1 Relation between the significant and maximum wave heights based on experimental data.

that we may expect maximum wave heights of about 20 m, or even greater". In the paper by Polonsky et al. (2011), the authors estimate the characteristics of the wave fields of the Black Sea in 1979—2008. They show that waves with the maximum heights of significant waves exceeding 12 m are possible. The region of occurrence of such waves is the southwestern part of the sea.

We also note two works (Akpınar et al., 2016; Van Vledder and Akpinar, 2016). In the first article spatial maps of the maximum wave heights in the period from 1979 to 2009 were constructed, with the wave heights for wind seas limited to 8 m, which seems to be underestimated. In the second article, over the same period, the distributions of the maximum significant wave heights in the Black Sea area were obtained. The areas in which the magnitudes of significant wave heights reach maximum values are identified: southwest (9.7 m), east (9.5 m) and in the region of the Crimean peninsula (8.3 m).

Thus, the question of maximum waves in the Black Sea is still pressing. In this relation, in the work suggested here: (1) we study the space-time properties of the manifestation of the maximum waves over a climatic time period; (2) we analyze wave heights possible once in a given number of years. Studies have been carried out both for the wave field components (pure wind waves and swell) and total (mixed) waves.

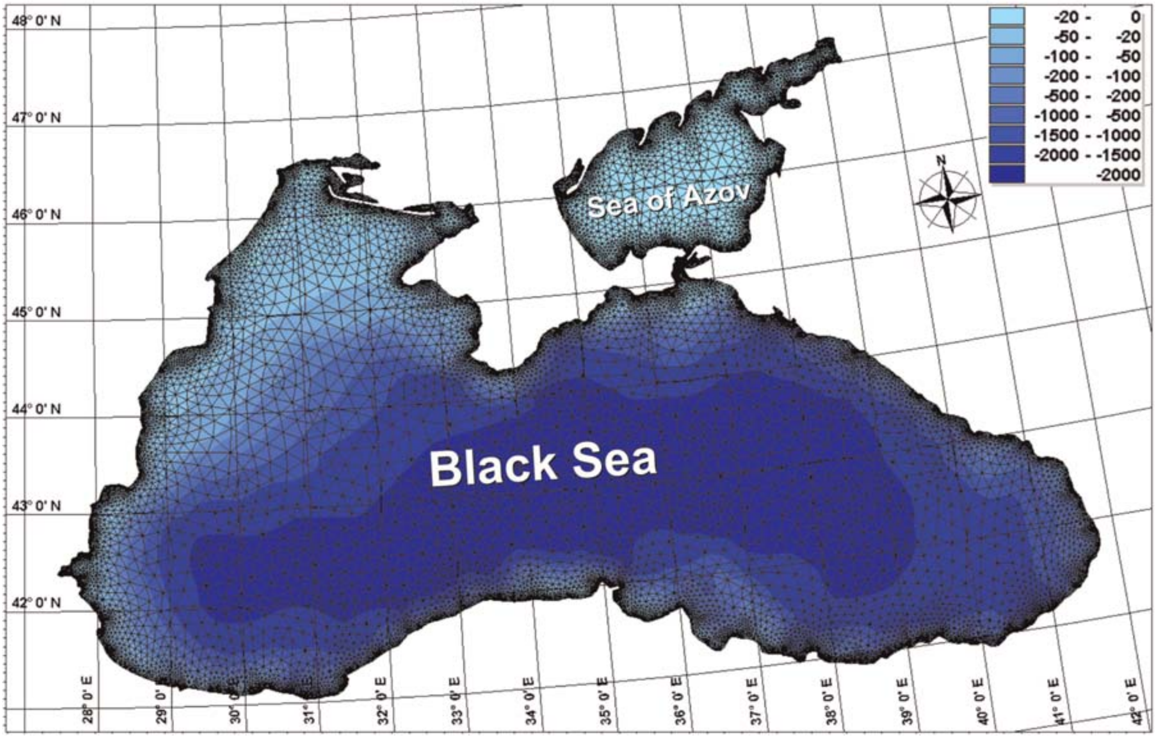

Figure 2 Grid for calculations and bathymetric chart of the Black and Azov seas.

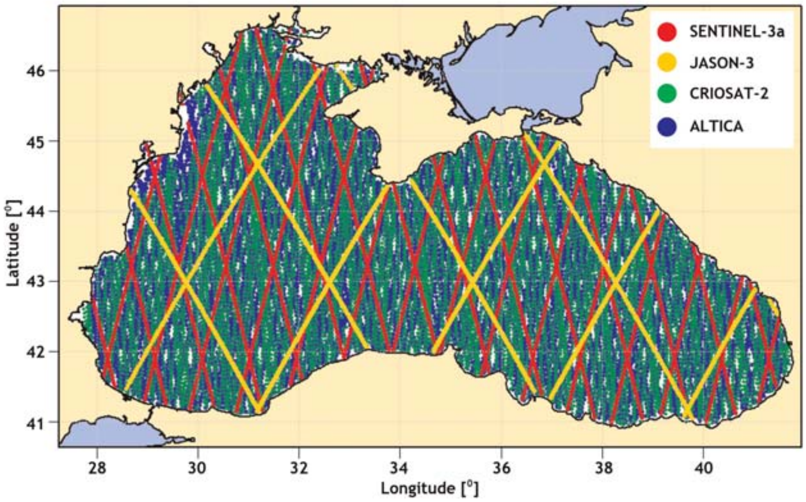

Figure 3 Distribution of satellite altimetry observations over the Black Sea from December 2017 to October.

2. Methods and approaches

2.1. Numerical model

In this work, we use the MIKE 21 SW spectral wave model developed at the Danish Hydraulic Institute (DHI, 2007). A description of the model and stages of its verification as applied to the measurements in the Black Sea is presented in Divinsky and Kosyan (2017). Here, we note only the most important issues:

- the model realizes the main physical mechanisms of the generation, transformation, and decay of wind waves;
- irregular grid for computations covers the basins of the Black and Azov seas, it consists of 10 000 elements (Fig. 2);
- the ERA-Interim reanalysis data prepared by the European Centre for Medium-Range Weather Forecasts (http://apps.ecmwf.int) are used as the initial wind fields. The model domain is limited by coordinates: 40.5°N and 47.5°N by latitude, 27°E and 42°E by longitude. The spatial resolution by latitude and longitude is 0.25°; the time resolution is 3 h.

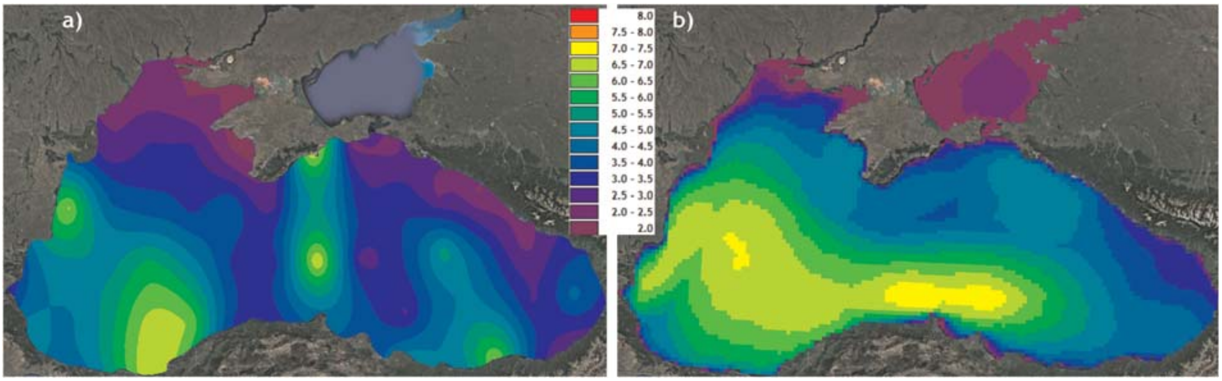

Figure 4 Maximum significant wave heights [m] in the Black Sea in the period from December 1, 2017 to September 30, 2018. (a) Generalization of satellite data; (b) modeling results.

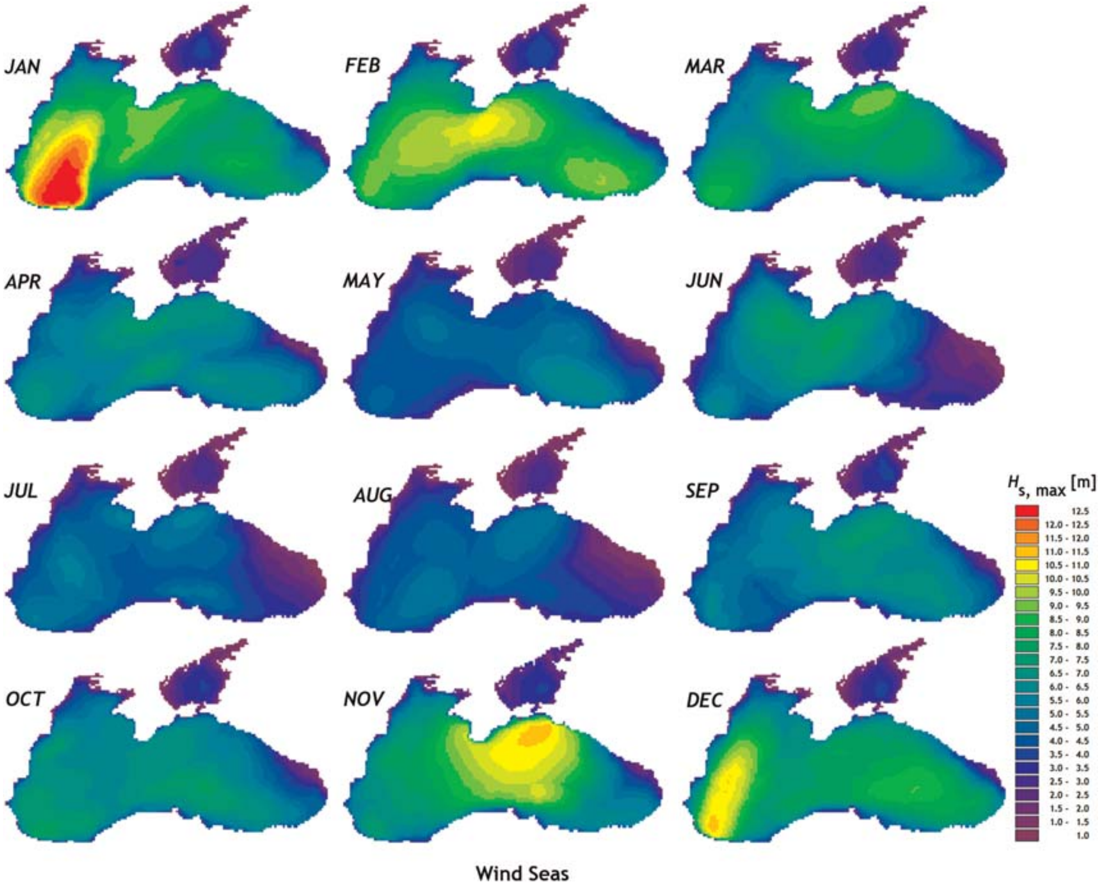

Figure 5 Wind waves. Maximum significant wave heights [m] over the Black Sea from 1979 to 2017.

We note that despite the fact that the grid covers the Azov Sea, the results in this sea are not completely representative without the account for the ice cover in the winter months; therefore, we do not discuss these results here.

Tuning of the DHI MIKE 21 SW spectral wave model for automatic separation of surface wave components is described in detail in Divinsky and Kosyan (2018). Here, we only give the parameters of optimum configuration of the spectral model:

- 50 spectral frequencies are distributed in the range of periods from 1.6 to 17.3 s using the following relation $f_n = f_0 C^n$ ($f_0 = 0.055$ Hz, $C = 1.05$, $n = 1, 2, \ldots, 50$);
- the number of discrete directions is 32; hence, the directional resolution of the model is 11.25°;
- the coefficients determining energy dissipation caused by wave breaking are: $C_{\text{dis}} = 5.5$, $\delta_{\text{dis}} = 0.15$;
- separation of wave components is performed using the criterion that takes into account the wave age. The wave component corresponds to swell if the following condition is satisfied $\frac{U_{10}}{c}\cos(\theta-\theta_w) < 0.83$, where U_{10} is wind speed; c is phase velocity of waves; θ, θ_w are the directions of waves and wind, respectively.

As a result of calculations, we prepared a data set of spatial fields of parameters of wind waves, swell, and mixed waves for the period from January 1979 to December 2017 with a time step of one hour. Fields of significant wave heights were used for further analysis.

Since we are analyzing spatial maps, we note the following important issues related to the possibility of using satellite data. A clear advantage of the results of altimetric measurements is the possibility of their spatial generalization. In 2018, the EU Copernicus Marine Service (http://marine.copernicus.eu) developed a new product that includes the results of restoring the height of significant waves from the data of several satellites starting from July 2017. As an example, we take the time interval from December 1, 2017 to September 30, 2018. The spatial distribution of the tracks of the Saral/Altica, Criosat-2, Jason-3, and Sentinel-3a satellites in the specified period is shown in Fig. 3.

The spatial resolution of the data is approximately 7 km. This is the best satellite altimetry configuration, providing the most reliable results. The maximum wave heights were determined in the spatial cells with sizes of 0.1 × 0.1, 0.25 × 0.25, 0.5 × 0.5, and 1 × 1 degrees. When the spatial cell size is 0.1 × 0.1 degrees, from 1 to 20 measurements per year generally fall into each cell; and from 1000 to 3000 measurements per year appear in the spatial cell sizes of 1 × 1 degrees. The largest number of measurements appear in the cells through which the tracks of the Jason-3 and Sentinel-3a satellites pass, since they have strictly repeated orbits with periods of 10 and 27 days. This factor precisely determines the reliability of data on maximum wave heights.

Fig. 4 shows the spatial distributions of the maximum significant heights of mixed waves based on the analysis of

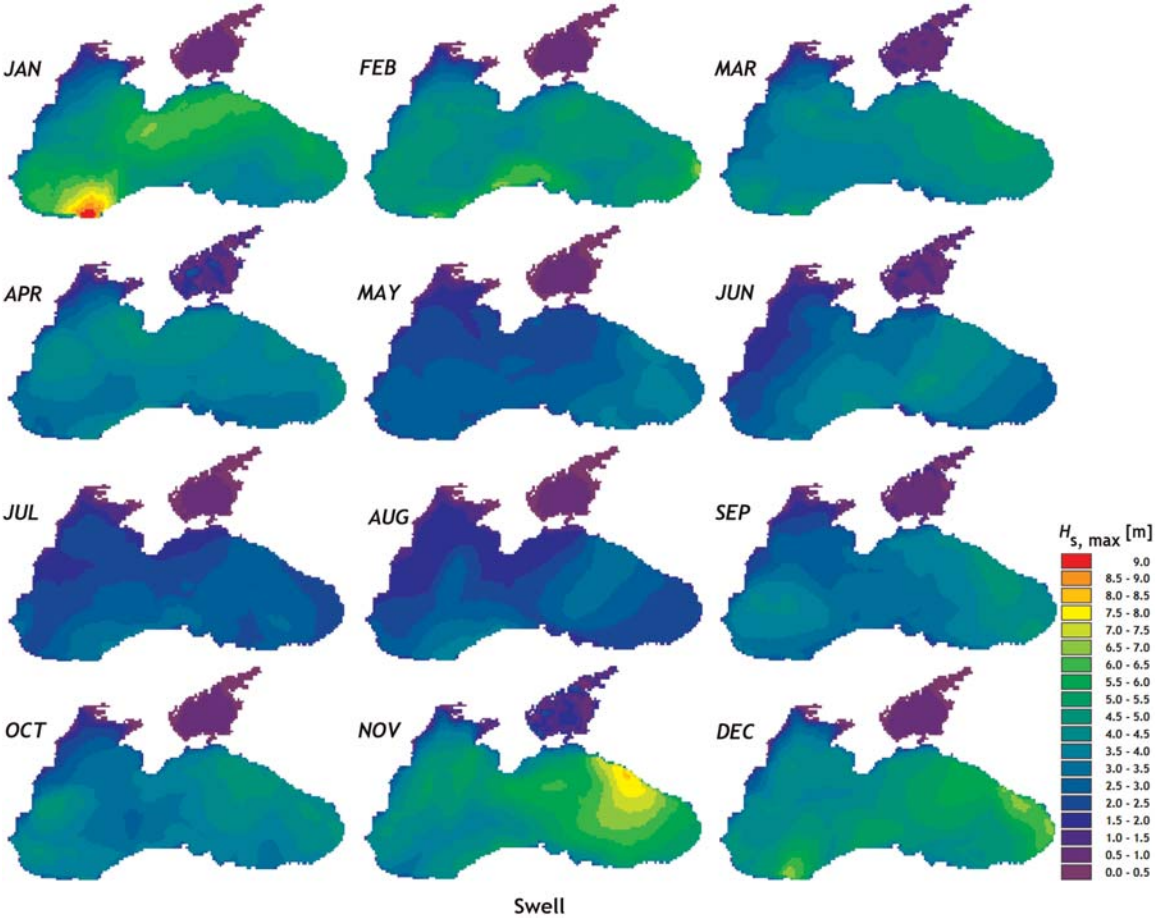

Figure 6 Swell. Maximum significant wave heights [m] over the Black Sea from 1979 to 2017.

satellite data (Fig. 4a) and calculated estimates using the spectral wave model (Fig. 4b).

It follows from Fig. 4 that there is no reason to talk about sufficient compliance of satellite and calculated fields, due to uneven coverage of the Black Sea area with satellite data in both space and time. As we mentioned above, the data of the Jason-3 and Sentinel-3a satellites are most representative, but unfortunately, the total coverage of the basin by these satellites is low. Nevertheless, let us point out some general properties of satellite and calculation charts: (1) both maps, in principle, reflect the fact that during the studied period of time stronger waves were observed in the southern part of the sea, compared to the northern part; (2) both maps give somewhat similar estimates of the maximum heights of significant waves. The latter fact provides some confidence in the correctness of tuning the main research tool: the spectral wave model.

2.2. Method of estimating extreme wave heights

The method of annual maxima, based on the Gumbel integral distribution function, was used to estimate the extreme heights of surface waves (Kamphuis, 2000; Lopatoukhin et al., 2000):

$$F(h) = \exp\left(-\exp\left(-\frac{h-\alpha}{\beta}\right)\right), \qquad (1)$$

where $F(h)$ is the probability that wave height does not exceed h; and α and β are parameters determined for each specific point from the time series of annual maxima wave heights. Parameters α and β are determined for each node of the calculation grid using the least square method.

The following expression for wave height corresponding to the given value of quantile F follows from (1):

$$h = \alpha + \beta(-\ln(-\ln F)). \qquad (2)$$

Taking (2) into account, the estimate of wave height possible once in T years is determined as quantile $(1 - 1/T)100\%$ of statistical reliability of distribution (1):

$$h_T = \alpha - \beta \ln\left(-\ln\left(1 - \frac{1}{T}\right)\right). \qquad (3)$$

The field of significant wave heights possible once in a given number of years is a result of the above procedure.

3. Results and discussion

3.1. Maximum waves in the sea basin based on modeling

A data set has been formed, consisting of fields of calculated parameters of the components of wind waves, swell, and mixed waves in the Black Sea, covering a period of 39 years (from 1979 to 2017) with a time step of one hour. Figs. 5—7

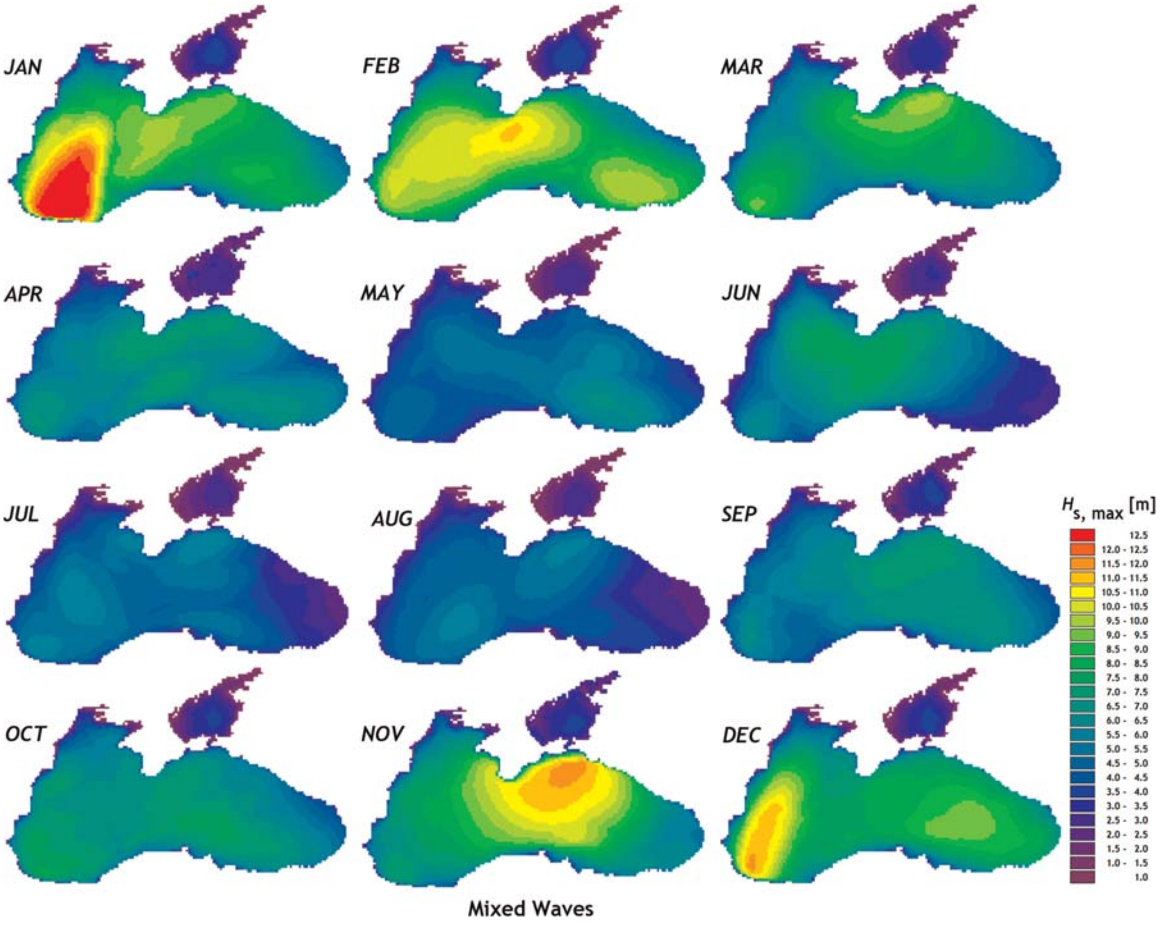

Figure 7 Mixed waves. Maximum significant wave heights [m] over the Black Sea from 1979 to 2017.

show the spatial distributions of the maximum significant heights of the components of surface waves, and total (mixed) waves.

We note that the wave dynamics of the Black Sea is generally determined by two processes: propagation of Atlantic cyclones over the Black Sea, resulting in strong waves in the northeastern part of the sea, and anticyclones with centers in Eastern Europe, causing waves in the southwestern regions of the sea.

These features are fully reflected in the maps of maximum wave heights (in our case, in the terms of significant as mentioned above). The strongest wind waves with heights exceeding 12 m appear in the southwestern part of the sea. The months with the strongest storms are January and December. In the northeastern part, waves may develop with altitudes of the order of 11 m; as a rule, this occurs in November. In February, the southern coast of the Crimea Peninsula appears in the zone of the greatest waves. In March, zones of dynamic activity are quite clearly pronounced (southwestern and northeastern parts of the sea), which is associated with the restructuring of the atmospheric systems between winter and summer

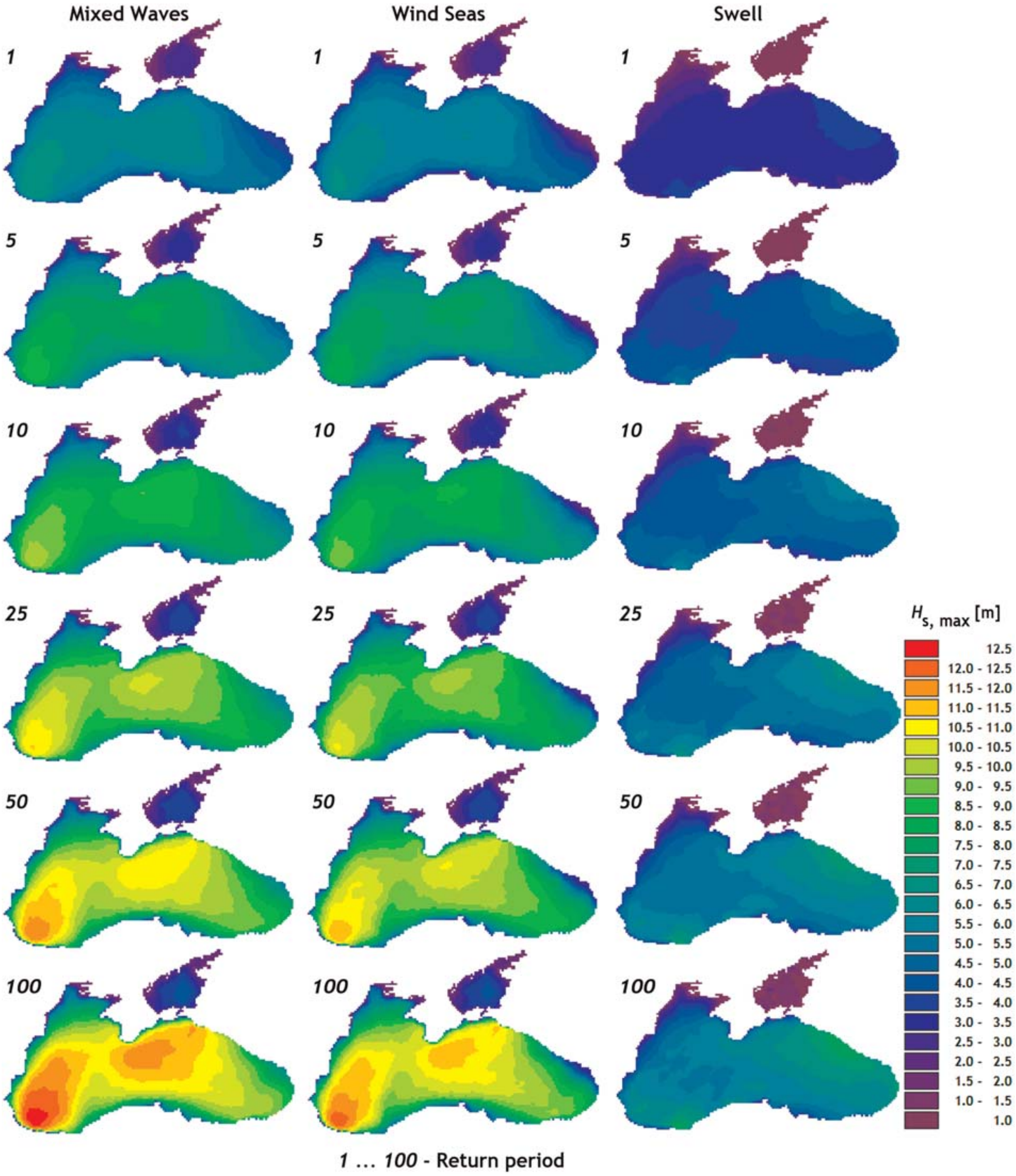

Figure 8 Maximum wave heights possible once in the given number of years.

types. July and August are the calmest months over the entire sea.

The distribution of maximum swell waves is, of course, different from the wind waves, since the swell propagates beyond the zones of surface wave generation. The main regions of maximum swell waves are in the south-southwestern and eastern parts of the sea. The height of the swell usually does not exceed 6—7 m. The 9-m swell recorded in January (Fig. 6) is a single case over the analyzed period of time; it is related to the catastrophic storm in 2004.

Spatial indicators of fields of mixed waves (Fig. 7) repeat, in general, the maps of wind waves, excluding the extreme eastern regions of the sea, in which swell prevails. The stormiest regions with wave heights of the order of 11—12 m are: the Bosporus region, the southern coast of Crimea, and the northern-northeastern part of the sea.

3.2. Wave heights of given recurrence

Let us estimate the spatial distribution of the maximum wave heights possible once in a given number of years using the simple procedure described in Section 2.

Note that the choice of the type of distribution is not very important. As noted in Van Vledder et al. (1993), in which the authors analyzed three methods for finding extreme values and eight distribution functions, the results do not differ from each other by more than 10% (when determining the wave height possible once in a hundred years).

Fig. 8 shows spatial maps of the height distribution of the maximum (significant) waves, possible once in 1 year, as well as in 5, 10, 25, 50, and 100 years for the components of surface waves and mixed waves.

It follows from Fig. 8 that 10-m waves are not very rare in the Black Sea; in the south-western part they can appear once in 10 years. Once every 100 years, waves of about 12 m (and possibly higher) are possible. The most dangerous areas are the southwestern part of the sea and the region in the central part, adjacent to the southern coast of Crimea. The largest swell is observed in the south-southeastern part of the sea and at the eastern coast. The recurrence of swell waves with a height of 8 m is every hundred years.

4. Conclusions

As a result of this work, a data set of calculated wave fields was processed. The data set consisted of the fields of significant wave heights of the components of surface waves, and mixed (total) waves in the period from 1979 to 2017. The spatial distributions of the maximum waves in the Black Sea provide evidence that favorable conditions for the development of storm waves with significant wave heights of about 12 m may develop in the Black Sea. This means that the real maximum waves can be as high as 18—19 m.

Three regions are clearly distinguished from the wave potential. The time of manifestation of extreme situations is slightly different: in the southwestern part of the sea, extreme events usually occur in January and December; extreme events south of the southern coast of the Crimea Peninsula occur in February; while in the northeastern part of the sea they appear in November.

The southeastern and extreme eastern parts of the sea are most subjected to strong swell.

The interannual variability of maximum wind waves and swell in the sea will be the subject of further research.

Acknowledgments

This work was supported by the Russian Foundation for Basic Research, project no. 18-05-80035. The computer calculations were supported by the Russian Foundation for Basic Research (Projects no. 19-05-00041 and no. 19-45-230002). Analysis of the results was carried out within the State task programs 0149-2019-0014 and 0827-2018-0004. Processing of altimetry data was supported by the Russian Foundation for Basic Research, project no. 18-45-920059.

References

Akpınar, A., Bingölbali, B., Van Vledder, G., 2016. Wind and wave characteristics in the Black Sea based on the SWAN wave model forced with the CFSR winds. Ocean Eng. 126, 276—298, http://dx.doi.org/10.1016/j.oceaneng.2016.09.026.

DHI, 2007. MIKE 21, Spectral Wave Module. Danish Hydraulic Institute, Water & Environment.

Divinsky, B., Kosyan, R., 2017. Spatiotemporal variability of the Black Sea wave climate in the last 37 years. Cont. Shelf Res. 136, 1—19, http://dx.doi.org/10.1016/j.csr.2017.01.008.

Divinsky, B., Kosyan, R., 2018. Parameters of wind seas and swell in the Black Sea based on numerical modeling. Oceanologia 60 (3), 277—287, http://dx.doi.org/10.1016/j.oceano.2017.11.006.

Kamphuis, J.W., 2000. Longterm wave analysis. In: Introduction to Coastal Engineering and Management. World Scientific, Singapore, 81—102.

Kos'yan, R.D., Divinsky, B.V., Pushkarev, O.V., 1998. Measurements of parameters of wave processes in the open sea near Gelendzhik. In: The Eight Workshop of NATO TU-WAVES/Black Sea, METU, Ankara, Turkey, 5—6.

Lopatoukhin, L.J., Rozhkov, V.A., Ryabinin, V.E., Swail, V.R., Boukhanovsky, A.V., Degtyarev, A.B., 2000. Estimation of extreme wind wave heights. World Meteorological Organisation, JCOMM Tech. Rep. WMO/TD-No. 1041.

Matushevsky, G.V., 1978. Computation of maximum wind-driven wave heights in oceans and seas. Meteorol. Hydrol. 5, 63—69, (in Russian).

Matushevsky, G.V., 1979. On the extremally possible wind-generated wave heights on oceans and seas. Meteorol. Hydrol. 11, 78—81, (in Russian).

Polonsky, A.B., Fomin, V.V., Garmashov, A.V., 2011. Characteristics of wind waves of the Black Sea. Rep. National Academy of Sciences of Ukraine 8, 108—112.

Rusu, E., 2016. Reliability and applications of the numerical wave predictions in the Black Sea. Front. Mar. Sci. 3, Article no. 95, http://dx.doi.org/10.3389/fmars.2016.00095.

Rusu, E., Rusu, L., Guedes Soares, C., 2006. Prediction of extreme wave conditions in the Black Sea with numerical models. In: 9th International Workshop on Wave Hindcasting and Forecasting, Victoria, B.C., Canada, 24—29 September.

Van Vledder, G., Akpinar, A., 2016. Spectral partitioning and swells in the Black Sea. Coastal Eng. Proc. 35, 14 pp., http://dx.doi.org/10.9753/icce.v35.waves.21.

Van Vledder, G., Goda, Y., Hawkes, P., Mansard, E., Martin, M.Y., Mathiesen, M., Peltier, E., Thompson, E., 1993. Case studies of extreme wave analysis: a comparative analysis. In: Proc. Second International Symposium honoring Professor Robert L. Wiegel, WAVES'93, New Orleans, Louisiana, United States, July 25—28, 1993, 978—992.

Oceanologia (2020) 62, 31—44

Available online at www.sciencedirect.com

ScienceDirect

journal homepage: www.journals.elsevier.com/oceanologia/

ORIGINAL RESEARCH ARTICLE

Geochemical fractionation of heavy metals in sediments of the Red Sea, Saudi Arabia

Bandar A. Al-Mur *

Department of Environmental Sciences, Faculty of Meteorology, Environment and Arid Land Agriculture, King Abdulaziz University, Jeddah, Saudi Arabia

Received 3 March 2019; accepted 28 July 2019
Available online 21 August 2019

KEYWORDS
Heavy metal;
Speciation;
Bioavailability;
Sediments;
Jeddah

Summary The geochemical fractionation of heavy metals, including Mn, Fe, Cu, Pb, Zn, Cd and Ni, collected from the surface sediments of the Jeddah coastal zone of the Red Sea in Saudi Arabia was determined using a sequential extraction technique. The data obtained from the five fractions indicated that the concentration of metals varies among different locations in the study area. The total metal concentrations (%) in the exchangeable (F_1), carbonate (F_2), reducible (F_3) and organic-bound (F_4) fractions were measured to determine the mobility of each studied metal. The sum of the two fractions F_3 and F_4 represented 70% of the Cu, 72% of the Zn and 36% of the Pb. However, the sum of the three fractions F_2, F_3 and F_4 represented 76%, 74%, 68% and 58% of the Cd, Ni, Fe and Mn, respectively. Approximately 46% of the total copper was related to organics, which could reflect a high mobility of copper in these sediments. The maximum mobility of metals in the sediments was confirmed by the bioavailability factor (BF), which was within the ranges of 0.47—0.93, 0.34—0.92, 0.62—0.95, 0.69—0.95, 0.24—0.82, 0.54—0.98, and 0.60—0.95 for Fe, Mn, Cu, Zn, Pb, Cd, and Ni, respectively. Based on the BF, the metals exhibited the following order: $\mathrm{Cu} \approx \mathrm{Zn} > \mathrm{Cd} \approx \mathrm{Ni} \approx \mathrm{Fe} > \mathrm{Mn} > \mathrm{Pb}$. The high levels of BF for the studied metals could reflect the potential for toxic metals to be easily released into the marine environment. The risk assessment code for Cd showed a medium risk in five sediment samples of the northern and southern regions and a high risk to the aquatic environment in the other sediment samples. However, the speciation of Fe, Mn, Cu, Zn, Pb and Ni in the studied sediments exhibited low to medium risks to the aquatic environment.

---

* Corresponding author at: Department of Environmental Sciences, Faculty of Meteorology, Environment and Arid Land Agriculture, King Abdulaziz University, P.O. Box 80208, Jeddah 21589, Saudi Arabia. Tel.: +966 500031003.
E-mail address: Balmur@kau.edu.sa.

Peer review under the responsibility of Institute of Oceanology of the Polish Academy of Sciences.

Production and hosting by Elsevier

https://doi.org/10.1016/j.oceano.2019.07.001

1. Introduction

Sediments consist of organic and inorganic detrital grains with heterogeneous physical, chemical and biological characteristics (Hakanson, 1992). Sediments are rich in trace metals, which occur in various chemical forms with different mobilities, bioavailabilities, chemical interactions and potential toxicities (El Zokm et al., 2015; Masoud et al., 2010; Okbah et al., 2005). The presence of trace elements in sediments was studied by Tessier et al. (1979) to understand the chemical forms of metals present in the environment. Such research is performed because the chemical forms of metals play a certain role in the mobility of metals at the sediment/water interface and their subsequent transfer to the food chain (Rattan et al., 2005). Therefore, the fate of such trace metals should be investigated to understand their effects on surrounding organisms and what risks they could pose. Metals in sediments can occur in five categories: soluble and exchangeable; carbonates; reducible forms (Fe and Mn oxides); organics and sulfides; and silicates and detrital materials. This diversity is because metals can have different remobilization conditions under changing environments, consequently affecting their bioavailability and solubility. The determination of the total content of trace metals is not enough to evaluate their impact on the environment. Thus, the identification of geochemical forms of trace metals is necessary to understand the mobilization capacity of the metals and their impact on the surrounding environment (Li et al., 2000).

The catchment area of the Red Sea consists of sedimentary, granitic and metamorphic rocks that are weathered and eroded by the Red Sea (coastal) waters via wind and seasonal floods. These natural conditions have been altered due to increased human activities in Red Sea coastal areas (Moufaddal, 2002). These activities are the most frequent on Jeddah City's coast and include refilling, dredging, waste discharge, fishing, and oil spills. Some sites in Jeddah have been investigated over the last few years to study the anthropogenic impacts and effects of pollution on the environmental conditions of lagoons and shorelines (Abu-Zied et al., 2013, 2016; Abu-Zied and Hariri, 2016; Al-Mur et al., 2017; Youssef et al., 2015).

The main objective of this study is to investigate the speciation of trace metals, such as Fe, Mn, Cu, Zn, Pb, Cd and Ni, using sediments from the coast of Jeddah to provide a better understanding regarding their mobility and bioavailability and to conduct an environmental risk assessment.

2. Material and methods

2.1. Sample location

Samples were collected at point-source areas impacted by anthropogenic activities based on field surveys and observations. These impacted areas included the Salman Gulf, Downtown, and Al-Khumrah. The study area was divided into three zones: the north zone is represented by five stations (I, II, III, IV and V), the middle zone is represented by two stations (VI and VII) and the south zone is represented by stations VIII, IX, X, XI and XII (Fig. 1). Fine and coarse sand composed the major fraction of the studied sediments.

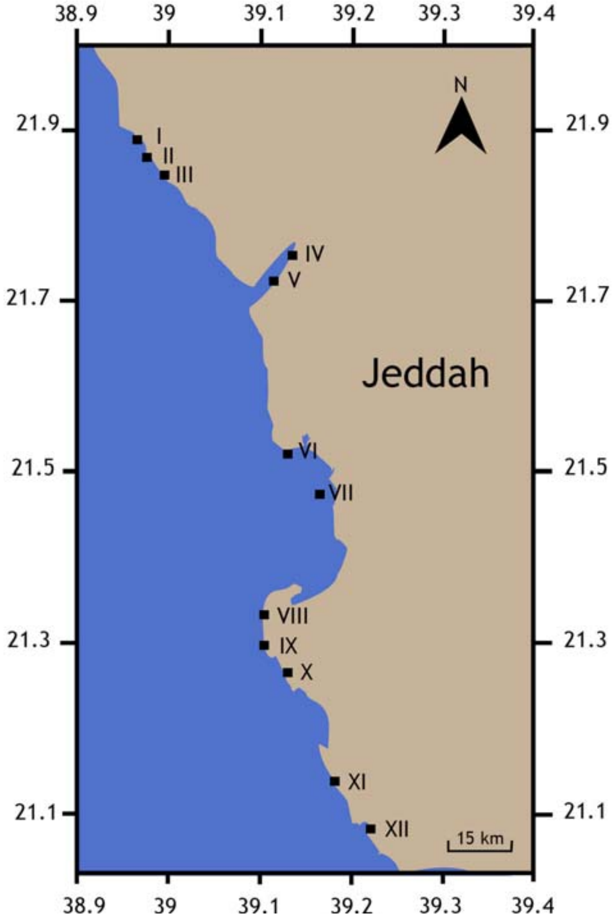

Figure 1 Location of sampling points of the coastal area of Jeddah, Red Sea.

2.2. Sample collection and preservation

Surface marine sediment samples (250 g, 7 cm from the surface) were collected using a plastic spatula to prevent any cross contamination. At each station, 3 sediment samples were collected using a grab sampler, immediately inserted into polyethylene bags and stored in an ice box until they could be transported to the lab. In the laboratory, all samples were kept cool at 4°C until analysis occurred. Before metal analysis, all sediment samples were homogenized and ground.

2.3. Geochemical analysis

Granulometric analysis of the sediment was performed by sieving techniques (Folk, 1974). The analysis was only performed on the finest sediments, which were separated using a sieving process. The majority of the sediment was the coarse sandy/gravel fraction, and we only focused on the fine fraction. In the first step, the foreign components and gravel were removed from the sediment samples through a 125 μm sieve. The remaining fraction was then ground and sieved through a 63 μm sieve. This fine fraction was then divided into four parts: 1. Part used for total organic carbon determination. 2. Part used to determine calcium carbonate (%).

3. Part used for the analysis of total metal concentration.
4. Part used to determine the different species of heavy metals (fractionation of heavy metals).

The TOC was measured using the procedure of Gaudette and Flight (1974). In this method, the powdered sediment sample was exothermically heated and oxidized with concentrated sulfuric acid (H_2SO_4) and potassium dichromate ($K_2Cr_2O_7$). The sample solution was titrated to remove excess dichromate using ferrous ammonium sulfate solution and the indicator diphenylamine. Then, the organic carbon values were converted to organic matter by multiplying the resulting values by 1.8.

Total carbonates were determined following the procedures described in Molina (1974). In the present study, $CaCO_3$ was determined by the dissolution of carbonate in an excess of 0.5 N HCl and titration of the remaining acid with 0.25 N NaOH (Rowell, 1994). This process involved two-phase analysis:

One gram (accurately weighed) of dried sediment sample was mixed with a known amount of hydrochloric acid (0.5 N HCl) in a conical flask and swirled slowly after the addition of the acid. The total $CaCO_3$ (%) was calculated by the following equation:

$$\mathrm{CaCO_3}\% = 100\times 0.05\times[(N_{\mathrm{HCl}}\times V_{\mathrm{HCl}})-(N_{\mathrm{NaOH}}\times V_{\mathrm{NaOH}})],$$

where N_{HCl} is the normality of standardized HCl, V_{HCl} the volume of standardized HCl, N_{NaOH} the normality of standardized NaOH and V_{NaOH} the volume of standardized NaOH.

The total concentration of heavy metals was determined according to Oregioni and Aston (1984). An accurately weighed 0.3 g sediment sample was completely digested in a cleaned and dried Teflon beaker at 80°C using a mixture of acids (in mL; HNO_3:$HClO_4$:HF; 3:2:1 v/v). The remaining supernatant for each sample was used to measure the total metal concentration using an inductively coupled plasma-optical emission spectrometer (Agilent ICP-OES 5100 VDV). The absorption wavelengths (in nm) were 259.943, 257.610, 213.857, 324.757, 220.356, 226.502 and 231.604. The operating parameters of the system were as follows: power 1.2 kW, plasma gas flow 12 L/min, auxiliary gas flow 1.0 L/min, nebulizer flow 0.7 L/min, and pump rate 15 rpm.

Working standard solutions of heavy metals were prepared with standards obtained from Fluka Analytical, St. Galen, Switzerland, with 1% HNO_3. Seven calibration standards, including a blank and concentrations ranging from 5—100 μg L^{-1}, were measured three times. HNO_3 was used as a blank, and all the analyses were performed in triplicate. The total metal concentration was calculated by the following formula:

$$C = \mathrm{Cs}\times\left(\frac{V}{\mathrm{Wt}}\right),$$

where C is the concentration of sediment sample in μg g^{-1}, Cs is the liquid supernatant concentration (ICP reported) in μg L^{-1}, V is the volume (mL) of acid used to dissolve the sediment sample and Wt is the weight (g) of the sediment sample. For each individual sample, triplicate measurements were recorded by the ICP-OES.

2.4. Sequential extraction procedure

Sequential extraction of the metals Fe, Mn, Cu, Zn, Pb, Cd and Ni was carried out based on the methodology of Tessier et al. (1979). This method was used because such metals can be remobilized into/out of sediments based on the surrounding solution characteristics, such as the formation of complexes, ionic strength, acidity and redox potential. In this study, the methodology used to obtain the five metal fractions was as follows:

The exchangeable and acid-soluble fraction (F_1) was obtained by adding 10 mL of 1 M sodium acetate solution (pH 8.2) into one gram of sediment sample and shaking the mixture in a mechanical shaker at 250 rpm at room temperature for 1 h. Then, after centrifugation at 7000 rpm for 20 min, the extract was placed in a polyethylene bottle and stored at 4°C until further analysis. After that, the residue was shaken for 20 min in 10 mL of deionized water, and then the supernatant was discarded.

The carbonate-bound fraction (F_2) was extracted by adding a sodium acetate solution (pH 5.0) to the residual from the first step. At room temperature, the mixture was shaken (250 rpm) for 1 h.

The reducible fraction (F_3), which was bound to iron-manganese oxides, was obtained by adding 0.05 M hydroxylamine HCl in 25% (v/v) acetic acid to the residue from the 2nd step. The mixture was agitated for 6 h at 70°C. The F_3 fraction was separated, and the residue was washed after completion of the first step.

The sulfide and organic-bound fraction (F_4) were obtained from the residual of the F_3 fraction. In this step, 3 mL of 0.02 M HNO_3 and 5 mL of 30% H_2O_2 were added to the residue, the pH was adjusted to 2 by HNO_3, and the mixture was heated at 85°C for 2 h. After that, 3 mL of 30% H_2O_2 was added, and heating continued for 3 h. The solution was then cooled, and 5 mL of NH_4OAC was added. Then, the extraction of F_4 and residue washing were carried out as performed in the first step.

The residual fraction (F_5) was obtained by complete digestion of 0.2 g of the residue left from step F_4 in a mixture of HNO_3, $HClO_4$ and HF (3:2:1 v/v). Then, the metal concentrations (μg g^{-1}) in this solution and in all other extracts and the total metal concentration were measured using inductively coupled plasma spectrophotometry.

The % recovery of trace metals in the five extracts/fractions, including the residual fraction, was determined using the following equation from Ahmadipour et al. (2014):

$$\text{Recovery }\% = \left\{\sum\frac{(\text{Exch.}+\text{Carb.}+\text{Red.}+\text{Org.}+\text{Resi.})}{\text{TM}}\right\}\times 100,$$

where Exch. = exchangeable, Carb. = carbonate, Red. = reducible, Org. = oxidizable organic, Resi. = residual and TM = total metal.

2.5. Quality control

All the chemicals were of analytical grade quality and purchased from Sigma-Aldrich, USA. Ultrapure, deionized water was used throughout the procedure, and glassware and plastics were soaked in 10% HNO_3 for 24 h. All analytical solutions were prepared using ultrapure water (resistivity $\geq$ 18.3 MΩ cm) obtained from a Milli-Q device (Millipore, Bedford, MA, USA). A quality control standard of 10 μg L^{-1} was used to check the calibration and had to pass with 90% confidence before any samples were run.

Table 1 Comparison of the analytical results of the certified reference materials (HISS-1, National Research Council of Canada in $\mu g\ g^{-1}$) with the measured data.

Metal	Measured value	Certified value	Recovery %
Fe	0.24 ± 0.09	0.236 ± 0.017	101.7
Mn	60.85 ± 4.20	61.24 ± 2.30	99.4
Zn	4.74 ± 0.79	4.60 ± 1.21	103.0
Cu	2.10 ± 0.37	2.08 ± 0.08	101
Pb	2.75 ± 0.40	2.83 ± 0.74	97.2
Cd	0.020 ± 0.09	0.022 ± 0.028	91.0
Ni	2.16 ± 0.29	1.99 ± 0.55	92.1

To validate the method in this work, QA/QC concerns were addressed through the use of certified reference materials (CRM), blank reagents and triplicate samples. Quality control for the total metal concentrations was performed using a certified reference material, and the indicated heavy metals in marine sediments (HISS-1, National Research of Council of Canada, in $\mu g\ g^{-1}$) were analyzed (Table 1). Six batches were analyzed in duplicate, and the accuracy of the results ranged from 90–110%; the precision of the analytical process was determined as the relative standard deviation (RSD). The precision for the analysis of the standard solution was within 10%. The coefficients of variation were 8.0% for Fe, 8.5% for Mn, 7.4% for Zn, 4.2% for Cu, 6.5% for Pb, 5.9% for Cd and 6.2% for Ni. Sequential extraction reagent blanks showed no detectable contamination. The detection limit (LOD) was 2.5 $\mu g\ L^{-1}$ for Fe, Mn, Zn, Cu, and Cd and 5.0 $\mu g\ L^{-1}$ for Pb.

3. Results and discussion

3.1. Carbonates, total organic matter (TOM) and grain size distribution

The percentages of carbonates ($CaCO_3$) and TOM in the sediments of the studied stations are shown in Table 2. The carbonate percentages exhibited the highest levels at four stations (V, VIII, IX and XII), with values of approximately 40–60%, indicating that biogenic materials constitute an important part of the nearshore sediments in the study area. $CaCO_3$ decreased at stations I, III, IV, VI, X, and XI, with values of approximately 20–30%, and at stations II and VII, it decreased to less than 20%.

The distribution of TOC (Table 2) in the studied sediments showed that the highest value of 1.44% occurred at station X and the lowest value of 0.26% was recorded at station II. However, the average value was $0.95 \pm 0.4\%$. The organic carbon from stations VI to XII fluctuated between 1.03% and 1.44% with a mean value of 1.0%. In general, the variations in total TOC in the bottom sediments of the study area could be related to algal and seagrass cover, terrigenous and domestic wastewater input, and local hydrodynamics (El-Metwally et al., 2017; Mansour et al., 2013).

The grain size distribution revealed that the sand fraction was the dominant component of the studied sediments (Table 2). The sand fraction was high, ranging from 95 to 100%, except at stations II and X, where it displayed values of 61% and 85.5%, respectively. The clay and silt fractions fluctuated from 0–39%. Additionally, the sediments in the study area contained a considerable amount of shell fragments.

3.2. Distribution of total heavy metals

Sediment particles consist mainly of biogenic and nonbiogenic (lithogenous) components, which are considered the final sinks for heavy metals delivered to the marine environment. Sediments are able to absorb a higher level of both toxic and persistent chemicals than water (Rodríguez-Barroso et al., 2009; Yuan et al., 2004). The total metal concentrations of Fe, Mn, Zn, Cu, Pb, Cd and Ni in the marine sediments of the coastal zone of Jeddah are presented in Table 2. The concentrations of these metals showed average values (in units of $\mu g\ g^{-1}$) of 3433–5883 (4472 ± 838), 483–1200 (784 ± 253), 241–532 (390 ± 109), 43–92 (67 ± 16),

Table 2 Sediments characterization and total metals concentrations, Jeddah coastal zone (Saudi Arabia).

	Locations		Grain size		TOC %	$CaCO_3$ %	Fe	Mn	Zn	Cu	Pb	Cd	Ni
St.	Latitude (N)	Longitude (E)	Sand %	Silt clay %			Total concentrations ($\mu g\ g^{-1}$)						
I	21.876617	38.972557	98.0	2.0	0.35	25.80	3800	550	241	58	121	2.04	110
II	21.866340	38.975300	61.0	39.0	0.26	5.03	3683	567	257	60	170	1.58	134
III	21.845668	38.993319	95.8	4.2	0.70	21.44	3950	1083	314	83	206	1.08	117
IV	21.751210	39.132770	96.2	3.8	0.66	29.36	3433	783	326	65	226	1.22	153
V	21.720934	39.113549	100.	0.0	0.63	53.34	4433	483	309	63	138	1.37	167
VI	21.520035	39.130082	96.0	4.0	1.03	31.45	5883	1200	410	43	155	2.32	147
VII	21.473369	39.163543	100.	0.0	1.09	16.59	4467	700	511	87	225	1.75	150
VIII	21.332450	39.119300	100.	0.0	1.09	42.60	4233	650	485	68	186	2.55	142
IX	21.320480	39.104820	98.5	1.5	1.18	46.47	4133	633	519	92	240	1.74	172
X	21.265594	39.128387	85.5	14.5	1.44	29.50	5683	1083	462	77	76	1.69	136
XI	21.136170	39.178060	97.3	2.7	1.37	30.05	4300	633	532	55	68	1.65	106
XII	21.082930	39.219490	94.9	5.1	1.30	61.37	5300	933	334	57	85	1.47	162
Min			61.0	0.00	0.26	5.03	3433	483	241	43	68	1.08	106
Max			100.	39.0	1.44	61.37	5883	1200	532	92	240	2.55	172
Avg.			93.3	6.8	0.95	35.06	4472	784	390	67	157	1.72	141
±SD			13.1	13.0	0.4	17.6	838	253	109	16	63	0.47	23

68—240 (157 ± 63), 1.08—2.55 (1.72 ± 0.47) and 106—172 (141 ± 23), respectively.

The lowest Fe concentrations were recorded at station IV, while the highest concentrations occurred at station VI (Table 2). The lowest concentrations of Mn were recorded at station V, while the highest values occurred at station VI. The minimum value of Zn (241 $\mu g\ g^{-1}$) was recorded at station I, whereas its maximum value (532 $\mu g\ g^{-1}$) was recorded at station XI. When comparing the Zn concentrations in this study with those obtained for the Red Sea, the studied sediments yielded an average concentration of Zn (390 ± 109 $\mu g\ g^{-1}$) 8 times higher than that previously reported in the sediment of the Red Sea (51 ± 14 $\mu g\ g^{-1}$) (Okbah et al., 2005). This may be related to the effect of industrial activities along the study area.

Cu ranged from 43 to 92 $\mu g\ g^{-1}$ (average value 67 ± 16 $\mu g\ g^{-1}$), exhibiting the lowest values at station VI, while the highest levels were recorded at station IX (Table 2). Cu was introduced into the sediments in lithogenic and biogenic forms. Clay minerals represent the main source of lithogenic Cu. However, the decomposition of organic matter releases Cu that can be adsorbed to the surface of clay minerals. Additionally, anthropogenic Cu and metal pollutants can enter the environment via the effluents of mining and industrial activities, fuel burning, sewage discharge and agriculture activity (fertilizers and pesticides).

The total Pb, Cd and Ni concentrations in the sediments of the coastal zone of Jeddah are shown in Tables 2 and 3. Their values varied from 68—240, 1.08—2.55 and 106—172 $\mu g\ g^{-1}$, respectively. The lowest concentrations of Pb and Ni were recorded at station XI, while their highest values occurred at station IX. Their average values were 157 ± 63 $\mu g\ g^{-1}$ and 141 ± 23 $\mu g\ g^{-1}$, respectively. The highest concentration of Cd (2.55 $\mu g\ g^{-1}$) was recorded at station VIII, with an average value of 1.72 ± 47 $\mu g\ g^{-1}$ (Table 2).

Comparisons of the heavy metal concentrations in the current study with other works in the same area and other areas of the world, such as the Red Sea coast (Hurghada area, Red Sea), Caspian Sea (Iran), Black Sea (Turkey), and Al-Hodeidah coast (Yemen) (Table 3) indicated that Fe, Mn, Zn, Cu, Pb and Ni revealed values higher than those demonstrated by Badr et al. (2009), Salem et al. (2014), El-Moselhy and Gabal (2004), Heba et al. (2004), Mora and Sheikholeslami (2002), Topcuoglu et al. (2002), while Cd presented lower concentrations than those reported by El-Moselhy and Gabal (2004). The sediments of Jeddah (Red Sea) studied by Al-Mur et al. (2017) showed higher levels of Fe, Mn, Zn, Cu and Pb than those reported in the present study.

3.3. Fractionation of heavy metals

The heavy metals in the studied sediments were fractionated into five categories according to binding, including exchangeable, carbonate, Fe-Mn oxide, organic matter (oxidizable) and residual fractions. This is because each of these categories has a different remobilization regime under changing environments. Thus, the speciation of heavy metals is important for measuring their bioavailability in the environment and for evaluating their potential risks to living organisms (Sadhana Pradhanang, 2014). In the present study, the investigated

Table 3 Heavy metal concentrations ($\mu g\ g^{-1}$ dry weight) from Jeddah coast, Red Sea during 2017 in comparison with other studies in the same area and other areas of the world.

Location	Fe	Mn	Zn	Cu	Pb	Cd	Ni	References
Jeddah, Red Sea	3433—5883	483—1200	241—532	43—92	68—240	1.08—2.55	106—172	Present study
Jeddah, Red Sea	8506.13	478.45	623.09	251.82	362.75	—	—	Al-Mur et al. (2017)
Jeddah, Rabigh, Yanbu, Red Sea	2.0—2671	34—205	52—76	17—24	80—99	1.8—3.95	67—90	Badr et al. (2009)
Egyptian Red Sea coast	3490	127.09	22.64	1.94	3.26	0.102	11.41	Salem et al. (2014)
Hurghada area, Red Sea	2000	177	4.66	0.67	12.89	2.30	1.91	
Caspian Sea, Iran	—	—	—	—	11—24	0.10—0.24	29—67	Mora and Sheikholeslami (2002)
Black Sea, Turkey	5000	206—870	34—267	4—95	0.05—31	0.02—0.93	13.65	Topcuoglu et al. (2002)
Al-Hodeidah, coast, Yemen	100—200	9—24	4.18	36—80	5—6	—	7—116	Heba et al. (2004)
North of Suez Gulf	—	—	4.26—23.68	1.84—10.25	13.9—28.34	2.26—4.4	—	El-Moselhy and Gabal (2004)

Table 4 Minimum, maximum and average content ± SD, and its relative percentage of trace metals in the five fractions extracted.

		Exchangeable		Carbonate		Reducible		Oxidizable		Residual		Total conc.
		Conc.	%	Conc.	%	Conc.	%	Conc.	%	Conc.	%	
Fe	Min	85	2	420	10	820	21	460	12	321	7	343
	Max	156	4	770	15	2320	52	1660	34	2010	53	5883
	Avg.	116	3	600	13	1530	34	1009	23	1230	29	4472
	SD	20	1	102	2	572	11	373	7	588	15	839
Mn	Min	6	1	5	0.4	20	3	40	4	52	8	483
	Max	23	4	105	12	300	47	380	50	726	67	1200
	Avg.	14	2	53	7	176	24	196	27	344	40	784
	SD	5	1	31	4	98	15	108	15	250	22	254
Zn	Min	2	1	10	3	84	24	52	17	20	5	241
	Max	21	6	70	21	227	66	237	50	117	31	532
	Avg.	10	3	36	10	147	39	137	33	66	17	391
	SD	6	2	22	7	47	12	74	13	34	9	110
Cu	Min	1	1	5	6	11	16	20	33	2	5	43
	Max	3	6	12	22	29	34	45	58	21	38	92
	Avg.	2	3	5	12	17	25	31	46	12	16	67
	SD	1	2	3	5	6	6	8	8	9	10	16
Pb	Min	2	1	10	5	11	5	14	12	15	18	68
	Max	8	10	24	28	32	32	46	39	165	73	240
	Avg.	5	4	14	11	19	15	30	21	90	50	158
	SD	2	3	5	8	8	9	10	8	57	20	63
Cd	Min	0.02	0.78	0.18	21	0.14	13	0.24	12	0.04	2	1
	Max	0.05	2.78	0.55	47	0.54	32	1.08	28	0.69	44	3
	Avg.	0.03	1.58	0.37	34	0.37	22	0.60	21	0.35	21	2
	SD	0.01	1	0.13	10	0.1	7	0.28	5	0.22	14	0.5
Ni	Min	1	1	11	6	32	20	26	22	6	6	106
	Max	7	5	27	21	65	47	61	43	63	38	172
	Avg.	3	2	20	14	42	30	43	30	34	23	141
	SD	2	1	6	4	11	9	13	8	19	1	23

metals revealed differences in the concentrations that were recorded at each step of the extraction. The results of the sequential extraction of Fe, Mn, Zn, Cu, Pb, Cd and Ni in the studied sediments are presented in Table 4 and Figs. 2—4 and discussed in the following text.

3.3.1. Exchangeable fraction (F_1)

Fraction F_1 includes the weakly sorbed metal forms held on the surfaces of soil and sediment grains by weak electrostatic interactions and ion-exchange processes. The metals of fraction F_1 can be released into the environment when conditions become more acidic, promoting a dangerous effect on the environment (Bakircioglu et al., 2011; Nemati et al., 2009). The range and mean content of the exchangeable metals of this study and the relative percentage of their equivalents are presented in Table 4 and Figs. 2—4. The range and average ($\mu g\ g^{-1}$) of released heavy metals in F_1 varied as follows: 85—156 (116 ± 20) for Fe, 6—23 (14 ± 5) for Mn, 2—21 (10 ± 6) for Zn, 1—3 (2 ± 1) for Cu, 2—8 (5 ± 2) for Pb, 0.02—0.05 (0.03 ± 0.01) for Cd and 1—7 (3 ± 2) for Ni (Table 4). It is evident that the metal concentrations of F_1 were lower than those of the other fractions in the present study (or negligible).

The relative percentage of total metals in this fraction corresponded to an average of 2—3% for Fe, Mn, Zn, Cu, and Ni, decreased to 1.58% for Cd and increased to 4% of the total for Pb (Figs. 2—4). The lower percentages of these metals might be explained by the decrease in metal sorption with increasing sediment pH, whereas the metal cations in sediments increase with increasing pH, likely due to an increase in surface negative charges. Additionally, the lower concentrations of the exchangeable fractions of Fe, Mn, Zn, Cu, Ni, Cd and Pb in the studied sediments might indicate the potential mobility of these metals. However, the percentages of Cd and Pb in this fraction were low, indicating that their potential environmental and ecological risks cannot be ignored. As shown in Figs. 2—4, the mobility order of heavy metals for the first fraction (F_1) was Fe > Mn > Zn > Pb > Ni > Cu > Cd.

3.3.2. Carbonate-bound metals fraction (F_2)

The fractionation results (minimum, maximum and mean concentrations) of the presently studied metals bound to carbonate are shown in Table 4. The ranges and the average concentrations were as follows: Fe had the highest value (420—770; 600 ± 102 $\mu g\ g^{-1}$), followed by Mn (5—105; 53 ± 31 $\mu g\ g^{-1}$), Zn (10—70; 36 ± 22 $\mu g\ g^{-1}$), Ni (11—27; 20 ± 6 $\mu g\ g^{-1}$), Pb (10—24; 14 ± 5 $\mu g\ g^{-1}$), Cu (5—12; 5 ± 3 $\mu g\ g^{-1}$) and Cd (0.18—0.55; 0.37 ± 0.13 $\mu g\ g^{-1}$). As

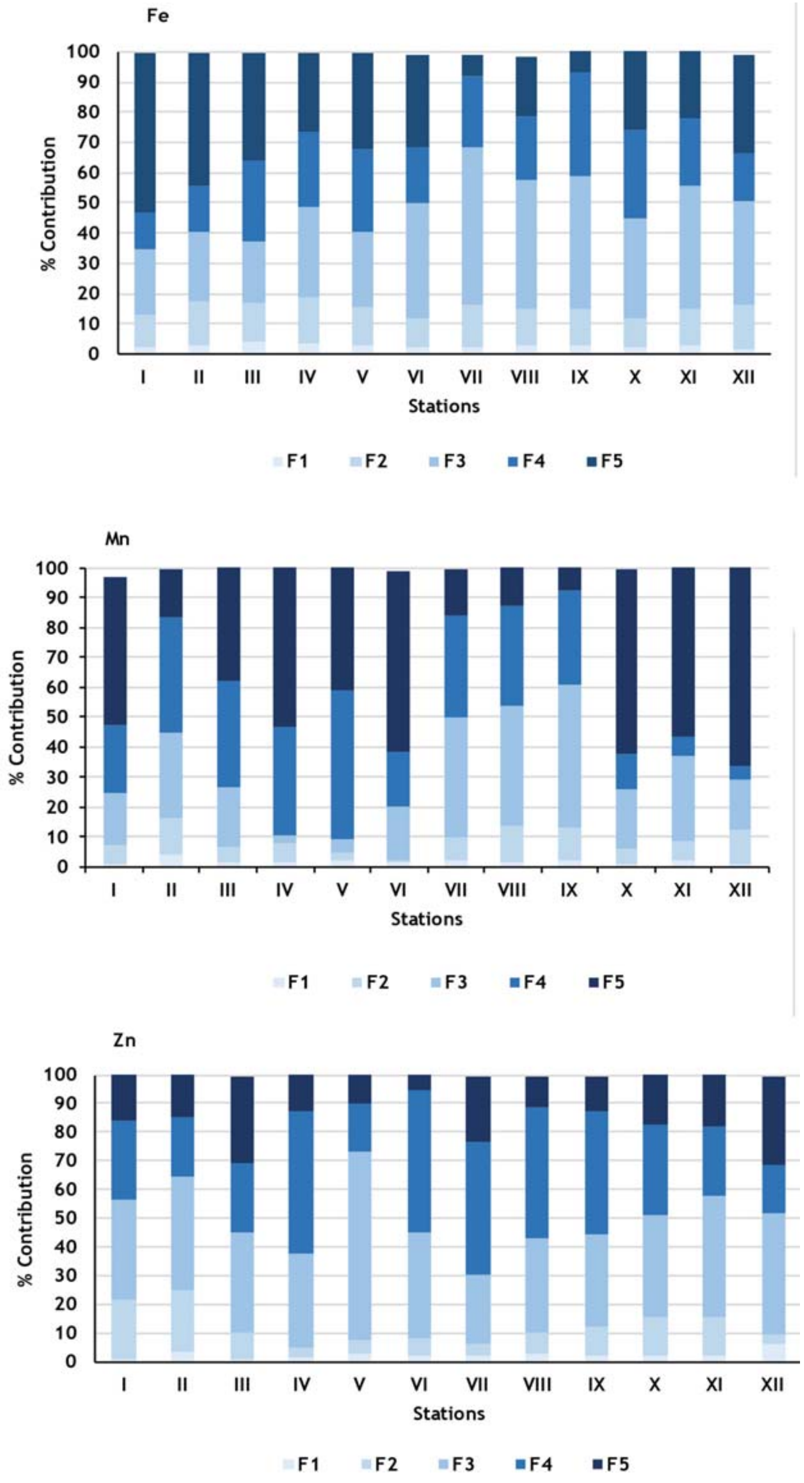

Figure 2 The relative percentage of Fe, Mn, and Zn from the total concentration in each fraction of the studied sediments.

shown in Table 4, the metals in the carbonate fraction (average value) in the study area were arranged in the following order: Cd (34%) > Ni (14%) > Fe (13%) > Cu (12%) > Pb (11%) > Zn (10%) > Mn (7%). This trend in the levels of metal concentrations differs partially from those of Egyptian Red Sea coastal sediments, which had metal concentrations following this order: Mn > Cu > Ni > Pb > Co > Cd (El-Said and Youssef, 2013).

3.3.3. Reducible fraction (F_3)

The metals in fraction F_3 are those bound to the hydrous oxides of Mn and Fe; they are released into the environment when a reducing condition develops. Thus, a reducing solution was used as the extractant (Gleyzes et al., 2002). The concentrations of heavy metals in this fraction, associated with Mn-Fe hydrous oxides (range and average; in $\mu g\ g^{-1}$), were 820—2320 (1530 ± 572) for Fe, 20—300 (176 ± 98) for

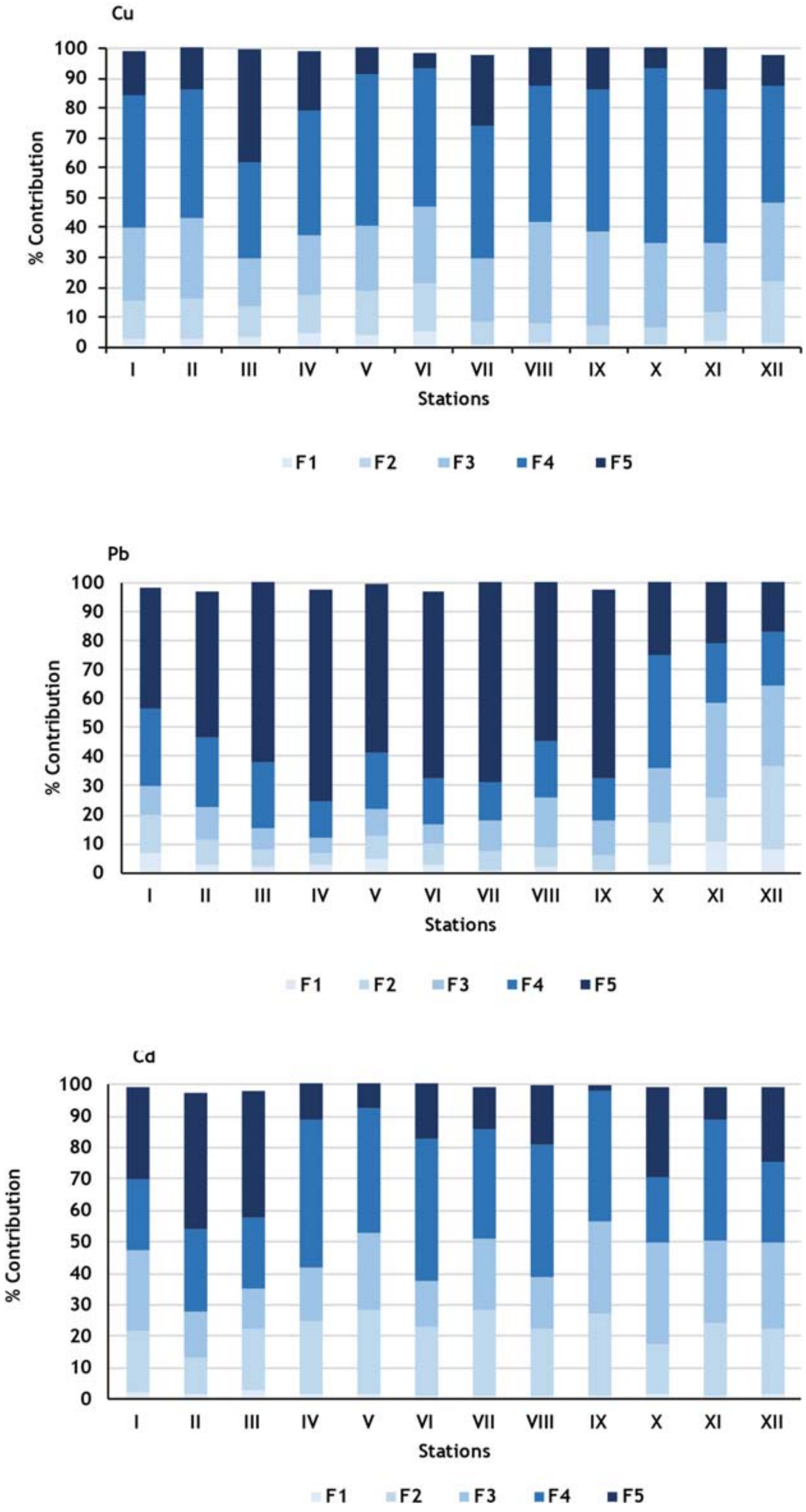

Figure 3 The relative percentage of Cu, Pb, and Cd from the total concentration in each fraction of the studied sediments.

Mn, 84—227 (147 ± 47) for Zn, 11—29 (17 ± 6) for Cu, 11—32 (19 ± 8) for Pb, 0.14—0.54 (0.37 ± 0.14) for Cd and 32—65 (42 ± 11) for Ni (Table 4). The relative percentages of Fe, Mn, Zn, Cu, Pb, Cd and Ni in the reducible fraction were 34%, 24%, 39%, 25%, 15%, 22% and 30%, respectively (Table 4 and Figs. 2—4). As shown in Figs. 2—4, the mobility of the metals in F_3 followed this order: Fe > Mn > Zn > Ni > Pb > Cu > Cd.

3.3.4. Oxidizable fraction (F_4)

The metals of fraction F_4 are known to bind with organic matter and sulfide compounds that can be released into the environment when oxidizing conditions develop. The heavy metals associated with organic and sulfide compounds can remain in the sediments and soils for a long time until they are released by decomposition processes or oxidizing agents,

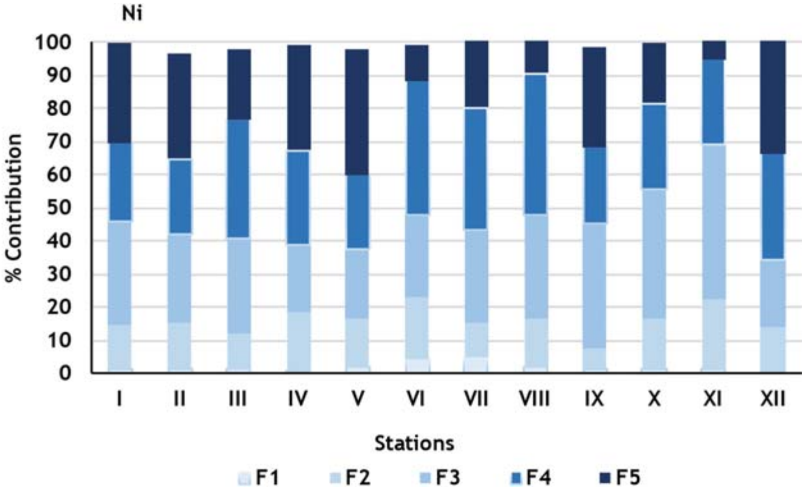

Figure 4 The relative percentage of Ni from the total concentration in each fraction of the studied sediments.

leading to their complexation and bioaccumulation (Kennedy et al., 1997). This fraction may be linked to humic substances with high molecular weights and is therefore considered to be of low mobility, releasing small amounts of metals into the environment (Filgueiras et al., 2002).

F_4 showed wide variations in the concentrations of certain metals in the studied sediments. The range and mean values (in μg g^{-1}) of F_4 were 460—1600 (1009 ± 373) for Fe, 40—380 (196 ± 108) for Mn, 52—237 (137 ± 74) for Zn, 20—45 (31 ± 8) for Cu, 14—46 (30 ± 10) for Pb, 0.24—1.08 (0.60 ± 0.28) for Cd and 26—61 (43 ± 13) for Ni (Table 4). The relative percentages of the studied metals (Fe, Mn, Zn, Cu, Pb, Cd and Ni) in F_4 were 23 ± 7%, 27 ± 15%, 33 ± 13%, 46 ± 8%, 21 ± 8%, 21 ± 5% and 30 ± 8%, respectively (Table 4 and Figs. 2—4).

The present data revealed that more than 46% of the total Cu is related to the organic carbon in the studied sediments, whereas Cu could be transported to surface sediments in association with a biogenic carrier phase or via anthropogenic waste (Abu-Zied et al., 2013). Additionally, Chester et al. (1988) noted that approximately 50% of the Cu in surface water particulates was associated with organics.

3.3.5. Residual fraction (F_5)

F_5 includes the rest of the metals and is associated with minerals that are bound via their crystalline structure, immobilized, and that will not constitute a threat to the ecosystem. The residual fraction contains metals that are chemically stable, immobile, and biologically inert. The relative percentage of metals in this fraction was at a level of approximately 7—53% for Fe, 8—67% for Mn, 5—31% for Zn, 5—38% for Cu, 18—73% for Pb, 2—44% for Cd and 6—38% for Ni (Table 4).

The Fe content in the residual fraction of the sediments ranged between 321 μg g^{-1} at station IX and 2010 μg g^{-1} at station II, with an average of 1230 ± 588 μg g^{-1} (Table 4). A high relative percentage of Fe was found in the residual fraction, but Fe presented low concentrations in the other fractions of this study. The value ranged between 7% at station XI and 53% at station I, with some exceptions, such as stations VII, VIII and IX, where it ranged from 7 to 20%. This may also indicate that Fe tends to be incorporated into the lattice structure of the sediment. Mn showed a similar tendency to that of Fe, bound to the residual form with a relative percentage from 35 to 67% of the total concentration for all the sediment samples, except for the sediment samples of stations II, VII, VIII and IX, where the percentage ranged from 8—15% of the total concentration (Figs. 2—4). The data observed in Table 4 show that the range and mean value of Mn are between 52 and 726 μg g^{-1} (344 ± 250 μg g^{-1}). These results may indicate that Fe and Mn have a greater affinity for the nonresidual fraction, which may increase the potential bioavailability and mobility of Fe and Mn in the environment.

The range and mean concentration of Zn in the residual fraction are presented in Table 4 and Fig. 2. The concentrations ranged between 20 μg g^{-1} at station VI and 117 μg g^{-1} at station VII, with an average of 66 ± 34 μg g^{-1}. The relative percentage of Zn ranged from 4.9—31% at stations III (95 μg g^{-1}, 30%) and XII (103 μg g^{-1}, 31%), whereas at the remaining stations, the relative percentages of Zn ranged from 5—23%. The residual form of Cu was relatively high at station III (31 μg g^{-1}, 38% of the total Cu) and decreased to its lowest level (2 μg g^{-1}, 5% of the total Cu) at station VI. These results showed that low concentrations of Cu were recorded in the residual fraction, while high Cu concentrations were dominant in the other extracts in the present study, indicating that Cu could be more bioavailable in the studied sediments (Fig. 3).

Pb was dominant in the residual extract of the studied sediment samples at nine stations, ranging between 15 and 165 μg g^{-1} (from station XI to station IV) and representing 41 to 73% of the total Pb (Fig. 3), and decreased to its lowest level at station XII (16 μg g^{-1}, 18% of the total Pb). The Pb at the sampling sites showed remarkable variations within the study area, likely due to variations in the mineralogical composition of the sediments, which are the main carrier of Pb. The distribution of Cd content in various chemical forms reflects the extent of Cd contamination in Jeddah coastal area sediments. The residual form ranged between 0.04 and 0.69 μg g^{-1} (24% to 44% of the total content) for stations I, II, III, X, and XII and from 0.04 to 0.69 μg g^{-1} (2% to 44% of the total content) for the other stations. The Ni in the residual fraction ranged between 6 and 63 µg g^{-1}, with a mean value of 34 ± 20 µg g^{-1}; its relative percentage ranged between 9 and 38% of the total content. Three sediment samples exhibited low levels in this fraction and were from stations VI (15 µg g^{-1}, 10%), VIII (14 µg g^{-1}, 10%) and XI (6 µg g^{-1}, 6%).

A comparison of the five sequential extracts showed that a large proportion of metals in this study were found in three phases (the carbonate, reducible and oxidizable fractions). This is likely due to the occurrence of low pH values, which prevented reabsorption and caused the metals to be more soluble in the extracting solution.

3.4. Bioavailability factor (BF)

The BF was described by Bielicka-Giełdoń et al. (2013). The BF was computed from the total concentration of heavy metals and the content of bioavailable forms according to the following formula:

$$\mathrm{BF} = \frac{C_{\mathrm{bio}}}{C_{\mathrm{total}}},$$

where C_{bio} and C_{total} are the concentration of bioavailable metals and the total concentration of metals in the studied sediments, respectively. The bioavailable metals are those in fractions F_1, F_2, F_3 and F_4, according to the protocol described in Tessier et al. (1979), and may be analogous to changes in environmental marine conditions and affect heavy metal binding in sediments. The bioavailability factor allows for the determination of possibly toxic elements in marine sediments.

The largest amount of Fe was extracted from the non-residual fractions (F_1, F_2, F_3 and F_4) and was in ranges of 2—4%, 10—15%, 21—52% and 12—34% of the total Fe for the exchangeable, carbonate, oxidizable and organic fractions, respectively. The smallest concentrations of Fe were found in the exchangeable and carbonate fractions. The BF ranged from 0.47 to 0.93, indicating the mobilization of more than 50% of the Fe in the studied sediment samples.

The largest contents of Mn were recorded in the reducible and organic forms, with nearly 50% of the total Mn content in the studied sediments. The smallest amounts of this metal were present in the exchangeable and carbonate fractions in the ranges of 1—4% and 0.4—12%, respectively. The bioavailability factor was in the range of 0.34 to 0.47 for six stations: I, IV, VI, X, XI and XII. The largest bioavailability factor was in the range of 0.60 to 1 for six stations: II, III, V, VII, VIII and IX. This reflects the considerably higher mobility of Mn in the sediments of these sampling sites.

The concentrations of Zn in the most mobile fractions of the present study, the reducible and oxidizable fractions (F_3 and F_4), represented an average of approximately 72% of the total content. The lowest content of Zn was obtained in the exchangeable fraction (F_I; approximately 0.6—6% of the total Zn). The bioavailability factor of the study area was in the range of 0.70 to 1%. Generally, the BF value of Zn in sediments was more than 1 for all of the sediment samples, except for those of stations III and XII (approximately 0.70%). This result illustrated the high Zn bioavailability and demonstrates a potential risk to aquatic life.

The highest levels of Cu concentration were observed in the reducible fraction (F_3, ranging from 16—34%) and in the oxidizable fraction (F_4, ranging from 33—58%). Approximately 46% of the total Cu was linked to the organic fraction. The smallest amounts of Cu, ranging from 0.7—6% of the total Cu, were present in the exchangeable fraction (F_I) and the carbonate fraction (F_2, ranging from 6—22%). The maximum mobility of Cu in the sediments was confirmed by its BF, which was in the range of 0.60 to 1%. This reflects the high mobility of Cu in the studied sediments.

High concentrations of Pb were recorded in the organic extract (F_4) and ranged from 12.4—39.1% of the total Pb, followed by the reducible fraction (F_3, 5—32% of the total Pb) and the carbonate fraction (F_2, 5—28% of the total Pb), while the smallest amounts of Pb occurred in the exchangeable fraction (F_I), ranging from 1% to 10% of the total Pb. In general, a high Pb bioavailability factor of greater than 0.70% was reported at three stations (stations X, XI and XII).

Table 5 Risk assessment code (RAC).

Criteria (%), Singh et al. (2005)	Sites	Mn	Zn	Cu	Pb	Cd	Ni
		Percentage of Exchangeable + Carbonate					
No risk <1	I	7.45	21.58	15.50	20.05	25.00	14.70
Low risk 1—10	II	16.41	24.90	16.39	11.65	27.85	15.50
Medium risk 11—30	III	6.56	10.19	13.94	8.37	25.00	12.10
High risk 31—50	IV	8.18	4.60	17.65	7.02	48.36	18.10
Very high risk >50	V	4.55	7.44	18.49	12.95	41.61	16.70
	VI	2.00	8.05	21.32	10.00	46.12	22.80
	VII	10.15	5.87	8.79	7.38	36.00	15.20
	VIII	13.69	10.11	8.00	8.85	43.13	16.40
	IX	13.27	11.94	7.01	6.17	42.53	7.70
	X	6.10	15.37	6.57	17.21	22.49	16.40
	XI	8.85	15.23	11.51	25.77	40.00	22.20
	XII	12.43	9.28	23.03	36.01	27.21	14.20
	Min	2.00	4.60	6.57	6.17	22.49	7.70
	Max	16.41	24.90	23.03	36.01	48.36	22.80
	Avg.	9.15	12.43	14.13	15.26	35.44	15.89
	±SD	4.61	6.77	5.89	10.10	9.62	4.59

However, the lowest BF values were found at the other stations (ranging from 0.20 to 0.40%), except for station I.

The Cd concentration in the most mobile fractions relative to the total content of the study area sediments was in the range of 21—47% (average of 34%) for the carbonate fraction, followed by the reducible fraction (13—32%; average of 22%). Another 12—27% (average of 21%) of Cd was associated with organic matter (F_4). The exchangeable form represented low amounts of the total Cd, ranging from 1 to 3%, with an average of 1%. The BF of Cd was in the range of 0.5% (station II) to 1% (station IX). Generally, the BF values of Cd in the sediments were greater than 1 for all of the sediment samples, except for stations II and III (which were approximately 0.60). This confirms the high bioavailability of Cd and demonstrates a potential risk to aquatic life.

As shown in Table 4 and Fig. 4, the highest Ni content was determined in the nonresidual extracts (F_1, F_2, F_3 and F_4), ranging from 1—5%, 6—21%, 20—47% and 22—43% of the total Ni for the exchangeable, carbonate, oxidizable and organic fractions, respectively. Much of this metal was also linked to the reducible and organic carbon extracts (F_3 and F_4), approximately 43—89% of the total content. The smallest levels of Ni were present in the exchangeable and carbonate/acid-soluble fractions. The bioavailability factor was less than 1% for sediments from stations II, IV, V, IX and XII and ranged from 0.70 to 0.95 for the other stations. The results obtained may reflect a high loading of contaminants due to enhanced anthropogenic activity in urbanized areas.

The sequential leaching procedure for the studied sediments showed potentially toxic metals, as indicated by the mobility and bioavailability characteristics (BF). The maximum mobility of the metals in the sediments (the metal species in the bioavailable fraction) (range; average) was (0.47 to 0.93; 0.71), (0.34 to 0.92; 0.60), (0.69 to 0.95; 0.83), (0.62 to 0.95; 0.84), (0.24 to 0.82; 0.49), (0.54 to 0.98; 0.78) and (0.60 to 0.95; 0.76) for Fe, Mn, Zn, Cu, Pb, Cd and Ni, respectively. In general, the high levels of BF for the studied metals could reflect their potential toxicity and that they could be easily released into the marine environment and ingested by marine organisms, thereby entering the food chain (Oyeyiola et al., 2011).

3.5. Risk assessment code (RAC)

The RAC was applied in this study based on the values of the exchangeable and carbonate fractions (Table 5) to measure the availability of the metals in solution, such as in an aquatic system. According to the RAC calculations, the concentration of metals in the fractionated sediments varied from fraction to another, showing different strengths (Singh et al., 2005). In the RAC (Table 5), when the percentage of metals in the exchangeable and carbonate fractions is less than 1%, the release of metals into solution is undetectable and safe to the environment. However, if the percentages in the same fractions are $>50\%$, the metals are considered highly dangerous and can easily enter the food chain (Jain, 2004). The RAC of Cd displayed a medium risk at five sediment sample stations (I, II, III, X and XII) and a high risk to the aquatic environment for the other sediment samples. The other metals (Fe, Mn, Zn, Cu, Pb and Ni) exhibited low to medium risks. This elevated risk in the studied environment is

Table 6 Principal component analysis with Varimax rotation.

	OC	$CaCO_3$	T-Fe	NR-Fe	T-Mn	NR-Mn	T-Zn	NR-Zn	T-Cu	NR-Cu	T-Pb	NR-Pb	T-Cd	NR-Cd	T-Ni	NR-Ni	% of Variance	% Cumulative
PC1	0.817	0.353	0.93	0.941	0.589	0.102	0.710	0.778	0.711	0.736	−0.293	−0.342	0.311	0.425	0.346	0.749	83.106	83.106

Extraction Method: Principal Component Analysis; Rotation Method: Varimax with Kaiser Normalization.

Table 7 Correlation matrix for the different studied components in Jeddah sediments, Red Sea.

	OC	CaCO3	T-Fe	NR-Fe	T-Mn	NR-Mn	T-Zn	NR-Zn	T-Cu	NR-Cu	T-Pb	NR-Pb	T-Cd	NR-Cd	T-Ni	NR-Ni
OC	1.000															
CaCO3	0.435	1.000														
T-Fe	**0.644**[*]	0.341	1.000													
NR-Fe	**0.873**[**]	0.336	**0.753**[**]	1.000												
T-Mn	0.395	−0.019	**0.658**[*]	0.425	1.000											
NR-Mn	0.071	−0.300	−0.085	0.239	0.279	1.000										
T-Zn	**0.823**[**]	0.141	0.318	**0.802**[**]	0.083	0.319	1.000									
NR-Zn	**0.715**[**]	0.155	0.309	**0.755**[**]	0.028	0.262	**0.951**[**]	1.000								
T-Cu	**0.878**[**]	−0.088	−0.248	0.240	−0.067	**0.655**[*]	0.369	0.236	1.000							
NR-Cu	**0.747**[**]	0.150	−0.005	0.436	−0.185	0.379	0.491	0.452	**0.831**[**]	1.000						
T-Pb	−0.313	−0.237	−0.499	−0.079	−0.114	**0.716**[**]	0.059	0.098	0.554	0.298	1.000					
NR-Pb	−0.197	−0.084	−0.415	−0.236	−0.267	**0.615**[*]	−0.043	−0.124	0.504	0.343	0.445	1.000				
T-Cd	0.193	0.050	0.316	0.275	−0.030	0.081	0.356	0.497	−0.277	−0.024	−0.067	0.112	1.000			
NR-Cd	0.396	0.312	0.306	0.492	−0.115	0.046	**0.601**[*]	**0.742**[**]	−0.145	0.132	0.059	−0.059	**0.871**[**]	1.000		
T-Ni	**0.680**[*]	0.573	0.217	0.435	−0.041	0.127	0.129	0.187	0.226	0.432	0.370	0.039	−0.058	0.213	1.000	
NR-Ni	**0.665**[*]	0.334	0.551	**0.837**[**]	0.329	0.387	**0.727**[**]	**0.776**[**]	0.110	0.282	0.224	-0.064	0.525	**0.717**[**]	0.531	1

[*] Correlation is significant at the 0.05 level.

[**] Correlation is significant at the 0.01 level.

No. of samples = 12. T: total metal concentration; NR: non-residual of heavy metal represents the sum of the four fractions (exchangeable + carbonate + reducible + oxidizable).

probably a result of the usage of gasoline and the discharge of uncontrolled industrial and sewage wastes (Abu-Zied et al., 2013, 2016; Al-Mur et al., 2017; Badr et al., 2009), which began in the early 1970s; however, as of recently, there has been a decrease in these activities due to the implementation of environmental laws.

3.6. Statistical analyses

Primary component analysis was applied to the present data obtained from the heavy metal fractionation of Jeddah surface sediments (Table 6). One component (PC), with a variance of 83.11%, is highly correlated with organic carbon, total heavy metals (Fe, Zn, Cu, and Ni) and the nonresidual fraction of the same metals (the nonresidual fraction represents the sum of the four fractions F_1, F_2, F_3 and F_4); the high loadings among this group exceed 0.7 (0.817, 0.930, 0.941, 0.710, 0.778, 0.711, 0.346, 0.746 and 0.749, respectively).

The correlation matrix between the total metals, nonresidual fractions of heavy metals and organic carbon can also be used to assess the degree of contribution of human sources to the examined metals (Table 7). The total organic carbon content is significantly positively correlated with total Fe, total Zn, total Cu, total Ni, nonresidual Fe, nonresidual Zn, nonresidual Cu and nonresidual Ni ($r = 0.644$, 0.873, 0.823, 0.715, 0.878, 0.747, 0.680 and 0.665, respectively). This reflects that the strong affinity of organic matter for Fe, Zn, Cu and Ni was mostly due to anthropogenic sources. The relationships between organic matter and the total concentrations of Mn, Pb and Cd were poor ($r = 0.395$, −0.313 and 0.193, respectively). On the other hand, no association was observed between the same elements in the nonresidual fractions and organic matter content.

4. Conclusion

One important environmental issue that is investigated in this study area is the concentration of heavy metals in sediments linked to different geochemical fractions. The heavy metals present in the marine sediments revealed variations in the type of different chemical phases in the study area. Cu showed a strong affinity with the organic fraction in all sediments of this study area. Cu, Zn and Pb were present in the reducible and oxidizable forms. Some metals, such as Cd, Ni, Fe and Mn, tend to accumulate in the carbonate, reducible and organic fractions.

Acknowledgments

This work was supported by the Deanship of Scientific Research (DSR), King Abdulaziz University, Jeddah under grant No. (D-170-155-1439). The author therefore gratefully acknowledges the DSR for its technical and financial support.

References

Abu-Zied, R.H., Al-Dubai, T.A.M., Bantan, R.A., 2016. Environmental conditions of shallow waters alongside the southern Corniche of Jeddah based on benthic foraminifera, physico-chemical parameters and heavy metals. J. Foramin. Res. 46, 149—170, http://dx.doi.org/10.2113/gsjfr.46.2.149.

Abu-Zied, R.H., Basaham, A.S., El Sayed, M.A., 2013. Effect of municipal wastewaters on bottom sediment geochemistry and benthic foraminifera of two Red Sea coastal inlets, Jeddah, Saudi Arabia. Environ. Earth Sci. 68, 451—469, http://dx.doi.org/10.1007/s12665-012-1751-7.

Abu-Zied, R.H., Hariri, M.S., 2016. Geochemistry and benthic foraminifera of the nearshore sediments from Yanbu to Al-Lith, eastern Red Sea coast, Saudi Arabia. Arab. J. Geosci. 9, 245, http://dx.doi.org/10.1007/s12517-015-2274-9.

Ahmadipour, F., Bahramifar, N., Ghasempouri, S.M., 2014. Fractionation and mobility of cadmium and lead in soils of Amol area in Iran, using the modified BCR sequential extraction method. Chem. Spec. Bioavailab. 26 (1), 31—36, http://dx.doi.org/10.3184/095422914X13884321932037.

Al-Mur, B.A., Quicksall, A.N., Al-Ansari, A.M.A., 2017. Spatial and temporal distribution of heavy metals in coastal core sediments from the Red Sea, Saudi Arabia. Oceanologia 59 (3), 262—270, http://dx.doi.org/10.1016/j.oceano.2017.03.003.

Badr, N.B.E., El-Fiky, A.A., Mostafa, Al.R., Al-Mur, B.A., 2009. Metal pollution records in core sediments of some Red Sea coastal areas, Kingdom of Saudi Arabia. Environ. Monit. Assess. 155, 509—526, http://dx.doi.org/10.1007/s10661-008-0452-x.

Bakircioglu, D., Kurtulus, Y.B., Ibar, H., 2011. Investigation of trace elements in agricultural soils by BCR sequential extraction method and its transfer to wheat plants. Environ. Monit. Assess. 175, 303—314, http://dx.doi.org/10.1007/s10661-010-1513-5.

Bielicka-Giełdoń, A., Ryłko, E., Żamojć, K., 2013. Distribution, bioavailability and fractionation of metallic elements in allotment garden soils using the BCR sequential extraction procedure. Pol. J. Environ. Stud. 22 (4), 1013—1021.

Chester, R.A., Thomas, F.J., Lin, A.S., Basaham, G., Jacinto, 1988. The solid state speciation of copper in surface water particulates and oceanic sediments. Mar. Chem. 24, 261—292, http://dx.doi.org/10.1016/0304-4203(88)90036-9.

El Zokm, G.M., Okbah, M.A., Younis, A.M., 2015. Assessment of heavy metals pollution using AVS-SEM and fractionation techniques in Edku Lagoon sediments, Mediterranean Sea. J. Environ. Sci. Health A 50, 571—584, http://dx.doi.org/10.1080/10934529.2015.994945.

El-Metwally, M.E.A., Madkour, A.G., Fouad, R.R., Mohamedein, L.I., Nour Eldine, H.A., Dar, M.A., El-Moselhy, Kh.M., 2017. Assessment the leachable heavy metals and ecological risk in the surface sediments inside the Red Sea ports of Egypt. Int. J. Mar. Sci. 7 (23), 214—228, http://dx.doi.org/10.5376/ijms.2017.07.0023.

El-Moselhy, K.M., Gabal, M.N., 2004. Trace metals in water, sediments and marine organisms from the northern part of the Gulf of Suez, Red Sea. J. Mar. Syst. 46, 39—46, http://dx.doi.org/10.1016/j.jmarsys.2003.11.014.

El-Said, G.F., Youssef, D.H., 2013. Ecotoxicological impact assessment of some heavy metals and their distribution in some fractions of mangrove sediments from Red Sea, Egypt. Environ. Monit. Assess. 185, 393—404, http://dx.doi.org/10.1007/s10661-012-2561-9.

Filgueiras, A.V., Lavilla, I., Bendicho, C., 2002. Chemical sequential extraction for metal partitioning in environmental solid samples. J. Environ. Monit. 4, 823—857, http://dx.doi.org/10.1039/B207574C.

Folk, R.L., 1974. Petrography of Sedimentary Rocks. Univ. Texas, Hemphill, Austin, TX, 182 pp.

Gaudette, H.E., Flight, W.R., 1974. An inexpensive titration method for the determination of organic carbon in recent sediments. J. Sediment. Petrol. 44 (1), 249—253, http://dx.doi.org/10.1306/74D729D7-2B21-11D7-8648000102C1865D.

Gleyzes, C., Tellier, S., Astruc, M., 2002. Fractionation studies of trace elements in contaminated soils and sediments: a review of sequential extraction procedures. Trac-Trend. Anal. Chem. 21 (6), 451—467, http://dx.doi.org/10.1016/S0165-9936(02)00603-9.

Hakanson, L., 1992. Sediment variability. In: Burton (Eds.), Sediment Toxicity Assessment. Lewis Publ., Boca Raton, FL, 19—36.

Heba, H.M.A., Al-Edresi, M.A.M., Al-Saad, H.T., Abdelmonesim, M. A., 2004. Background levels of heavy metals in dissolved, particulate phases of water and sediment of Al-Hodeidah, Red Sea coast of Yemen. J. King Abdulaziz Univ. — Mar. Sci. 15, 53—71, http://dx.doi.org/10.4197/mar.15-1.3.

Jain, C.K., 2004. Metal fractionation study on bed sediments of River Yamuna, India. Water Res. 38, 569—578, http://dx.doi.org/10.1016/j.watres.2003.10.042.

Kennedy, V.H., Sanchez, A.L., Oughton, D.H., Rowland, A.P., 1997. Use of single and sequential chemical extractants to assess radionuclide and heavy metal availability from soils for root uptake. Analyst 122, 89—100, http://dx.doi.org/10.1039/A704133K.

Li, X., Shen, Z., Wai, O.W.H., Li, Y., 2000. Chemical partitioning of heavy metal contaminants in sediments of the Pearl River Estuary. Chem. Spec. Bioavailab. 12 (1), 17—25, http://dx.doi.org/10.3184/095422900782775607.

Mansour, A.M., Askalany, M.S., Madkour, H.A., Assran, B.B., 2013. Assessment and comparison of heavy-metal concentrations in marine sediments in view of tourism activities in Hurghada area, northern Red Sea, Egypt. Egypt. J. Aquat. Res. 39, 91—103, http://dx.doi.org/10.1016/j.ejar.2013.07.004.

Masoud, M.S., Said, T.O., El-Zokm, G., Shreadah, M.A., 2010. Speciation of Fe, Mn and Zn along the Egyptian Red Sea Coasts. Chem. Spec. Bioavailab. 22 (4), 257—269, http://dx.doi.org/10.3184/095422910X12894975123773.

Molina, B.F., 1974. A rapid and accurate method for the analysis of calcium carbonate in small samples. J. Sediment. Petrol. 44 (2), 589—590, http://dx.doi.org/10.1306/74D72A9F-2B21-11D7-8648000102C1865D.

Mora, S.D., Sheikholeslami, M.R., 2002. ASTP: Contaminant Screening Program. Final Report: Interpretation of Caspian Sea sediment data. Caspian Environ. Program (CEP) 27, 227—251, http://dx.doi.org/10.1007/978-94-007-0967-6_9.

Moufaddal, W.M., 2002. Assessment of anthropogenic and natural changes along the Red Sea coastal zone between Ras Gemsha and Safaga, Egypt, using multidata satellite data. PhD Thesis. Saint Petersburg State Univ.

Nemati, K., Abu Bakar, N.K., Sonhanzadeh, E., Abas, M.R., 2009. A modification of the BCR sequential extraction procedure to investigate the potential mobility of copper and zinc in shrimp aquaculture sludge. Microchem. J. 92, 165—169, http://dx.doi.org/10.1016/j.microc.2009.03.002.

Okbah, M.A., Shata, M.A., Shridah, M.A., 2005. Geochemical forms of trace metals in mangrove sediments — Red Sea (Egypt). Chem. Ecol. 21 (1), 23—36, http://dx.doi.org/10.1080/02757540512331323953.

Oregioni, B., Aston, S.R., 1984. The Determination of Selected Trace Metals in Marine Sediments by Flame Atomic Absorption Spectrophotometry. UNEP reference methods for marine pollution studies No 38, Internal Report. IAEA Monaco Laboratory, Monaco City.

Oyeyiola, A.O., Olayinka, K.O., Alo, B.I., 2011. Comparison of three sequential extraction protocols for the fractionation of potentially toxic metals in coastal sediments. Environ. Monit. Assess. 172 (1—4), 319—327, http://dx.doi.org/10.1007/s10661-010-1336-4.

Rattan, R.K., Datta, S.P., Chhonkar, P.K., Saribatu, K., Singh, A.K., 2005. Long-term impact of irrigation with sewage effluent on heavy metal content in soils, crops and ground water — a case study. Agric. Ecosyst. Environ. 109 (3—4), 310—322, http://dx.doi.org/10.1016/j.agee.2005.02.025.

Rodríguez-Barroso, R.M., Benhamou, Y., El Moumni, B., El Hatimi, I., García-Morales, J.L., 2009. Evaluation of metal contamination in sediments from north of Morocco: geochemical and statistical approaches. Environ. Monit. Assess. 159 (1—4), 169—181, http://dx.doi.org/10.1007/s10661-008-0620-z.

Rowell, D.L., 1994. Soil Science: Methods and Applications. Longman Sci. Tech., Harlow, Essex, 350 pp., http://dx.doi.org/10.1002/jsfa.2740660423.

Sadhana Pradhanang, 2014. Distribution and fractionation of heavy metals in sediments of Karra River, Hetauda, Nepal. Technology 19 (2), 123—128, http://dx.doi.org/10.3126/jist.v19i2.13865.

Salem, D.M.S.A., Khaled, A., El Nemr, A., El-Sikaily, A., 2014. Comprehensive risk assessment of heavy metals in surface sediments along the Egyptian Red Sea coast. Egypt. J. Aquat. Res. 40, 349—362, http://dx.doi.org/10.1016/j.ejar.2014.11.004.

Singh, K.P., Mohan, D., Singh, V.K., Malik, A., 2005. Studies on distribution and fractionation of heavy metals in Gomti river sediments—a tributary of the Ganges. India. J. Hydrol. 312, 14—27, http://dx.doi.org/10.1016/j.jhydrol.2005.01.021.

Tessier, A., Campbell, P.G.C., Bisson, M., 1979. Sequential extraction procedure for the speciation of particulate trace metals. Anal. Chem. 51, 844—851, http://dx.doi.org/10.1021/ac50043a017.

Topcuoglu, S., Kirbasoglu, C., Gungor, N., 2002. Heavy metals in organisms and sediments from Turkish Coast of the Black Sea. Environ. Int. 27, 521—526, http://dx.doi.org/10.1016/S0160-4120(01)00099-X.

Youssef, M., El-Sorogy, A.S., Al-Kahtany, K.H., Al-Otaibi, N., 2015. Environmental assessment of coastal surface sediments Tarut Island, Arabian Gulf (Saudi Arabia). Mar. Pollut. Bull. 96, 424—433, http://dx.doi.org/10.1016/j.marpolbul.2015.05.010.

Yuan, C.G., Shi, J.B., He, B., Liu, J.F., Liang, L.N., Jiang, G.B., 2004. Speciation of heavy metals in marine sediments from the East China Sea by ICP-MS with sequential extraction. Environ. Int. 30, 769—783, http://dx.doi.org/10.1016/j.envint.2004.01.001.

Oceanologia (2020) 62, 45—55

Available online at www.sciencedirect.com

ScienceDirect

journal homepage: www.journals.elsevier.com/oceanologia/

ORIGINAL RESEARCH ARTICLE

Evaluation of morphodynamics of Miani Hor, a coastal lagoon of Lasbela, Balochistan, Pakistan

Naeem Ahmed Syed [a,*], **Tahira Siddiqa** [a], **Niamatullah Sohoo** [b]

[a] *Nusrat Jahan College, Rabwah, Chenab Nagar, Chinniot, Pakistan*
[b] *National Institute of Oceanography, Clifton, Karachi, Pakistan*

Received 11 January 2019; accepted 29 July 2019
Available online 17 August 2019

KEYWORDS
Coastal water body;
Lagoon;
Tidal constituents;
Inlet dynamics

Summary In compliance to the estuarine areas having access to the sea and riverine water, Miani Hor, a coastal water body in Lasbela, Pakistan could be categorized as a lagoon due to its shallowness, elongation to the coast, connectivity with the adjacent Sonmiani Bay and occasional receiving of rainwater. In the present paper, Miani Hor was studied to understand its dynamics, and to compare it with the categories of lagoons as proposed by Kjerfve (1986). The result of the field data of water quality and water movement as well as satellite imagery of different years show that this is a tide-dominated lagoon with a single inlet, and it was formed in the last glaciation period. Its only inlet is stable and remains open even during the period of high energy waves offshore Sonmiani Bay that generate strong littoral drift. The data suggest that unlike choked lagoons, as proposed by Kjerfve (1986) for classification of the single-inlet lagoons with limited tidal influence, Miani Hor has a small (0.08) ratio of the channel cross-sectional area to the lagoon surface area. The lagoon channel filters out high energy waves but allows strong tidal signals to penetrate the lagoon. The paper suggests that Kjerfve (1986) classification requires modification by incorporating another class "relaxed lagoons" for the single inlet tide-dominated lagoons.

---

[*] Corresponding author at: Department of Earth Sciences, Nusrat Jahan College, Dar-Ul-Rehmat Wasti, Chenab Nagar, Chiniot, Pakistan. Tel.: +92 (47) 6213405.

E-mail addresses: dr.naeem@njc.edu.pk, nasyed.phd@gmail.com (N.A. Syed), sohoonu_gwd@hotmail.com (N. Sohoo).

Peer review under the responsibility of Institute of Oceanology of the Polish Academy of Sciences.

Production and hosting by Elsevier

https://doi.org/10.1016/j.oceano.2019.07.002

1. Introduction

Coasts with a connection to the river and seawater are described as estuarine areas (Pritchard, 1952). The term estuary is further expanded and classified as (a) coastal plain/drowned river valley estuaries, (b) fjord estuaries, (c) bar-built estuaries, and (d) tectonically formed estuaries (Cameron and Pritchard, 1963). Based on detailed surveys, Kjerfve (1986) argues that Cameron and Pritchard (1963) definition is insufficient to cover some particular type of coastal water bodies. Kjerfve (1986) redefined them as (1) estuary — an inland river valley; (2) coastal lagoon — separated from the ocean by a barrier, connected to the sea by one or more restricted inlets; (3) fjord — a glacially scoured inland marine area; (4) bay — a coastal indentation; (5) tidal river — an inland river valley, subject to tidal sea-level variations; and (6) strait — an inland marine waterway, connecting two oceans or seas. The extended definition covers the coastal lagoons describing them as a water body with shallow depths, elongated parallel to the coast (Barnes, 1980; Colombo, 1977; Kennish and Paerl, 2010; Kjerfve, 1994). Lagoons covering 15% of the World's coastline are identified by three prominent features: (i) the presence of an isolating barrier beach, spit or chain of barrier islands; (ii) the retention of all or most of the water mass within the system during periods of low tide in the adjacent sea; and (iii) the persistence of natural water exchange between the lagoon and the parent sea by percolation through and/or overtopping of the barrier, through inlet/outflow channels, etc. permitting the lagoon water to remain saline or brackish (Barnes, 1980).

Pakistan in its 990 km long coastline, contains many coastal water bodies such as; Indus deltaic creeks system, occasional freshwater Hub River, Miani Hor, Kalmat Khor and Dasht River (Snead, 1993). The water bodies, along the Pakistan coast, have diversified physiographic features and could be categorized as estuaries with varying degree of freshwater mixing conditions. Miani Hor (Fig. 1) is one of such coastal water bodies in Pakistan that facilitates mixing the seawater and freshwater, however, it is least known and studied. Snead (1966) was the first who identified and described it geographically and mentioned that it is 65 km long meandering channel with varying width, connected to the Arabian Sea by a single inlet. In recent years, Qureshi (2005) and Rasool et al. (2002) explained its importance to marine life due to the presence of flourishing mangrove forest, but none of them ever discussed its hydrodynamical behavior. Therefore, this study was aimed to understand the characteristics of Miani Hor coastal water body following Cameron and Pritchard (1963) and Kjerfve (1986) criteria and classification for lagoons.

The results of the study suggest that Miani Hor is an estuary in adherence to Cameron and Pritchard (1963). Further to this, it follows the description of the coastal lagoon as provided by Barnes (1980), Colombo (1977), and Kennish and Paerl (2010). As and when there is rain in the catchment areas of Porali and Windar rivers, the rainwater is drained into Miani Hor and mixes with seawater within the lagoon. Its single inlet allows the tidal wave to move in but filter out the high energy waves. The tidal signal within the lagoon is so strong that the impact makes lagoon uncomparable with the three classes proposed for lagoons. The results of the study demonstrate that Miani Hor lagoon with a single inlet is influenced substantially by long-period tidal waves as against the choked lagoons. The lack of Miani Hor similarity with the three classes suggests the need to expand the number of lagoon classes to encompass tidally influenced single-inlet lagoons. Although this study is based on limited data that was collected with different objectives, the results obtained will set the future course of investigations based on planned data type and selection of observation sites.

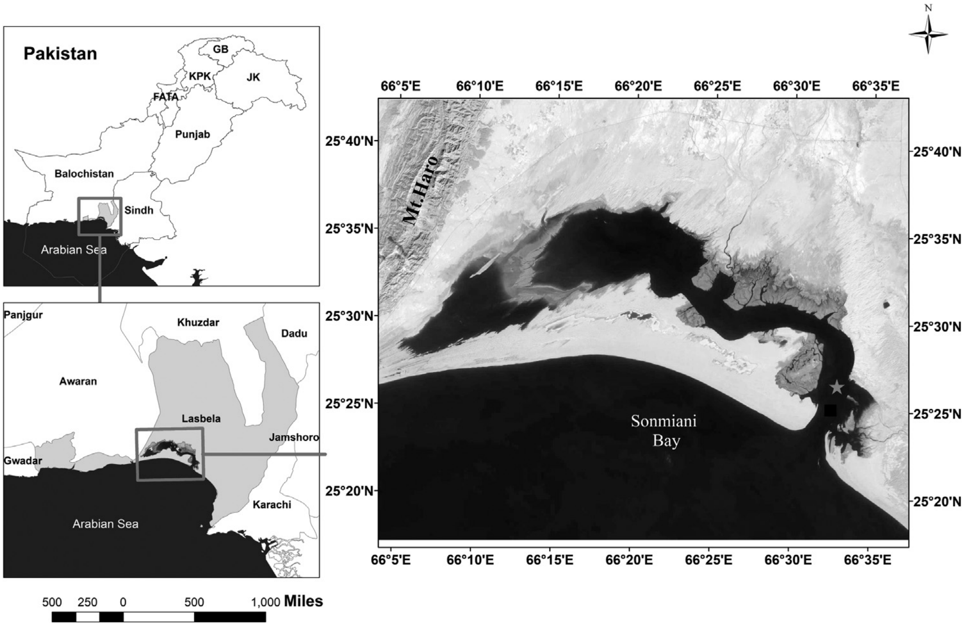

Figure 1 Location map of Miani Hor lagoon in Lasbela district, Balochistan, Pakistan. The data collection site is indicated with a star. (For interpretation of the references to color in this figure, the reader is referred to the web version of this article.)

2. Material and methods

The hydrodynamic characteristics of Miani Hor lagoon were studied using archived data that was recorded during October and November 2017 with different objectives. The data of lagoon water quality and water movement, along with the meteorological data, were used in this study. The vertical and horizontal variation of lagoon water was recorded for 29 days without any break. Aanderaa-made single-point SeaGuard RCM Doppler Current Meter was equipped with Wave and Tide Recording WTR sensor to measure wave and tide with the silicon pressure sensor. The SeaGuard RCM was moored at a depth of 6 m from surface of the water at the location marked with a star in Fig. 1. The instrument was retrieved, and data were downloaded and processed accordingly. One-time water properties within the same period and location were measured using Valeport made MIDAS CTD Profiler.

Offshore Sonmiani Bay hindcasted data by NOAA CFSR model was downloaded from metoceanview.com and used for drawing marine wind condition by plotting wind-rose diagrams. The Climate Forecast System Reanalysis (CFSR) model is developed by NOAA's National Centers for Environmental Prediction (NCEP). The global, high-resolution model was designed and executed as a coupled atmosphere-ocean-land surface-sea ice system to provide the best estimate of the state of these coupled domains over the 32 years of record from January 1979 to March 2011. It has been extended as an operational real-time product (NCDC, NOAA).

The study was substantiated with the earlier processed SPOT XS imagery for 3rd September 2005 level 2A by Naeem et al. (2014) to ascertain the littoral drift pattern along the seaward coast of Miani Hor. The shoreline change was determined using the Landsat 8 OLI/TIRS C1 Level 1 imagery for November: 2013, 2014, 2015, 2016 and 2017 with the respective dates: 22, 25, 28, 30 and 17, processed on ERDAS IMAGINE and computed the surface area of the lagoon by controlling the tidal level at image acquisition time. The purpose of regulating the imagery acquisition time was to ascertain the extent of coverage of water in the lagoon with tidal level (Table 1). The Operational Land Imager (OLI) onboard Landsat 8 satellite provides two new spectral bands: a deep blue visible channel (band 1) specifically designed for water resources and coastal zone investigation, and infrared channel (band 9) for the detection of cirrus clouds (https://lta.cr.usgs.gov, 2015). ESRI ArcGIS software was used for image classification and thematic mapping, whereas Matlab for the computation of tidal constituents, calculation of residual levels from the collected water level data by using Codiga (2011) codes and performing spectral analysis functions written by Torrence and Compo (1998).

The maximum combined nonharmonic water levels: Mean High Water Spring (MHWS), Mean Low Water Spring (MHWS), Mean High Water Neap (MHWN), and Mean Low Water Neap (MLWN), along with residual water levels, were determined from computed harmonic tidal constituents as proposed by Pugh (1987). The Form Factor r was also determined using Eq. (1) taken from Pugh (1987) by incorporating the amplitudes of K_1, O_1, M_2, and S_2 tidal constituents:

$$r = \frac{K_1 + O_1}{M_2 + S_2}. \tag{1}$$

The lagoon inlet stability proposed by O'Brien (1969) was computed using the formula:

$$A = xP^n, \tag{2}$$

where x and n are empirical constants. O'Brien (1969) concluded after surveying many lagoons that there might be a relationship between the entrance area and tidal prism and proposed the use of the following values $x = 4.69 \times 10^{-4}$ and $n = 0.85$. Based on his experience, he suggested that for the inlets without jetties good results could be obtained by incorporating $x = 2 \times 10^{-5}$ and $n = 1$. Therefore, the selection of appropriate value for empirical constants depends upon the volume of the tidal prism of the lagoon.

3. Observation and results

3.1. Description of the area

Geographically, Miani Hor lagoon (Fig. 1) is located in between 25°22′26.4″N to 25°37′40.8″N and 066°4′33.6″E to 066°35′45.6″E. It is approximately 95 km west of Karachi in the Lasbela district, Balochistan province of Pakistan (Naeem et al., 2014; Quraishee, 1988; Snead, 1966). The Lasbela is geographically well documented by Snead (1966) and described as an area of the alluvial plain of Porali and other small seasonal rainwater rivers. The analysis of imagery shows that Miani Hor lagoon is 64.73 km long, meandering channel varying in width, covering an average surface area of 401.87 km^2. It is connected with the Arabian Sea through a single, 5.3 km wide inlet that allows seawater to penetrate the lagoon during the rising tide period. The values obtained are similar to Snead (1966) but slightly higher than the values previously reported by Naeem et al. (2014) due to the use of a different approach.

Table 1 Dimensions of Miani Hor lagoon and inlet computed from Landsat 8 imagery.

Image date	Lagoon		Inlet		Tidal stage at imagery acquisition time
	Area [km^2]	Length [km]	Width [km]	Cross-sectional area [m^2]	
11/22/2013	407.25	64.62	5.18	41,440	Falling slack, 1.3 m
11/25/2014	422.5	64.63	5.22	41,760	Rising, 1.5 m
11/28/2015	491.73	64.87	5.26	42,080	Rising, 1.2 m
11/30/2016	349.33	64.85	5.18	41,440	High water slack, 2.4 m
11/17/2017	338.552	64.7	4.81	38,480	Rising, 1.7 m
Mean	401.87	64.73	5.13	41,040	

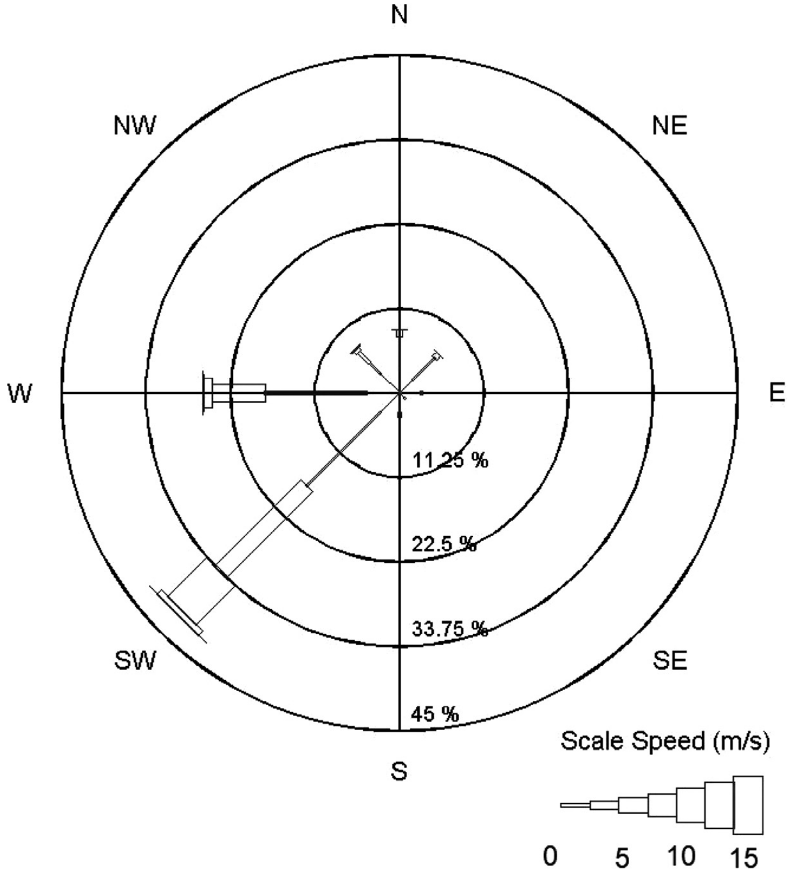

Figure 2 The wind-rose diagram with the percentage of occurrence of wind velocity and direction in the vicinity of Miani Hor (drawn from CFSR modeled data).

Miani Hor lagoon is barricaded from the open sea by two spits. The Adi Spit is situated west of the inlet, it extends to the southern tip of the Haro Mountain range. The Sonmiani Spit, a relatively shorter one, lies east of the inlet (Fig. 1). Porali and Windar rivers were the primary sources of sediment-laden freshwater supply to Miani Hor making it estuarine lagoon. The Windar River used to drain in the area before it ceased to exist, whereas the Porali River and its tributaries still contribute to Miani Hor during rainy seasons diluting the seawater.

3.2. Wind condition

Wind condition for the year 2017, at the coastal belt of the Sonmiani Bay, is hindcasted by the Climate Forecast System (CFS) model. The result of the model (Fig. 2) indicates that prevailing winds blow from west and southwest direction with velocities reaching to 17 m/s. Whereas, during the winter season, the wind stress is not active as compared to summer season but still has a considerable impact on the coastal areas in stabilizing the coast.

Table 2 Summary of wave condition recorded within Miani Hor in 2017.

	Significant wave height [m]	Wave period [s]
Maximum	0.367	7.876
Minimum	0.014	3.215

3.3. Wave condition within Miani Hor

Wave data was recorded by the moored instrument within Miani Hor during October and November 2017, the pre-winter monsoon period with variable offshore winds. The data indicate that waves are negligible within Miani Hor. The maximum height of significant wave recorded during the period is 0.4 m, which is relatively small. The summary of recorded wave data is given in Table 2.

3.4. Tidal level variation

Hourly water level data, recorded at the mooring site, is plotted as time series along with the predicted tide and residual water levels in Fig. 3. The tidal constituents computed from the recorded data, after converting to GMT, are given in Table 3. The values in the table represent the amplitudes and phases of the tidal constituents from true North used to predict the tidal water levels. The maximum-combined nonharmonic water levels computed from tidal constituent amplitudes are given in Table 4.

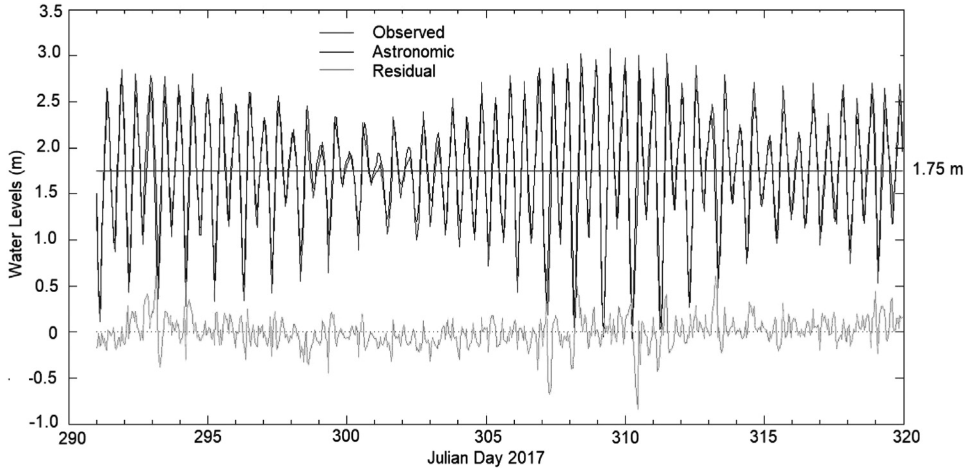

Figure 3 Time series plot of water levels as observed, predicted and residual for the recording period at recording site in Miani Hor.

Table 3 Some of the major tidal constituents computed from 29 days of hourly recorded data.

Constituent	Amplitude [m]	Phase [degrees]
Z0	1.75	
Diurnal		
K1	0.240	148
O1	0.123	188
OO1	0.034	283
J1	0.066	152
Q1	0.051	220
2Q1	0.028	265
NO1	0.047	126
UPS1	0.033	181
Semidiurnal		
M2	0.670	168
S2	0.253	178
N2	0.134	162
Overturn		
M4	0.031	159
M6	0.040	142
MK3	0.097	155
S4	0.001	124
MN4	0.019	47.9
MSF	0.051	35.2
M3	0.015	94.6
M8	0.004	103
MS4	0.015	198
MO3	0.109	206
2MS6	0.050	144
3MK7	0.019	95.3
SK3	0.017	279
2MN6	0.017	141
2SM6	0.011	163
ETA2	0.011	184
2SK5	0.003	332
2MK5	0.002	263

Table 4 Nonharmonic engineering levels at Miani Hor.

Mean water	Level [m]
MHWS	2.673
MLWS	0.827
MHWN	2.167
MLWN	1.333
ISLW	0.464

3.5. Tidal current variation

The seawater velocity data within the lagoon, recorded at a depth of 6 m at the mooring site, reveals that maximum ebb velocity is 0.86 m/s, which is higher than the flood velocity. The water current plotted as current rose diagram (Fig. 4) prominently indicates that Miani Hor is under the influence of tidal flow. The direction and magnitude of the seawater change with the change of tidal stage from ebb to flood or vice versa. The plotted current rose diagram (Fig. 4) further indicates that the dominant flow of lagoon water is in the alignment with the lagoon channel.

3.6. Lagoon water quality

The water quality was determined from temperature and salinity recorded at the mooring site and showed that temperature and salinity are almost mixed from the surface to bottom with relatively higher values at the surface and lower near the bottom (Fig. 5). The plotted profiles depict the average water column temperature of 29.56°C and salinity of 38.19 PSU.

4. Discussion

4.1. Characteristic of Miani Hor

Similarly to the majority of the coastal lagoons of the World, Miani Hor was also formed as a result of past million years

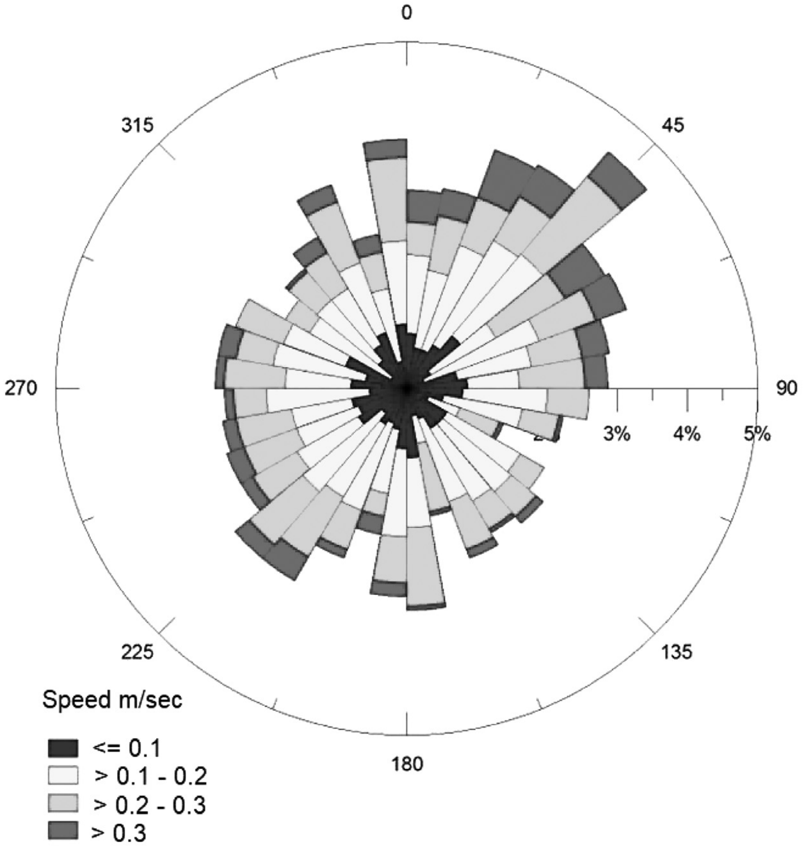

Figure 4 The current-rose-plot of hourly recorded sea water current data from 6 m water depth from the surface.

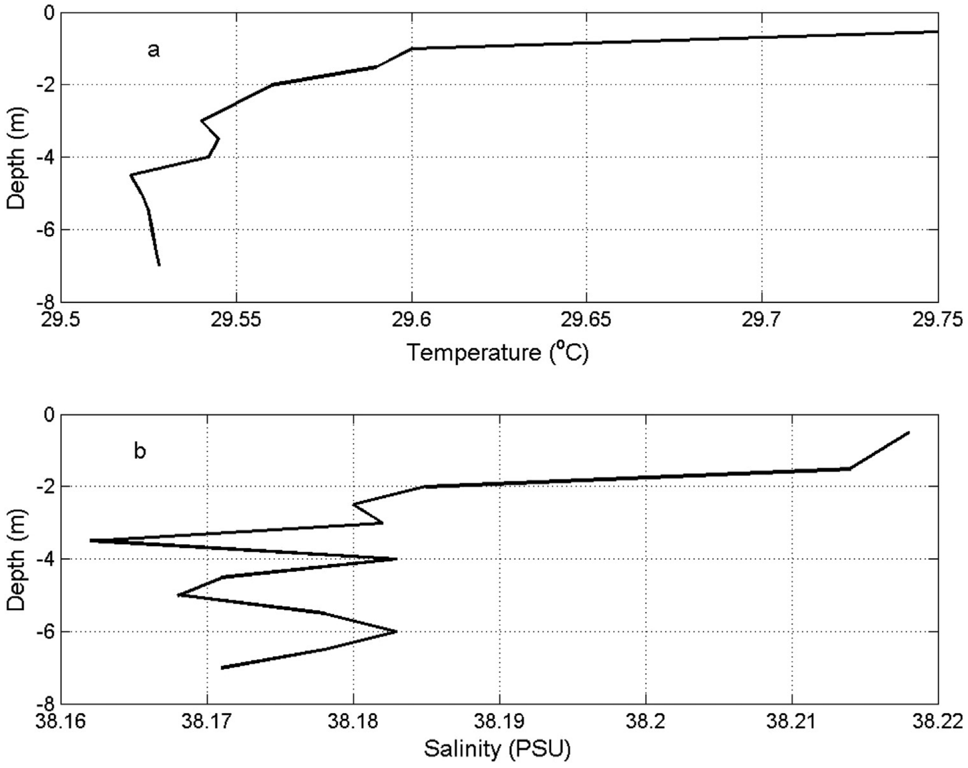

Figure 5 Temperature profile (a) and salinity profile (b) recorded at instrument mooring site in Miani Hor.

alternating filling and erosion in the Lasbela valley, that accompanied the four major glacial stages. Every deglaciation stage caused alluvial deposition in the Lasbela plain, while during the glacial phase, shallow Sonmiani Bay was exposed and supplied voluminous amount of fine material to the coast. The accretion of the accessive amount of sediments on the beach developed series of recurved spits across the shoreline of Sonmiani Bay by the action of strong southwest winds and seawater currents preventing the encroachment of the sea forming Miani Hor lagoon (Snead, 1966). The development of crescent bar and deposition of sediments at the coast made Miani Hor a shallow inland marine water body, oriented parallely to the coast. The crescent-shaped coast was bifurcated into Adi, and Sonmiani spits by a 5 km wide channel. Phleger (1969) described such configured water bodies as coastal lagoons. The elongated configuration of the lagoon is the sign of an easterly drift of sediment. Blue arrows indicate this phenomenon in Fig. 6. The lagoon channel remains open in all seasons due to the flushing of sediment-laden water out of the lagoon through the inlet and because the converged sediments are transported from both sides of barrier spits and are being pushed offshore into the deeper areas of Sonmiani Bay.

The southeasterly summer winds get large fetch area that helps to develop high energy waves all along the Pakistan coast. The average significant waves along the Karachi coast have been reported as 2.5 m, with 80% of them above 1.0 m (Rizvi et al., 1993). However, during winter, mild winds coming from land to sea generate only low energy waves. The yearlong wave data partially reported by Rizvi et al. (1993) is rearranged and presented as the wave-rose diagram in Fig. 7. The diagram indicates the dominant incoming waves striking the coast from southwest and south. As Sonmiani Bay is not far from Karachi, therefore, the Karachi approaching deep water waves are comparable. The high energy waves, developed during summer, drive the coastal sediments west to east along the Adi Spit and east to west along the Sonmiani Spit (Fig. 6) accumulating in front of the lagoon inlet. Unlike the open sea wave condition, waves within the lagoon are insignificant. The waves condition recorded within the lagoon during 2017 (Table 2 and Fig. 4) shows that within the lagoon the waves are entirely filtered out by the narrow lagoon inlet. The low energy waves within the lagoon are a locally generated waves due to the limited fetch (Naeem et al., 2014).

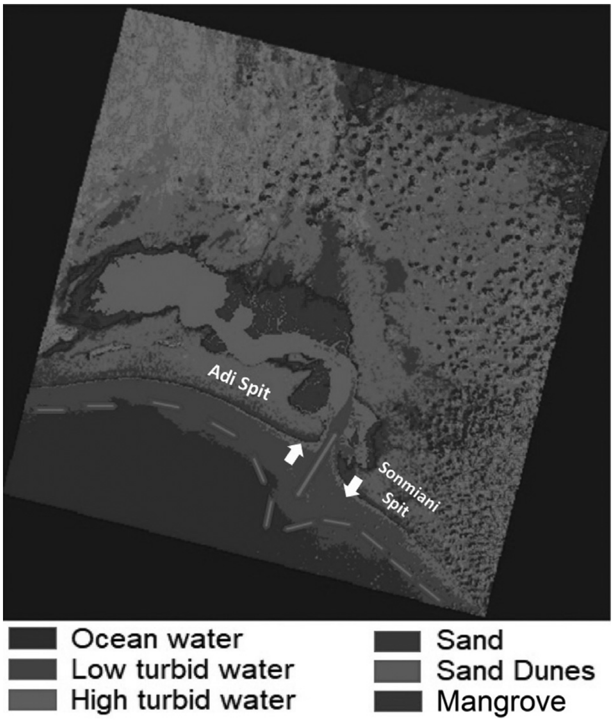

Figure 6 Classification of Spot XS imagery of 3rd September 2005 showing the alongshore, onshore—offshore sediment plume movement with blue arrows, whereas two white arrows indicate the downdrift offset inlet. (For interpretation of the references to color in this figure legend, the reader is referred to the web version of this article.)

The analysis of water level data indicates that tidal behavior within Miani Hor lagoon is similar to the other coastal areas of Pakistan. The form factor, a parameter widely used to describe the tide (Pugh, 1987) was computed as 0.393 which suggests that tide within Miani Hor lagoon is significantly mixed but mainly behave as a semidiurnal tide. The presence of tidal wave within Miani Hor is further verified with the spectral analysis of water level data. The results of the spectral analysis plotted in Fig. 8 indicates the presence of strong diurnal, semidiurnal, and third-diurnal tidal signals.

The rise and fall of the tide in the adjacent sea fluctuate the water level within the lagoon and hence, the surface area. The comparison of satellite imagery with the tidal stage at imagery acquisition time (Table 1) shows that on 30th November 2016 (Fig. 9D) it was high tide in the vicinity of lagoon inlet and water was spread over an area of 349.33 km^2. The image further depicts that while it was high-water near the lagoon inlet, there was a low-water condition at the far end of the lagoon. Similarly, the acquisition time of 28th November 2015 imagery (Fig. 9C) coincided with the low tide near the inlet, but water spread over an area of 491.73 km^2 in the lagoon. The extensive coverage of the lagoon seawater area indicates the extent of tidal crust up to the tail of lagoon. The analysis of imagery further reveals that high-water condition at the far end of the lagoon forces the water to spread over the Adi Spit from the southern bank and to move eastward through low lying areas of the spit, flooding the two-third of the spit length. It is, therefore, inferred that by the time tidal crust reaches the far end of the lagoon, the lagoon inlet is at the low tidal stage. The gentle banks of the lagoon surrounded by numerous mangrove-covered mudflats become exposed during low tide (Fig. 9D).

With the fluctuation of the tidal prism, the perimeter of the lagoon and inlet width also varies. The variation in the computed surface area determined from different years of imagery (Table 1) is the indication of tidal water level fluctuation. The surface area of the lagoon reported by Qureshi (2005), Rasool et al. (2002) and Snead (1966) was based on instantaneous measurements. The difference in reported values suggests that a systematic approach is required to determine the surface area of the lagoon and inlet at local chart datum.

Miani Hor lagoon, although relatively widespread at the upper half, changes further down into a narrow distinguishable meandering channel with an average depth of 8 m. The peculiar geometry of the lagoon could be explained as the combination of sediment deposits of Porali and Windar rivers

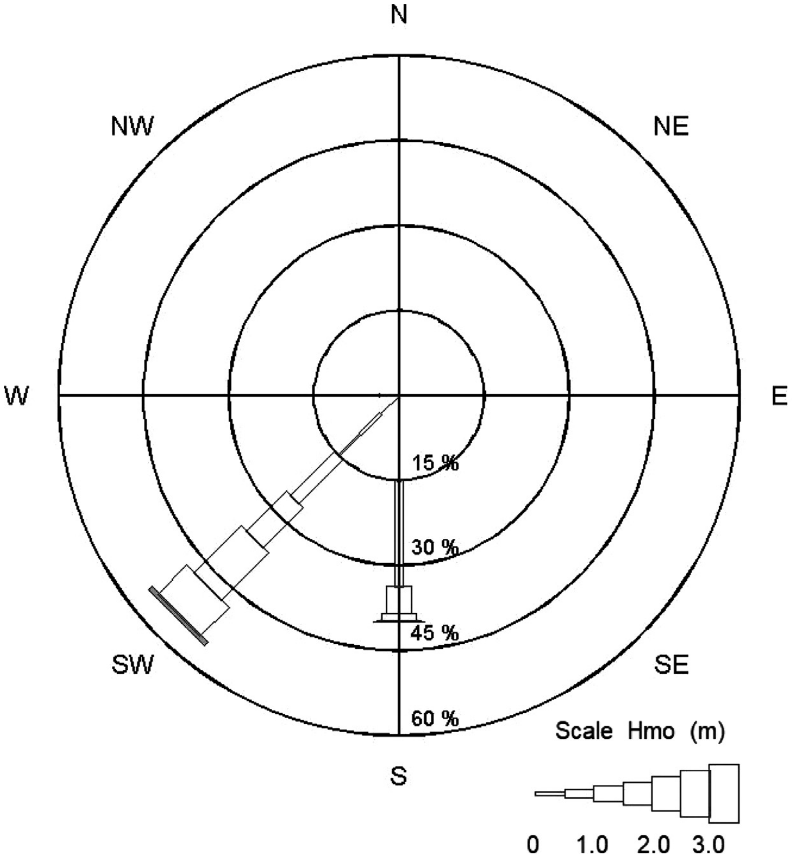

Figure 7 The wave-rose-diagram made from yearlong wave data for offshore Karachi (modified from Rizvi et al., 1993).

into the northern part of the lagoon and migration of the sand bar of the Adi Spit. The lagoon sediments confirm this inference as they are composed of silty clay with few sandy patches (Snead, 1966). The continuous filling of the lagoon forces the main channel to migrate southward. The constant migration of dry sand from Adi Spit pushes the main channel to the northeast (Snead, 1966). The Windar River used to drain at the eastern corner of the lagoon forming the significant size of the delta. However, since the last 150 years, with the upstream usage of Windar water, the delta is devoid

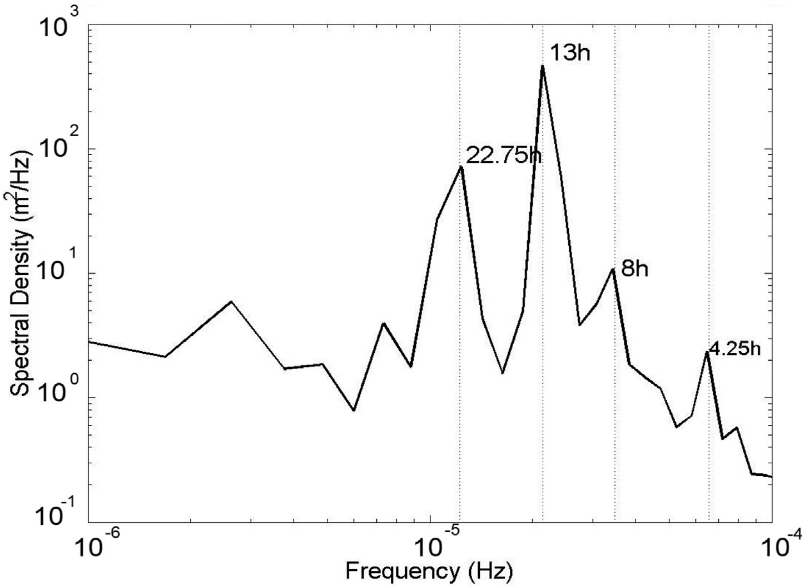

Figure 8 The plot of spectral analysis of observed water levels. The dominant tidal constituent signals are marked in the plot.

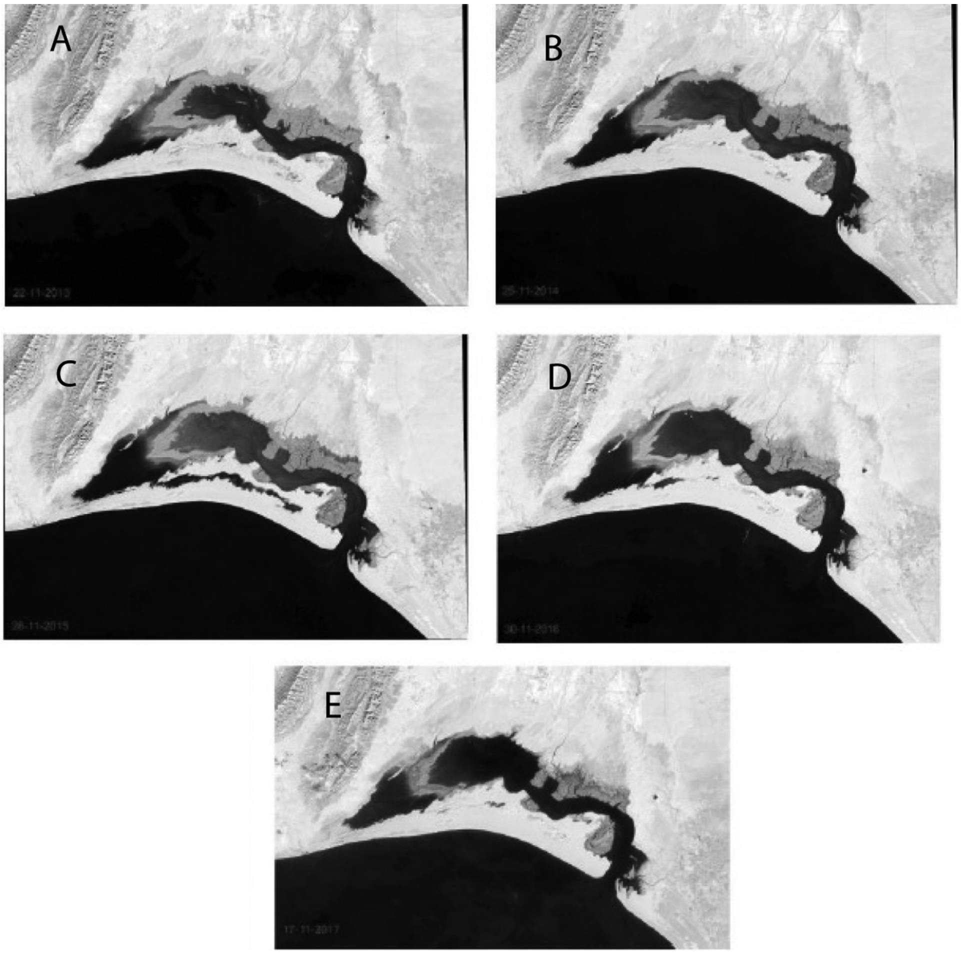

Figure 9 Landsat 8 temporal imagery: (A) 2013, (B) 2014, (C) 2015, (D) 2016, and (E) 2017.

of sediment-laden water. The unavailability of sediment is eroding the northern side of the Adi Spit to balance the sediment budget (Fig. 9B and C). The continuous erosion of Adi Spit and habitable land in the north bank of the lagoon had forced the local communities to retreat and move their houses to a more secure place. This situation has further been intensified by the construction of ill-designed nonfunctional fish landing jetty (Naeem et al., 2014) and two incomplete protection groins.

The data of tidal variation used in this study is the only available data for this study area to understand the tidal behavior within the lagoon. Unfortunately, data collected from a single point is not sufficient to cover the entire lagoon length. Therefore, to know the lagoon dynamics, spatially selected sites all along the lagoon need to be established for simultaneous recording of tidal data.

4.2. Inlet dynamics

Miani Hor lagoon inlet depth profiles show that the eastern side of the inlet is deeper (~10 m) than the western side (~6 m) (Snead, 1966) which is indicative of the forceful flow of water on the eastern bank of the inlet. The different inlet cross-sectional areas (38,480—42,080 m^2), and widths (4.81—5.26 km) are obtained from the analysis of the Landsat 8 imagery from 2013 to 2017 (Table 1) during different tidal stages. Morphologically, inlets are grouped into four classes: (1) overlapped inlet, overlapped by downdrift, (2a) significantly offset updrift side, (2b) significantly offset downdrift side and (3) negligible offset (Galvin, 1971). The analysis of satellite imagery shows that Miani Hor inlet is offset to downdrift (highlighted in Fig. 6 with white arrows) and is comparable to the 2b class. The Adi Spit, west of the inlet is offset northward, whereas, the Sonmiani Spit extends offshore (see Fig. 6). The longshore sediment movement is interrupted by the strong ebb currents jetting out of Miani Hor lagoon inlet. Therefore, the formation of type 2b tidal inlet is the result of steady littoral drift and tidal flow that maintain the opening of the channel (Galvin, 1971).

The stability of the inlet is determined from Eq. (2) by incorporating the tidal prism; 7.42×10^8 m^3 the volume of water that enters within the lagoon during high tide. The cross-sectional area of inlet is taken as 43,810 m^2 while empirical constants $x = 4.18 \times 10^{-4}$ and $n = 0.85$ were used (O'Brien, 1969). The resultant cross-sectional area is higher than the area measured from imagery (Table 4). O'Brien (1969) suggested that the empirical constants of Eq. (2) $x = 2 \times 10^{-5}$ and $n = 1$ could be used for inlets without jetties, and lagoons having their tidal prism in between 3.3×10^7 and 1.3×10^{10} m^3. The tidal prism of

Miani Hor is within the range, however, we used empirical constants; $x = 5.59 \times 10^{-5}$ and $n = 1$ to get the measured cross-sectional area (41,478 m^2). The nature of the inlet is the prime parameter that controls the lagoon function and it is the deterministic parameter along with the ratio of the channel cross-sectional area to surface area, that categorizes the lagoon as one of the three classes: choked, restricted or leaky (Kjerfve, 1986).

In accordance with the explanation provided by O'Brien (1969) for the stability of inlet, the dispersion of sediment plum, traced in Fig. 6 by blue arrows, is indicative of coastal sediment-laden water movement toward the lagoon-channel, accumulating the sediment as a result of tide and wave action. Whereas, the ebb and flood of tidal currents that rush through the inlet are responsible for sweeping accumulated bar, built as a result of sediment deposition, away from the channel and keeping it there even during summer monsoon high-energy wave climate. The phenomenon of a littoral drift is comparable to the stabilized inlets as described by O'Brien (1969). It is, therefore, inferred that the tidal inlet of Miani Hor lagoon is stable due to the equilibrium condition. In the absence of significant wave action during the winter monsoon, sediments flushed from lagoon develop into a bar in the Sonmiani Bay that is wiped out in summer.

Salinity values recorded in this study (Fig. 5b) are almost the same as reported by Naeem et al. (2014) but higher than the open sea salinities published by Ali and Naeem (1999) and Rizvi et al. (1993). The difference in salinities in the adjacent sea and lagoon waters indicates that the lagoon behaves as a negative estuary during the dry season and a positive estuary during the rainy season. During the dry season, the water evaporates from the lagoon leaving behind high salinity water. However, some traces of lower salinity at the subsurface layer are indicative of occasional freshwater input from the Porali River. Continuous contribution of freshwater into the lagoon on geologic time scale is further substantiated by the presence of healthy mangrove forest (Fig. 6) within Miani Hor, particularly, in the vicinity of the Porali River mouth and lagoon inlet (Naeem et al., 2014; Qureshi, 2005; Rasool et al., 2002; Saima and Usman, 2006; Snead, 1966). *Rhizophora mucronata* is a dominant species among other two, *Aviciennia marina* and *Ceriops tagal* varieties of mangroves, which are also present in Miani Hor lagoon (Qureshi, 2005; Snead, 1966).

Results of the analysis and the presence of healthy mangrove forest suggest that Miani Hor is a well-established lagoon in accordance with all three identifying features described by Barnes (1989). However, even though it has a single inlet and small ratio of channel cross-sectional area compared to the lagoon surface area, its dynamics are not in agreement with Kjerfve's (1986) choked lagoon classification scheme. Unlike the choked lagoons, Miani Hor lagoon is under the strong influence of tidal dynamics.

The results of the study suggest that Kjerfve (1986) classification of lagoons should be expanded to another class — relaxed lagoon, to encompass the single inlet lagoons with strong tidal influence. The proposed new classification of lagoons could be grouped as:

1. Choked lagoons — with a single inlet and limited tidal influence confined to the entrance.
2. Relaxed lagoons — with a single inlet and strong tidal influence.
3. Restricted lagoons — with two or more inlets and located on low/medium wave energy coasts with low tidal ranges.
4. Leaky lagoons — connected with the ocean by wide tidal passes that transmit oceanic effects with minimum resistance.

5. Conclusion

Miani Hor lagoon is located in the Lasbela district of Balochistan, Pakistan, and connected to the sea with the single inlet. It was formed as a result of the past million years of alternate filling and erosion in the Lasbela valley that accompanied the four major glacial stages. During the glacial stages, the shallow continental shelf of Arabian Sea was exposed at Sonmiani Bay which became a voluminous source of fine material for the formation of series of recurved spits by the southwest winds action. Formation of spits created barrier separating Miani Hor lagoon from Sonmiani Bay. Analysis of water level data collected for this study suggests that the lagoon is under the strong influence of tidal action. The form factor computed from the harmonic tidal constituents is 0.393, characterizing it as mixed but mainly semidiurnal tide. Miani Hor lagoon is a shallow inland marine water body, oriented parallely to the coast, separated from the Arabian Sea by a barrier but connected to the sea by an inlet. The characteristics mentioned by Phleger (1969) describe Miani Hor as a well established coastal lagoon.

The surface area of the lagoon changes prominently twice a day between high and low tides, that enter the lagoon from single inlet connecting it with the sea. The rise and fall of the tide in the adjacent sea causes horizontal flow of water into and out of the channel that in turn causes fluctuation of water level of the lagoon and hence the volume of water. Miani Hor lagoon inlet is more closely comparable with the Galvin (1971) 2b class due to significant offset in the downdrift of the inlet. Wave condition within the lagoon and adjacent sea indicate that offshore deepwater waves do not penetrate the lagoon due to the single narrow inlet. Strong tidal currents cause most of the erosion and accretion within and out of the lagoon. The sediments used in this process are either being eroded by the inundation of seawater to Adi Spit from lagoon side, or erosion of Windar delta and its vicinity.

Miani Hor lagoon was compared with Kjerfve (1986) classification, which is based on the number of inlets and tidal influence. The scheme of classification categorized lagoons into choked, restricted, and leaky groups. However, Miani Hor lagoon characteristics suggest that it cannot be ultimately compared with the mentioned classes. Unlike the lagoons with single inlet classified as choked lagoons, Miani Hor, even though it is connected with the sea by a single inlet and has a small ratio (0.08) of inlet cross-sectional area to the lagoon surface area, is strongly influenced by the tide but not wind-generated gravity waves. The results of the study based on limited data suggest that recognized classification of lagoons is incomplete and should be expanded to include single inlet lagoons with strong tidal effects. This study proposes the inclusion of another class — relaxed lagoon, for the tide-dominated single inlet lagoons.

Acknowledgments

Authors acknowledge the National Institute of Oceanography, Karachi for the facility provided during visits to the study area and for giving access to the archived data, Dr. Mirza Naseer Ahmad of Nusrat Jahan College Rabwah for encouraging and facilitating the study. Authors are also in debt of anonymous reviewers for their constructive comments that significantly improved this paper.

References

Ali, A., Naeem, A.S., 1999. Spreading of Persian Gulf water in the Northwestern Arabian Sea during the month of January. Pakistan J. Mar. Sci. 8 (1), 1—9.

Barnes, R.S.K., 1980. Coastal Lagoons: The Natural History of a Neglected Habitat. Cambridge Univ. Press, Cambridge, 106 pp.

Barnes, R.S.K., 1989. Coastal lagoons of Britain: an overview and conservation appraisal. Biol. Conserv. 49, 295—313, http://dx.doi.org/10.1016/0006-3207(89)90049-9.

Cameron, W.M., Pritchard, D.W., 1963. Estuaries. In: Hill, N.M. (Ed.), The Sea, vol. II. John Wiley & Sons, New York, London, 306—324.

Climate Forecast System, 2019. National Centers for Environmental Prediction (NCEP) Web. 02 July 2019, https://www.ncdc.noaa.gov/data-access/model-data/model-datasets/climate-forecast.

Codiga, D.L., 2011. Unified tidal analysis and prediction using the UTide Matlab functions. Technical Report 2011—01. Graduate School of Oceanography, University of Rhode Island, Narragansett, RI, 59 pp.

Colombo, G., 1977. Lagoons. In: Barnes, R.S.K. (Ed.), The Coastline. Wiley, London, 63—81.

Galvin Jr., C.J., 1971. Inlet and wave direction. In: Wave Climate and Coastal Processes. Symposium on Water, Environment and Human Needs. Massachusetts Institute of Technology, 44—78.

Kennish, M.J., Paerl, H.W., 2010. Coastal lagoons. In: Kennish, M.J., Paerl, H.W. (Eds.), Critical Habitats of Environmental Change. CRC Press, Boca Raton, 1—15.

Kjerfve, B., 1986. Comparative oceanography of coastal lagoons. In: Wolfe, D.A. (Ed.), Estuarine Variability. Acad. Press, New York, 63—81.

Kjerfve, B., 1994. Coastal lagoons. In: Kjerfve, B. (Ed.), Coastal Lagoon Processes. Elsevier, Amsterdam, 1—8.

MetOceanView, 2019. MetOceanView hindcast data, https://app.metoceanview.com/hindcast/.

Naeem, A.S., Razzaq, D.A., Sohoo, N., Ahmed, S.G., 2014. A study of the dynamics of Miani Hor coastal lagoon, Pakistan and failure of Damb fish harbour. Int. J. Sci. Technol. 3 (8), 501—510.

O'Brien, M.P., 1969. Equilibrium flow areas of inlets on sandy coasts. J. Waterw. Harbors Div. 95 (WW1), 43—52.

Phleger, F.B., 1969. Some general features of coastal lagoons. In: Ayala-Castañeres, A. (Ed.), Lagunas Costeras, un Simposio. Universidad Nacional Autónoma de México, México, DF., 5—26.

Pritchard, D.W., 1952. Estuarine hydrography. In: Landsberg, H.E. (Ed.), Advances in Geophysics, vol. 1. Acad. Press, New York, 243—280.

Pugh, D.T., 1987. Tides, Surges, and Mean Sea Level. John Wiley & Sons Ltd., New York, London, 486 pp.

Quraishee, G.S., 1988. Feasibility studies for the extraction of energy from current and haliohydrogravity along Pakistan coast. Final Tech. Rep. No. S-NIO/Ocean (9).

Qureshi, T., 2005. Mangroves of Pakistan: Status and Management. IUCN Pakistan Repot.

Rasool, F., Tunio, S., Hasnain, S.A., Ahmad, E., 2002. Mangrove conservation along the coast of Sonmiani, Balochistan, Pakistan. Trees 16 (2—3), 213—217, http://dx.doi.org/10.1007/s00468-001-0151-5.

Rizvi, S.H.N., Ali, A., Naeem, A.S., Tahir, M., Baquer, J., Saleem, M., Tabrez, S.M., 1993. Comparison of the physical properties of seawater offshore the Karachi coast between the northeast and southwest monsoons. In: Thompson, M., Tirmizi, N.M. (Eds.), The Arabian Sea. Living Marine Resources and Environment. CRC Press, Boca Raton, 619—626.

Saima, P.B., Usman, A.I., 2006. Are the mangroves for the future? Empirical evidence of the value of Miani Hor mangrove ecosystem as the basis for investments. IUCN Pakistan Rep., 33 pp.

Snead, R.E., 1966. Physical Geography Reconnaissance: Las Bela Coastal Plain, West Pakistan, Coastal Stud. Ser. 13. Louisiana State Univ. Press, Baton Rouge, 118 pp.

Snead, R.E., 1993. Uplifted marine terraces along the Makran coast of Pakistan and Iran. In: Schroder, J.F. (Ed.), Himalaya to the Sea. Geology, Geomorphology and the Quaternary. Routledge, London, 205—226.

Torrence, C., Compo, G.P., 1998. A practical guide to wavelet analysis. Bull. Amer. Meteor. Soc. 79, 61—78.

Oceanologia (2020) 62, 56—69

Available online at www.sciencedirect.com

ScienceDirect

journal homepage: www.journals.elsevier.com/oceanologia/

ORIGINAL RESEARCH ARTICLE

Evaluation of the carbon sequestration capacity of arid mangroves along nutrient availability and salinity gradients along the Red Sea coastline of Saudi Arabia

Kamal H. Shaltout [a], Mohamed T. Ahmed [a,b], Sulaiman A. Alrumman [b], Dalia A. Ahmed [a], Ebrahem M. Eid [b,1,*]

[a] *Botany Department, Faculty of Science, Tanta University, Tanta, Egypt*
[b] *Biology Department, College of Science, King Khalid University, Abha, Saudi Arabia*

Received 24 April 2019; accepted 22 August 2019
Available online 12 September 2019

KEYWORDS
Carbon sequestration;
Coastal wetlands;
Mangroves;
Red Sea;
Saudi Arabia;
Climate change

Summary In the present work, we assessed the carbon sequestration capacity of mangrove forests (*Avicennia marina*) in relation to nutrient availability and salinity gradients along the Red Sea coast of Saudi Arabia. This was achieved through estimating the sediment bulk density (SBD), sediment organic carbon (SOC) concentration, SOC density, SOC pool, carbon sequestration rate (CSR) and carbon sequestration potential (CSP). The present study was conducted at 3 locations (northern, middle and southern), using 7 sites and 21 stands of mangrove forests (*A. marina*) along ~1134 km of the Red Sea coastline of Saudi Arabia (from Duba in the north to Jazan in the south), all of which are in an arid climate. The correlation coefficients between the water characteristics and the first two Canonical Correspondence Analysis (CCA) axes indicated that the separation of the sediment parameters along the first axis were positively influenced by TDS (total dissolved solids) and EC (electric conductivity) and were negatively influenced by total N and total P. On the other hand, the second axis was negatively correlated with total N, total P, EC and TDS. The SOC pools at the northern (10.5 kg C m^{-2}) and southern locations (10.4 kg C m^{-2}) were significantly

---

* Corresponding author at: Botany Department, Faculty of Science, Kafr El-Sheikh University, Kafr El-Sheikh 33516, Egypt. Tel.: +966 55 2717026; fax: +966 17 241 8205.

E-mail addresses: ebrahem.eid@sci.kfs.edu.eg, eeid@kku.edu.sa, ebrahem.eid@gmail.com (E.M. Eid).

[1] Permanent address: Botany Department, Faculty of Science, Kafr El-Sheikh University, Kafr El-Sheikh, Egypt.

Peer review under the responsibility of Institute of Oceanology of the Polish Academy of Sciences.

Production and hosting by Elsevier

https://doi.org/10.1016/j.oceano.2019.08.002

higher than the SOC pool at the middle location (6.7 kg C m^{-2}). In addition, the average CSR of the northern (5.9 g C m^{-2} yr^{-1}) and southern locations (6.0 g C m^{-2} yr^{-1}) were significantly higher than they were in the middle location (5.0 g C m^{-2} yr^{-1}).

1. Introduction

Carbon dioxide (CO_2) is one of the greenhouse gases, and it plays a major role in climate change and global warming, where its concentration increased from 280 ppmv in 1850 to 411 ppmv in 2019 (Page, 2019); thus, many scientists have suggested that CO_2 sequestration in soil organic carbon may significantly contribute to reducing the effects of climate change (Alongi, 2012, 2014; Siikamäki et al., 2012; Taillardat et al., 2018). Furthermore, increasing soil carbon pools and protecting carbon rich soils are key for achieving the Paris Climate Agreement's climate targets (Rumpel et al., 2018).

Mangroves are one of the most important blue carbon ecosystems because they act as a carbon sink and contribute to the mitigation of atmospheric greenhouse gas emissions (Taillardat et al., 2018). Mangroves cover approximately 137,600 km^2 in 118 countries (Bunting et al., 2018); they are typically composed of shrubs and trees and form extensive forested wetlands along both muddy and carbonate coasts in tropical and subtropical climates (Rovai et al., 2018; Twilley et al., 2018). They usually grow in estuaries where nutrients are plentiful; they also grow in nutrient-poor areas such as carbonate coasts in the Caribbean and Red Sea regions where trees are dwarfed (Lovelock et al., 2004). Compared to terrestrial carbon pools, mangroves store more sedimentary carbon per area than any other terrestrial ecosystem (Twilley et al., 2018), where mangrove sediments contain up to 36.1 kg m^{-2} of blue carbon within the top 1 m of sediment (Sanderman et al., 2018). This amount is much greater than soil carbon pools estimated for other ecosystems such as closed shrublands (11.0 kg m^{-2}), savannas (11.2 kg m^{-2}), croplands (12.7 kg m^{-2}), deciduous broadleaf forests (13.4 kg m^{-2}), evergreen broadleaf forests (15.1 kg m^{-2}), grasslands (15.5 kg m^{-2}), open shrublands (16.9 kg m^{-2}), mixed forests (19.8 kg m^{-2}), evergreen needleleaf forests (21.0 kg m^{-2}), permanent wetlands (24.1 kg m^{-2}), and deciduous needleleaf forests (25.3 kg m^{-2}) (Sanderman et al., 2018). Mangroves also provide many beneficial environmental services to coastal communities (Almahasheer et al., 2017) such as protection of the coast from winds, erosion, and provision of food and shelter for many types of marine life and birds (Eid et al., 2016; Shaltout, 2016).

Mangrove forests are one of the most threatened ecosystems due to urban expansion and other land uses; thus, understanding the distribution of soil carbon in mangrove forests is very important for prioritizing protection and restoration efforts for climate mitigation (Sanderman et al., 2018). In the Arabian Peninsula, mangrove forests are found along its east and west coasts (Kumar et al., 2010). The Red Sea is near the northern limit of mangroves in the Indo-Pacific region, situated in the Sinai Peninsula at 28°N (Almahasheer et al., 2016a). The harsh environment of the Red Sea region is considered a limiting agent for the growth and prosperity of mangroves (Edwards and Head, 1987). However, the area of Red Sea mangroves (135 km^2) has increased by 12% over the past forty years, which may be attributed to repairing and afforestation projects (Almahasheer et al., 2016a). Mangrove forests of the Red Sea include examples of euhaline-metahaline and hard-bottomed mangroves (Price et al., 1987). Kumar et al. (2010) reported that the mangroves along the Saudi Arabian Red Sea coast are found as fragmented stands in intertidal zones. Price et al. (1998) reported that mangroves of the Saudi Arabian Red Sea coast were significantly more abundant along coastal sites than offshore sites, as well as more abundant in southern latitudes compared to northern latitudes. This type of vegetation is of special interest as it flourishes in the most unfavourable conditions, such as areas with high salinity, devoid of rivers, scarce rainfall and dry land (Saifullah, 1994). *Avicennia marina* in Saudi Arabia, covers approximately 48.4 km^2 along the Red Sea coast (Almahasheer, personal communication), and some 10.4 km^2 along the Arabian Gulf (Almahasheer, 2018). On the Red Sea coast of Saudi Arabia, mangrove stands extend from the Jordanian border in the north to the southern border in Jazan (El-Juhany, 2009) but are not continuous due to severe environmental conditions (Saifullah, 1997).

Some studies have been conducted to assess the carbon sequestration potential (CSP) of mangrove forests along the Saudi Arabian Red Sea coast and all these studies were carried out in southern locations and only one was carried out in a central location. Eid et al. (2016) explored the efficiency of mangrove forests along the southern Saudi Arabian Red Sea coast for CSP. Almahasheer et al. (2017) assessed the sediment organic carbon (SOC) pools and carbon sequestration rate (CSR) in mangroves along the central Saudi Red Sea coast. Arshad et al. (2018) evaluated the CSR in polluted and non-polluted mangrove sediments near Jazan, an urban city (southern Saudi Red Sea coast). Eid et al. (2019) evaluated the impact of land use changes due to conversion of areas of mangrove growth to shrimp farms on the SOC pool in the sediment along the southern Saudi Red Sea coast.

As a result of human activities, nutrient availability varies from north to south along the Saudi Red Sea coast today. Moreover, salinity in Red Sea surface water increases northwards (Edwards, 1987). To our knowledge, no study has been carried out in Saudi Arabia to evaluate the carbon sequestration capacity of mangrove forests along nutrient availability and salinity gradients along the entire Saudi Red Sea coast. Thus, the present study was carried out to evaluate sediment bulk density (SBD), SOC concentration, SOC density, the SOC pool, the CSR and CSP in the mangrove sediments along nutrient availability and salinity gradients along

~1134 km of the Saudi Arabian Red Sea coastline (from Duba in the north to Jazan in the south). Hence, the goal of the current investigation was to evaluate probable changes in "blue carbon" due to nutrient availability and salinity effects. The results of this study have worldwide applications because they can be extrapolated to similarly high-value ecosystems to mitigate carbon emissions in other parts of the planet and serve to mitigate their degradation.

2. Material and methods

2.1. Study area

The Red Sea coast of Saudi Arabia extends in the NW-SE direction to a distance of 1700 km and lies between the northern end of the Gulf of Suez at a latitude of 30°N and the southern end at Bab El-Mandeb at approximately 13°N (Fig. 1) (Saifullah, 1997). The climate of Saudi Arabia is arid and very severe with high temperatures and minimal rainfall (Siraj, 1984). Winds are northerly in winter and southerly in summer (Morley, 1975). Rainfall in southwestern Saudi Arabia is caused by monsoons formed in the Indian Ocean; thus, rainfall increases significantly from north to south (Eid et al., 2016). Red Sea surface temperatures increase southward, while surface water salinity increases northwards (Edwards, 1987). *Avicennia marina* (Forssk.) Vierh. is the dominant species in mangrove forests along the Saudi Red Sea coast, while *Rhizophora mucronata* Lam. can be found only in scattered patches in the Farasan Islands (Mandura et al., 1987). According to El-Juhany (2009), mangrove forests have been subjected to many stresses, such as camel grazing, trash in the sea and on the beaches, and the establishment of other human activities such as shrimp farms.

2.2. Sampling locations

Sampling was carried out (supplementary material 1) at 3 locations (northern, middle and southern), 7 sites and in 21 stands of mangrove forests (*A. marina*) along the Saudi Arabian Red Sea coast (Fig. 1). The distance between the northern and middle location is 736 km and the distance between the middle and southern location is 398 km. The northern location is characterized by high salinity, relatively low temperatures, dry land and minimal rainfall (Saifullah, 1997). The middle location is characterized by extreme climatic conditions such as high temperatures and sporadic rainfall (Almahasheer et al., 2016b); furthermore, eutrophication is occurring as the result of sewage and fertilizer discharging into the sea which affects mangrove growth (Almahasheer et al., 2017). The southern location is characterized by low salinity, favourable temperatures, soft muddy soil, plentiful rainfall and an abundance of nutrients (Saifullah, 1997). Sampling in the northern and middle locations occurred at one site with three mangrove stands (Duba and Jeddah Cities, respectively), while in the southern location sampling occurred at 5 sites with 15 mangrove stands (three per site) (Fig. 1).

2.3. Sediment sampling

Sampled stands were selected to cover mangroves' habitats evenly to enable an accurate evaluation of mangroves' capacity to sequester carbon along the Saudi Red Sea coast. A total of 187 sediment cores were collected from 21 sampled stands to ensure a proper estimate of carbon sequestration in mangrove sediments. The sediment samples were collected with a 7 cm diameter hand sediment corer, which provides a

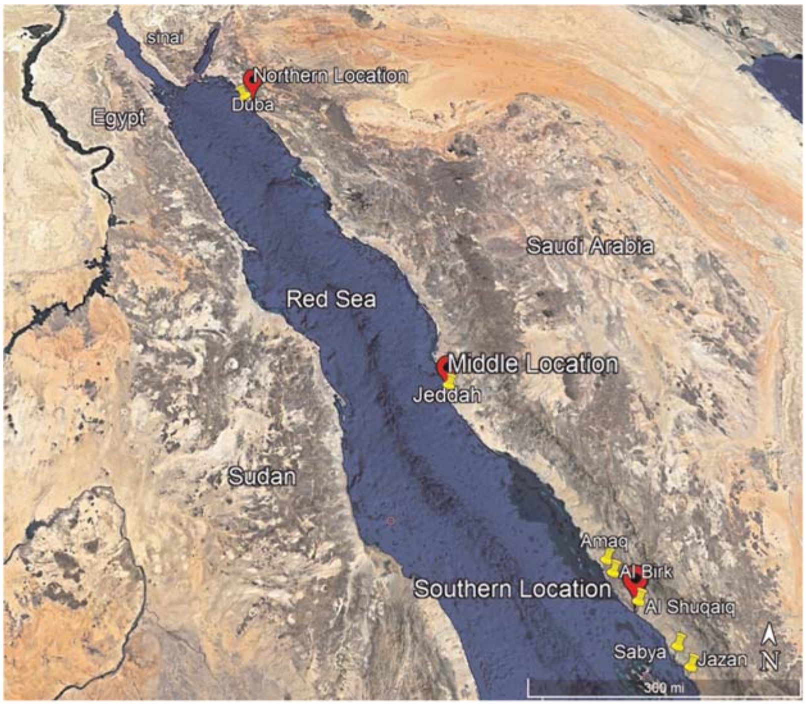

Figure 1 Map of the study area indicating the 3 locations [📍] and the 7 sampling sites [📌].

perfect sediment core (Tan, 2005). The corer was pushed down to a depth of 50 cm, and then the sediment core was removed from the corer carefully. The sediment core was immediately sectioned with a blade into 10 samples each of 5 cm thick (0—5, 5—10, 10—15, 15—20, 20—25, 25—30, 30—35, 35—40, 40—45 and 45—50 cm) and packed in plastic containers. The sample containers were tightly sealed and stored on ice to avoid volatilization losses and to minimize microbial activity until analysis (Eid and Shaltout, 2016). Thus, 1383 sediment samples were collected to determine SBD, SOC concentration, SOC density and the SOC pool.

2.4. Population characteristics

At each sampling stand, population density, height, and crown diameter of all mangrove trees (*A. marina*) were estimated inside three randomly distributed quadrates (each of 10 × 10 m).

2.5. Sediment analysis

Each sediment sample was oven-dried at 105°C for three days, cooled in a desiccator, and weighed to determine SBD as follows (Wilke, 2005):

$$\rho_{sj} = \frac{m_j}{v_j},$$

where ρ_{sj} is SBD [g cm^{-3}] of the j^{th} layer, m_j is mass of sediment sample [g] of the j^{th} layer dried at 105°C, and v_j is the volume of the sediment sample [cm^3] of the j^{th} layer. Dry samples were grinded and sieved to pass through a 2 mm mesh size. Nóbrega et al. (2015) recommended using the loss on ignition method to estimate SOC in mangrove sediments in the absence of a CHN analyser. Thus, each sample was analyzed for SOC concentration by measuring sediment organic matter (SOM) using the loss on ignition method at 550°C for two hours as follows (Jones, 2001): SOM concentration [g C kg^{-1}] = 1000 × (weight of oven dried sample [g] − weight of sample after ignition [g])/weight of oven dried sample [g]); SOC [g C kg^{-1}] = 0.5 × SOM [g C kg^{-1}] (Pribyl, 2010).

SOC density [kg C m^{-3}] was estimated as follows (Han et al., 2010): $SOC_{dj} = \rho_{sj} \times SOC_j$, where SOC_{dj} is the SOC density [kg C m^{-3}] of the j^{th} layer, ρ_{sj} is the SBD [g cm^{-3}] of the j^{th} layer, and SOC_j is the SOC concentration [g C kg^{-1}] of the j^{th} layer.

SOC pool [kg C m^{-2}] of a profile, expressed as a mass per unit surface area to a fixed depth, was calculated as follows (Meersmans et al., 2008):

$$SOC_p = \frac{\sum_{j=1}^{k} SOC_{dj} \times T_j}{\sum_{j=1}^{k} T_j} \times D_r,$$

where SOC_p is the SOC pool [kg C m^{-2}], D_r is the reference depth (=0.5 m), T_j is the thickness [m] of the j^{th} layer and k is the number of the layers. CSR [g C m^{-2} yr^{-1}] was estimated based on the sedimentation rate, SBD and SOC concentration (Xiaonan et al., 2008):

$$CSR_i = \rho_{si} \times SOC_i \times R,$$

where CSR_i is the CSR [g C m^{-2} yr^{-1}] of the i^{th} location, ρ_{si} is the mean SBD [g cm^{-3}] of the i^{th} location, SOC_i is the mean SOC concentration [%] of the i^{th} location and R is the sedimentation rate in the mangrove forests (the Saudi mean = 2.2 mm yr^{-1}; Almahasheer et al., 2017).

CSP [Gg C year^{-1}] was calculated as follows (Xiaonan et al., 2008):

$$CSP = CSR \times A,$$

where CSP is the CSP [Gg C yr^{-1}] of the mangrove stands and A is the area [m^2] of the mangrove stands.

2.6. Water sampling and analysis

At each stand, three polyethylene bottles (1000 ml) were used to collect water samples during low tide (<0.3 m water depth) from the water surface and were brought to the laboratory. EC (electric conductivity) and TDS (total dissolved solids) were measured immediately after collection using a conductivity meter (Hanna Instruments, HI 98130). Then, samples were filtered using nylon Whatman membrane filters (pore size 0.45 μm, diameter 47 mm). The filtrates were acidified to a pH of 2.0 using nitric acid (Analar) in order to preserve the nutrients in the samples. Molybdenum blue (Strickland and Parsons, 1972) and indo-phenol blue (Novozamsky et al., 1974) methods were applied for the determination of total P and total N, using a spectrophotometer (Perkin Elmer, Lambda 25) at 885 and 660 nm, respectively.

2.7. Statistical analysis

Before performing an analysis of variance (ANOVA), the data were tested for their normality of distribution and homogeneity of variance, and when necessary, the data were log-transformed. One-way analysis of variance (ANOVA-1) was used to identify statistically significant differences in the estimated chemical parameters of seawater, SOC pool, CSR, tree density, individual height and crown diameter of *A. marina* populations among the different studied locations. Two-way analysis of variance (ANOVA-2) was used to identify statistically significant differences in SBD, SOC concentrations and SOC density among the different studied locations and sediment depths. Significant differences between means among the studied locations were identified using Tukey's HSD test at $P < 0.05$. The relationship between SOC concentration and SBD was examined with non-linear regression and by calculating the Pearson correlation coefficient (Arshad et al., 2018; Eid et al., 2019, 2016; Eid and Shaltout, 2016). To detect the ordination of the population (tree density, individual height and crown diameter) and sediment (SBD, SOC concentration, SOC density, SOC pool, CSR and CSP) parameters along the nutrient availability and salinity gradients, Canonical Correspondence Analysis (CCA) was conducted using the population and sediment parameters along with the water properties using CANOCO 5.0 for Windows (Ter Braak and Šmilauer, 2012). Relationships between the ordination axes and the water properties were tested using Pearson's simple linear correlation (r). All statistical analyses were performed using SPSS 15.0 software (SPSS, 2006).

3. Results

For seawater samples, TDS showed a significant concentration gradient, with highest values in the north and lowest

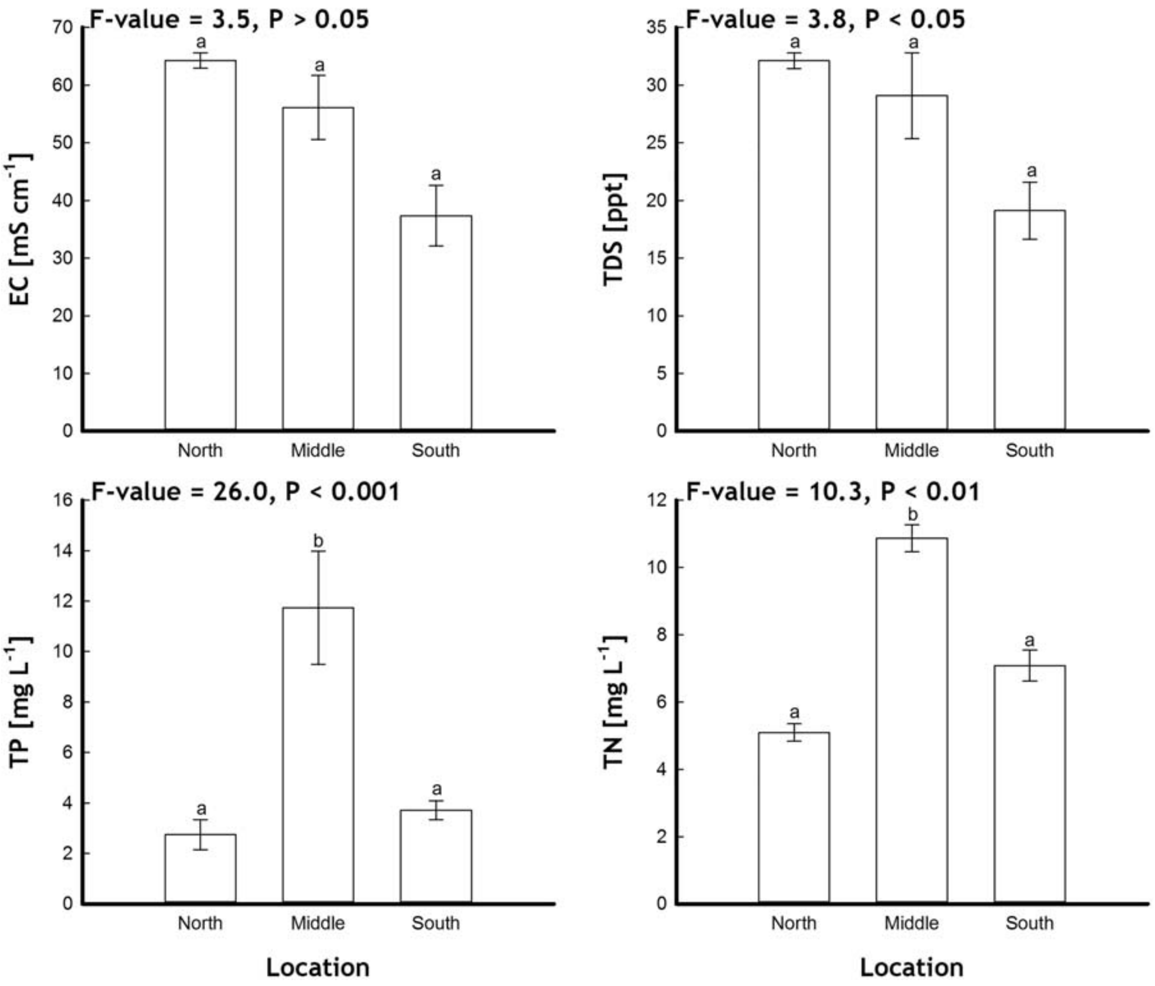

Figure 2 Variation in the water characteristics of the three locations supporting *Avicennia marina* populations along the Red Sea coast of Saudi Arabia. Vertical bars indicate the standard errors of the means. *F*-values represent the one-way ANOVA. Means followed by different letters are significantly different at $P < 0.05$ according to the Tukey's HSD test.

Table 1 Characteristics [mean ± standard error] of *Avicennia marina* populations along the Red Sea coast of Saudi Arabia.

Location	Tree density [ind. 100 m^2]	Tree height [cm ind.$^{-1}$]	Tree crown diameter [cm ind.$^{-1}$]
North	$7.7^{a} \pm 0.9$	$106.1^{b} \pm 6.2$	$100.7^{b} \pm 5.7$
Middle	$26.4^{c} \pm 2.3$	$75.6^{a} \pm 2.4$	$66.5^{a} \pm 3.4$
South	$13.6^{b} \pm 0.7$	$198.6^{c} \pm 4.4$	$226.5^{c} \pm 4.7$
F value	24.4^{***}	173.1^{***}	257.9^{***}

F-values represent the one-way ANOVA, ***: $P < 0.001$. Means in the same columns followed by different letters are significantly different at $P < 0.05$ according to Tukey's HSD test.

values in the south, while EC reflected a similar but insignificant concentration gradient. Total P and total N in seawater samples differed significantly among studied locations, where highest concentrations in the middle, and lowest concentrations in the north (Fig. 2).

The population of *A. marina* in the middle location had the highest tree density (26.4 ind. 100 m^2), but the lowest tree height (75.6 cm ind.$^{-1}$) and crown diameter (66.5 cm ind.$^{-1}$). In contrast, its population in the southern location had the highest tree height (198.6 cm ind.$^{-1}$) and crown diameter (226.5 cm ind.$^{-1}$), but a medium tree density (13.6 ind. 100 m^2) (Table 1). The correlation coefficients between the water characteristics and the first two CCA axes (Fig. 3 and Table 2) indicated that the separation of *A. marina* population parameters along the first axis was positively influenced by total N and total P, while the second axis was negatively correlated with total P.

The correlation coefficients between the water characteristics and the first two CCA axes (Fig. 4 and Table 2) indicated that the separation of the sediment parameters along the first axis were positively influenced by TDS and EC and negatively influenced by total N and total P. In contrast,

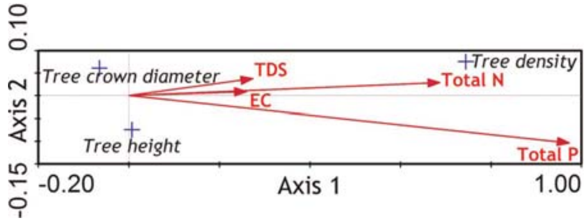

Figure 3 CCA biplot with water characteristics [→] and population parameters [+] of *Avicennia marina* growing along the Red Sea coast of Saudi Arabia.

Table 2 Inter-set correlations of water properties with CCA axes.

Water property	Axis 1	Axis 2
Sediment parameters		
EC [mS cm^{-1}]	0.53	−0.56
TDS [ppt]	0.55	−0.54
Total P [mg L^{-1}]	−0.29	−0.57
Total N [mg L^{-1}]	−0.44	−0.61
Population parameters		
EC [mS cm^{-1}]	0.24	0.01
TDS [ppt]	0.26	0.04
Total P [mg L^{-1}]	0.91	−0.10
Total N [mg L^{-1}]	0.64	0.03

EC: electric conductivity; TDS: total dissolved solids.

the second axis was negatively correlated with total N, total P, EC and TDS. The total mean of SBD, SOC concentration, SOC density, SOC pool and CSR differed significantly among the studied locations (Table 3). The distribution of SBD in the northern location showed higher mean values where it increased significantly from 1.6 g cm^{-3} at a depth of 0—5 cm up to 2.3 g cm^{-3} at a depth of 25—30 cm. On the other hand, the distribution of SBD in the middle location increased significantly from 1.3 g cm^{-3} at a depth of 0—5 cm and up to 1.6 g cm^{-3} at a depth of 10—15 cm. The distribution of mean SBD in the southern location increased significantly from 1.3 g cm^{-3} at a depth of 0—5 cm and up to 1.7 g cm^{-3} at a depth of 30—35 cm (Fig. 5).

SOC concentrations in the southern location showed higher mean values where they declined significantly from 19.7 g C kg^{-1} at a depth of 0—5 cm to 13.7 g C kg^{-1} at a depth of 40—45 cm, while SOC concentrations in the

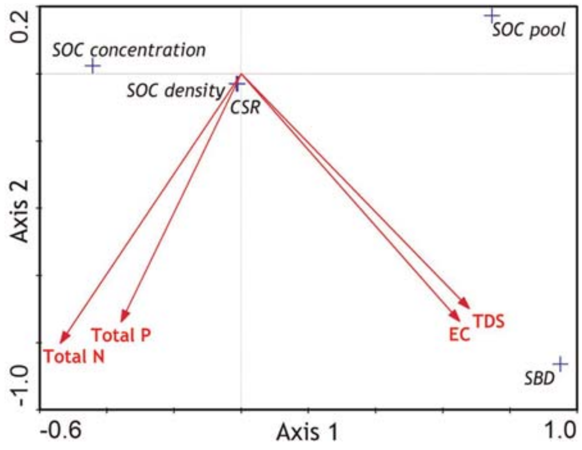

Figure 4 CCA biplot with water characteristics [→] and sediment parameters [+] supporting *Avicennia marina* populations along the Red Sea coast of Saudi Arabia.

middle location declined significantly from 16.7 g C kg^{-1} at a depth of 0—5 cm to 13.6 g C kg^{-1} at a depth of 20—25 cm. In contrast, SOC concentrations in the northern location showed lower mean values, declining significantly from 15.3 g C kg^{-1} at a depth of 0—5 cm to 12.1 g C kg^{-1} at a depth of 20—25 cm (Fig. 6). Consistent with the results, an exponential function was developed between SBD [g cm^{-3}] and SOC concentrations [g C kg^{-1}] for the sediments in Saudi Arabian Red Sea mangroves, where SOC concentrations and SBD were negatively correlated (Fig. 7).

In the northern location, SOC density significantly declined from 27.2 kg C m^{-3} at a depth of 10—15 cm to a minimum of 23.9 kg C m^{-3} at a depth of 20—25 cm then increased to 32.5 kg C m^{-3} at a depth of 30—35 cm, before finally decreasing to 25.4 kg C m^{-3} at a depth of 35—40; SOC density in the southern location significantly decreased from 27.2 kg C m^{-3} at a depth of 5—10 cm to 26.1 kg C m^{-3} at a depth of 10—15 cm, and then it increased to 29.4 kg C m^{-3} at a depth of 30—35 cm and finally decreased to 21.2 kg C m^{-3} at a depth of 45—50 cm. On the other hand, the middle location showed lower mean SOC density values where they significantly decreased from 25.8 kg C m^{-3} at a depth of 10—15 cm to 21.0 kg C m^{-3} at a depth of 20—25 cm (Fig. 8).

The northern and southern locations have similar SOC pools (10.5 and 10.4 kg C m^{-2}, respectively), while the value

Table 3 Mean ± standard error of sediment bulk density [SBD], sediment organic carbon [SOC] concentration, SOC density, SOC pool and carbon sequestration rate [CSR] in the 3 *Avicennia marina* locations along the Red Sea coast of Saudi Arabia.

Location	SBD [g cm^{-3}]	SOC concentration [g C kg^{-1}]	SOC density [kg C m^{-3}]	SOC pool [kg C m^{-2}]	CSR [g C m^{-2} yr^{-1}]
North	$1.9^{b} \pm 0.04$	$14.4^{a} \pm 0.3$	$26.9^{b} \pm 0.9$	$10.5^{b} \pm 0.5$	$5.9^{b} \pm 0.2$
Middle	$1.5^{a} \pm 0.03$	$15.9^{b} \pm 0.3$	$22.7^{a} \pm 0.5$	$6.7^{a} \pm 0.4$	$5.0^{a} \pm 0.1$
South	$1.5^{a} \pm 0.01$	$18.1^{c} \pm 0.2$	$27.1^{b} \pm 0.3$	$10.4^{b} \pm 0.3$	$6.0^{b} \pm 0.1$
F value	42.9^{***}	10.5^{***}	9.1^{***}	17.0^{***}	13.5^{***}

F-values represent the one-way ANOVA, ***: $P < 0.001$. Means in the same columns followed by different letters are significantly different at $P < 0.05$ according to Tukey's HSD test.

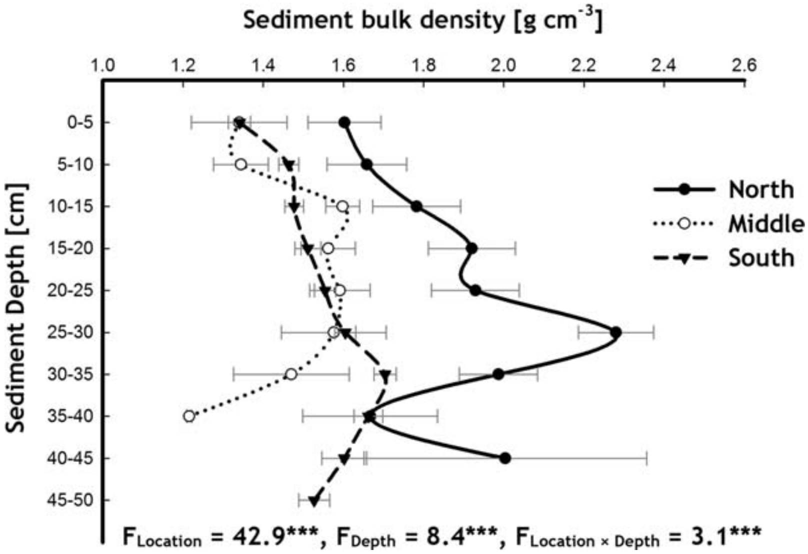

Figure 5 Distribution of sediment bulk density [g cm^{-3}] in relation to sediment depth [cm] in three locations of *Avicennia marina* populations along the Red Sea coast of Saudi Arabia. Horizontal bars indicate the standard errors of the means. *F*-values represent the two-way ANOVAs. Location: North/Middle/South; Depth: 0—5, 5—10, 10—15, 15—20, 20—25, 25—30, 30—35, 35—40, 40—45, 45—50 cm. ***: $P < 0.001$.

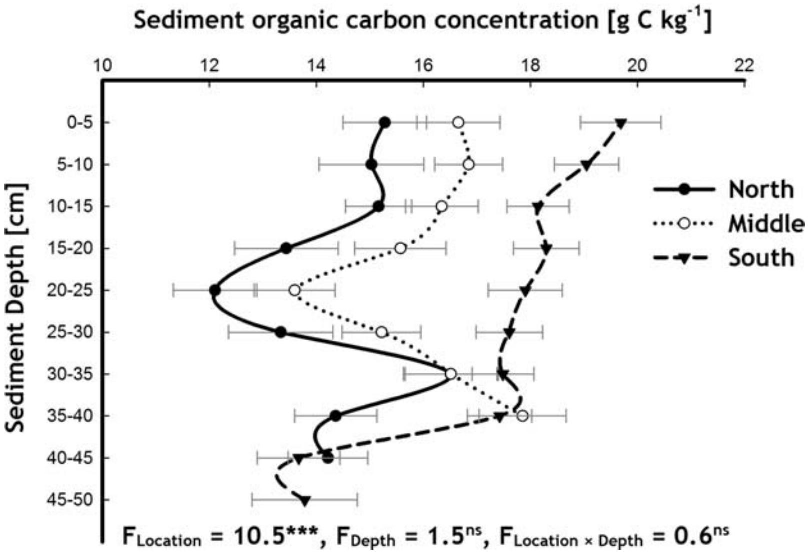

Figure 6 Distribution of sediment organic carbon concentration [g C kg^{-1}] in relation to sediment depth [cm] in three locations of *Avicennia marina* populations along the Red Sea coast of Saudi Arabia. Horizontal bars indicate the standard errors of the means. *F*-values represent the two-way ANOVAs. Location: North/Middle/South; Depth: 0—5, 5—10, 10—15, 15—20, 20—25, 25—30, 30—35, 35—40, 40—45, 45—50 cm. ***: $P < 0.001$, *ns*: not significant [i.e., $P > 0.05$].

of the middle location was 6.7 kg C m^{-2}. In addition, the average CSR of the middle location (5.0 g C m^{-2} yr^{-1}) was significantly lower than those of the northern (5.9 g C m^{-2} yr^{-1}) and southern locations (6.0 g C m^{-2} yr^{-1}) (Table 3). Based on the area of the mangrove stands (48.4 km^2) in the study area and the CSR, the total CSP of mangrove forests along the Saudi Arabian Red Sea coast was 0.27 Gg C yr^{-1}.

4. Discussion

The present results indicate that SOC concentrations were adversely affected by the increase in total P and total N. On the other hand, SBD was positively affected by higher EC and TDS. Salinity and nutrient abundance have been shown to affect the productivity of mangroves. High salinity levels can result in physiological stress to mangrove trees, forcing them

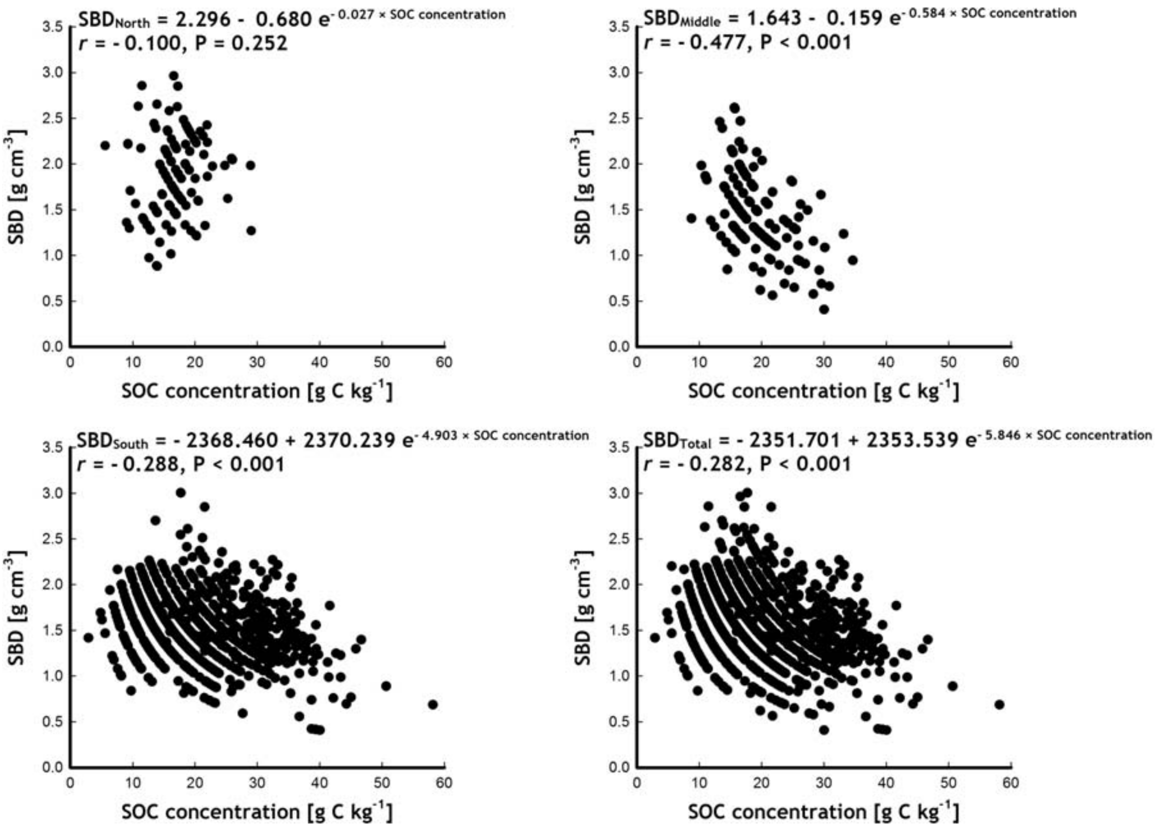

Figure 7 Non-linear correlation between sediment organic carbon [SOC] concentration [g C kg^{-1}] and sediment bulk density [SBD, g cm^{-3}] for sediment samples from three locations of *Avicennia marina* populations along the Red Sea coast of Saudi Arabia.

to shift more energy to osmotic regulation within the plant and reducing energy in plant growth (Alongi, 2014; Mizanur Rahman et al., 2015); this added stress ultimately leads to a decrease in leaf and stem production, making them less available to become incorporated into the sediments (Arshad et al., 2018). Vaiphasa et al. (2007) reported that shrimp pond effluents had dramatic effects on the survival of mangroves surrounding the ponds, where it has been reported that the disposal of nutrients (e.g., N and P) can accelerate the decomposition of mangrove SOM and thereby reduce SOC pools (Feller et al., 2003; Suárez-Abelenda et al., 2014). Moreover, Arshad et al. (2018) showed that sewage discharge lead to death of pneumatophores, which have been shown to affect mangrove productivity. The death of pneumatophores decreases the aeration area which apparently affects the respiration rate of the root system, nutrient uptake and plant growth, consequently leading to retarded growth of mangroves (Mandura, 1997). In the current study, seawater analysis reflected decreasing gradients of EC and TDS from the north to the south. The middle location was characterized by the highest concentrations of total P and total N, while the northern location had the lowest. These results are consistent with the studies of Saifullah (1997), Alongi (2011) and Triantafyllou et al. (2014).

The inverse relationship between density and the size of *A. marina* individuals in the middle location (highest density versus smallest size), as found by the present study, may be partially related to the effect of intraspecific competition (Shaltout and Ayyad, 1988). Plants with neighbours close by will grow less than plants with few or distant neighbours (Weiner, 1984). However, assessing the effect of intraspecific competition on the population dynamics of *A. marina* along the Saudi Arabian Red Sea coast, needs further field and experimental studies. In addition, the patchy distribution and stunting nature of mangroves in this location may also be due to dry land, paucity of rainfall, land use changes and high concentrations of P and N in the seawater due to the discharge of sewage and fertilizers (Almahasheer et al., 2017; Alongi, 2011; Kumar et al., 2010; Naidoo, 2009; Saifullah, 1997). On the other hand, the largest mangroves were recorded in the southern location, but they were associated with a relatively low population density; this may be partially due to a decrease in intraspecific competition that often leads to an increase in plant size. The present study showed that the density of *A. marina* was positively correlated with total N and total P. Thus, the relatively low concentrations of N and P in the seawater in the southern location may explain the relatively low density of mangroves trees at this location compared with the middle location (Sato et al., 2011).

SBD is a dynamic feature that differs with structural conditions within the sediment. SBD is the dry weight of specific sediment volume (Pravin et al., 2013); it is used as an indicator of sediment strength and/or mechanical resistance to plant growth and is used as a first step in evaluating SOC concentrations (Drewry et al., 2008). Our results showed that SBD gradually increased with depth in all the studied locations; this finding is consistent with those of Eid and Shaltout (2016) along the Egyptian Red Sea coast, and Eid et al. (2016)

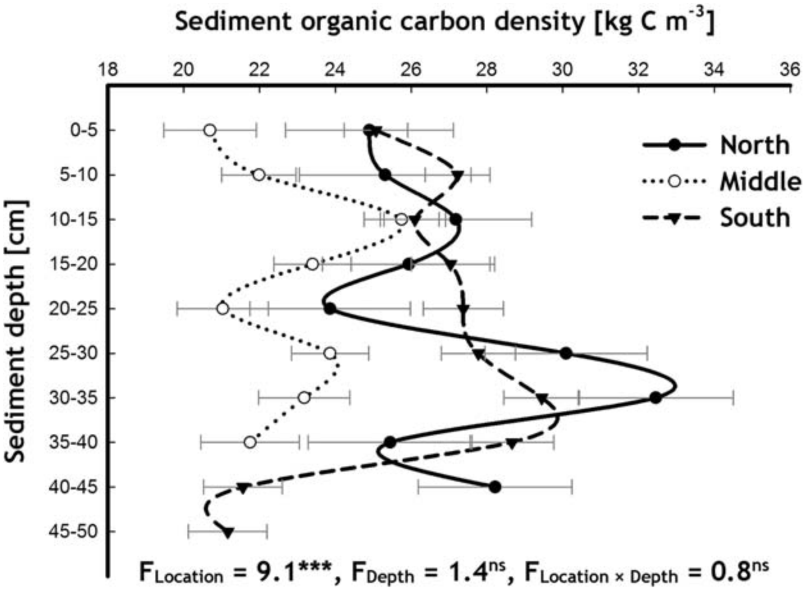

Figure 8 Distribution of sediment organic carbon density [kg C m^{-3}] in relation to sediment depth [cm] in three locations of *Avicennia marina* populations along the Red Sea coast of Saudi Arabia. Horizontal bars indicate the standard errors of the means. *F*-values represent the two-way ANOVAs. Location: North/Middle/South; Depth: 0—5, 5—10, 10—15, 15—20, 20—25, 25—30, 30—35, 35—40, 40—45, 45—50 cm. ***: $P < 0.001$, *ns*: not significant [i.e., $P > 0.05$].

and Arshad et al. (2018) along the southern Saudi Arabian Red Sea coast. This behaviour of SBD can be attributed to the accumulation of tailings and plant remains in the surface and sub-surface layers of the sediments (Sherry et al., 1998), which lead to changes in the organic matter content, porosity and compaction (Pravin et al., 2013).

SOC concentrations in mangrove forests originate from local mangrove production (litter falls and underground roots: autochthonous; Alongi, 1998), trapped seaweeds and seagrasses (Mandura et al., 1988), benthic algae (Yong et al., 2011), and the tidal flux from adjacent coastal environments (allochthonous; Allison et al., 2003), which is subsequently deposited within the mangroves (Bouillon et al., 2003; Chen et al., 2012). There were gradual decreases in SOC concentrations in all locations of the study area, from surface sediments where most carbon inputs occur to the deeper sediment layers. Eid and Shaltout (2016), Eid et al. (2016) and Arshad et al. (2018) reported a similar pattern for *A. marina* sediments in the Egyptian and Saudi Arabian Red Sea mangroves. In addition, Schile et al. (2017) reported a similar pattern for mature (*A. marina*) and planted (*A. germinans*) mangrove sediments along 600 km of coastline in the United Arab Emirates. The variation in SOC concentrations with depth may be due to the interaction of complex processes such as hydrologic/sediment regimes, decomposition, biological cycling, leaching, illuviation, soil erosion, weathering of minerals, and atmospheric deposition (Girmay and Singh, 2012; Sanderman et al., 2018).

The mean SOC concentration in our study (16.1 g C kg^{-1}) was lower than the global mean value (22.0 g C kg^{-1}; Kristensen et al., 2008), and it was lower than that of mangrove forests in many other countries (Table 4) such as Australia, Thailand, Indonesia, Palau, Mexico, Brazil, and Micronesia; however, it is higher than reported values in Egypt, China, Japan, India, and Vietnam. The global variations in mangrove SOC concentrations are driven by specific regional carbon dynamics (Twilley et al., 2018). Thus, the low SOC concentrations in the study area may be attributed to an absence of riverine sediments and organic matter along the coasts and in the seawater due to the lack of rivers (Almahasheer et al., 2017), a rocky ground and a low population density of mangroves in the north, stunted trees and pollution in the middle and the relatively high SBD in the north and south.

In the current study, we developed negative exponential functions for the studied locations, where SBD increased while SOC decreased with soil depth. Comparable results were reported by Yang et al. (2014) for mangrove coasts of the Leizhou Peninsula (southern China), by Eid et al. (2016) and Arshad et al. (2018) for mangrove sediments along the Red Sea in southern Saudi Arabia, by Schile et al. (2017) for sediments of mature and planted mangroves along the coastline in the United Arab Emirates, by Eid and Shaltout (2016) for mangrove sediments along the Egyptian Red Sea coast, and by Donato et al. (2011) for mangrove sediments in the tropics. It is also consistent with the study of Pravin et al. (2013), who reported that the increase in organic matter leads to decreased bulk density of soil.

The current study showed that SOC density significantly declined with depth, which is consistent with many previous studies such as that of Arshad et al. (2018), Almahasheer et al. (2017) and Eid et al. (2016). Additionally, the mean SOC density for mangroves sediments of the Saudi Arabian Red Sea coast, as estimated in the present study (25.6 kg C m^{-3}), was lower than those of mangrove forests in many regions, such as estuarine mangroves sediments (38.0 kg C m^{-3}), oceanic mangroves sediments (61.0 kg C m^{-3}), Rookery Bay in Florida (510.0 kg C m^{-3}) and Abu Dhabi, UAE (1200.0 kg C m^{-3}) (Almahasheer et al., 2017). In addition, the mean SOC density in the present study was higher than that of Kosrae Island mangroves (23.0 kg C m^{-3}; Almahasheer et al., 2017) and some Egyptian mangroves (21.4 kg C m^{-3}; Eid and Shaltout, 2016). The relatively low SOC density along the Saudi Arabian

Table 4 Mean of sediment organic carbon [SOC] concentration [g C kg^{-1}] and SOC pool [kg C m^{-2}] in the *Avicennia marina* locations along the Red Sea coast of Saudi Arabia compared with those reported in different mangrove forests around the globe.

Location	SOC concentration	SOC pool	Depth [cm]	Reference
Red Sea coast, Saudi Arabia	16.1	9.2	50	Present study
Central Saudi Red Sea coast	6.0	4.3	100	Almahasheer et al. (2017)
Arabian Gulf, United Arab Emirates		10.2—15.6	100	Schile et al. (2017)
Red Sea coast, Egypt	15.7	8.6	40	Eid and Shaltout (2016)
Africa Sahel, Senegal		9.0	40	Woomer et al. (2004)
Arid Western Australia	37.0	14.4	100	Alongi et al. (2000), Alongi et al. (2003)
Ao Sawi, Thailand	39.2		100	Alongi et al. (2001)
Fujian province, Southeastern China	11.3		60	Xue et al. (2009)
Leizhou Peninsula, China	9.5	8.7	100	Yang et al. (2014)
Shenzhen Bay, China	1.1—61.4	6.6	100	Lunstrum and Chen (2014)
Okinawa Island, Japan	7.7—20.1	5.7	100	Khan et al. (2007)
Sundarbans, India	6.1	2.6	30	Ray et al. (2011)
Xuan Thuy National Park, Vietnam	7.8		2	Tue et al. (2012)
Segara Anakan Lagoon, Kongsi Island and Thousand Islands, Indonesia	42.4	39.1	100	Kusumaningtyas et al. (2019)
La Paz Bay, Mexico		10.0—23.9	45	Ochoa-Gómez et al. (2019)
Karastic coastal region, Mexico	168.9	48.4	100	Adame et al. (2013)
Tamandaré, Brazil	58.4		46	Sanders et al. (2010)
Sepetiba Bay, Brazil	36.5		15	Lacerda et al. (1995)
Ceará State, Brazil		8.2	40	Nóbrega et al. (2019)
Sao Paulo, Brazil	210.6		80	Ferreira et al. (2010)
Ruunuw mangrove forest, Micronesia	104.3	12.1	100	Kauffman et al. (2011)
Airai mangrove forest, Palau	182.6	56.7	100	Kauffman et al. (2011)

Red Sea coast may be due to certain habitat characteristics and geomorphological settings that are not favourable for organic carbon sequestration (Almahasheer et al., 2017).

The current results indicate that the SOC pool in the middle location (6.7 kg C m^{-2}) was lower than that in the northern (10.5 kg C m^{-2}) and southern (10.4 kg C m^{-2}) location, proving that anthropogenic factors resulting from the industrial and urban expansion in the middle location in recent years, played a significant role in the SOC pool value (Almahasheer et al., 2017; Arshad et al., 2018). Moreover, the mean SOC pool in southern locations (10.4 kg C m^{-2}) in the present study was found to be below that mean reported (29.2 kg C m^{-2}) by Eid et al. (2019) in three homogenous sites near Jazan. This is clearly related to different sampling depths as they sampled sediments to 100 cm depth, while in the current study, the sediments were sampled to a 50 cm depth from five heterogeneous sites (Amaq, Al-Birk, Al-Shuqaiq, Sabya and Jazan). The low SOC pool capacity of Red Sea mangroves, especially in the middle part of the coast, may also be attributed to severe environmental conditions, leading to limited mangrove growth with dwarfed trees and a low biomass (Almahasheer et al., 2016b,c).

In the present study, the sediment profile in the mangrove forests along the Saudi Arabian Red Sea coast (0—50 cm) had a mean SOC pool of 9.2 kg C m^{-2}, which was lower than that of Indonesian, Palauan, Mexican, Australian and Micronesian mangrove sediments (Table 4) at a depth of 100 cm. On the other hand, it was higher than Egyptian mangrove sediments at a depth of 40 cm depth. This hemispheric variation in SOC pools is due to local and regional geomorphic and geophysical drivers (Rovai et al., 2018; Twilley et al., 2018), vegetation type or density, forest age, anthropogenic impacts, tidal range, biotic influences, hydrology and climate (Nóbrega et al., 2019; Taillardat et al., 2018). Donato et al. (2011) added that the mangrove organic sediments can exceed a depth of 3 m in some places; thus, the SOC pool in the current study may underestimate the carbon sequestration capacity because we only sampled sediments to a depth of 50 cm.

The accumulation of organic carbon in soils is the result of a balance between the input of autochthonous material through primary production or the deposition of allochthonous material versus the output due to decomposition/mineralization, erosion, and leaching (see Nóbrega et al., 2019). In our study, the mean CSR of mangrove forests along the Saudi Arabian Red Sea coast is 5.6 g C m^{-2} yr^{-1}. This value is consistent with the value of Arshad et al. (2018), who reported an average CSR of 4.7 g C m^{-2} yr^{-1} in southern Saudi Red Sea mangrove sediments, and it is close to the value of Almahasheer et al. (2017), who reported an average CSR of 3.5 g C m^{-2} yr^{-1} in central Red Sea mangrove sediments. On the other hand, the average CSR of the current study (5.6 g C m^{-2} yr^{-1}) is 29.0-fold lower than the average value of 163.0 g C m^{-2} yr^{-1} of the mangroves at the global scale (Breithaupt et al., 2012). The relatively low CSR in Saudi Red Sea mangroves is most likely due to the oligotrophic nature of the Red Sea, the lack of rivers, the extremely arid conditions affecting mangrove growth (Almahasheer et al., 2017), the lower primary productivity in Red Sea mangrove forests (Arshad et al., 2018), and the heavy metal pollution that may negatively influence primary production (Arshad et al., 2018; Bouillon et al., 2008).

Despite the importance of mangrove forests and their effective role in carbon sequestration and mitigating climate change (Sanderman et al., 2018), mangrove forests are one of the most threatened and rapidly degraded natural environments in the world (Sanderman et al., 2018; Siikamäki et al., 2012). Although Almahasheer et al. (2016a) stated that the area of mangrove forests along the Red Sea coasts have increased by 12% over the past forty years due to the efforts of local authorities, mangrove trees in the Red Sea still face many threats such as the establishment of resorts, oil industry development, overcutting, overgrazing (Hussain and Khojat, 1993), oil and sewage pollution (Shaltout et al., 2018), and the conversion of mangrove forests into shrimp farms (Eid et al., 2019). Therefore, in 2017, a decree was issued by the Council of Ministers of Saudi Arabia to form the Standing Committee for the Protection of the Environment of Coastal Areas. One of the tasks of this committee is to protect mangrove environments. Based on the area of mangrove stands along the Saudi Arabian Red Sea coast (48.4 km^2) and CSR, the total CSP of mangrove forests distributed along the Saudi Arabian Red Sea coast is 0.27 Gg C yr^{-1}. The relatively low CSP of Saudi Arabian Red Sea mangroves may be due to harsh environmental conditions such as low rainfall and high temperatures. Moreover, the sediments are composed mainly of biogenic coarse carbonates making the contribution of Saudi Arabian Red Sea mangroves to the carbon sequestration process limited (Almahasheer et al., 2017). It is, therefore, necessary to protect Saudi Arabian Red Sea mangrove ecosystems to improve their carbon sequestration potential and to benefit the other ecosystem services that they offer.

5. Limitations and uncertainties

To explore the effect of nutrient availability and salinity gradients on mangrove forests, the present study was conducted at 3 locations (northern, middle and southern), 7 sites and in 21 stands of mangrove forests (*A. marina*) along ~1134 km of the arid climate of the Saudi Arabian Red Sea coast. Although EC, TDS, total P and total N were determined in 3 seawater samples, which were collected from each stand to represent the nutrient availability and salinity gradients, factors other than EC, TDS, total P and total N might have also contributed to the differences in sediment (SBD, SOC concentration, SOC density, SOC pool and CSR) parameters among the locations. These factors include the geomorphologic settings, tidal input, human interference, seasonal variations (which play a role in changing the carbon dynamics in arid mangroves; Ray and Weigt, 2018) and finally methodological assumptions that were made in the manuscript: the relation between organic matter and organic carbon (SOM vs. SOC) and a constant sedimentation rate in the investigated sites. Thus, future research should examine the effects of each of the abovementioned factors on carbon dynamics of mangroves in greater detail.

Acknowledgements

The authors extend their appreciation to the Deanship of Scientific Research at King Khalid University for funding this work through General Research Project under grant number G.R.P. 117—39. We thank Dr. M.A. Al-Faidi and Dr. N.A. Al-Harbi (Biology Department, College of Science, Tabuk University); and Dr. M.A. Taher (Biology Department, College of Science, King Khalid University), for their valuable help during the field work.

Appendix A. Supplementary data

Supplementary material related to this article can be found, in the online version, at doi:10.1016/j.oceano.2019.08.002.

References

Adame, M.F., Kauffman, J.B., Boone, J., Medina, I., Gamboa, J.N., Torres, O., Caamal, J.P., Reza, M., Herrera-Silveira, J.A., 2013. Carbon stocks of tropical coastal wetlands within the karstic landscape of the Mexican Caribbean. PLoS One 8 (2), e56569.

Allison, M.A., Khan, S.R., Goodbred Jr., S.L., Kuehl, S.A., 2003. Stratigraphic evolution of the late Holocene Ganges-Brahmaputra lower delta plain. Sediment Geol. 155 (3—4), 317—342.

Almahasheer, H., 2018. Spatial coverage of mangrove communities in the Arabian Gulf. Environ. Monit. Assess. 190 (2), art. no. 85, 10 pp., http://dx.doi.org/10.1007/s10661-018-6472-2.

Almahasheer, H., Aljowair, A., Duarte, C.M., Irigoien, X., 2016a. Decadal stability of Red Sea mangroves. Estuar. Coast. Shelf Sci. 169, 164—172, http://dx.doi.org/10.1016/j.ecss.2015.11.027.

Almahasheer, H., Duarte, C., Irigoien, X., 2016b. Nutrient limitation in central Red Sea mangroves. Front. Mar. Sci. 3 , art. no. 271, 14 pp., http://dx.doi.org/10.3389/fmars.2016.00271.

Almahasheer, H., Duarte, C., Irigoien, X., 2016c. Phenology and growth dynamics of *Avicennia marina* in the central Red Sea. Sci. Rep. 6 (1), art. no. 37785, 9 pp., http://dx.doi.org/10.1038/srep37785.

Almahasheer, H., Serrano, O., Duarte, C., Arias-Ortiz, A., Masque, P., Irigoien, X., 2017. Low carbon sink capacity of Red Sea mangroves. Sci. Rep. 7 (1), art. no. 9700, 10 pp., http://dx.doi.org/10.1038/s41598-017-10424-9.

Alongi, D., Tirendi, F., Clough, B., 2000. Below-ground decomposition of organic matter in forests of the mangroves *Rhizophora stylosa* and *Avicennia marina* along the arid coast of Western Australia. Aquat. Bot. 68 (2), 97—122, http://dx.doi.org/10.1016/S0304-3770(00)00110-8.

Alongi, D., Wattayakorn, G., Pfitzner, J., Tirendi, F., Zagorskis, I., Brunskill, G., Davidson, A., Clough, B., 2001. Organic carbon accumulation and metabolic pathways in sediments of mangrove forests in southern Thailand. Mar. Geol. 179 (1—2), 85—103, http://dx.doi.org/10.1016/S0025-3227(01)00195-5.

Alongi, D.M., Clough, B.F., Dixon, P., Tirendi, F., 2003. Nutrient partitioning and storage in arid-zone forests of the mangroves *Rhizophora stylosa and Avicennia marina*. Trees 17 (1), 51-60, http://dx.doi.org/10.1007/s00468-002-0206-2.

Alongi, D.M., 1998. Coastal Ecosystem Processes. CRC Press, Florida, 448 pp.

Alongi, D.M., 2011. Early growth responses of mangroves to different rates of nitrogen and phosphorus supply. J. Exp. Mar. Biol. Ecol. 397 (2), 85—93, http://dx.doi.org/10.1016/j.jembe.2010.11.021.

Alongi, D.M., 2012. Carbon sequestration in mangrove forests. Carbon Manage. 3 (3), 313—322, http://dx.doi.org/10.4155/cmt.12.20.

Alongi, D.M., 2014. Carbon cycling and storage in mangrove forests. Annu. Rev. Mar. Sci. 6 (1), 195—219, http://dx.doi.org/10.1146/annurev-marine-010213-135020.

Arshad, M., Alrumman, S., Eid, E.M., 2018. Evaluation of carbon sequestration in the sediment of polluted and non-polluted locations of mangroves. Fund. Appl. Limnol. 192 (1), 53—64, http://dx.doi.org/10.1127/fal/2018/1127.

Bouillon, S., Borges, A., Casteneda-Moya, E., Diele, K., Dittmar, T., 2008. Mangrove production and carbon sinks: a revision of global budget estimates. Global Biogeochem. Cy. 22 (2), art. no. GB2013, 12 pp., http://dx.doi.org/10.1029/2007GB003052.

Bouillon, S., Dahdouh-Guebas, F., Rao, A.V.V.S., Koedam, N., Dehairs, F., 2003. Sources of organic carbon in mangrove sediments: variability and possible ecological implications. Hydrobiologia 495 (1—3), 33—39, http://dx.doi.org/10.1023/A:1025411506526.

Breithaupt, J., Smoak, J., Smith, T., Sanders, C., Hoare, A., 2012. Organic carbon burial rates in mangrove sediments: strengthening the global budget. Global Biogeochem. Cy. 26 (3), art. no. GB3001, 11 pp., http://dx.doi.org/10.1029/2012GB004375.

Bunting, P., Rosenqvist, A., Lucas, R.M., Rebelo, L.-M., Hilarides, L., Thomas, N., Hardy, A., Itoh, T., Shimada, M., Finlayson, C.M., 2018. The global mangrove watch — a new 2010 global baseline of mangrove extent. Remote Sens. 10 (1), art. no. 1669, http://dx.doi.org/10.3390/rs10101669.

Chen, L., Zeng, X., Tam, N.F.Y., Lu, W., Luo, Z., Du, X., Wang, J., 2012. Comparing carbon sequestration and stand structure of monoculture and mixed mangrove plantations of *Sonneratia caseolaris* and *S. apetala* in Southern China. Forest Ecol. Manage. 284, 222—229, http://dx.doi.org/10.1016/j.foreco.2012.06.058.

Donato, D., Kauffman, J., Murdiyarso, D., Kurnianto, S., Stidham, M., Kanninen, M., 2011. Mangroves among the most carbon-rich forests in the tropics. Nat. Geosci. 4 (5), 293—297, http://dx.doi.org/10.1038/ngeo1123.

Drewry, J.J., Cameron, K.C., Buchan, G.D., 2008. Pasture yield and soil physical property responses to soil compaction from treading and grazing — a review. Aust. J. Soil Res. 46 (3), 237—256, http://dx.doi.org/10.1071/SR07125.

Edwards, A.J., Head, S.M., 1987. Key Environment: Red Sea. Pergamon Press, Headington Hill Hall, Oxford, 451 pp., http://dx.doi.org/10.1016/C2009-0-07683-1.

Edwards, F.J., 1987. Climate and oceanography. In: Edwards, A.J., Head, S.M. (Eds.), Key Environment: Red Sea. Pergamon Press, New York, 45—69.

Eid, E.M., Arshad, M., Shaltout, K.H., El-Sheikh, M.A., Alfarhan, A.H., Picó, Y., Barcelo, D., 2019. Effect of the conversion of mangroves into shrimp farms on carbon stock in the sediment along the southern Red Sea coast, Saudi Arabia. Environ. Res. 176, art. no. 108536, 7 pp., http://dx.doi.org/10.1016/j.envres.2019.108536.

Eid, E.M., El-Bebany, A.F., Alrumman, S.A., 2016. Distribution of soil organic carbon in the mangrove forests along the southern Saudi Arabian Red Sea coast. Rend. Fis. Acc. Lincei. 27 (4), 629—637, http://dx.doi.org/10.1007/s12210-016-0542-6.

Eid, E.M., Shaltout, K.H., 2016. Distribution of soil organic carbon in the mangrove *Avicennia marina* (Forssk.) Vierh. along the Egyptian Red Sea coast. Reg. Stud. Mar. Sci. 3, 76—82, http://dx.doi.org/10.1016/j.rsma.2015.05.006.

El-Juhany, L.I., 2009. Present status and degradation trends of mangrove forests on the southern Red Sea coast of Saudi Arabia. Am. Euras. J. Agric. Environ. Sci. 6 (3), 328—340.

Feller, I.C., McKee, K.L., Whigham, D.F., O'Neill, J.P., 2003. Nitrogen vs. phosphorus limitation across an ecotonal gradient in a mangrove forest. Biogeochemistry 62 (2), 145—175, http://dx.doi.org/10.1023/A:1021166010892.

Ferreira, T.O., Otero, X.L., de Souza Junior, V.S., Vidal-Torrado, P., Macías, F., Firme, L.P., 2010. Spatial patterns of soil attributes and components in a mangrove system in Southeast Brazil (São Paulo). J. Soils Sediments 10 (6), 995—1006, http://dx.doi.org/10.1007/s11368-010-0224-4.

Girmay, G., Singh, B.R., 2012. Changes in soil organic carbon stocks and soil quality: land-use system effects in northern Ethiopia. Acta Agric. Scand., Sect. B - Soil Plant Sci. 62 (6), 519—530, http://dx.doi.org/10.1080/09064710.2012.663786.

Han, F., Hu, W., Zheng, J., Du, F., Zhang, X., 2010. Estimating soil organic carbon storage and distribution in a catchment of Loess Plateau, China. Geoderma 154 (3—4), 261—266, http://dx.doi.org/10.1016/j.geoderma.2009.10.011.

Hussain, M., Khojat, T., 1993. Intertidal and subtidal blue-green algal mats of open and mangrove areas in the Farasan Archipelago (Saudi Arabia), Red Sea. Bot. Mar. 36 (5), 377—388, http://dx.doi.org/10.1515/botm.1993.36.5.377.

Jones, J.B., 2001. Laboratory Guide for Conducting Soil Tests and Plant Analysis. CRC Press, Florida, 384 pp.

Kauffman, J.B., Heider, C., Cole, T.G., Dwire, K.A., Donato, D.C., 2011. Ecosystem carbon stocks of Micronesian mangrove forests. Wetlands 31 (2), 343—352, http://dx.doi.org/10.1007/s13157-011-0148-9.

Khan, M., Suwa, R., Hagihara, A., 2007. Carbon and nitrogen pools in a mangrove stand of *Kandelia obovata* (S., L.) Yong: vertical distribution in the soil-vegetation system. Wetlands Ecol. Manage. 15 (2), 141—153, http://dx.doi.org/10.1007/s11273-006-9020-8.

Kristensen, E., Bouillon, S., Dittmar, T., Marchand, C., 2008. Organic carbon dynamics in mangrove ecosystems: a review. Aquat. Bot. 89 (2), 201—219, http://dx.doi.org/10.1016/j.aquabot.2007.12.005.

Kumar, A., Asif Khan, M., Muqtadir, A., 2010. Distribution of mangroves along the Red Sea Coast of the Arabian Peninsula: Part-I: the Northern Coast of Western Saudi Arabia. Earth Sci. India 3 (3), 28—42.

Kusumaningtyas, M.A., Hutahaean, A.A., Fischer, H.W., Pérez-Mayo, M., Ransby, D., Jennerjahn, T.C., 2019. Variability in the organic carbon stocks, sources, and accumulation rates of Indonesian mangrove ecosystems. Estuar. Coast. Shelf Sci. 218, 310—323, http://dx.doi.org/10.1016/j.ecss.2018.12.007.

Lacerda, L., Ittekkot, V., Patchineelam, S., 1995. Biogeochemistry of mangrove soil organic matter: a comparison between *Rhizophora* and *Avicennia* soils in south-eastern Brazil. Estuar. Coast. Shelf Sci. 40 (6), 713—720, http://dx.doi.org/10.1006/ecss.1995.0048.

Lovelock, C., Feller, I., McKee, K., Engelbrecht, B., Ball, M., 2004. The effect of nutrient enrichment on growth, photosynthesis and hydraulic conductance of dwarf mangroves in Panama. Funct. Ecol. 18 (1), 25—33, http://dx.doi.org/10.1046/j.0269-8463.2004.00805.x.

Lunstrum, A., Chen, L., 2014. Soil carbon stocks and accumulation in young mangrove forests. Soil Biol. Biochem. 75, 223—232, http://dx.doi.org/10.1016/j.soilbio.2014.04.008.

Mandura, A.S., 1997. A mangrove stand under sewage pollution stress: Red Sea. Mangroves Salt Marshes 1 (4), 255—262, http://dx.doi.org/10.1023/A:1009927605517.

Mandura, A.S., Khafaji, A.K., Saifullah, S.M., 1988. Ecology of a mangrove stand of a central Red Sea coast area: Ras Hatiba (Saudi Arabia). Proc. Saudi Biol. Soc. 11, 85—112.

Mandura, A.S., Khafaji, A.K., Saifullah, S.M., 1987. Mangrove ecosystem of southern Red Sea coast of Saudi Arabia. Proc. Saudi Biol. Soc. 10, 165—193.

Meersmans, J., De Ridder, F., Canters, F., De Baets, S., Van Molle, M., 2008. A multiple regression approach to assess the spatial distribution of soil organic carbon (SOC) at the regional scale (Flanders Belgium). Geoderma 143 (1—2), 1—13, http://dx.doi.org/10.1016/j.geoderma.2007.08.025.

Mizanur Rahman, M., Nabiul Islam Khan, M., Fazlul Hoque, A.K., Ahmed, I., 2015. Carbon stock in the Sundarbans mangrove forest: spatial variations in vegetation types and salinity zones. Wetlands Ecol. Manag. 23 (2), 269—283, http://dx.doi.org/10.1007/s11273-014-9379-x.

Morley, N.J.F., 1975. The coastal waters of the Red Sea. Bull. Mar. Res. Cen. 5, 8—19.

Naidoo, G., 2009. Differential effects of nitrogen and phosphorus enrichment on growth of dwarf *Avicennia marina* mangroves. Aquat. Bot. 90 (2), 184—190, http://dx.doi.org/10.1016/j.aquabot.2008.10.001.

Nóbrega, G.N., Ferreira, T.O., Artur, A.G., Mendonça, E.S., Leão, R. A., Teixeira, A.S., Otero, X.L., 2015. Evaluation of methods for quantifying organic carbon in mangrove soils from semi-arid region. J. Soil. Sediment. 15 (2), 282—291, http://dx.doi.org/10.1007/s11368-014-1019-9.

Nóbrega, G.N., Ferreira, T.O., Neto, M.S., Mendonça, E.S., Romero, R.E., Otero, X.L., 2019. The importance of blue carbon soil stocks in tropical semiarid mangroves: a case study in Northeastern Brazil. Environ. Earth Sci. 78 (12), art. no. 369, 10 pp., http://dx.doi.org/10.1007/s12665-019-8368-z.

Novozamsky, I., van Eck, R., van Schouwenburg, J., Walinga, I., 1974. Total nitrogen determination in plant material by means of the indophenol blue method. Neth. J. Agric. Sci. 22, 3—13.

Ochoa-Gómez, J.G., Lluch-Cota, S.E., Rivera-Monroy, V.H., Lluch-Cota, D.B., Troyo-Diéguez, E., Oechel, W., Serviere-Zaragoza, E., 2019. Mangrove wetland productivity and carbon stocks in an arid zone of the Gulf of California (La Paz Bay, Mexico). Forest Ecol. Manage. 442, 135—147, http://dx.doi.org/10.1016/j.foreco.2019.03.059.

Page, M.L., 2019. Carbon dioxide levels will soar past the 410 ppm milestone in 2019. NewScientist 3214.

Pravin, R., Dodha, V., Vidya, D., Manab, C., Saroj, M., 2013. Soil bulk density as related to soil texture, organic matter content and available total nutrients of Coimbatore soil. IJSRP 3 (2), 1—8.

Pribyl, D.W., 2010. A critical review of the conventional SOC to SOM conversion factor. Geoderma 156 (3—4), 75—83, http://dx.doi.org/10.1016/j.geoderma.2010.02.003.

Price, A., Jobbins, G., Dawson Shepherd, A., Ormond, R., 1998. An integrated environmental assessment of the Red Sea coast of Saudi Arabia. Environ. Conserv. 25 (1), 65—76, http://dx.doi.org/10.1017/S0376892998000101.

Price, A.R., Medley, P.A., McDowall, R.J., Dawson-Shepherd, A.R., Hogarth, P.J., Ormond, R.F., 1987. Aspects of mangal ecology along the Red Sea coast of Saudi Arabia. J. Nat. Hist. 21 (2), 449—464, http://dx.doi.org/10.1080/00222938700771121.

Ray, R., Ganguly, D., Chowdhury, C., Dey, M., Das, S., Dutta, M., Mandal, S., Majumder, N., De, T., Mukhopadhyay, S., Jana, T., 2011. Carbon sequestration and annual increase of carbon stock in a mangrove forest. Atmos. Environ. 45 (28), 5016—5024, http://dx.doi.org/10.1016/j.atmosenv.2011.04.074.

Ray, R., Weigt, M., 2018. Seasonal and habitat-wise variations of creek water particulate and dissolved organic carbon in arid mangrove (the Persian Gulf). Cont. Shelf Res. 165, 60—70, http://dx.doi.org/10.1016/j.csr.2018.06.009.

Rovai, A., et al., 2018. Global controls on carbon storage in mangrove soils. Nat. Clim. Change 8 (6), 534—538, http://dx.doi.org/10.1038/s41558-018-0162-5.

Rumpel, C., Amiraslani, F., Koutika, L.-S., Smith, P., Whitehead, D., Wollenberg, E., 2018. Put more carbon in soils to meet Paris climate pledges. Nature 564 (7734), 32—34, http://dx.doi.org/10.1038/d41586-018-07587-4.

Saifullah, S.M., 1994. Mangrove ecosystem of Saudi Arabian Red Sea coast — an overview. J. KAU: Mar. Sci. 7, 263—270.

Saifullah, S.M., 1997. Mangrove ecosystem of Red Sea coast (Saudi Arabian). Pak. J. Mar. Sci. 6 (1—2), 115—124.

Sanderman, J., Hengl, T., Fiske, G., Solvik, K., Adame, M., Benson, L., Bukoski, J., Carnell, P., Cifuentes-Jara, M., Donato, D., Duncan, C., Eid, E., zu Ermgassen, P., Ewers Lewis, C., Macreadie, P., Glass, L., Gress, S., Jardine, S., Jones, T., Nsombo, E., Rahman, M., Sanders, C., Spalding, M., Landis, E., 2018. A global map of mangrove forest soil carbon at 30 m spatial resolution. Environ. Res. Lett. 13 (5), art. no. 055002, 12 pp., http://dx.doi.org/10.1088/1748-9326/aabe1c.

Sanders, C.J., Smoak, J.M., Naidu, A.S., Sanders, L.M., Patchineelam, S.R., 2010. Organic carbon burial in a mangrove forest, margin and intertidal mud flat. Estuar. Coast. Shelf Sci. 90 (3), 168—172, http://dx.doi.org/10.1016/j.ecss.2010.08.013.

Sato, G., Negassi, S., Tahiri, A., 2011. The only elements required by plants that are deficient in sea water are nitrogen, phosphorous and iron. Cytotechnology 63 (2), 201—204, http://dx.doi.org/10.1007/s10616-011-9342-0.

Schile, L.M., Kauffman, J.B., Crooks, S., Fourqurean, J.W., Glavan, J., Megonigal, J.P., 2017. Limits on carbon sequestration in arid blue carbon ecosystems. Ecol. Appl. 27 (3), 859—874, http://dx.doi.org/10.1002/eap.1489.

Shaltout, K.H., 2016. Economic and Environmental Values of Mangroves in Arabic Region. In: Proc. The First Saudi Conference on Environment: Sustainable Management of Natural Resources, King Khalid University & Center of Prince Sultan Ben Abd El-Aziz for Environmental and Touristic Research and Studies. Abha, Saudi Arabia, 7—9 March 2016.

Shaltout, K.H., Ayyad, M., 1988. Structure and standing crop of Egyptian *Thymelaea hirsuta* populations. Vegetatio 74 (2—3), 137—142, http://dx.doi.org/10.1007/BF00044738.

Shaltout, K.H., El-Bana, M.I., Eid, E.M., 2018. Ecology of the Mangrove Forests along the Egyptian Red Sea Coast. LAP Lambert Acad. Publ., Saarbrücken, 168 pp.

Sherry, S., Ramon, A., Eric, M., Richard, E., Barry, W., Peter, D., Susan, T., 1998. Precambrian shield wetlands: hydrologic control of the sources and export of dissolved organic matter. Clim. Change 40 (2), 167—188, http://dx.doi.org/10.1023/A:1005496331593.

Siikamäki, J., Sanchirico, J., Jardine, S., 2012. Global economic potential for reducing carbon dioxide emissions from mangrove loss. PANAS 109 (36), 14369—14374, http://dx.doi.org/10.1073/pnas.1200519109.

Siraj, A., 1984. Climate of Saudi Arabia. Fauna of Saudi Arabia 6, 32—52.

SPSS, 2006. SPSS Base 15.0 User's Guide. SPSS Inc., Chicago.

Strickland, J.D., Parsons, T.R., 1972. Determination of reactive phosphorus. In: A Practical Handbook of Seawater Analysis. Bull. Fisheries Res. Board Canada, no. 167, 49—56.

Suárez-Abelenda, M., Ferreira, T.O., Camps-Arbestain, M., Rivera-Monroy, V.H., Macías, F., Nóbrega, G.N., Otero, X.L., 2014. The effect of nutrient-rich effluents from shrimp farming on mangrove soil carbon storage and geochemistry under semi-arid climate conditions in northern Brazil. Geoderma 213, 551—559, http://dx.doi.org/10.1016/j.geoderma.2013.08.007.

Taillardat, P., Friess, D.A., Lupascu, M., 2018. Mangrove blue carbon strategies for climate change mitigation are most effective at the national scale. Biol. Lett. 14 (10), art. no. 20180251, 6 pp., http://dx.doi.org/10.1098/rsbl.2018.0251.

Tan, K.H., 2005. Soil Sampling, Preparation, and Analysis. Taylor & Francis Group, CRC Press, Florida, 672 pp., http://dx.doi.org/10.1201/9781482274769.

Ter Braak, C.J.F., Šmilauer, P., 2012. Canoco Reference Manual and User's Guide: Software for Ordination (Version 5.0). Microcomputer Power, Ithaca.

Triantafyllou, G., Yao, F., Petihakis, G., Tsiaras, K., Raitsos, D., Hoteit, I., 2014. Exploring the Red Sea seasonal ecosystem functioning using a three-dimensional biophysical model. J. Geophys. Res. Oceans 119 (3), 1791—1811, http://dx.doi.org/10.1002/2013JC009641.

Tue, N., Ngoc, N., Quy, T., Hamaoka, H., Nhuan, M., Omori, K., 2012. A cross-system analysis of sedimentary organic carbon in the mangrove ecosystems of Xuan Thuy National Park Vietnam. J. Sea Res. 67 (1), 69—76, http://dx.doi.org/10.1016/j.seares.2011.10.006.

Twilley, R.R., Rovai, A.S., Riul, P., 2018. Coastal morphology explains global blue carbon distributions. Front. Ecol. Environ. 16 (9), 1—6, http://dx.doi.org/10.1002/fee.1937.

Vaiphasa, C., de Boer, W.F., Skidmore, A.K., Panitchart, S., Vaiphasa, T., Bamrongrugsa, N., Santitamnont, P., 2007. Impact of solid shrimp pond waste materials on mangrove growth and mortality: a case study from Pak Phanang, Thailand. Hydrobiologia 591 (1), 47—57, http://dx.doi.org/10.1007/s10750-007-0783-6.

Weiner, J., 1984. Neighbourhood interference amongst *Pinus rigida* individuals. J. Ecol. 72 (1), 183—195, http://dx.doi.org/10.2307/2260012.

Wilke, B.M., 2005. Determination of chemical and physical soil properties. In: Margesin, R., Schinner, F. (Eds.), Manual for Soil Analysis-Monitoring and Assessing Soil Bioremediation. Springer, Heidelberg, 47—95.

Woomer, P.L., Tieszen, L.L., Tappan, G., Touré, A., Sall, M., 2004. Land use change and terrestrial carbon stocks in Senegal. J. Arid Environ. 59 (3), 625—642, http://dx.doi.org/10.1016/j.jaridenv.2004.03.025.

Xiaonan, D., Xiaoke, W., Lu, F., Zhiyun, O., 2008. Primary evaluation of carbon sequestration potential of wetlands in China. Acta. Ecol. Sinica 28 (2), 463—469, http://dx.doi.org/10.1016/S1872-2032(08)60025-6.

Xue, B., Yan, C., Lu, H., Bai, Y., 2009. Mangrove-derived organic carbon in sediment from Zhangjiang Estuary (China) mangrove wetland. J. Coast. Res. 25 (4), 949—956, http://dx.doi.org/10.2112/08-1047.1.

Yang, J., Gao, J., Liu, B., Zhang, W., 2014. Sediment deposits and organic carbon sequestration along mangrove coasts of the Leizhou Peninsula, southern China. Estuar. Coast. Shelf Sci. 136, 3—10, http://dx.doi.org/10.1016/j.ecss.2013.11.020.

Yong, Y., Baipeng, P., Guangcheng, C., Yan, C., 2011. Processes of organic carbon in mangrove ecosystems. Acta Ecol. Sinica 31 (3), 169—173, http://dx.doi.org/10.1016/j.chnaes.2011.03.008.

Oceanologia (2020) 62, 70—82

Available online at www.sciencedirect.com

ScienceDirect

journal homepage: www.journals.elsevier.com/oceanologia/

ORIGINAL RESEARCH ARTICLE

Dependence of acoustic noise emission on the dissipated energy of plunging waves

Zygmunt Klusek [a],*, Maciej Paprota [b], Wojciech Sulisz [b], Aneta Zdolska [b], Sebastian Sorek [b]

[a] *Institute of Oceanology, Polish Academy of Sciences, Sopot, Poland*
[b] *Institute of Hydro-Engineering, Polish Academy of Sciences, Gdańsk, Poland*

Received 13 December 2018; accepted 21 August 2019
Available online 6 September 2019

KEYWORDS
Wave breaking;
Wave energy dissipation;
Underwater noise

Summary The results of experiments performed in a wave flume designed to explore associations between the dissipation of surface wave energy during breaking and acoustic noise emission are presented. The experiments were carried out using tap water in the wave laboratory of the Institute of Hydro-Engineering of the Polish Academy of Sciences, Gdańsk, Poland. In particular, being shown are the parameters of empirical dependency between the dissipated wave energy during plunging and the energy of pre-breaking wave trains. Relationships between wave energy losses in the case of breakers with an amplitude of about 10 cm and the noise acoustic energy in the frequency band from 80 to 12,500 Hz were estimated. Taking into consideration the phenomena of reverberations and propagation in an acoustical waveguide, a numerical model was used for the correction of the observed noise's acoustic spectra. A detailed analysis of the factors affecting the noise level in the semi-enclosed volume allowed us to specify the rate of conversion of the wave energy dissipated during breaking into acoustic energy, which was found to be in the order of 10^{-8}.

---

* Corresponding author at: Institute of Oceanology, Polish Academy of Sciences, ul. Powstańców Warszawy 55, 81-712 Sopot, Poland. Tel.: +48 58 7311825. Fax: +48 58 551 21 30

E-mail address: klusek@iopan.gda.pl (Z. Klusek).

Peer review under the responsibility of Institute of Oceanology of the Polish Academy of Sciences.

Production and hosting by Elsevier

https://doi.org/10.1016/j.oceano.2019.08.001

1. Introduction

When a wind wave is broken, a stream of water mixed with air is transferred into the water body.

To some extent, the energy of the pre-breaking wave is dissipated throughout this turbulent motion and doing work on newly created air bubbles by pushing them down. Despite great efforts, the present parametrisation of wave energy dissipation is far from completion.

Due to turbulence, clouds of mechanically agitated bubbles are formed. The bubbles are advected outwards from the breaking volume and upwards to the water surface, forming white caps. Plumes of aerated water are associated with emissions of wave-origin low-frequency (less than 1 kHz) ambient noise in the ocean (Carey and Browning, 1988; Carey and Fitzgerald, 1993; Prosperetti, 1988).

On the other hand, mechanically agitated individual bubbles ringing mainly at their radial resonance are a source of noise in the higher frequency range of up to tens of kilohertz (Medwin and Daniel, 1990; Prosperetti, 1988).

It is well recognised (for example, Kerman, 1984) that a predominant component of wind/wave-driven underwater noise exists in the ocean due to bubbles created throughout and immediately after wave breaking. Hence, it was observed that some functional dependency exists between dissipated wave energy in relation to the amount of acoustically active bubbles and emitted noise (Melville et al., 1988). Further, this idea has been put forward and tested (Lamarre and Melville, 1991), such that the intensity of underwater sound emitted during wave breaking correlates with the intensity of breakers and dissipation of wave energy.

Several laboratory and field experiments have supported the idea of associations between the character of wave breaking and some parameters of the emitted underwater noise (Deane, 1999; Deane and Stokes, 2010; Hollett, 1994; Kolaini,1998; Loewen and Melville, 1994; Means and Heitmeyer, 2001, 2002; Melville et al., 1993). Due to this relation, assessment of wind-wave energy dissipation in the ocean via measurements of the generated noise has been suggested, tested, and concluded that O (10^{-8}) of the dissipated wave energy is transformed into acoustic energy (Melville, Loewen and Lamarre, 1993).

However, observations performed on noise energy emitted during wave breaking contain a high degree of uncertainty concerning the rate of acoustic energy to the dissipated wave energy. The values differ by up to several orders of magnitude, ranging from 10^{-10} to 10^{-6} (Carey et al., 1993; Klusek and Lisimenka, 2013; Kolaini and Crum, 1994; Li and Farmer, 1993, 1994; Tęgowski, 2004). One of the reasons for this inconsistency concerns the different simulations of the wave breaking processes. On the other hand, as in the case of laboratory experiments, the distinctiveness of the sound propagation conditions in limited volumes was ignored.

Presented here experiment is one of the series of investigations designed to develop the relationships between breaking and noise at different scales of wave breaking intensities. In one of two earlier papers, the noise emitted by waves with a height exceeding 2 m was evaluated (Klusek and Lisimenka, 2013). In the other paper, it showed how salinity, microbubble presence and surface tension would influence sound generation during small-scale splash events (Szuszkiewicz and Klusek, 2018).

The motivation for this study is to determine more correctly the relations between energy dissipation of low amplitude waves (mainly plunged breakers) on the one hand, and the characteristics of emitted underwater noise aimed at monitoring breaking processes at sea on the other.

The paper is organised as follows. In Section 2, the wave flume and wave characteristics are briefly presented. Moreover, the acoustic setup, methods of signal recording and signal post-processing are there reported. Section 3 presents the parameters of acoustic noise, and in the next section, the acquired relationships between noise intensity and wave energy are presented and discussed. The paper ends with a discussion on the results obtained by some other authors.

2. Material and methods

2.1. Hydrodynamic investigations in the wave flume

The experiments were performed in a wave flume located at the Institute of Hydro-Engineering, Polish Academy of Sciences, Gdansk, Poland. The flume is 64 m long, 0.6 m wide, and 1.4 m high. The walls are made of 18 mm thick glass, which permits the application of imaging techniques of

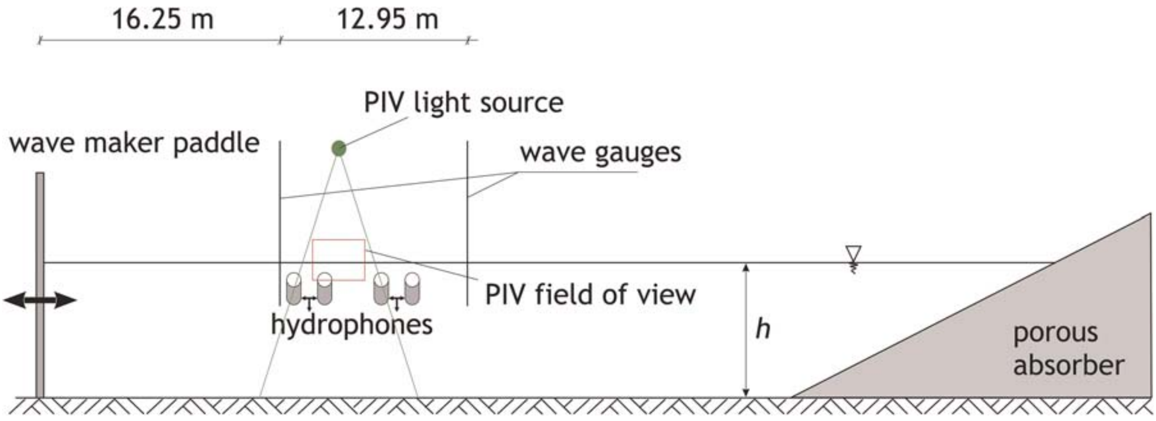

Figure 1 Wave flume setup and the arrangement of wave gauges and hydrophones.

measurements. The flume was filled with fresh water to a depth of 0.65 m. The temperature of water at the moment of the experiment varied between 14 and 16°C, depending on the date of the experiment.

In the hydraulic laboratory, waves are generated by a mechanical piston-type wave maker driven by an electric motor. The system's DHI Wave Synthesizer Online 8.1 software is used to control the generated sequences. At the far end of the flume, a porous wave absorber is installed to prevent wave reflections (Fig. 1).

The waves created and studied in the present experiments correspond to focusing wave packets comprising several component waves of fixed height and fixed wave period. The system is capable of creating both spilling and plunging breakers with various intensities. The maximum height of the generated waves may reach as high as 0.5 m. However, in the experiments, the maximum wave height usually does not exceed 0.3 m. Surface displacement is recorded with resistance type wave gauges placed in the prior- and post-breaking area, with a distance of 12.95 m between them (Fig. 1). Free-surface elevation time series are sampled at a frequency of 100 Hz. The gauges are calibrated before each experimental run.

In order to estimate the wave energy, the following spectral approach is applied. The free-surface elevation recordings are represented as the sum of harmonic wave components of frequency (ω_n), amplitude (A_n), and phase (φ_n) (Dean and Dalrymple, 1984; Goda, 2000):

$$\eta(t) = \sum_n A_n \cos(\omega_n t - \varphi_n), \tag{1}$$

where $\eta(t)$ is a function of free-surface elevation (displacement).

Applying Fourier analysis to the free-surface elevation time series, amplitudes of wave components (A_n) are determined. The wave energy of an individual component by a unit of the crest is calculated according to this equation (Dean and Dalrymple, 1984):

$$E_n = \frac{1}{2}\rho g A_n^2, \tag{2}$$

where g is the acceleration due to gravity and ρ is water density.

The total wave energy (E_T) of the wave packet is a sum of energies of individual wave components according to the formula

$$E_T = \frac{1}{2}\rho_w g l b \sum_n A_n^2, \tag{3}$$

where b is the width of the flume and l is the length of a wave packet.

The dissipation of wave energy may be estimated using the spectra of the two time series of the surface displacement taken before and after breaking. The lessening of wave energy after wave breaking event in relation to the initial wave energy would be presented in the form

$$C_d = \frac{E(x_1) - E(x_2)}{E(x_1)}, \tag{4}$$

where C_d is the dissipation coefficient, $E(x_1)$ is for the wave energy for the wave gauge positioned before wave breaking area, and $E(x_2)$ is for the wave gauge position behind the wave breaking area.

The coefficient C_d plays an important role in defining the intensity of the total energy dissipation.

In the course of some experiments, video recordings with a particle image velocimetry (PIV) system were performed, and the identification of bubbles' depth injection and behaviour was recorded. The 2D FlowMaster software from LaVision was used. The PIV system comprises a high-speed CCD camera with a resolution of 1280 × 1024 pixels and Nd: YAG 200 mJ dual laser-head system (described as PIV light source in Fig. 1). The system allows for collecting images in memory at a 15 Hz sampling rate. The measurements were performed in a plane parallel to the wave flume walls (described as PIV field of view in Fig. 1). The PIV camera records the movement of air bubbles illuminated by laser light in the selected field of view. The impulse of a laser light 'freezes' the moving air bubbles in a few mm thick layer, parallel to the wave flume walls. The laser and the camera measurement system is capable of providing high-quality data for the computation of air bubbles' displacement based on the identification of the bubble position in two successive images taken within a very short time span between them (~1 ms). The recorded raw images are then post-processed using a PIV double frame — double exposure method. This technique implicates the calculation of vector velocity fields based on a spatial cross-correlation between two images (Paprota, 2017). The 2D cross-correlation method is applied to a number of smaller windows (32 × 32 pixels) that cover the entire field of view and allow for visualising the spatial mean displacement of illuminated bubbles distribution within the whole window. Finally, the vector of instantaneous velocity between two camera exposures is calculated. This procedure is repeated 15 times per second to capture the temporal evolution of fields of the bubble velocity vector in the course of the breaking event.

2.2. Hydrodynamics data processing

The generated wave packets were focused at a distance of around 20—22 m away from the mean position of the wave maker paddle. As soon as the wave's steepness exceeds a certain critical value of the wave-breaking criterion, a plunging breaker or spiller occurs. The maximum recorded wave height upstream of the breaking point was about 0.2 m. The particular run was repeated 3 times for each of the selected wave energy. In total, 103 runs were performed, including 12 spilling breaker events generated for different wave energy packets. However, due to the fact that the experiments were carried out in different seasons at slightly different water temperatures (14°C in wintertime and 19°C in summertime), only a subsample of 48 runs from the experiments in the winter season was used in this analysis.

In Fig. 2, examples of wave sequences initiating spilling (top graphs) and plunging (bottom graphs) breakers are presented in terms of the free-surface elevation records and corresponding spectra of relative wave energy (normalised by the specific weight $\gamma = g\rho$). The elevations measured by the upstream gauge are denoted in black, while downstream ones are denoted in blue.

In the example presented, the wave sequence leading to the plunging breaker comprises waves in a frequency ranging from 0.2 to 1 Hz, while the spilling breaker occurs in a

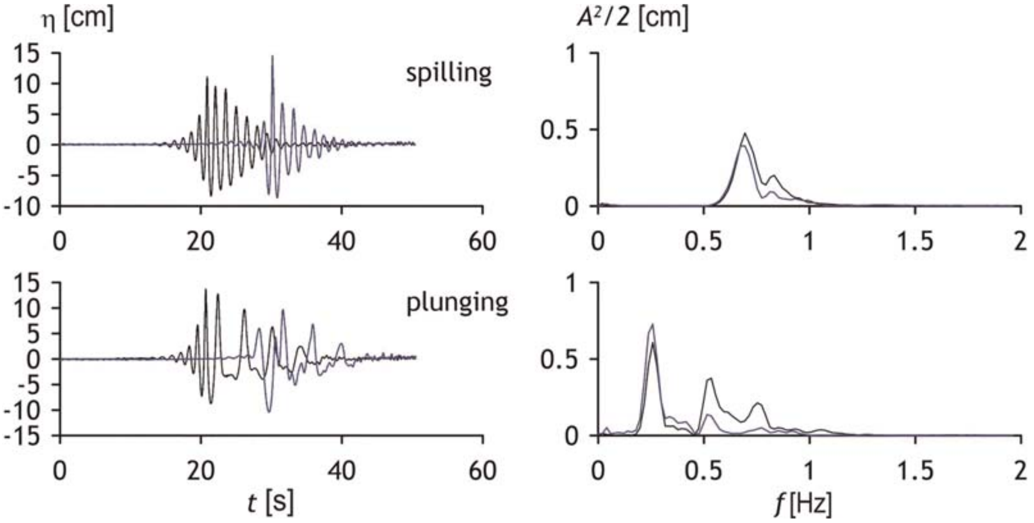

Figure 2 Free-surface elevation time series and corresponding wave energy spectra before (black) and after (blue) the occurrence of a spilling breaker (top); plunging breaker (bottom). (For interpretation of the references to color in this figure legend, the reader is referred to the web version of this article.)

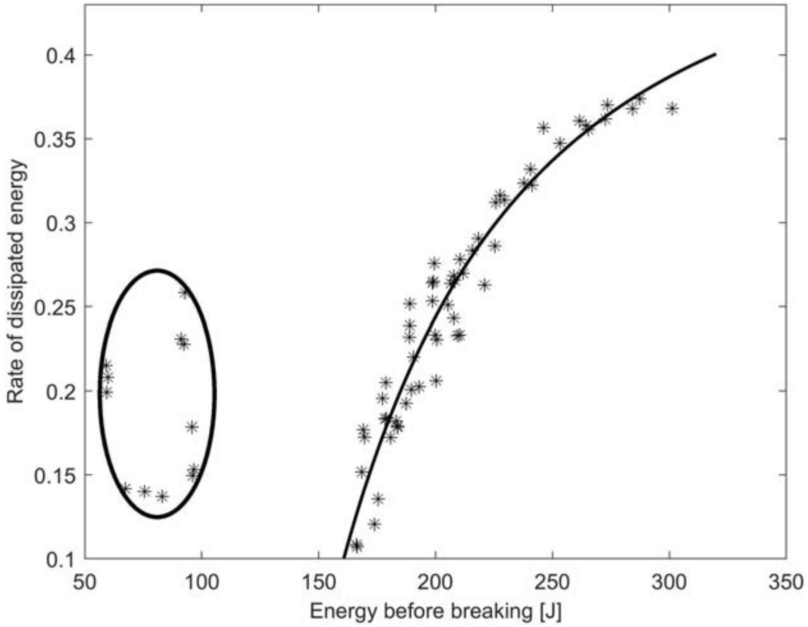

Figure 3 Energy of wave packets before breaking and dissipation rates of energy as a function of initial wave packet energy. The best fitted curve is proposed in the form $C_d \sim E_{T1}^{-1.69}$, where T1 — the energy of a wave packet before breaking. The set of spiller events is inside the ellipse.

narrower frequency ranging from 0.5 to 1 Hz. The spilling process usually occurs in the case of less energetic wave packets when compared to plungers.

The way in which the dissipation coefficient C_d relates to the pre-breaking wave energy suggests that possible dependency is in the form of power-law function.

Fig. 3 demonstrates a more rapid increment in the lowest range of the investigated energy of plungers than in the middle of the scale, and furthermore the gradual decrease in the growth rate at the end of the scale. The latter is probably due to the saturation of the dissipation process.

The relationship is proposed in the form of:

$$C_d = \frac{\Delta E}{E(x_1)} = a \cdot E(x_1)^b + c, \tag{5}$$

where the exponent is $b = -1.69$ and the adjusted R-square value is 0.99.

The observed rate of dissipated energy is growing from about 10% for the less energetic waves, and at up to about 37% in the largest breaking (Fig. 3).

Dissipation rates for spillers, which are marked with an ellipse, show rather random differences depending on the

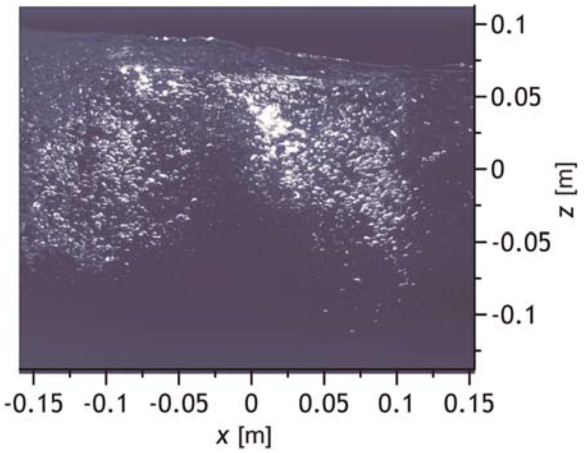

Figure 4 The PIV camera image of air bubbles under a plunging breaker.

wave character, and are noticeably distinguished between the similar spilling events. Additionally, higher energy dissipation is observed for higher energies of the wave trains.

At the next stage, the dynamics of air bubbles produced during the breaking events were determined qualitatively. In Fig. 4, the recorded camera image of the illuminated air bubbles, allowing for the determination of bubble kinematics, is presented.

Comparing different runs, we observe the entrainment depth of bubbles as rather regular which is approx. in the range of 0.12—0.15 m. The horizontal length of the bubble plume stays within a range of 0.2—0.4 m depending on the breaker intensity.

Fig. 5 illustrates the velocity field of bubbles for the case of the generated wave train consisting of several component waves of periods ranging from 1.0 s to 5.6 s with the corresponding wavelength ranging between 1.6 and 14 m. The estimated minimum and maximum phase celerity of component waves is 1.6 m/s^{-1} and 2.5 m/s^{-1}, respectively. It can be seen from Fig. 5 that the air bubble velocity field reveals a dynamic and complex nature of wave breaking phenomenon. In the example presented, the highest bubble velocities may reach 3.2 m/s, which constitute approximately 130% of the highest phase celerity, thus corresponding to the longest component wave.

Although laboratory conditions do not fully reproduce the situations in the sea, bubble plumes formed by plunging waves and the waves themselves may be easily reproduced and carefully controlled, thus allowing hydrodynamic and acoustic parameters to be investigated quantitatively.

In numerous studies, a lot of attention was paid to the issue of how salinity affects the number of created bubbles (Anguelova and Huq, 2018; Blenkinsopp and Chaplin, 2007, 2011; Cartmill and Su, 1993; Chanson, Aoki and Hoque, 2006; Haines and Johnson, 1995; Kolaini, Roy and Gardner, 1994; Orris and Nicholas, 2000; Slauenwhite and Johnson, 1999; Wu, 2000). To date, the interpretations have been contradictory. However, comprehensive research conducted by Blenkinsopp and Chaplin (2011) shows that the number of very small bubbles inside a breaking-induced plume in seawater is greater than that in fresh water even though the overall differences in air entrainment and bubble size distribution are negligible.

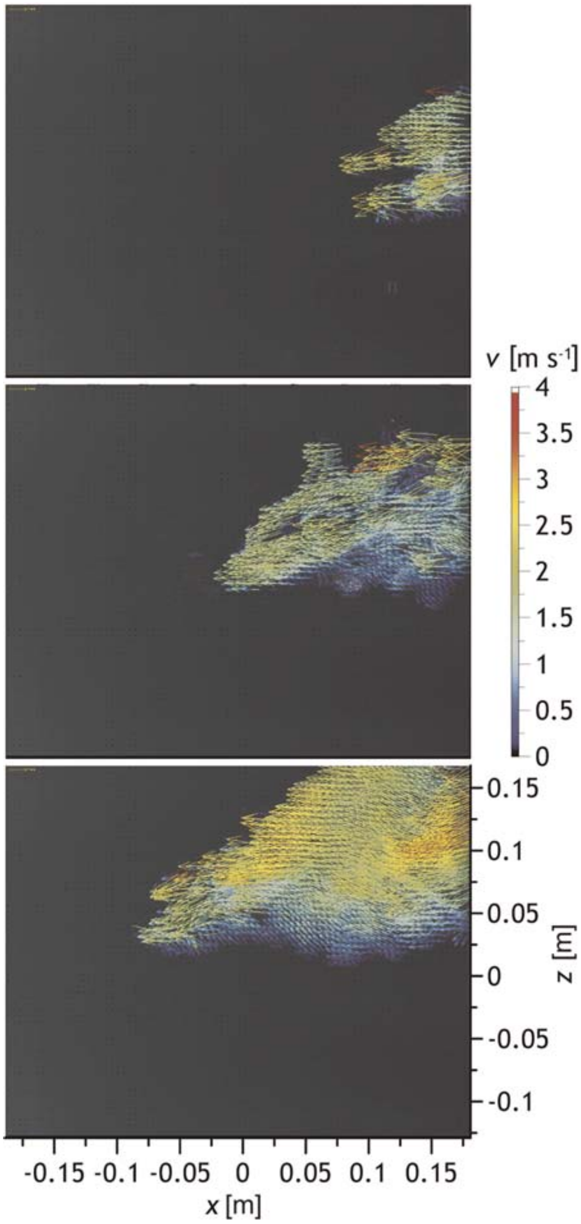

Figure 5 The velocity field of air bubbles produced by a plunging breaker. The images represent subsequent instants of a wave breaking process recorded every 1/15 s.

2.3. Underwater noise recordings

Noise recordings were realised using a setup of four omnidirectional hydrophones spaced horizontally along the flume axis. The hydrophones were grouped pairwise, with a distance inside each pair of 65 cm, positioned midway between the walls and 25—30 cm beneath the still water surface. In the case of plungers, one pair of hydrophones was placed upstream and another downstream of the breaking area at a distance of 6.1 m between the group's centres. In the case of spillers, the location of the array of hydrophones was extended under the whole spilling area.

The transducers were broadband RESON TC 4032 hydrophones calibrated by the manufacturer.

For some runs, rubber sheets were attached to the bottom and to the walls of the flume to diminish reverberations of the acoustic waves. The tests showed that the sheets insignificantly affect acoustic observations. But then, the dynamics of breaking waves were disturbed when compared to the conditions without the sheets. Consequently, presented here are the results of the experiments devoid of any additional attachments aimed at reducing reverberations.

The acoustic signal was acquired using a 16-bit resolution National Instrument 6251 Analog Digital Converter and further analysed using specially designed (and developed by the authors) software in the MATLAB environment.

The sampling rates in each of the four channels started at 50 Ksamples/s, and in one of the series, they increased to 70 Ksamples/s. The low- and high-pass analogue filters were set at the amplifier with a bandwidth in the range of 100 Hz to 25 kHz.

To estimate the duration of the noise generated by the active bubbles, the information at the level of the background noise of the tank was taken into account. High-resolution power spectra were calculated by means of the sliding FFT algorithm operating on 8192 long sub-samples with a rectangular window. One-third octave frequency band spectra were calculated at the outcome set of the narrow-band spectrum as the mean of frequency power component in a given frequency band.

2.4. Adjustment of acoustic data in view of propagation in waveguide

The advantages of tests in a flume are well known and are mainly due to performing the experiments under strongly controlled wave conditions, such as their spectra and energy. Furthermore, the geometry of experiments could be designed and it is possible to repeat them.

Nevertheless, in the field of acoustics, we face major environmental challenges such as signal contamination by ambient noise in laboratories and the surrounding area, and wave-maker sounds and strong reverberation in small tanks. The other disadvantage is that due to proportions of the cross-section of the acoustic waveguide in relation to the wavelength in the investigated range of frequencies, the cut-off frequency phenomenon in the middle range of audio frequencies is observed, and requires the use of data correction algorithms.

Moreover, as was mentioned above, the difference compared to the seawater physicochemical properties of tap water regularly utilised in tanks, i.e. salinity, surface tension or presence of microbubbles might change noise emission.

From an acoustic standpoint, the flume would be regarded as a waveguide with rectangular cross-section enlarged in one dimension.

In such cases of enclosures, the method of images would be applied in the frame of the geometrical acoustics approximation (ray acoustics) (Allen and Berkley, 1979; Gibbs and Jones, 1972), while the concept of a sound wave is replaced by the concept of sound rays.

However, for boundaries that have a finite admittance, only an approximate solution for the pressure can be obtained (Ingard, 1951). Formally, the correct solutions are obtained in the case where the distances of both the source and observation point are greater than a quarter of the acoustic wavelength from the wall. Nonetheless, as stated by Deane and Stokes (2010), the method of image yields a reasonable approximation of the observed noise spectra in a size similar to a flume.

However, our modelling research, performed with the method of images, satisfies recorded spectra only at small distances between the source and receiver.

Using the method of images for a point source, the sum of pulses can be expressed as:

$$\begin{aligned} h(t,\vec{x}_S,\vec{x}_r) = {} & \frac{\delta(t-R_0/c)}{R_0} + \frac{\delta(t-R_B/c)}{R_B}\tilde{V}_B + \frac{\delta(t-R_S/c)}{R_S}V_S \\ & + \frac{\delta(t-R_{W1}/c)}{R_{W1}}\tilde{V}_B + \ldots \frac{\delta(t-R_{W2}/c)}{R_{W2}}\tilde{V}_B \\ & + \frac{\delta(t-R_{BS}/c)}{R_{BS}}\tilde{V}_B V_S + \frac{\delta(t-R_{W1S}/c)}{R_{W1S}}\tilde{V}_B V_S + \cdots, \end{aligned} \tag{6}$$

where R is the length of a sound path from a source to the receiver bouncing at the bottom, sidewalls and water surface; for example, R_{BS} means the path between a source and the receiver reflected once at the flume bottom and once at the water surface.

$\tilde{V}[\ldots]$ are the complex reflection coefficients at the boundaries, respectively at the water surface and flume walls or bottom, depending on the frequency and angle of incidence. In view of the fact that the sidewalls and bottom of the flume are the same, we have $V_{w1} = V_{w2} = V_B$.

δ is the Dirac delta-function which generates a peak in an impulse response (IR) at arrival time $t = R/c$.

For the estimation of interactions at each boundary, the angle of incidence is computed and the reflection coefficient from a water-glass-air sandwich-type layer is modelled by the frequency and angle independent of reflection coefficients with the standard formula according to Brekhovskikh and Godin (Brekhovskikh and Godin, 1990, formula 2.4.9):

$$V = \frac{(Z_1+Z_2)(Z_2+Z_3)\exp(-2i\varphi)+(Z_1-Z_2)(Z_2+Z_3)}{(Z_1-Z_2)(Z_2+Z_3)\exp(-2i\varphi)+(Z_1-Z_2)(Z_2-Z_3)}, \tag{7}$$

where Z_1, Z_2, Z_3 are respectively the acoustic impedance of air, glass, and water; while the acoustic impedance of a medium is $Z = \rho c$, where ρ is the medium density and c is the sound speed in each of the media.

$\varphi = 2\times k_2 d\cos\theta_2$, and k_2 is the acoustic wave number in the glass layer, θ_2 is the angle of refraction in the glass, and $d = 0.018$ m is the thickness of the flume walls.

In order to calculate the acoustic impedance, densities and sound speeds in the media were applied as follows:

water $\rho = 999.8$ kg/m^3, $c = 1470$ m/s;
glass $\rho = 2500$ kg/m^3, $c = 4500$ m/s;
air $\rho = 1.2$ kg/m^3, $c = 343$ m/s.

In the considered frequency range below 12 kHz, the reflection coefficient from the flume walls is complex, with the absolute value close to unity and is practically not dependent on frequency and incident angle. In contrast, the phase shift of reflected waves depends, in a smooth

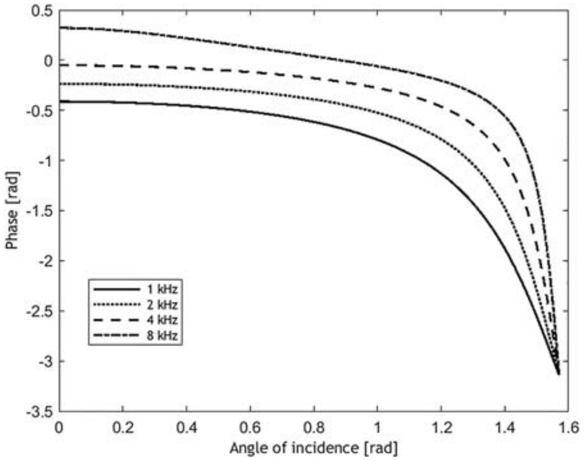

Figure 6 The dependence of the phase shift of reflected waves from the flume's walls upon frequency and incident angle.

manner, on the frequency and incident-reflected angle and at higher frequencies above 10 kHz in a rather complicated one (Fig. 6).

To determine the amplification of sound level at some frequencies and attenuation in another frequency band due to wave propagation in the limited volume of the flume, the reverberation was initially computed as the incoherent sum of the sound pressure at each of the receiver locations. And, subsequently, the incoherent sum of the sound pressure was normalised by the sound pressure in the absence of reverberation. It means that the sum of terms in Eq. (5), multiplied by noise in some frequency band and divided by the first term, gives a series of normalisation coefficients used for the correction of the observed power noise spectra.

The numerical tests were taken by planting a number of point sources near the duct's surface which corresponds to bubbles dispersed in the volume of the size of images of bubble clouds recorded by the camera.

In the model, the receivers were placed along the flume axis. The generated signals were white noise time series filtered in one-sixth octave bands.

Illustrations of the behaviour of spectra for a discrete set of frequencies corresponding to steps with the 1/6 octave-bands in the 80—12,500 Hz range at different distances from sources are given in Fig. 7.

After running tens of realisations, correction (compensation) for the observed sound spectra and acoustic energy in 1/6 octave bands emitted during the plunging was carried out.

Due to the relatively small dimensions of the flume's cross-section in relation to acoustic wavelengths in the middle of the audio frequency band, the cut-off phenomenon is observed. Hence, strengthening or reducing the sound intensity, which depends on the frequency and distance of the observation point to the source, is evident.

In the illustrated example, a number of point sources n are equal to 300. The sources are uniformly and randomly distributed between the walls of the flume, in the water column from the mean water surface down to $d/4$, and along the flume at a distance of up to 0.2 m. Here, the points of observations are situated in the centre of the flume's cross-section at distances of 0.5, 1, 1.5, 2.0 and 1.5 m from the front edge of a bubble cloud. As was shown by Deane (1999), the sound attenuation in an air-water mixture under the breaking wave would reach tens of dB/m, so the noise recorded outside of the mixed area is coming from a relatively thin "skin" of bubble cloud.

3. Results

3.1. Characteristic features of the noise

High-resolution periodograms of plunging noise, recorded by each of the hydrophones, and estimated with the short-time Fourier transform (STFT), are given in Fig. 8.

The spectra of signals received at each of the hydrophones, arranged along the flume at different locations in

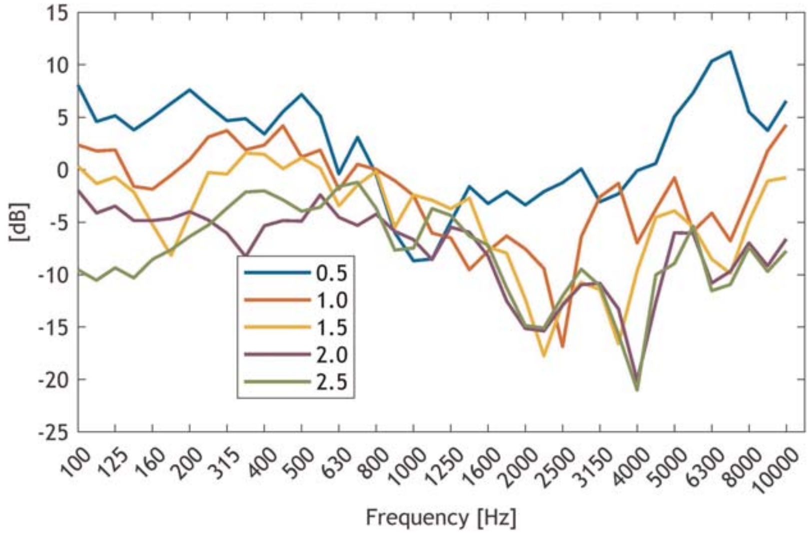

Figure 7 Normalised, spectral characteristics of reverberation, computed from the model for the set of frequencies in 1/6th octave bands ranging from 80 to 12,500 Hz. Hydrophones are placed in the geometrical centre of the water column's cross-section. Numbers in the legend are for hydrophones placed at distances of 0.5, 1, 1.5, 2 and 2.5 m from the edge of volume with bubbles.

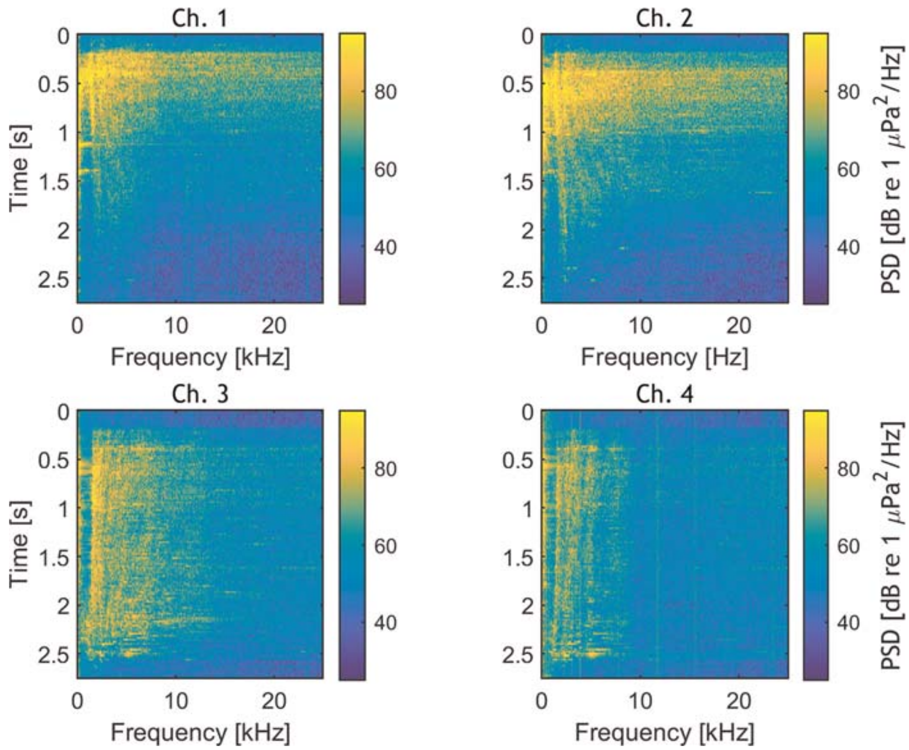

Figure 8 Examples of time evolution of the noise power spectrum in narrow frequency bands during the course of breaking, registered by all the hydrophones. The example illustrates one of the most energetic events. Colours represent the Power Spectral Density Level of the noise. (For interpretation of the references to color in this figure legend, the reader is referred to the web version of this article.)

relation to the breaking area, are presented in subsequent panels. The upper panel is for data from the hydrophone situated at the most distant point, which is upstream in relation to the breaking area. Each periodogram presents an evolution in time of noise radiation at different stages of the breaking process. Additionally, the effects of the modal broadband sound propagation on the acoustic waveguide in the case of a source moving in relation to the observer are observable. Subsequently, for frequencies above the lowest in the set of cut-off frequencies, the interference pattern predicted by the wave theory of guided waves is evident.

The plunging event shown here is relatively fast, with the highest sound emission lasting only 1.5—2.5 s.

In the middle of the audio frequencies' range, and going down in line with the frequency axis, we observe a notch with a sharp decline in the noise spectra. It corresponds to the lowest cut-off frequency (which matches the length of acoustic wave equalling four of the water depths in the flume). When an acoustic active volume drifts off from a receiver, the increasing mode number of the cut-off frequency also increases. We observe that at frequencies approximately below 1600 Hz, due to the excessive attenuation, the noise intensity decreases exponentially with the increasing distance to a source. At further distances from the breaking area and in the lowest frequency range, only plane waves would propagate.

On the other hand, in the vicinity of a bubble cloud, both the acoustic properties of the flume walls and its geometry do not have much influence on the noise spectrum.

Examples of the evolution of noise spectral density for the duration of breaking in 1/6-octave bands, registered at two hydrophones, are shown in Fig. 9.

It is evident in the time history of noise in selected frequency bands that at the hydrophone situated upstream from the breaking region (the upper panel, Channel 2), the noise level at the lowest observed frequencies increases at the very moment that the breaking happens. We believe that at this moment the noise is emitted simultaneously by single bubbles and by the first produced bubble cloud.

Generally, in the course of the first half-second of the rolling, the central frequency displays a shift towards higher frequencies and is correlated with changes in the spectral slope.

The active generation of the sound after plunging depends on the wave intensity, and in our experiments, it lasts up to about 3 s. The noise intensity decayed exponentially in time, and in the first 1—2 s after maximum, the intensity diminishes by a factor $-6\div-10$ dB/s.

The mean noise spectra are reasonably similar for all wave heights. The negative slope of the spectrum envelope above 1.5 kHz is about $-6\div-10$ dB/octave, reaching the minimum in the first second of breaking.

It is understandable that in the tank, the noise intensity should be higher due to multiple reflections from the water surface, tank bottom and walls, and at the same distance from the breaking area as in boundless space. Therefore, the real spectral slope and total sound energy emitted during a breaking event at the source would be obtained using

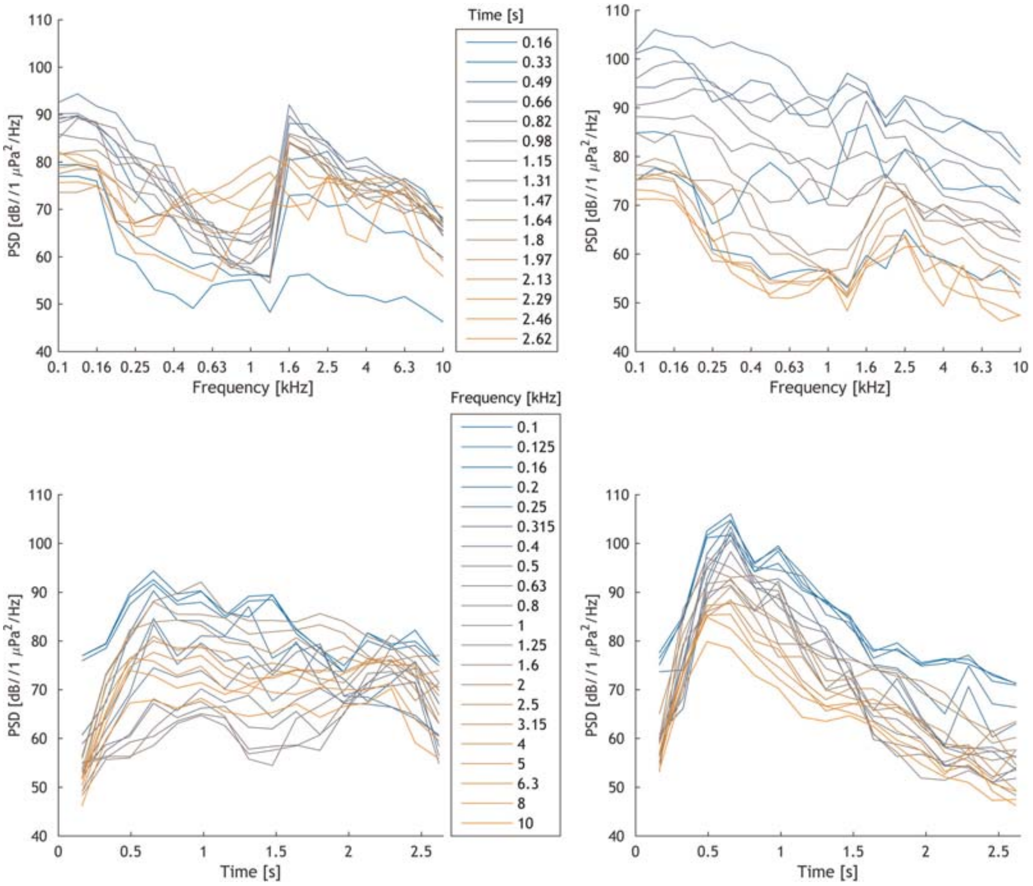

Figure 9 The time history of unprocessed noise signals recorded by the two hydrophones observed at different frequencies (upper panels). The receivers are placed upstream (Ch.2) and downstream (Ch.3) in relation to a plunger in the vicinity of the breaking area. Numbers in legends are central frequencies in 1/3-octave bands. The bottom panels are spectra at different moments of the breaking process. Numbers in the legends represent time in seconds.

correction for the spectra of signals received at different hydrophones.

With the model results, we would then correct the received sound spectra. The appropriateness of doing this kind of adjustment is confirmed by comparing the observed slope of the noise spectra in the flume with the noise spectra from plungers in the sea, which have similar typical values of −5 to −6 dB/octave. However, when introducing adjustment to the noise spectra attributable to reverberation and excessive attenuation, the notch at the middle of the spectra is corrected though only to some extent.

3.2. Estimating the energy of the emitted noise

As a consequence of the extent of the sound generation volume in relation to the channel cross-section, and due to small distances from a set of sources to an observation point, estimation of the total source intensity with the application of the model of dipole point source placed in a boundless medium (as among others by Kolaini and Crum, 1994 or Tęgowski, 2004) is not appropriate here. At the observation point located outside of the breaking area, noise is coming from different directions due to multiple reflections. On the other hand, at higher distances in the lower frequency range, only plane waves do arrive. In general, both effects are predicted by the theory of sound propagation in an enclosed space, though only for an idealised case of propagation in a medium with uniform acoustic properties.

The estimation of the sound energy generated in a single breaking is carried out under the following steps:

- estimation of the power spectrum in the third-octave bands for 8192 points sampled at 50 or 70 kHz;
- multiplying the spectral values of energy of raw recorded signals in each of the third-octave bands by appropriate weights resulting from amplification or weakening of the signal in different frequency bands (based on smoothed data from Fig. 7);
- summing up over frequency and time;
- and at the last stage, acoustic energy transferred through the flume's cross-section is computed.

The released acoustic energy in the course of breaking events at each observation point would be performed according to the following formula:

$$\prod = \frac{s}{\rho_w c_w}\sum_{i}^{n}\sum_{j}^{m} w_{ij}\langle P_{j,k}^2\rangle df_i dt, \tag{8}$$

where ρ_w is the water density [kg/m^3], c_w is the sound speed in water [m/s], n is the number of one-third octave bands, m

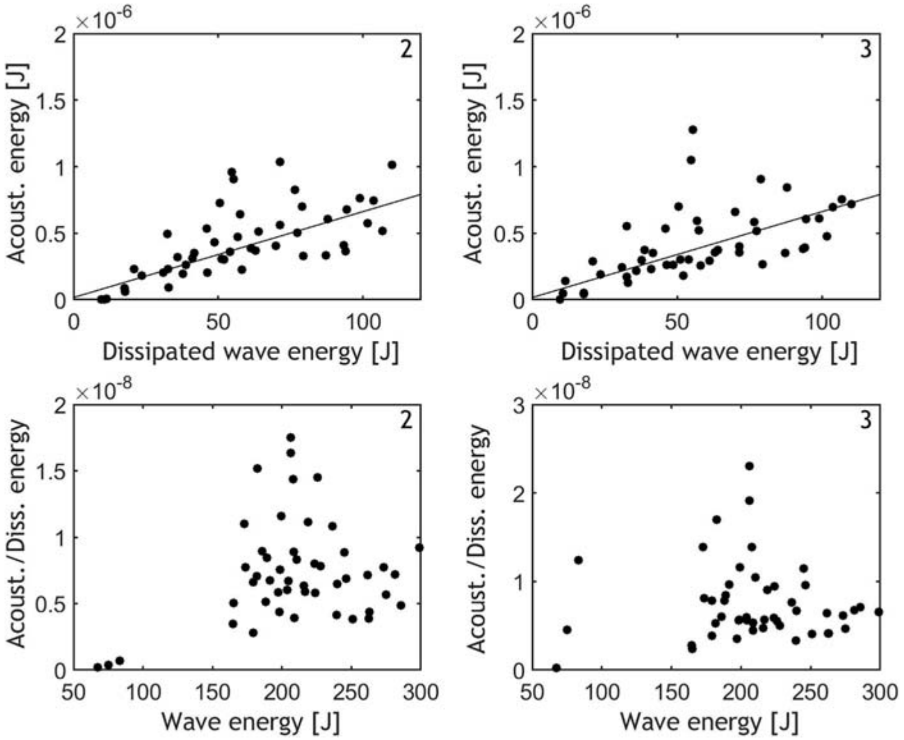

Figure 10 Rate of emitted acoustic energy to wave energy dissipated during breaking events estimated at selected observation points as functions of the dissipated wave energy (upper panels) and the wave packet energy before breaking (bottom panels). In the panels, numbers of hydrophones represent their positions along the flume.

is the number of segments taken into instantaneous spectral analysis, $\langle P_{j,k} \rangle$ is the mean acoustic pressure in frequency band and each of segment [Pa], df_i is the frequency range in each of one-third octave bands, w_{ij} is the correction coefficients for each frequency band and distance from a bubble cloud to a hydrophone, and s is the cross-section of the flume's water body.

3.3. Energy of the emitted noise vs. dissipation of wave energy

The rate between the emitted acoustic energy and the wave energy dissipated during breaking as well as the wave energy predating breaking is demonstrated in Fig. 10. The hydrophones are numbered as in Fig. 8; numbers 1 and 3 are for hydrophones placed afterwards (hydrophone No. 3) and in advance of the breaking area (hydrophone No. 1). The lines in the upper panels denote tendency towards increasing acoustic emission with the dissipated wave energy. Fitting was performed with the robust nonlinear methods using “bisquare” weights (MATLAB) to diminish the effects of accidental data points, which do not follow the general trend in other observations.

Some effects are evident: firstly, there is increased efficiency in the conversion of dissipated wave energy into acoustic energy with increasing losses of wave energy; secondly, emission in the direction of the wave propagation is higher as from the rear of a bubble cloud. The latter effect supports the hypothesis that noise is predominantly emitted in the direction of wave propagation, i.e. at the front edge of rollers. Comparing the upper and bottom panels, it is also clearly visible and distinctive that noise emission is more orderly dependent on energy dissipation than on wave energy.

Observations of the time-frequency behaviour of noise and then comparing them to the results from the model indicate that the sound energy at frequencies greater than the cut-off frequency varied less than in the lower frequency range. Additionally, in this frequency range, due to the acoustic waveguide geometry, the sound is less excessively attenuated in the flume, and the noise level is generally more predictable than at lower frequencies. Besides, within a frequency range between 1 and 8 kHz at the sea, we observe the highest correlation between noise and wind speed (Klusek and Lisimenka, 2007, for example), which means stronger interrelations between the noise intensity and intensity of wave breaking, and associated with this is the dissipation of wave energy.

Consequently, to diminish the impreciseness of the adopted model for the spectrum correction, the energy of the high-frequency component of noise as a measure of the integrated total noise estimation has been proposed. The cumulative noise level in the frequency band (f, $f + df$) over a given time of emission is defined as:

$$CNL(f, f + df) = 10 \log \frac{\int_0^T p^2(f, f + df, t)dt}{p_0^2}, \tag{9}$$

where CNL is the cumulative noise level, f is the acoustic frequency of interest, df is the width of the frequency band, and t is time.

The relationship between a cumulative noise level in one of the higher frequency bands and dissipated wave packet

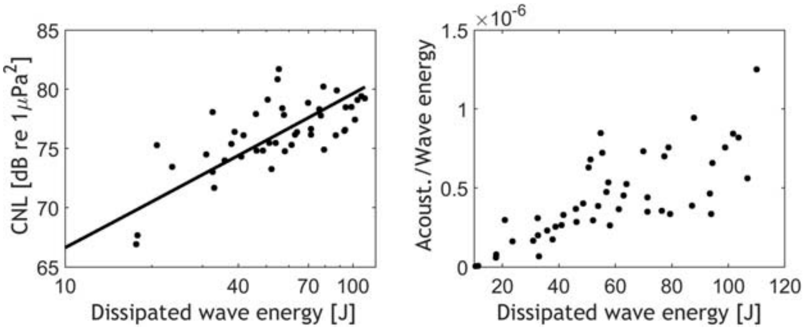

Figure 11 Cumulative noise level emitted during breaking events in 1/3rd octave band with a central frequency of 5 kHz, as a function of dissipated wave energy (on the left) and projected on the basis of this noise energy in broad frequency range (on the right). Presented data are recorded by the hydrophone 3 placed downstream of the breaking area.

energy during breaking is shown in Fig. 11. The noise data are only in the one-third octave band, with a central frequency of 5 kHz. Noise is recorded on the hydrophone placed downstream, in the vicinity of the acoustically active water volume.

Data are then fitted by means of the least square method using equally weighting data with a linear relation between decimal logarithm of dissipated wave energy during breaking and cumulative noise level.

$$CNL(@5\,\text{kHz}) = p_1 \log_{10}(\Delta E_n) + p_2, \tag{10}$$

where the estimated value of p_1 is 11.12, meaning that we have the approximately linear relation between the level of acoustic energy at higher frequencies and the logarithm of dissipated wave energy (expressed in dB).

There are experimentally well-documented facts, verified on large datasets, that the acoustic radiation from the turbulent volume of a water-air mixture under plunge breakers both at sea in a coastal zone by Bass and Hay (1997) or in a laboratory (Kolaini and Crum, 1994) has some universal properties. The broad maximum in noise spectra is placed within a range of 500—800 Hz; in addition, within a range of 1 to 10/20 kHz the slope of the spectral envelope is reasonably repeatable and has a negative roll-off rate of −5 to −6 dB/octave.

Hence, in principle, we can deduce the noise energy emitted during breaking in a broader frequency range via extrapolation and integrating noise spectra towards lower and higher frequencies from the frequency band presented here.

The results of interpolation of the PSD, with the straight line passing through the point of the noise level at 5 kHz, down to 500 Hz and up to 12,500 Hz (with a spectrum slope of −6 dB/octave) gives similar results for the ratio of energy conversion as using measurements in broad frequency band.

As a result, on the basis of the experiments presented, we would state that the ratio of the emitted acoustic energy to the mechanical energy of the waves dissipated in the plunging is in the order of 10^{-8} which coheres with the results of other investigations (Klusek and Lisimenka, 2013).

4. Discussion

In this section, our results are compared with the existing research on the relations between the emitted acoustic energy and wave energy dissipation that are either observed in the field or simulated. The experiments have different objectives and approaches but are nonetheless representative of a broad range of wave energy, hence the intensity of breaking.

In laboratory experiments, Loewen and Melville (1994) showed that the acoustic energy generated by a breaking wave was increasing with the wave energy dissipated by the breaking event. They estimated that the ratio of acoustically radiated energy to the energy dissipated by the breaking wave was O (10^{-8}).

Kennedy (1992, 1993) estimated that the ocean acoustic energy radiated during breaking comprised between 10^{-6} (Kennedy, 1992) and later after some correction 10^{-8} (Kennedy, 1993) of the dissipated wave energy.

Carey et al. (1993) simulated wave breaking with a wedge by releasing salt or freshwater into a semi-enclosed submerged rubber bag. Pouring was performed from different heights — from 0.34 to 0.9 m above the water surface. It was meant to imitate breaking waves with various potential energy. The experiments were conducted in a deep lake, and acoustic records were performed in the far field with respect to the noise source in the environment without reverberations.

The efficiency of the process of converting water energy to acoustic energy was within a range of 0.3—2.3 × 10^{-8}. Generally, they found 5-times lower acoustic energy emitted in the case of saltwater compared to a freshwater environment.

Kolaini and Crum (1994) performed an experiment using a set of wave packets with potential wave energy between 4 and 11.5 J. They observed both spillers and plungers events, and found different relations between the radiated noise energy and the energy of surface waves. The acoustic energy was rising more steeply in the case of higher energies of breakers, and sloping or just lacking any functional relationship for spillers (Fig. 11 in Kolaini and Crum, 1994). The latter observations have been supported by the measurements presented here.

The acoustic records were performed in an anechoic tank. The ratio between the emitted acoustic energy and potential energy of the wave before breaking was estimated within a relatively narrow range of 0.8 × 10^{-7} to 1.09 × 10^{-6}, with a higher conversion rate in the case of "stronger" waves.

When converting the results of Kolaini and Crum according to the convention adopted in our work regarding the ratio of the acoustic energy to the wave energy dissipated during breaking, and assuming the value of the dissipation coefficient to be $C_d = 0.1$, the transformation of the dissipated wave energy to acoustic energy is from 0.8×10^{-8} to 1.09×10^{-7}.

The ratio of the acoustic energy generated by breaking waves to the energy dissipated in breaking waves was estimated by Tęgowski (2004) in the Ocean Basin Laboratory at MARINTEK, Trondheim, Norway. The 3D-sea wave spectra were reproduced in a more realistic way than in 2D the wave flumes. The efficiency of transformation of the dissipated wave energy into acoustic energy with amplitudes in the order of 10 cm was found to vary within a range of 1.0×10^{-7} to 4.1×10^{-7}. However, in the estimations, the author disregarded the multiple sound reflections between the bottom and water surface, therefore the results might well be overestimated. Also, due to the fact that the waves were not in the form of packets, the author did not specify in a direct manner the dissipated wave energy participating in the breaking process.

Noise emission under the extremely high intensity of the breaking process was investigated by Klusek and Lisimenka (2013) in the Large Wave Flume, GWK LUH (Leibniz University, Hannover). Energies of wave trains were larger by several orders of magnitude than in other experiments. It was rather surprising that the values of conversion between the two forms of energy were rather low, below 10^{-8}, in contrast to those reported in other experimental patterns, in particular, the increasing efficiency of energy conversion with the intensity of breaking.

It should be noted that the dispersion of outcomes regarding energy transformation would issue from incompatibilities in physicochemical parameters of medium and methods of simulation. Besides, the class of acoustic source models used in processing would have an effect on noise computation, because authors proceed by assuming, not always rightly, that the noise source has the character of a near-surface acoustic dipole. This is despite the fact that recording was performed in the near zone of an extended bubble cloud. In some field observations, sound data would likely contain input from other than solitary local sources.

The most striking outcome of a comparative analysis of all experiments is that in individual experiments, values of fraction of converted forms of energy tend to increase with the intensity of breaking. However, the results of separate experiments performed with different wave energies do not follow a specific pattern, which requires a separate exploration.

5. Conclusions

Based on a physical model aimed at clarifying the connections between the wave energy dissipation in the two breaking regimes and the emitted acoustic energy, the experiments were performed and the relationships parametrised.

The motivation for this investigation is the large scattering of values in the fraction of the dissipated wave energy's conversion into the energy of the emitted noise.

The experiments were performed using plunging and spilling wave packets with the pre-breaking energy of the plungers within a range of about 150 J to 300 J — an energy range in which this type of experiment has yet to be conducted.

In order to avoid the uncertainty due to multiple sound reflections in the channel and the impact of the cut-off propagation phenomenon on the recorded noise, modelling of sound propagation in the flume was applied. This approach used a relatively standard model of sound propagation in waveguides, not taking into account both the multiple scattering inside the bubble cloud and attenuation by bubbles. Within the frequency range around the cut-off frequency for this waveguide, corrections of the spectrum level on the basis of the model of images were used in order to calculate the total noise energy.

Having been corrected, the characteristic pattern of the noise spectral parameter of the spectral slope is in a frequency range of 1—12.5 kHz, and thus comparable to the case of the wind-driven noise spectra observed in the ocean, i.e. −5 to −6 dB/octave.

The effectiveness of the conversion of wave energy dissipated in the breaking to acoustic energy increases with the breaking intensity. It was also established that the rate of the dissipation coefficient is diminishing in the course of increasing the pre-breaking energy of wave packets.

Due to the simultaneous recordings of noise at several points along the breaking area, the hypothesis of a higher level of noise in the direction of propagation wave packets, in relation to the area behind the breaking wave, was demonstrated.

In particular, we emphasised that the ratio of conversion of the dissipated wave energy into acoustic is in the order of 10^{-8}, which confirms the outcome of several earlier investigations into higher intensity breaking events.

It may be hoped that these findings may inspire the further development of passive acoustic methods as the most appropriate for determining the dissipation of wave energy during breaking at sea.

Especially interesting for future investigations would be low energetic spillers, for which the wave's dissipation coefficient is still rather poorly correlated with the wave packet energy.

Acknowledgements

These results have been achieved thanks to financing within the framework of the grant “Experimental studies on dependence on energy dissipation of breaking waves and acoustic noise generated during process of breaking”, No. 2011/03/B/ST10/05977 by the National Science Centre of Poland.

References

Allen, J.B., Berkley, D.A., 1979. Image method for efficiently simulating small-room acoustics. J. Acoust. Soc. Am. 65 (4), 943—950, http://dx.doi.org/10.1121/1.382599.

Anguelova, M.D., Huq, P., 2018. Effects of salinity on bubble cloud characteristics. J. Mar. Sci. Eng. 6 (1), art. no. 1, http://dx.doi.org/10.3390/jmse6010001.

Bass, S.J., Hay, A.E., 1997. Ambient noise in the natural surf zone: wave breaking frequencies. In: IEEE OCEANS '98 Conference Proceedings. 1373—1377, http://dx.doi.org/10.1109/OCEANS.1998.726293.

Blenkinsopp, C.E., Chaplin, J.R., 2007. Void fraction measurements in breaking waves. Proc. Roy. Soc. A 463, 3151—3170, http://dx.doi.org/10.1098/rspa.2007.1901.

Blenkinsopp, C.E., Chaplin, J.R., 2011. Void fraction measurements and scale effects in breaking waves in freshwater and seawater. Coast. Eng. 58, 417—428, http://dx.doi.org/10.1016/j.coastaleng.2010.12.006.

Brekhovskikh, L.M., Godin, O.A., 1990. Acoustic of Layered Media, Part I. Springer-Verlag, 240 pp.

Carey, W.M., Browning, D., 1988. Low-frequency ocean ambient noise: measurements and theory. In: Kerman, B.R. (Ed.), Natural Mechanisms of Surface-Generated Noise in the Ocean. Reidel, Dordrecht, 361—376, http://dx.doi.org/10.1007/978-94-009-3017-9_26.

Carey, W.M., Fitzgerald, J.W., 1993. Low frequency noise from breaking waves. In: Kerman, B.R. (Ed.), Natural Physical Sources of Underwater Sound. Springer, Dordrecht, 277—304, http://dx.doi.org/10.1007/978-94-011-1626-822.

Carey, W.M., Fitzgerald, J.M., Monahan, E.C., Wang, Q., 1993. Measurement of the sound produced by a tipping through with fresh and salt water. J. Acoust. Soc. Am. 93, 3178—3192, http://dx.doi.org/10.1121/1.405702.

Cartmill, J.W., Su, M.Y., 1993. Bubble size distribution under saltwater and freshwater breaking waves. Dynam. Atmos. Oceans 20, 25—31, http://dx.doi.org/10.1016/0377-0265(93)90046-A.

Chanson, H., Aoki, S., Hoque, A., 2006. Bubble entrainment and dispersion in plunging jet flows: freshwater versus seawater. J. Coastal Res. 22 (3), 664—677, http://dx.doi.org/10.2112/03-0112.1.

Dean, R.G., Dalrymple, R.A., 1984. Water Wave Mechanics for Engineers and Scientists. World Scientific, Singapore, 353 pp.

Deane, G.B., 1999. Acoustic hot-spots and breaking wave noise in the surf zone. J. Acoust. Soc. Am. 105 (6), 3151—3167, http://dx.doi.org/10.1121/1.424646.

Deane, G.B., Stokes, M.D., 2010. Model calculations of the underwater noise of breaking waves and comparison with experiment. J. Acoust. Soc. Am. 127 (6), 3394—3410, http://dx.doi.org/10.1121/1.3419774.

Gibbs, B.M., Jones, K., 1972. A simple image method for calculating the distribution of sound pressure levels within an enclosure. Acta Acust. United Ac. 26, 24—32.

Goda, Y., 2000. Random Seas and Design of Maritime Structures. World Scientific, Singapore, http://dx.doi.org/10.1142/3587.

Haines, M.A., Johnson, B.D., 1995. Injected bubble populations in seawater and fresh water measured by a photographic method. J. Geophys. Res. 100, 7057—7068, http://dx.doi.org/10.1029/94JC03226.

Hollett, R.D., 1994. Observations of underwater sound at frequencies below 1500 Hz from breaking waves at sea. J. Acoust. Soc. Am. 95, 165—170, http://dx.doi.org/10.1121/1.408374.

Ingard, U., 1951. On the reflection of a spherical sound wave from an infinite plane. J. Acoust. Soc. Am. 23, 329—335, http://dx.doi.org/10.1121/1.1906767.

Kennedy, R.M., 1992. Sea surface sound dipole source dependence on wave-breaking variables. J. Acoust. Soc. Am. 91 (4), 1974—1982, http://dx.doi.org/10.1121/1.403681.

Kennedy, R.M., 1993. Acoustic radiation due to surface wave breaking. J. Acoust. Soc. Am. 94 (4), 2443—2445, http://dx.doi.org/10.1121/1.407466.

Kerman, B.R., 1984. Underwater sound generation by breaking wind waves. J. Acoust. Soc. Am. 75 (1), 149—165, http://dx.doi.org/10.1121/1.390409.

Klusek, Z., Lisimenka, A., 2007. Ambient sea noise in the Baltic Sea. In: Proceed. of the 2nd Intern. Conf. & Exhibition on Underwater Acoustic Measurements: Technologies & Results, Heraklion, Crete, 625—634.

Klusek, Z., Lisimenka, A., 2013. Acoustic noise generation under plunging breaking waves. Oceanologia 55 (4), 809—836, http://dx.doi.org/10.5697/oc.55-4.809.

Kolaini, A.R., 1998. Sound radiation by various types of laboratory breaking waves in fresh and salt water. J. Acoust. Soc. Am. 103 (1), 300—308, http://dx.doi.org/10.1121/1.421115.

Kolaini, A.R., Crum, L.A., 1994. Observations of underwater sound from laboratory breaking waves and the implications concerning ambient noise in the ocean. J. Acoust. Soc. Am. 96 (3), 1755—1765, http://dx.doi.org/10.1121/1.410254.

Kolaini, A.R., Roy, A., Gardner, D.L., 1994. Low-frequency acoustic emissions in fresh and salt water. J. Acoust. Soc. Am. 96 (3), 1766—1772, http://dx.doi.org/10.1121/1.411323.

Lamarre, E., Melville, W.K., 1991. Air entrainment and dissipation in breaking waves. Nature 351, 469—472, http://dx.doi.org/10.1038/351469a0.

Li, D., Farmer, D., 1993. Passive acoustical measurements of scale, probability, and intensity of wave breaking. In: IEEE Proceedings of OCEANS '93 Engineering in Harmony with Ocean, vol. 2, 193—197, http://dxdoi.org/10.1109/OCEANS.1993.326090.

Li, D., Farmer, D., 1994. Observations of breaking surface wave statistics. J. Phys. Oceanogr. 24, 1368—1387, http://dx.doi.org/10.1175/1520-0485(1994)024<1368:OOBSWS>2.0.CO;2.

Loewen, M.R., Melville, W.K., 1994. An experimental investigation of the collective oscillations of bubble plumes entrained by breaking waves. J. Acoust. Soc. Am. 95 (3), 1329—1343, http://dx.doi.org/10.1121/1.408573.

Means, S.L., Heitmeyer, R.M., 2001. Low-frequency sound generation by an individual open-ocean breaking wave. J. Acoust. Soc. Am. 110, 761—767, http://dx.doi.org/10.1121/1.1379729.

Means, S.L., Heitmeyer, R.M., 2002. Surf-generated noise signatures: a comparison of plunging and spilling breakers. J. Acoust. Soc. Am. 112 (2), 481—489, http://dx.doi.org/10.1121/1.1491256.

Medwin, H., Daniel, A.C., 1990. Acoustical measurements of bubble production by spilling breakers. J. Acoust. Soc. Am. 88 (1), 408—412, http://dx.doi.org/10.1121/1.399917.

Melville, W.K., Loewen, M., Felizardo, F., Jessup, A., Buckingham, M., 1988. Acoustic and microwave signatures of breaking waves. Nature 336, 53—56.

Melville, W.K., Loewen, M.R., Lamarre, E., 1993. Bubbles, noise and breaking waves: a review of laboratory experiments. In: Kerman, B.R. (Ed.), Natural Physical Sources of Underwater Sound. Kluwer Acad. Publ., 483—501, http://dx.doi.org/ 10.1007/978-94-011-1626-8_36.

Orris, G.J., Nicholas, M., 2000. Collective oscillations of fresh and salt water bubble plumes. J. Acoust. Soc. Am. 107 (2), 771—787, http://dx.doi.org/10.1121/1.428253.

Paprota, M., 2017. Experimental study on wave-current structure around a pneumatic breakwater. J. Hydro-Environ. Res. 17, 8—17, http://dx.doi.org/10.1016/j.jher.2017.09.002.

Prosperetti, A., 1988. Bubble-related ambient noise in the ocean. J. Acoust. Soc. Am. 84 (3), 1042—1054, http://dx.doi.org/10.1121/1.396740.

Slauenwhite, D.E., Johnson, B.D., 1999. Bubble shattering: differences in bubble formation in fresh water and seawater. J. Geophys. Res. 104 (C2), 3265—3275, http://dx.doi.org/10.1029/1998JC900064.

Szuszkiewicz, J., Klusek, Z., 2018. Underwater noise emitted during small-scale air entrainment events. Oceanol. Hydrobiol. Stud. 47 (1), 87—97, http://dx.doi.org/10.1515/ohs-2018-0010.

Tęgowski, J., 2004. A laboratory study of breaking waves. Oceanologia 46 (3), 365—382.

Wu, J., 2000. Bubbles produced by breaking waves in fresh and salt waters. J. Phys. Oceanogr. 30 (7), 1809—1813, https://doi.org/10.1175/1520-0485(2000)030<1809:BPBBWI>2.0.CO;2.

Oceanologia (2020) 62, 83—100

Available online at www.sciencedirect.com

ScienceDirect

journal homepage: www.journals.elsevier.com/oceanologia/

ORIGINAL RESEARCH ARTICLE

Natural and anthropogenic factors influencing abundance of the benthic macrofauna along the shelf and slope of the Gulf of Guinea, a large marine ecosystem off West Africa

Krzysztof Pabis [a,*], Robert Sobczyk [a], Jacek Siciński [a], Tor Ensrud [b], Bjorn Serigstadt [b]

[a] *Laboratory of Polar Biology and Oceanobiology, University of Łódź, Poland*
[b] *Institute of Marine Research, Bergen, Norway*

Received 29 March 2019; accepted 29 August 2019
Available online 14 September 2019

KEYWORDS
Ghana;
Continental margin;
Distribution patterns;
Oil excavation;
Disturbance

Summary The West African continental margin belongs to the least known areas in terms of the ecology of benthic ecosystems. At the same time, this region is influenced by various threats associated with human activities, including industrialisation and oil excavation. Here, we analyse the abundance and distribution patterns of macrozoobenthic communities along the coast of Ghana. The material was collected in 2012 on nine transects at depths ranging from 25 to 1000 m. Over 200 quantitative samples were collected using a 0.1-m^2 van Veen grab. Generally, the mean density of macrozoobenthos decreased gradually from the shallow zone (25 m: 231.4 ± 262.2 ind./0.1 m^2) down to bathyal depths (1000 m: 55.4 ± 51.4 ind./0.1 m^2), but we observed intermediate scale variability in distribution patterns among the transects along the Ghanaian coast. Analysis of environmental factors showed no evidence of substantial pollution, although levels of hydrocarbons, barium and some other toxic metals show some local increases at particular stations, especially on the continental slope. Cluster analysis based on Bray—Curtis similarity and abundance of higher taxonomic groups of macrofauna yielded five groups of stations, while SIMPER analysis demonstrated that polychaetes and amphipods contributed most

---

[*] Corresponding author at: Laboratory of Polar Biology and Oceanobiology, University of Łódź, Banacha 12/16, 90-237 Łódź, Poland.
E-mail address: cataclysta@wp.pl (K. Pabis).

Peer review under the responsibility of Institute of Oceanology of the Polish Academy of Sciences.

Production and hosting by Elsevier

https://doi.org/10.1016/j.oceano.2019.08.003

significantly to within-group similarity. Canonical Correspondence Analysis demonstrated that PAH, THC and toxic metal levels (Ba, Cd, Pb), as well as oxygen concentration, were the most important factors structuring benthic communities.

1. Introduction

Understanding the continental margin benthic community structure is crucial in marine studies. Continental margins are major marine oil repositories and host important fishery resources. Thus, studies describing ecological gradients may lead not only to a comprehensive description of ecological processes, but also guarantee the appropriate development of future management plans (Levin and Sibuet, 2012). The distribution of benthos along an oceanic depth gradient is influenced by a number of factors including dissolved oxygen concentration, sediment structure, the total organic carbon level in the sediment as well as various disturbance processes and pollution events (e.g. Bakus, 2007; Edros et al., 2011; Ellis et al., 2012 and references therein; Solan et al., 2012; Włodarska-Kowalczuk et al., 2004). Rex et al. (2006), in their global-scale analysis of the meio-, macro- and megafauna, have demonstrated that the abundance of benthic communities decreases with depth, although there are still numerous discrepancies between the global scale models (e.g. Rex and Etter, 2010; Rex et al., 2006) and specific studies conducted on the regional or local scale (e.g. Aller et al., 2002; Coleman et al., 1997; McCallum et al., 2015). Moreover, studies describing the changes in benthic fauna from the shallow shelf areas down to bathyal or abyssal depths are still scarce, and many regions have almost completely been neglected in earlier research programmes (Rex and Etter, 2010).

The benthic marine fauna of the West African continental margin is largely unknown. The majority of ecological studies have focused on the shallow coastal areas, often with a low sampling effort. For example, some studies have investigated coastal brackish lagoons and river estuaries on the Nigerian coast (Akanabi Bamikole et al., 2009; Brown and Ajao, 2004; Edokpayi et al., 2010; Ewa-Oboho et al., 2008), and on the Ivory Coast (Kouadio et al., 2008), while some focused on tidal flats on the Mauritanian coast (Duineveld et al., 1993; Wijnsma et al., 1999). Longhurst (1959) analysed the shelf macrobenthic communities of the coast of Sierra Leone, while Le Loeuff and Intés (1999) focused their attention on the spatio-temporal dynamics of the benthic fauna of the Ivory Coast shelf. The macroepifauna associated with oil platforms in Gabon was also a subject of a recent study (Friedlander et al., 2014). On the other hand, the area of the Angola-Congo margin (south-eastern part of the Gulf of Guinea) was subject of comprehensive hydrological, hydrographical and ecological studies in the framework of the programme BIOZAIRE (Sibuet and Vangriesheim, 2009). However, this initiative concentrated on the deep-sea benthic communities associated with highly restricted areas influenced by high levels of organic matter inflow from the Congo River (e.g. Brind'Amour et al., 2009; Gaever et al., 2009; Galeron et al., 2009; Menot et al., 2009) and on a giant pockmark area (Menot et al., 2009).

The northern part of the Gulf of Guinea, including the Ghanaian coast, is almost completely unsurveyed, including the shallow areas. The only studies of the marine benthic fauna of the coast of Ghana were performed in the 1950s and 1960s and concentrated on distribution patterns of the macrobenthic fauna of the shallow areas, down to a depth of 80 m (Bassindale, 1961; Buchanan, 1957; Longhurst, 1958).

Marine ecosystems of the tropical and subtropical part of the West African coast are shaped by a highly dynamic and diversified set of factors, including natural hypoxia (oxygen minimum zones) (Levin et al., 2009) and high dynamics of water masses (Djagoua et al., 2011), making it a separate marine ecoregion (Spalding et al., 2007). In this sense, there is an urgent need for studies describing the influences of those complex processes and numerous factors on marine fauna.

The Gulf of Guinea is also an area of high economic interest. It constitutes the Large Marine Ecosystem (LME) characterised by significant fishery resources and oil reserves (Ukwe et al., 2003). Human pressure on this ecosystem has constantly been increasing since the last 30 years due to high population growth, the development of various industrial activities and the excavation of oil deposits (Ayamdoo, 2016; Scheren et al., 2002). Therefore, studies analysing the influences of those processes are needed to find benchmarks against which we can assess the level of future changes and create baselines for further monitoring and environmental protection in this region. Such studies are especially important for scarcely studied regions and countries, such as the West African coast, which is highly influenced by the uncertain economic situation and have poorly developed environmental protection systems.

In this context, the aim of this study was to analyse distribution patterns and factors shaping benthic macrofauna communities along a 25—1000 m depth gradient off the Ghanaian coast of the Gulf of Guinea, including areas affected by oil excavation activities. The material was collected in the framework of the Oil for Development (OfD) program, supported by the Food and Agriculture Organization of the United Nations (FAO). This initiative offers assistance to developing countries in their efforts to manage petroleum resources in a sustainable manner and to develop environmental protection systems based on ecological studies.

2. Material and methods

2.1. Study area

The Gulf of Guinea is a large open bay on the Atlantic coast of West Africa between latitudes 5°N and 5°S and longitudes 8°W to 12°E (Ukwe et al., 2003), with a coastline of about 3000 km (Chukwuone et al., 2009). It is influenced by the Guinea Current, by the Benguela Current and by the South Equatorial Counter Current (Schneider, 1990; Ukwe et al., 2006). The area is characterised by the occurrence of oxygen minimum zones (Levin, 2003; Levin et al., 2009) as well as by dynamic sedimentation phenomena associated with coastal erosion (Ukwe et al., 2003). The coastal areas of Ghana are located in the atypical tropical climate region (Le Loeuff and Cosel, 1998) and characterised by high dynamics of water masses and upwellings (Djagoua et al., 2011). This part of the coastline contains no large river systems, except for the Volta River estuary, which is located in the eastern part of the coast. The Ghanaian coast stretches along a distance of 565 km.

2.2. Sampling

Material was collected in October and November of 2012 on nine transects distributed along the entire coast of Ghana, starting from New Town and ending near the Togo (Fig. 1). Samples were collected using a 0.1-m^2 van Veen grab supported with the VAMS (Video Assisted Monitoring System) allowing for appropriate sediment penetration. Each transect consisted of six stations: 25, 50, 100, 250, 500 and 1000 m. Five samples were collected at each station. The material was sieved through a 0.3-mm sieve and preserved in 4% formaldehyde solution. The methodology was consistent with the recommendations of the *Oil Spill Prevention, Administration and Response Fund* (OSPAR) guidelines (OSPAR, 2011).

2.3. Environmental data

Physical and chemical properties, including sediment structure, total organic matter (TOM) content in the sediments, level of hydrocarbons and various toxic metals, were analysed at each station. We also determined temperature, conductivity and oxygen level (Seabird 911 CTD Plus and SBE 21 Seacat thermosalinographs were used). Sediment grain size was determined by mixing the sediment with water and sieving it through a 0.063-mm sieve. Larger particles were then sieved through Endecott sieves; for calculation, the equations of Buchanan (1984) and Folk and Ward (1957) were used. Total organic matter was determined as the weight loss in a 2—3-g dried sample (dried at 105°C for 20 h) after 2 h of combustion at 480°C. Petroleum hydrocarbon content was determined using a gas chromatograph with a flame ionisation detector (GC/FID), as outlined in the Intergovernmental Oceanographic Commission, Manuals and Guides No. 11, UNESCO (1982). Metals (Ba, Cd, Cr, Cu, Pb, Zn, Hg) were analysed via Inductively Coupled Plasma-Atomic Emission Spectrometry (ICP-AES), except for mercury, which was determined via Cold Vapour Atomic Emission Spectrometry (CVAAS) after drying, sieving and digestion (Elezz et al., 2018; Jarvis and Jarvis, 1992).

2.4. Statistical analysis

To analyse trends in abundance along a depth gradient of the Ghanaian shelf, slope mean values of abundance with standard deviations (SD) were calculated for each station (25, 50, 100, 250, 500 and 1000 m) for the entire macrozoobenthos and for the most abundant taxonomic groups. Mean values were calculated separately for each transect and for the entire material. To determine statistically significant differences in macrozoobenthic abundance among depths, Kruskal—Wallis test was used. Post hoc testing was performed with the use of Dunn's test in the software package Statistica 6.

Multivariate analysis was performed in the Primer 7 package. Hierarchical agglomerative clustering analysis, based on the Bray—Curtis formula, was used to check faunistic

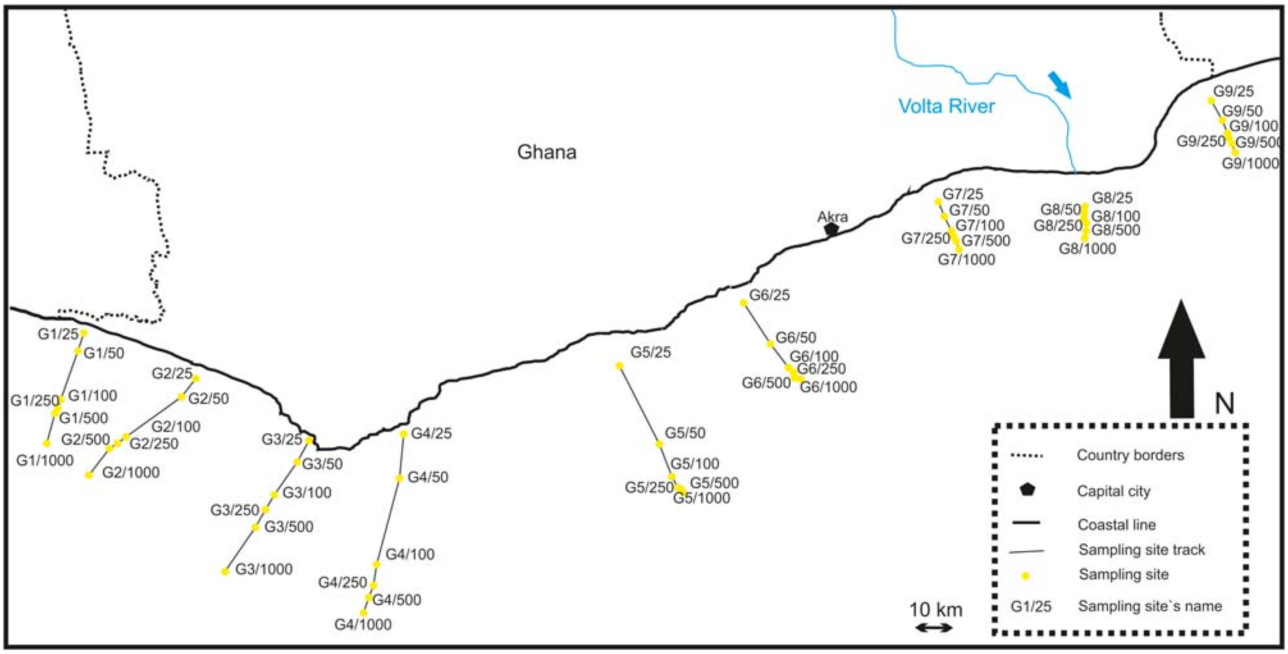

Figure 1 Distribution of sampling stations along the Ghanaian coast.

similarity among the samples. For the purpose of the cluster analysis, we used mean values of abundance calculated for each station; the analysis was based on higher taxa level. Data were square root-transformed, and the group average method was used. A SIMPROF test with 1% significance level was performed to check the multivariate structure within groups (Clarke and Gorley, 2015). Mean values of macrozoobenthos abundance and mean values of environmental variables with standard deviations were calculated for each group of stations (clusters). Frequency of occurrence (*F*, percentage of samples where a taxonomic group was found in the total number of samples) was calculated for each taxon in each cluster. We performed SIMPER analysis to determine the dissimilarity among groups separated by cluster analysis, using the R Studio environment (Clarke, 1993; Warton et al., 2012).

Canonical Correspondence Analysis (CCA) was performed in the R Studio (Legendre and Legendre, 2012; R Core Team, 2013) with the vegan package (Oksanen et al., 2019). For this, we used the Variance Inflation Factor (VIF) to determine which factors are significant in shaping biodiversity on each station (Fox, 2016; Fox and Monette, 1992). Subsequently, we removed factors with the highest VIF value and repeated the VIF analysis. Finally, nine factors remained in the analysis. Permutational Multivariate Analysis of Variance Using Distance Matrices (PERMANOVA) was performed for these nine factors to determine which were significant in the CCA. In addition, we calculated the Adjusted *R* Square (Zapala and Schork, 2006).

3. Results

Altogether, we found 28,754 individuals in the studied material; the fauna was dominated by polychaetes, bivalves and amphipods (Fig. 2).

The mean abundance of macrozoobenthos gradually decreased from shallow shelf areas (25 m: 231.4 ± 262.2 ind./0.1 m^2) down to bathyal depths (1000 m: 55.4 ± 51.4 ind./0.1 m^2) (Fig. 3). Statistically significant results were found between the shallowest (25—50 m) and the deepest stations (500—1000 m) (Kruskal—Wallis test, Dunn's test $p < 0.05$). On the other hand, general trends in abundance differed among the investigated transects (Fig. 4). On most of the transects, highest mean abundance was recorded on 25 m (five transects, including G3, G6—G9) or on 50 m (three transects G1, G2 and G5), while the lowest mean values were found on 1000 m (five transects: G4, G5, G 7—G9) or on 500 m (two transects, G2 and G6). Nevertheless, on transect G4, highest mean densities were observed on 500 m (125.6 ± 95.8 ind./0.1 m^2), while on transect G3, the lowest values were found on the lower shelf (250 m: 58.6 ± 23.3 ind./0.1 m^2). The highest mean values of macrozoobenthos abundance were recorded on transect G7 at the depth of 25 m (786.4 ± 466.0 ind./0.1 m^2). There were no statistically significant differences among the stations at five transects (G1—G4 and G8). Statistically significant results were found between the shallowest and the deepest stations on transects G5, G6, G7 and G9 (Kruskal—Wallis test, Dunn's test, $p < 0.05$).

General trends in abundance differed strongly among the various taxonomic groups. For example, polychaetes followed the general pattern observed for the entire macrofauna, with the highest abundance observed in the shallowest areas and a gradual decrease along the depth gradient. Amphipods were most abundant at 25 m (34.6 ± 43.7 ind./0.1 m^2) and 50 m, but their density sharply decreased at 100 m (Table 1). Nevertheless, the values of the abundance of particular taxonomic groups differed among the transects. The abundance of bivalves, polychaetes and amphipods varied among the transects, with highest densities observed on various depths, depending on the transect. The highest abundance of fauna, including exceptionally high polychaete densities (292.2 ± 279.4 ind./0.1 m^2 at station 25 m), was found on transect G7, while the lowest abundance values were found on transect G9, especially on the deepest stations (Table 2). Total organic matter content increased with depth on most of the transects. Oxygen depletion was recorded at 250-m stations. On most of the transects, the concentrations of barium and hydrocarbons were highest at 500 and 1000 m (Fig. 5). We also

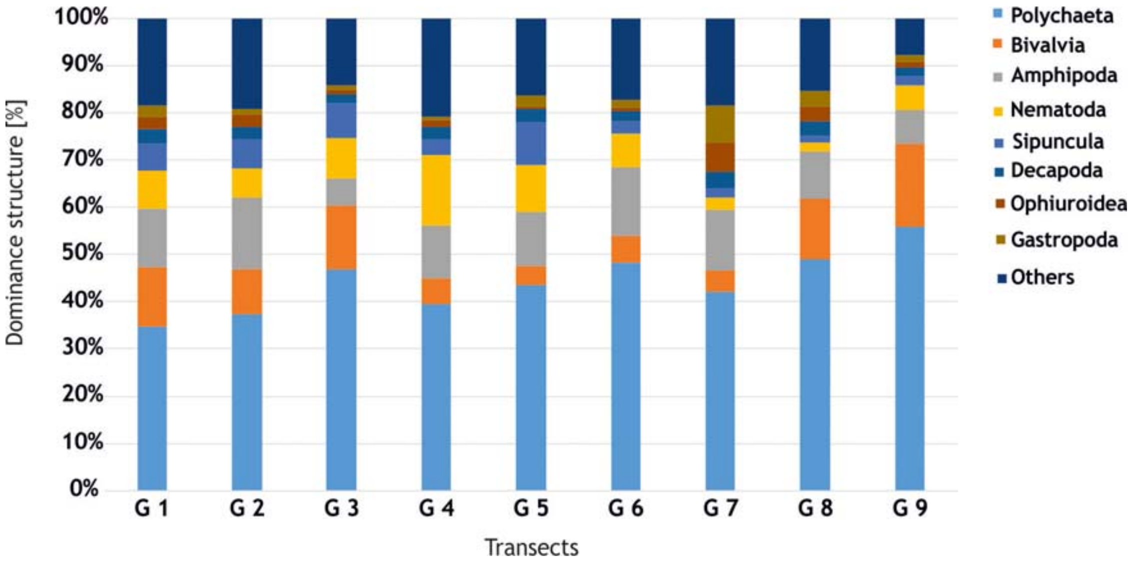

Figure 2 Dominance structure of macrozoobenthos at each of the depths.

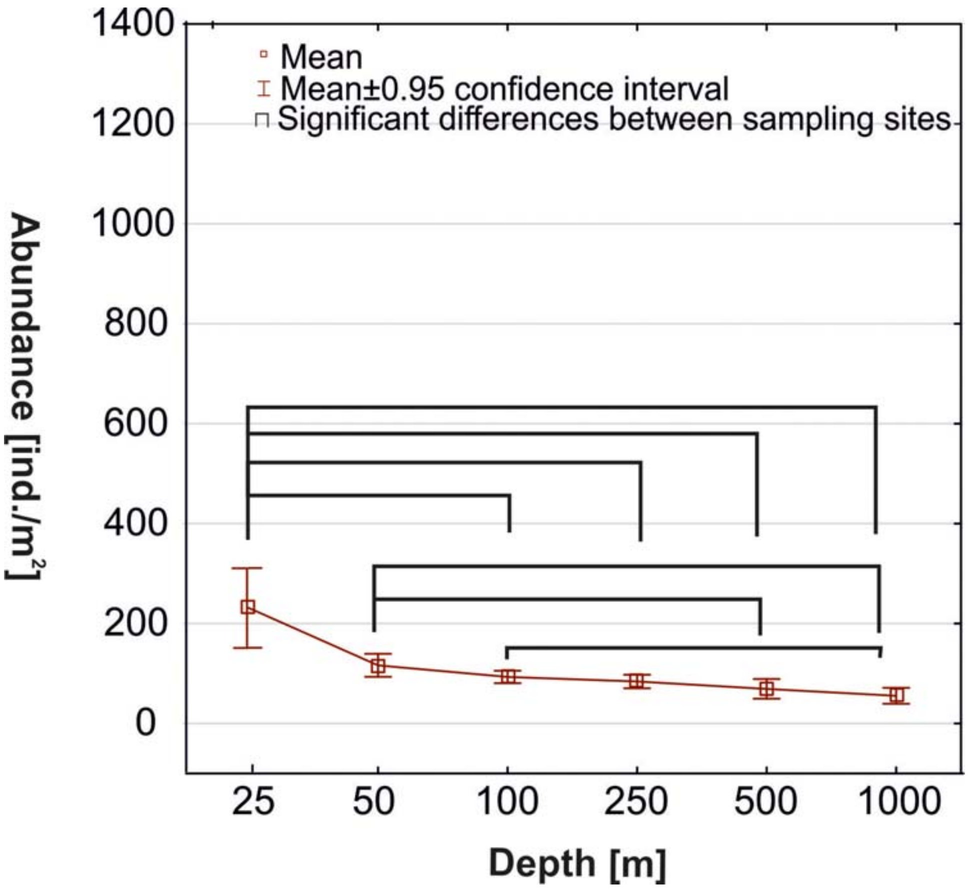

Figure 3 Mean densities at each of the studied depths (data from all transects analysed together).

noticed sediment changes with depth. Shallower shelf stations were characterised by sandy sediments, while on the slope, silt and clay fractions dominated (Table 3).

Five groups of stations were distinguished in the cluster analysis (Fig. 6). All groups were created at high levels of similarity (more than 50%) and significantly differentiated in SIMPROF analysis. The first two clusters grouped the stations characterised by higher levels of disturbance (e.g. higher contents of barium and THC), while clusters 3—5 grouped less disturbed or undisturbed stations. **Cluster 1** consisted of six samples representing various depths (from 50 to 1000 m). This group was characterised by generally low densities of macrozoobenthos (28.2 ± 12.5 ind./0.1 m^2). Stations were dominated only by polychaetes (15.6 ± 6.6 ind./0.1 m^2) and bivalves (3.8 ± 4.0 ind./0.1 m^2) (Table 4). Only 22 taxonomic groups were found in the samples from this group, and all stations from this cluster were characterised by high levels of barium, chromium, copper and THC as well as high levels of organic matter (Table 5). **Cluster 2** grouped the stations from a depth of 100 to 500 m. The macrofauna was dominated by polychaetes (25.4 ± 2.2 ind./0.1 m^2), with a high frequency of occurrence of some other taxonomic groups including nematodes, isopods, bivalves and amphipods (Table 4). Only 26 taxonomic groups were found in samples from this group. Generally, it was characterised by a low total macrozoobenthos abundance (65.9 ± 12.8 ind./0.1 m^2) and by high levels of barium, copper and nickel, as well as by silt and clay bottom deposits. **Cluster 3** grouped five shallow-water stations (25—50 m depth range) dominated by polychaetes (28.3 ± 7.9 ind./0.1 m^2) and amphipods (29.1 ± 17.1 ind./0.1 m^2), with 28 taxonomic groups across recorded. The total macrozoobenthos densities were considerably higher than in the previous two clusters (105.12 ± 32.8 ind./0.1 m^2). This area was characterised by lower contents of toxic metals and THC (Table 5). **Cluster 4** grouped 26 samples representing various depths from 50 to 1000 m, dominated by polychaetes (42.6 ± 12.7 ind./0.1 m^2) followed by bivalves, nematodes and amphipods (Table 4); in total, 40 taxonomic groups were found in samples from this group. Mean densities of macrozoobenthos equalled 92.7 ± 26.0 ind./0.1 m^2, and the stations were characterised by low levels of toxic metals and THC as well as by fine sand bottom deposits. **Cluster 5** grouped mostly shallow-water samples collected at 25 and 50 m (one sample from 250 m). It showed the highest mean densities of macrozoobenthos (185.1 ± 71.5 ind./0.1 m^2). The bottom fauna was dominated by polychaetes and characterised by a high diversity of taxa, with 42 taxonomic groups. Stations from this cluster were characterised by the lowest levels of barium, chromium, nickel and THC (Table 5).

Based on the results of the SIMPER analysis, polychaetes and amphipods contributed most significantly to within-group similarity (Table 6).

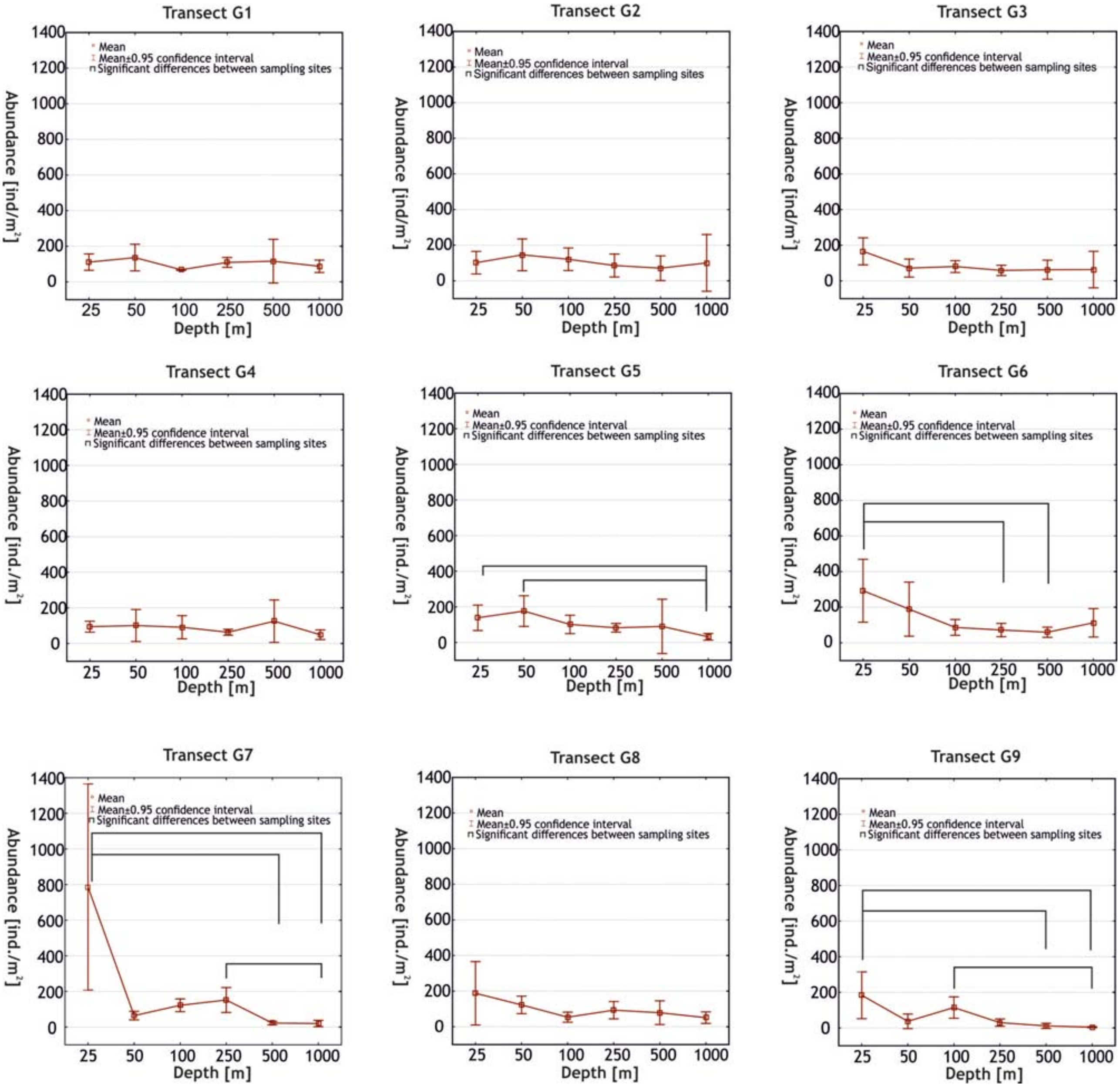

Figure 4 Mean densities at each of the studied depths on each of the transects.

The CCA demonstrated that PAH, THC, metal levels (Ba, Cd, Pb) and oxygen concentration plays a significant role in shaping biodiversity on the Ghanaian coast (Fig. 7). All these factors were statistically significant, and the VIF values were $<$10.0 (Table 7). The CCA represented 58% of all data from our analysis (Adj. $R^2 = 0.4114759$). The coefficient of determination of the CCA for this dataset is 0.5835628.

4. Discussion

The depth-related decrease in macrozoobenthos abundance was consistent with the general pattern observed for the deep-sea (Rex et al., 2006) and can be explained by the substantial decrease in nutrient supply in bathyal and abyssal depths as well as the distance from productive coastal waters (Carney, 2005; Nephin et al., 2014; Rex et al., 2006). At the same time, on the coast of Ghana, the highest TOM values were recorded for the deepest areas, and on most of the transects, the level of TOM increased along the depth gradient. In his study of the meiofauna of the West African coast, Soltwedel (1997) found areas characterised by high organic matter contents and low fauna densities, suggesting that the lighter fraction of organic matter, transported over longer distances with subsurface currents, probably does not have the same energy content. Discussions about the quality of detritus along a depth gradient pose the question about a meaningful assessment of poor- and high-quality detritus (Carney, 2005), although there are studies showing different levels of organic matter bioavailability in the deep-sea

Table 1 Mean and maximum density values [ind./0.1 m^2] with standard deviation (SD) on each of the depths (only most abundant taxa, data from all transects analysed together). The highest values are marked in bold.

Taxonomic group	25 m		50 m		100 m		250 m		500 m		1000 m	
	Mean ± SD	Max	Mean ± SD	Max	Mean ± SD	Max	Mean ± SD	Max	Mean ± SD	Max	Mean ± SD	Max
Polychaeta	**94.9 ± 131**	674	**41.6 ± 41.8**	161	**49.1 ± 21.2**	99	**46.6 ± 32.3**	123	**28.6 ± 24.9**	97	**24.7 ± 25.3**	115
Amphipoda	**34.6 ± 43.7**	189	**25.2 ± 23.3.**	91	7.1 ± 6.2	25	4.3 ± 4.4	81	2.2 ± 2.8	10	3.0 ± 3.5	15
Bivalvia	**22.7 ± 27.5**	154	**10.3 ± 19.2**	113	8.6 ± 13.7	53	7.4 ± 14	81	6.8 ± 11.5	51	2.0 ± 3.1	13
Nematoda	9.0 ± 11.4	41	5.9 ± 8.6	35	7.4 ± 10.2	45	4.6 ± 9.1	48	**10.3 ± 20.0**	91	6.5 ± 8.8	38
Sipuncula	5.4 ± 6.9	33	2.2 ± 2.5	9	4.2 ± 3.7	14	9.1 ± 11.1	46	6.1 ± 9.9	58	0.9 ± 1.8	9
Gastropoda	**13.5 ± 50.9**	329	2.5 ± 2.7	12	0.8 ± 1.9	9	1.2 ± 4.5	29	0.6 ± 1.1	4	0.3 ± 0.6	2
Tanaidacea	5.9 ± 18.7	90	4.5 ± 6.7	22	0.8 ± 1.6	7	0.6 ± 1.5	9	2.7 ± 4.9	29	4.0 ± 6.4	30
Decapoda	7.4 ± 9.8	40	5.1 ± 4.8	19	3.3 ± 3.4	13	1.5 ± 1.3	8	0.8 ± 1.3	6	0.1 ± 0.4	2
Ophiuroidea	8.5 ± 20.3	92	4.6 ± 4.2	22	0.9 ± 1.2	5	1.2 ± 1.7	8	0.3 ± 1.0	6	0.1 ± 0.4	2
Isopoda	5.0 ± 10	48	1.8 ± 2.2	9	1.0 ± 1.4	6	0.2 ± 0.7	18	1.8 ± 2.3	8	4.4 ± 5.2	18
Cumacea	2.3 ± 4	19	2.6 ± 3.2	12	1.5 ± 2.2	10	2.2 ± 2.8	12	1.2 ± 2.0	11	1.0 ± 1.4	6
Nemertea	2.7 ± 2.7	10	1.9 ± 1.7	6	1.2 ± 1.5	6	0.7 ± 1.1	4	0.4 ± 0.9	4	0.9 ± 1.3	6

Table 2 Mean and maximum density values [ind./0.1 m^2] with standard deviation (SD) on each of the transects (only most abundant taxa). The highest values are marked in bold.

	25 m		50 m		100 m		250 m		500 m		1000 m	
	Mean ± SD	Max	Mean ± SD	Max	Mean ± SD	Max	Mean ± SD	Max	Mean ± SD	Max	Mean ± SD	Max
G1												
Polychaeta	**34.6 ± 15.5**	59	**49.2 ± 28.3**	79	**32.2 ± 8.3**	41	**36.8 ± 21.7**	68	**54.8 ± 34.2**	97	**25.6 ± 16.2**	41
Amphipoda	**18.2 ± 6.8**	25	**42.2 ± 15.6**	66	5.4 ± 4.0	12	5.2 ± 3.3	11	6.3 ± 3.5	10	**7.6 ± 4.6**	15
Bivalvia	**27.8 ± 21.0**	60	3.2 ± 2.4	6	2.8 ± 4.1	9	**30.6 ± 32.3**	81	**9.5 ± 6.0**	18	5.2 ± 4.8	13
Nematoda	**7.2 ± 5.4**	14	6 ± 6.7	17	**8.6 ± 6.1**	17	3.4 ± 4.8	10	**19.0 ± 21.7**	42	**12.6 ± 4.8**	20
Sipuncula	5.8 ± 4.4	12	5.4 ± 2.4	8	5.2 ± 2.6	8	**13.8 ± 13.4**	31	**7.0 ± 5.4**	15	0.8 ± 0.8	2
Gastropoda	4.4 ± 4.8	12	3.0 ± 2.1	5	0.2 ± 0.4	1	**7.4 ± 12.6**	29	1.0 ± 0.8	2	0.4 ± 0.5	1
Tanaidacea	0.6 ± 0.9	2	4.6 ± 2.6	8	1.0 ± 2.2	5	—	—	1.3 ± 2.5	5	3.2 ± 4.1	9
Decapoda	3.6 ± 4.5	11	**10.8 ± 4.5**	18	4.0 ± 1.9	6	2.2 ± 1.9	5	0.5 ± 1.0	2	—	—
Ophiuroidea	1.4 ± 1.5	3	**11.4 ± 8.6**	21	1.2 ± 1.3	3	1.4 ± 1.5	3	—	—	—	—
Isopoda	0.8 ± 0.8	2	0.8 ± 0.8	2	0.4 ± 0.9	2	0.2 ± 0.4	1	1.3 ± 1.9	4	**13.8 ± 3.3**	18
Cumacea	3.4 ± 3.8	8	3.0 ± 2.7	7	1.6 ± 2.6	6	2.4 ± 2.2	6	2.3 ± 2.1	4	2.4 ± 1.5	4
Nemertea	5.2 ± 3.3	10	1.4 ± 1.1	3	0.6 ± 0.9	2	—	—	1.3 ± 1.0	2	1.0 ± 1.0	2
G2												
Polychaeta	**42.4 ± 14.9**	61	**28.6 ± 25.1**	56	**45.8 ± 8.3**	84	**43.8 ± 44.2**	112	**23.6 ± 14.3**	42	**56.8 ± 54.5**	115
Amphipoda	**16.8 ± 11.8**	37	**56.0 ± 33.7**	91	**11.2 ± 4.0**	25	5.8 ± 7.0	17	3.2 ± 4.1	10	2.0 ± 2.4	5

Table 2 (*Continued*)

	25 m		50 m		100 m		250 m		500 m		1000 m	
	Mean ± SD	Max	Mean ± SD	Max	Mean ± SD	Max	Mean ± SD	Max	Mean ± SD	Max	Mean ± SD	Max
Bivalvia	**22.4 ± 40.1**	94	4.2 ± 2.7	8	**10.8 ± 4.1**	27	**8.8 ± 11.6**	29	**7.6 ± 8.4**	22	4.8 ± 5.9	12
Nematoda	0.8 ± 1.8	4	5.2 ± 6.3	16	**17.4 ± 6.1**	45	4.8 ± 5.0	12	4.8 ± 6.0	15	3.5 ± 3.0	6
Sipuncula	2.8 ± 2.8	7	3.2 ± 2.8	6	**9.0 ± 2.6**	12	**11.6 ± 13.0**	32	**10.4 ± 4.8**	16	2.5 ± 4.4	9
Gastropoda	0.4 ± 0.5	1	1.2 ± 1.6	4	4.4 ± 0.4	9	0.2 ± 0.4	1	0.8 ± 1.8	4	0.3 ± 0.5	1
Tanaidacea	0.6 ± 1.3	3	5.4 ± 4.5	12	3.2 ± 2.2	7	2.0 ± 3.9	9	**7.0 ± 12.4**	29	0.5 ± 0.6	1
Decapoda	3.8 ± 3.1	7	6.8 ± 5.4	15	4.2 ± 1.9	13	1.4 ± 1.1	3	0.2 ± 0.4	1	–	–
Ophiuroidea	2.0 ± 2.1	5	**12.8 ± 7.1**	22	0.6 ± 1.3	2	1.0 ± 0.7	2	–	–	0.5 ± 0.6	1
Isopoda	0.2 ± 0.4	1	2.2 ± 1.8	5	1.0 ± 0.9	2	0.2 ± 0.4	1	2.8 ± 3.0	8	1.8 ± 2.2	5
Cumacea	0.4 ± 0.9	2	3.8 ± 4.0	9	1.2 ± 2.6	4	1.8 ± 1.1	3	0.6 ± 0.9	2	0.5 ± 1.0	2
Nemertea	1.2 ± 1.6	4	1.6 ± 1.1	3	2.0 ± 0.9	5	0.2 ± 0.4	1	–	–	2.3 ± 2.6	6
G3												
Polychaeta	**57.6 ± 51.4**	126	**39.8 ± 35.4**	94	**47.2 ± 9.2**	59	**41.4 ± 17.8**	64	**25.6 ± 13.1**	42	**21.5 ± 26.0**	59
Amphipoda	4.6 ± 4.8	12	7.2 ± 6.9	19	**7.6 ± 4.3**	13	4.6 ± 5.4	13	1.6 ± 1.5	3	4.0 ± 3.7	8
Bivalvia	**56.0 ± 58.9**	154	6.0 ± 3.3	9	1.2 ± 0.8	2	1.2 ± 1.3	3	1.4 ± 2.2	5	1.3 ± 1.5	3
Nematoda	8.8 ± 8.3	18	4.2 ± 5.6	14	2.4 ± 5.4	12	2.8 ± 5.2	12	**15.6 ± 20.2**	41	**10.5 ± 10.8**	24
Sipuncula	**16.0 ± 11.7**	33	2.0 ± 2.0	5	2.8 ± 1.5	5	2.8 ± 1.3	4	**11.2 ± 6.2**	19	2.8 ± 2.8	6
Gastropoda	1.4 ± 1.1	3	2.8 ± 1.6	5	0.6 ± 0.5	1	0.2 ± 0.4	1	0.4 ± 0.5	1	–	–
Tanaidacea	–	–	1.6 ± 3.0	7	1.6 ± 1.1	3	0.4 ± 0.5	1	1.4 ± 1.5	3	4.0 ± 4.3	10
Decapoda	3.2 ± 2.3	7	1.0 ± 1.2	3	3.4 ± 5.3	12	1.0 ± 1.4	3	1.0 ± 1.2	3	0.3 ± 0.5	1
Ophiuroidea	1.8 ± 1.6	3	1.2 ± 1.6	4	1.0 ± 1.0	2	0.2 ± 0.4	1	–	–	0.5 ± 1.0	2
Isopoda	1.2 ± 0.8	2	0.2 ± 0.4	1	2.0 ± 2.3	5	0.4 ± 0.5	1	1.6 ± 3.6	8	**6.8 ± 6.7**	16
Cumacea	0.8 ± 1.1	2	1.2 ± 1.3	3	1.8 ± 2.5	6	1.4 ± 2.2	5	0.6 ± 1.3	3	1.0 ± 1.4	3
Nemertea	4.6 ± 2.6	7	0.8 ± 1.3	3	2.0 ± 1.9	5	0.6 ± 1.3	3	–	–	1.3 ± 1.5	3
G4												
Polychaeta	**22.4 ± 20.6**	45	**34.8 ± 27.1**	74	**46.8 ± 19.3**	77	**29.6 ± 12.5**	42	**57.6 ± 24.8**	79	**13.6 ± 5.7**	22
Amphipoda	**17.6 ± 24.3**	61	**21.2 ± 16.6**	40	**8.8 ± 9.0**	22	5.6 ± 4.2	12	0.6 ± 0.5	1	3.4 ± 2.2	7
Bivalvia	**13.0 ± 5.7**	22	4.6 ± 5.4	13	3.6 ± 3.8	9	4.4 ± 3.0	7	2.0 ± 1.6	4	1.2 ± 1.3	3
Nematoda	**9.0 ± 9.2**	24	5.0 ± 4.7	10	**16.6 ± 12.9**	30	3.6 ± 3.2	8	**38.8 ± 41.5**	91	4.8 ± 5.8	12
Sipuncula	4.8 ± 3.7	9	3.2 ± 3.5	9	4.6 ± 5.5	14	3.8 ± 3.2	8	–	–	0.8 ± 0.8	2
Gastropoda	0.6 ± 0.9	2	2.0 ± 2.1	5	–	–	0.4 ± 0.5	1	–	–	0.4 ± 0.9	2
Tanaidacea	1.2 ± 1.6	4	**9.0 ± 8.2**	18	0.2 ± 0.4	1	1.2 ± 0.4	2	1.8 ± 1.3	4	**13.2 ± 9.9**	30
Decapoda	3.6 ± 3.6	8	3.6 ± 2.4	7	2.2 ± 2.9	7	1.6 ± 0.9	3	2.4 ± 2.5	6	–	–
Ophiuroidea	3.8 ± 2.6	7	1.4 ± 1.1	3	0.2 ± 0.4	1	2.6 ± 3.1	8	–	–	–	–
Isopoda	1.6 ± 2.1	5	2.2 ± 2.2	5	–	–	–	–	0.4 ± 0.5	1	3.8 ± 2.3	7
Cumacea	1.0 ± 1.7	4	4.4 ± 4.3	9	1.2 ± 1.3	3	5.2 ± 3.1	8	0.4 ± 0.9	2	1.0 ± 1.0	2
Nemertea	–	–	1.0 ± 1.2	3	0.2 ± 0.4	1	0.2 ± 0.4	1	0.4 ± 0.9	2	0.8 ± 1.3	3
G5												
Polychaeta	**47.2 ± 41.5**	112	**71.0 ± 65.0**	138	**58.2 ± 27.8**	90	**37.4 ± 18.7**	51	**37.5 ± 34.0**	85	**19.0 ± 6.6**	25
Amphipoda	**16.6 ± 5.0**	22	**40.2 ± 11.8**	59	**8.0 ± 4.6**	13	3.2 ± 2.9	8	1.5 ± 2.4	5	3.2 ± 4.0	10

Table 2 (*Continued*)

	25 m		50 m		100 m		250 m		500 m		1000 m	
	Mean ± SD	Max	Mean ± SD	Max	Mean ± SD	Max	Mean ± SD	Max	Mean ± SD	Max	Mean ± SD	Max
Bivalvia	**13.0 ± 4.9**	20	6.0 ± 3.7	10	2.4 ± 1.9	5	0.6 ± 0.9	2	1.5 ± 1.0	2	1.0 ± 0.7	2
Nematoda	**22.6 ± 16.8**	38	**13.8 ± 11.7**	33	**10.8 ± 11.3**	23	1.8 ± 2.0	5	5.8 ± 9.5	20	1.6 ± 1.7	4
Sipuncula	1.6 ± 3.0	7	2.2 ± 1.3	4	4.4 ± 3.5	9	**30.2 ± 9.6**	46	**22.0 ± 24.4**	58	–	–
Gastropoda	**10.4 ± 22.7**	51	3.0 ± 2.5	7	0.2 ± 0.4	1	–	–	1.5 ± 1.7	4	0.4 ± 0.5	1
Tanaidacea	0.4 ± 0.5	1	**10.8 ± 9.4**	22	1.0 ± 1.0	2	0.2 ± 0.4	1	2.5 ± 4.4	9	2.0 ± 2.8	6
Decapoda	4.2 ± 1.6	6	6.6 ± 8	19	4.2 ± 3.2	9	1.2 ± 1.3	3	1.0 ± 2.0	4	–	–
Ophiuroidea	0.8 ± 0.8	2	1.8 ± 3.5	8	1.2 ± 2.2	5	–	–	0.3 ± 0.5	1	–	–
Isopoda	2.0 ± 0.7	3	2.4 ± 2.7	7	1.0 ± 1.2	3	–	–	2.3 ± 3.3	7	2.6 ± 1.8	5
Cumacea	1.8 ± 1.5	4	2.4 ± 2.9	6	1.0 ± 1.7	4	4.2 ± 1.3	6	1.3 ± 1.0	2	0.4 ± 0.9	2
Nemertea	2.2 ± 1.5	4	2.0 ± 2.0	5	0.8 ± 0.4	1	0.6 ± 1.3	3	1.0 ± 1.4	3	0.2 ± 0.4	1
G6												
Polychaeta	**139.2 ± 133.1**	286	**77.6 ± 78.8**	161	**59.0 ± 26.9**	99	**38.6 ± 19.0**	66	**22.2 ± 16.5**	48	**54.8 ± 20.7**	77
Amphipoda	**60.2 ± 14.1**	71	**35.4 ± 18.6**	58	5.0 ± 3.4	9	**8.4 ± 5.8**	18	1.2 ± 0.4	2	6.0 ± 2.6	9
Bivalvia	**22.6 ± 18.0**	46	**12.0 ± 12.6**	32	1.8 ± 1.9	5	4.2 ± 2.3	8	3.2 ± 2.6	7	3.3 ± 3.4	8
Nematoda	6.6 ± 4.4	12	**16.2 ± 14.5**	35	4.8 ± 8.2	19	1.2 ± 1.3	3	**9.0 ± 6.9**	18	**23.8 ± 11.4**	38
Sipuncula	2.0 ± 2.1	5	1.6 ± 2.5	6	3.4 ± 4.1	10	6.6 ± 3.9	13	5.8 ± 5.8	12	0.3 ± 0.5	1
Gastropoda	8.2 ± 17.2	39	3.2 ± 5.0	12	0.2 ± 0.4	1	1.2 ± 1.1	2	0.4 ± 0.9	2	0.5 ± 1.0	2
Tanaidacea	1.0 ± 1.0	2	7.2 ± 9.1	19	0.4 ± 0.9	2	–	–	3.6 ± 3.5	8	2.8 ± 4.9	10
Decapoda	9.0 ± 5.8	18	3.2 ± 2.9	7	1.6 ± 1.5	4	1.4 ± 1.1	3	1.4 ± 0.9	2	0.8 ± 1.0	2
Ophiuroidea	1.6 ± 1.5	3	2.6 ± 2.7	7	0.8 ± 1.1	2	0.4 ± 0.9	2	–	–	–	–
Isopoda	7.2 ± 3.8	12	4.6 ± 3.4	9	0.8 ± 0.8	2	0.8 ± 1.8	4	4.0 ± 2.3	7	**7.8 ± 6.8**	17
Cumacea	9.2 ± 7.2	19	6.4 ± 4.6	12	1.0 ± 2.2	5	3.0 ± 5.1	12	1.0 ± 1.0	2	1.8 ± 1.0	3
Nemertea	3.0 ± 4.1	8	3.0 ± 2.1	6	0.6 ± 1.3	3	1.0 ± 1.2	3	1.2 ± 1.6	4	2.0 ± 1.8	4
G7												
Polychaeta	**292.2 ± 279.4**	674	**18.6 ± 16.6**	36	**63.0 ± 23.2**	91	**95.4 ± 26.2**	123	**12.0 ± 2.0**	14	**12.0 ± 5.9**	20
Amphipoda	**126.8 ± 64.0**	189	**14.8 ± 13.6**	37	6.4 ± 4.4	13	2.0 ± 1.4	4	0.4 ± 0.9	2	0.6 ± 0.5	1
Bivalvia	**17.0 ± 13.9**	31	6.4 ± 4.1	10	**22.8 ± 16.3**	49	4.0 ± 5.8	14	3.0 ± 2.2	7	0.6 ± 0.5	1
Nematoda	4.6 ± 4.5	9	0.2 ± 0.4	1	1.4 ± 2.2	5	**23.0 ± 17.2**	48	0.2 ± 0.4	1	0.2 ± 0.4	1
Sipuncula	6.4 ± 5.0	15	0.2 ± 0.4	1	4.8 ± 2.4	8	**8.6 ± 5.9**	16	1.4 ± 1.9	4	0.2 ± 0.4	1
Gastropoda	**90.8 ± 135.9**	329	1.8 ± 1.1	3	0.2 ± 0.4	1	0.6 ± 0.9	2	0.2 ± 0.4	1	–	–
Tanaidacea	**48.0 ± 35.2**	90	0.6 ± 0.9	2	–	–	1.6 ± 1.1	3	1.4 ± 1.1	3	2.4 ± 3.8	9
Decapoda	**30.8 ± 11.3**	40	4.6 ± 3.8	9	6.2 ± 3.5	8	2.6 ± 1.3	4	0.2 ± 0.4	1	–	–
Ophiuroidea	**59.6 ± 26.8**	92	6.0 ± 5.3	15	1.4 ± 1.1	3	2.4 ± 2.2	6	0.6 ± 0.9	2	–	–
Isopoda	**28.2 ± 15.8**	48	1.6 ± 1.8	4	0.8 ± 1.3	3	0.2 ± 0.4	1	1.6 ± 1.8	4	1.4 ± 1.1	3
Cumacea	0.8 ± 1.8	4	1.0 ± 1.0	2	4.0 ± 3.8	10	1.4 ± 2.2	5	0.8 ± 0.8	2	1.2 ± 2.7	6
Nemertea	2.0 ± 1.6	4	1.2 ± 1.6	4	0.8 ± 0.8	2	1.2 ± 1.3	3	–	–	0.6 ± 0.5	1
G8												
Polychaeta	**107.0 ± 83.8**	200	**39.0 ± 22.4**	61	**37.4 ± 16.7**	56	**75.4 ± 34.3**	116	**23.4 ± 25**	67	**28.2 ± 12.9**	45
Amphipoda	**36.5 ± 31.1**	79	7.2 ± 6.1	17	0.8 ± 1.3	3	2.4 ± 1.7	5	5.2 ± 2.9	9	0.8 ± 0.8	2

Table 2 (*Continued*)

	25 m		50 m		100 m		250 m		500 m		1000 m	
	Mean ± SD	Max	Mean ± SD	Max	Mean ± SD	Max	Mean ± SD	Max	Mean ± SD	Max	Mean ± SD	Max
Bivalvia	**11.0 ± 8.3**	20	**40.2 ± 46.3**	113	0.4 ± 0.5	1	4.4 ± 4.2	10	**31.6 ± 18.1**	51	1.2 ± 1.3	3
Nematoda	2.8 ± 3.0	7	2.6 ± 2.6	6	1.8 ± 0.8	3	0.2 ± 0.4	1	0.2 ± 0.4	1	5.2 ± 5.4	14
Sipuncula	7.5 ± 10.5	23	1.6 ± 1.5	4	–	–	0.2 ± 0.4	1	0.4 ± 0.5	1	1.0 ± 1.7	4
Gastropoda	0.8 ± 0.5	1	3.8 ± 3.3	9	0.4 ± 0.5	1	0.4 ± 0.5	1	1.0 ± 1.7	4	0.6 ± 0.5	1
Tanaidacea	0.3 ± 0.5	1	0.6 ± 0.9	2	–	–	0.2 ± 0.4	1	4.6 ± 4.4	11	6.8 ± 9.6	23
Decapoda	4.8 ± 2.5	8	7.4 ± 4.3	11	2.2 ± 2.0	4	1.8 ± 0.4	2	0.2 ± 0.4	1	–	–
Ophiuroidea	3.3 ± 2.5	6	4.6 ± 5.7	13	0.8 ± 0.4	1	0.4 ± 0.9	2	1.4 ± 2.6	6	–	–
Isopoda	1.8 ± 3.5	7	1.4 ± 1.5	3	0.2 ± 0.4	1	–	–	1.8 ± 1.6	4	2.6 ± 1.8	5
Cumacea	2.3 ± 4.5	9	0.4 ± 0.5	1	–	–	–	–	3.8 ± 4.5	11	0.2 ± 0.4	1
Nemertea	3.0 ± 0.0	3	4.2 ± 1.1	5	2.6 ± 2.2	6	2.0 ± 1.4	4	0.4 ± 0.9	2	0.6 ± 0.9	2
G9												
Polychaeta	**113.8 ± 86.3**	247	**16.0 ± 8.4**	27	**52.0 ± 21.8**	76	14.5 ± 3.9	18	**8.0 ± 8.1**	21	3.0 ± 1.6	5
Amphipoda	14.2 ± 9.5	24	2.4 ± 3.4	8	**10.4 ± 7.8**	20	0.5 ± 0.6	1	0.6 ± 0.9	2	–	–
Bivalvia	**19.0 ± 12.3**	35	**9.8 ± 17.5**	41	**31.2 ± 19.4**	53	**8.5 ± 7.4**	18	0.6 ± 0.5	1	0.2 ± 0.4	1
Nematoda	**17.0 ± 20.2**	41	–	–	3.0 ± 4.5	11	–	–	–	–	–	–
Sipuncula	1.8 ± 1.5	4	–	–	3.4 ± 3.1	8	2.8 ± 2.5	6	–	–	–	–
Gastropoda	2.0 ± 2.9	7	1.6 ± 3.6	8	1.2 ± 1.6	4	0.5 ± 1	2	0.4 ± 0.5	1	–	–
Tanaidacea	–	–	0.6 ± 0.9	2	0.2 ± 0.4	1	–	–	–	–	0.2 ± 0.4	1
Decapoda	3.2 ± 3.1	7	2.0 ± 1.6	4	1.8 ± 1.5	4	–	–	–	–	0.2 ± 0.4	1
Ophiuroidea	1.0 ± 1.7	4	–	–	1.0 ± 1.7	4	2.5 ± 1.3	4	0.6 ± 0.9	2	0.2 ± 0.4	1
Isopoda	1.0 ± 0.9	2	0.4 ± 0.5	1	2.4 ± 2.3	6	0.25 ± 0.5	1	0.4 ± 0.5	1	–	–
Cumacea	1.4 ± 2.2	5	0.6 ± 0.9	2	1.8 ± 1.3	3	–	–	0.2 ± 0.4	1	0.4 ± 0.9	2
Nemertea	3.4 ± 3.0	8	2.0 ± 1.6	4	1.2 ± 1.6	3	–	–	–	–	–	–

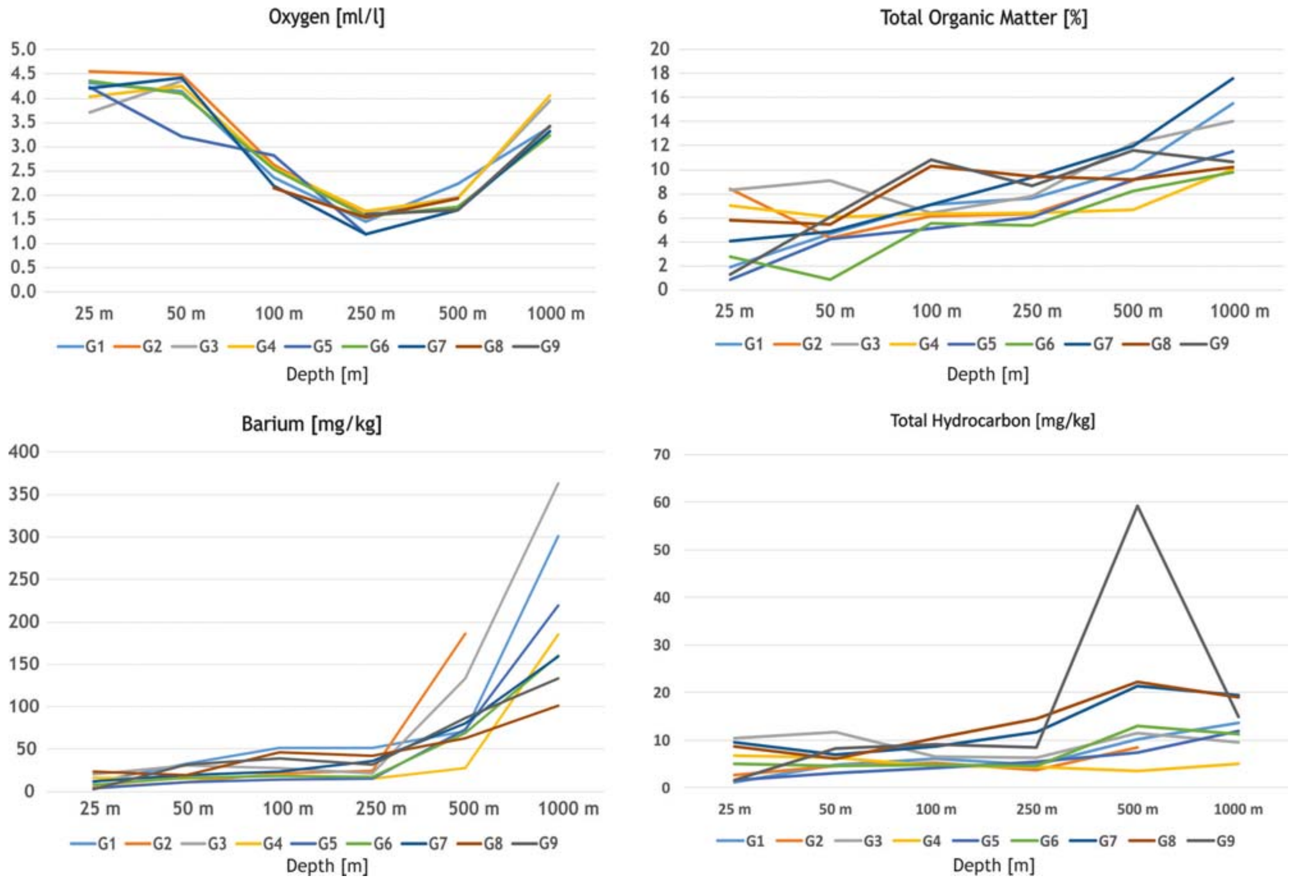

Figure 5 Concentrations of total organic matter, oxygen, barium and hydrocarbons on each of the studied transects.

Table 3 Characteristics of bottom deposits along a depth gradient on each of the transects.

	25 m	50 m	100 m	250 m	500 m	1000 m
G1	Fine sand	Very Fine sand	Very Fine sand	Fine sand	Silt clay	Silt clay
G2	Silt clay	Very Fine sand	Very Fine sand	Medium sand	Silt clay	—
G3	Silt clay	Silt clay	Very fine sand	Very fine sand	Silt clay	Silt clay
G4	Silt clay	Silt clay	Very fine sand	Very fine sand	Very fine sand	Silt clay
G5	Coarse sand	Fine sand	Very fine sand	Very fine sand	Silt clay	Silt clay
G6	Silt clay	Very fine sand	Fine sand	Fine sand	Silt clay	Silt clay
G7	Coarse sand	Very fine sand	Silt clay	Silt clay	Silt clay	Silt clay
G8	Medium sand	Silt clay	Silt clay	Silt clay	Silt clay	Silt clay
G9	Coarse sand	Fine sand	Silt clay	Silt clay	Silt clay	Silt clay

sediments (Dell'Anno et al., 2013). Moreover, deposit feeders associated with different depth zones might exploit different components of detritus (Carney, 2005). However, such functional analysis of the macrofauna is impossible on a higher taxa level. On the other hand, the highest values of polychaete and amphipod densities, observed at the 25-m station on transect G7, corresponded with the highest values of TOM observed for this depth at any of the transects, confirming the importance of TOM for macrofauna in the shallow shelf sites. The relationships between organic matter and the abundance of benthic communities might also be altered by the presence of oxygen minimum zones occurring in this region (Levin et al., 2009), although the lowest oxygen levels in our study were found between 250 and 500 m. Nevertheless, the highest values were recorded in the 25—50-m stations, which strongly corresponded with the areas of highest macrozoobenthos densities. Moreover, values below 0.5 ml/l (true oxygen minimum zone) (Levin, 2003) never occurred in our study. Nevertheless, it is also worth mentioning that the abundance of macrozoobenthos in the oxygen minimum zones might be relatively high. For example, in a study from northern Namibia, macrozoobenthos densities varied between 300 and 3350 ind./m^2 (Zettler et al., 2009) and were comparable to the highest values recorded on Ghana's coast, although the Namibian coast is characterised by a high productivity (Sakko, 1998).

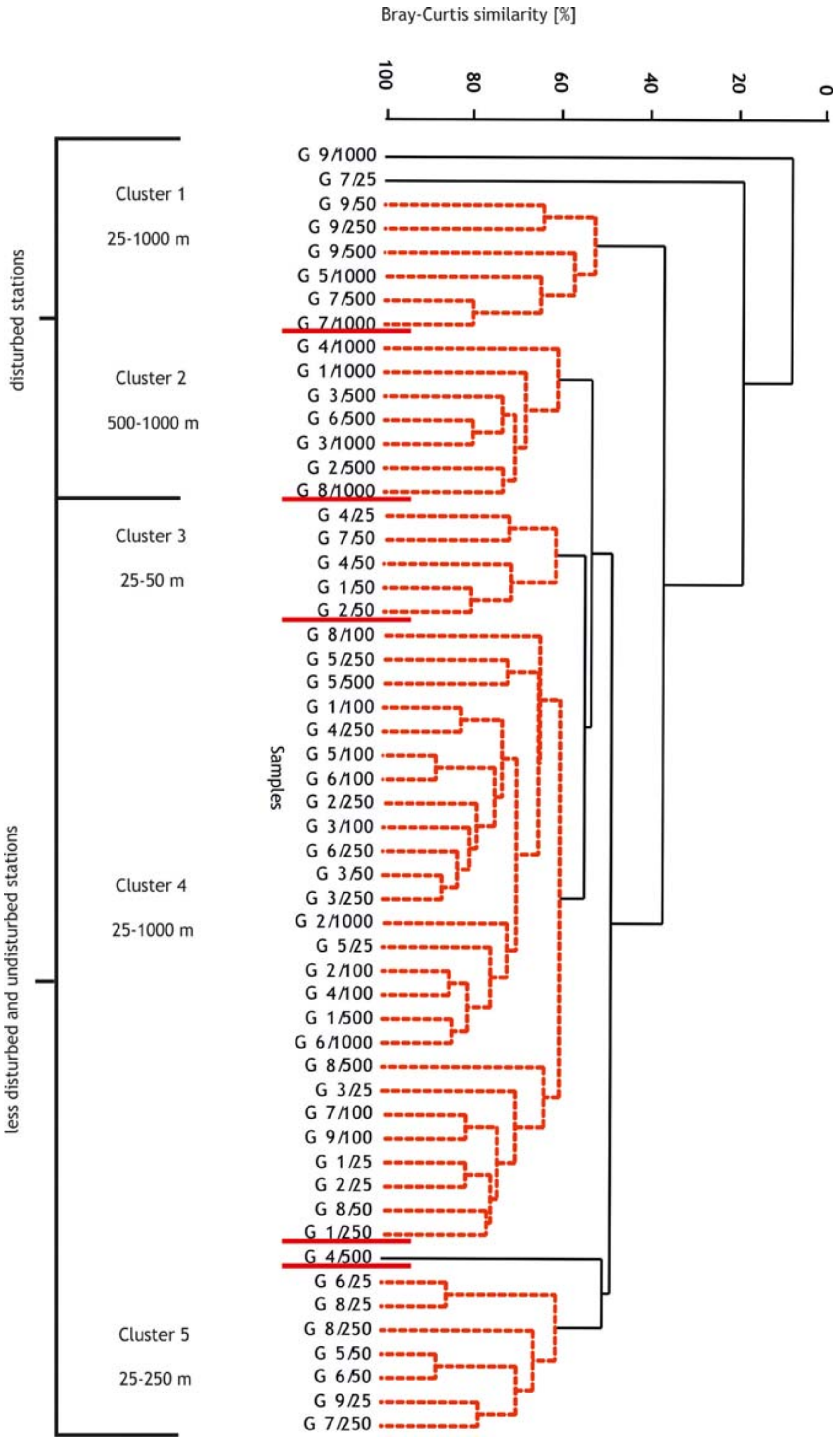

Figure 6 Dendrogram of stations for the Bray—Curtis similarity square root-transformed data and group average grouping method. (Spotted lines indicate the stations that cannot be significantly differentiated by SIMPROF.)

In the analysis of particular transects, the differences between the shallowest and the deepest stations were not statistically significant, while on one transect, the highest abundance was recorded for a depth of 500 m. These findings stress the importance of local conditions at the intermediate spatial scale along the coast of Ghana. Generally, such differences in abundance or diversity of benthic fauna across a scale of tens or hundreds of kilometres might be related to differences in sedimentary processes or productivity (Brind'Amour et al., 2009) and might be observed in vast

Table 4 Mean and maximum density values [ind./0.1 m^2] with standard deviation (SD) and frequency of occurrence *F* [%] in each of the groups of samples according to Bray—Curtis similarity analysis (only most abundant taxa). The highest values are marked in bold.

	Cluster 1			Cluster 2			Cluster 3			Cluster 4			Cluster 5		
	Mean ± SD	Max	*F* [%]	Mean ± SD	Max	*F* [%]	Mean ± SD	Max	*F* [%]	Mean ± SD	Max	*F* [%]	Mean ± SD	Max	*F* [%]
Polychaeta	**15.6 ± 6.6**	26.7	100.00%	**25.4 ± 2.2**	28.2	100.00%	**28.3 ± 7.9**	37.2	100.00%	**42.6 ± 12.7**	63.0	100.00%	**102.4 ± 30.6**	144.4	100.00%
Amphipoda	1.3 ± 1.2	3.2	100.00%	3.0 ± 2.5	7.6	100.00%	**29.1 ± 17.1**	56.0	100.00%	**7.5 ± 4.3**	18.2	100.00%	**17.0 ± 20.3**	54.6	100.00%
Bivalvia	**3.8 ± 4.0**	9.8	100.00%	3.4 ± 2.5	7.6	100.00%	6.2 ± 4.1	13.0	100.00%	11.6 ± 14.0	56.0	100.00%	**11.5 ± 7.3**	22.6	100.00%
Nematoda	0.4 ± 0.6	1.6	66.67%	**9.4 ± 4.2**	15.6	100.00%	4.4 ± 3.3	9.0	100.00%	**6.9 ± 6.6**	22.6	100.00%	8.7 ± 7.3	22.6	100.00%
Sipuncula	0.6 ± 1.0	2.2	50.00%	3.8 ± 4.1	11.2	100.00%	3.1 ± 1.7	4.8	100.00%	5.0 ± 4.1	16.0	100.00%	3.4 ± 3.2	8.6	100.00%
Gastropoda	0.5 ± 0.6	1.6	83.33%	0.5 ± 0.2	0.8	100.00%	1.5 ± 0.6	2.0	100.00%	1.4 ± 1.9	7.4	95.65%	5.2 ± 6.5	18.8	100.00%
Tanaidacea	1.1 ± 1.0	2.4	83.33%	4.2 ± 2.2	7.0	100.00%	3.9 ± 3.4	9.0	100.00%	1.1 ± 1.2	4.6	82.61%	3.1 ± 3.8	9.8	85.71%
Decapoda	0.4 ± 0.8	2.0	50.00%	0.5 ± 0.6	1.4	66.67%	5.5 ± 2.3	9.0	100.00%	2.6 ± 1.9	7.4	95.65%	5.2 ± 3.3	10.0	100.00%
Ophiuroidea	0.7 ± 1.1	2.8	50.00%	0.1 ± 0.2	0.5	16.67%	7.1 ± 4.9	12.8	100.00%	1.2 ± 1.0	4.6	95.65%	3.5 ± 4.9	14.5	100.00%
Isopoda	1.1 ± 0.9	2.6	100.00%	**5.2 ± 4.5**	13.8	100.00%	1.6 ± 0.7	2.2	100.00%	1.3 ± 1.5	6.7	91.30%	3.2 ± 3.2	7.4	85.71%
Cumacea	0.5 ± 0.4	1.2	83.33%	1.0 ± 0.8	2.4	100.00%	2.5 ± 1.6	4.4	100.00%	1.9 ± 1.2	5.2	100.00%	3.3 ± 3.3	9.2	85.71%
Nemertea	0.5 ± 0.8	2.0	66.67%	0.7 ± 0.6	1.4	66.67%	0.9 ± 0.6	1.6	80.00%	1.5 ± 1.4	5.2	95.65%	2.5 ± 0.8	3.4	100.00%
Total macrozoobenthos abundance	28.2 ± 12.5	45.9	—	65.95 ± 12.8	87.6	—	105.12 ± 32.8	145.8	—	92.7 ± 26.0	165.6	—	185.1 ± 71.5	308.76	—
No. of higher taxa per sample	13.2 ± 2.9	18	—	17.3 ± 3.6	23.0	—	22.0 ± 1.6	24	—	19.9 ± 2.6	24	—	24.1 ± 5.8	35	—

basins that can be considered Large Marine Ecosystem (Piacenza et al., 2015). Our results show also strong local discrepancies (even on neighbouring transects) and demonstrate that depth-related patterns of distribution (Table 3) might differ from the global scale patterns observed by Rex et al. (2006). As already shown, such differences can be seen in patterns of standing stock and diversity, depending on local oceanographic processes (Aller et al., 2002; Coleman et al., 1997; McCallum et al., 2015). For example, mean values of polychaete densities at the same depths varied from tens to hundreds of individuals, depending on the transect. At the same time, patterns observed for different taxonomic groups such as amphipods, polychaetes or bivalves differed strongly, even on the same transect. Similar discrepancies might be associated with differences in species composition and functional diversity of benthic communities at particular zone depths (Carney, 2005; Levin and Sibuet, 2012).

Disturbance processes associated with human activities also influenced faunal densities at some of the investigated stations. This was clearly visible in the results of the CCA analysis and the cluster analysis, where various shelf and slope stations were grouped together if the levels of barium and other toxic metals or hydrocarbons were elevated. Barium compounds are used during oil extraction and are poorly soluble in water, enabling them to survive for a long time in bottom sediments (Olsgard and Gray, 1995) and to move with the bottom currents (Guiavarch et al., 2008). Metals such as barium or cadmium may affect the development of benthic invertebrates and reduce their abundance (Lira et al., 2011); however, in case of some tolerant species, their densities in polluted areas might be elevated (Ellis et al., 2012). On the Ghanaian coast, the highest concentrations of metals and hydrocarbons were recorded in the deepest stations in the silt and clay sediments, and those factors might additionally affect the abundance of benthic communities. Only the arsenic values were elevated mostly in the shallowest sites, but there was no clear influence of this metal visible in our study. Since there are no obvious anthropogenic sources of this metal in the shallow areas (25—50 m), we suppose that it originated from a type of geological formation in the study region. Generally, the environmental status of the investigated sites was good, and the levels of barium and other toxic metals were similar to the background levels according to the OSPAR and KLIF (Norwegian Pollution Authority) guidelines (Iversen et al., 2011), although some local disturbance was visible even in the analysis of the higher taxa, stressing the need for repeated monitoring in this region. In the case of the Ghanaian coast, even low pollution in the deepest areas might be reflected in the lower abundance of benthic communities as a result of joint effect of various natural and anthropogenic causes. It is also worth mentioning that even relatively small levels of pollution might result in responses of the benthic community, depending on the studied region and on other factors specific for a given area (Olsgard and Gray, 1995). For example, hydrocarbons might affect deep-sea benthic oxygen uptake (Main et al., 2015).

The need for the further monitoring of Ghanaian waters is obvious, since data about the influences of oil platforms and other human activities on the benthic fauna of this region is extremely limited (Ayamdoo, 2016; Scheren et al., 2002). Our

Table 5 Mean and maximum values of environmental variables (means with standard deviation) for each of the clusters according to Bray–Curtis similarity analysis.

	Cluster 1			Cluster 2			Cluster 3			Cluster 4			Cluster 5		
	Mean ± SD	Max	Min	Mean ± SD	Max	Min	Mean ± SD	Max	Min	Mean ± SD	Max	Min	Mean ± SD	Max	Min
As	10.9 ± 6.4	23.4	5.9	9.7 ± 5.9	21.6	5.8	32.5 ± 41.6	106.8	12.4	27.6 ± 41.0	185.8	4.6	25.1 ± 37.5	109.5	4.7
Ba	101.5 ± 74.4	219.6	31.6	192.3 ± 116.8	363.3	69.5	19.2 ± 8.0	32.6	11.5	33.2 ± 33.4	160.5	3.5	20.1 ± 14.6	42.6	3.3
Cd	0.3 ± 0.1	0.4	0.2	0.2 ± 0.03	0.3	0.2	0.1 ± 0.02	0.1	0.0	0.1 ± 0.06	0.31	0.02	0.1 ± 0.1	0.2	0.0
Cr	63.3 ± 9.9	78.1	48.6	60.9 ± 8.4	71.8	46.4	58.3 ± 19.8	90.9	42.4	48.9 ± 16.9	89.2	15.1	37.0 ± 15.4	56.3	15.0
Cu	16.5 ± 5.0	22.1	9.7	15.7 ± 5.4	22.6	8.3	4.0 ± 0.9	5.4	3.1	6.3 ± 3.8	15.2	0.5	6.7 ± 5.7	14.6	1.4
Ni	32.8 ± 6.9	39.1	22.4	31.9 ± 7.4	43.2	22.4	15.6 ± 4.3	23.0	12.3	17.1 ± 7.3	29.5	2.4	14.5 ± 10.4	26.7	3.0
Pb	6.2 ± 1.5	7.6	4.4	4.7 ± 2.5	9.2	2.4	8.78 ± 8.5	24.0	4.8	5.4 ± 4.2	19.8	1.4	5.4 ± 3.8	12.7	1.4
Zn	64.2 ± 9.6	74.5	47.5	62.3 ± 11.3	76.7	47.9	51.4 ± 18.5	84.2	39.6	52.6 ± 23.7	102.0	8.1	36.4 ± 22.9	71.4	6.2
Hg	0.02 ± 0.01	0.02	0.01	0.02 ± 0.01	0.04	0.01	0.01 ± 0.004	0.01	0.01	0.01 ± 0.01	0.03	0.01	0.01 ± 0.01	0.04	0.01
THC	21.4 ± 19.3	59.2	8.3	12.5 ± 3.7	18.9	8.4	5.9 ± 1.1	6.9	4.6	6.8 ± 4.6	22.2	1.1	7.0 ± 4.8	14.5	1.6
PAH	241.5 ± 429.8	1117.1	36.0	44.4 ± 21.9	86.7	27.2	25.0 ± 23.9	67.0	8.5	22.5 ± 20.6	91.6	4.6	51.9 ± 70.9	204.0	6.7
NPD	88.4 ± 72.6	229.6	34.3	41.2 ± 14.2	67.1	27.5	24.6 ± 6.7	35.1	18.0	26.5 ± 19.6	87.1	4.1	32.4 ± 25.9	69.6	9.3
TOM [%]	11.2 ± 3.9	17.6	6.1	11.5 ± 2.8	15.5	8.3	5.34 ± 1.1	7.0	4.3	6.9 ± 2.4	10.8	0.9	4.8 ± 3.6	9.5	0.9
Grain size distribution %															
<	79.5 ± 24.6	99.5	41.5	90.3 ± 9.7	99.5	77.4	44.3 ± 10.1	56.9	34.5	48.8 ± 26.7	98.9	3.7	50.6 ± 38.2	97.9	1.1
Sand	19.9 ± 23.6	55.3	0.5	9.6 ± 9.5	22.1	0.5	52.8 ± 8.4	65.1	43.1	49.8 ± 26.0	94.0	1.1	39.2 ± 28.9	72.5	2.1
Gravel	0.6 ± 1.3	3.1	0.0	0.1 ± 0.2	0.5	0.0	3.0 ± 5.4	12.6	0.0	1.4 ± 1.4	5.2	0.0	10.2 ± 13.4	30.2	0.0
Pressure	636.6 ± 323.2	975.0	246.0	735.8 ± 334.3	1187.0	492.0	41.2 ± 10.4	48.0	23.0	209.3 ± 243.8	1010.0	23.0	107.2 ± 114.6	267.0	18.0
Temperature	23.4 ± 10.7	28.2	4.2	10.0 ± 10.2	28.1	4.2	27.3 ± 1.9	28.9	24.8	23.4 ± 7.1	28.9	6.2	28.3 ± 0.3	28.9	28.1
Salinity	34.9 ± 0.3	35.5	34.6	34.7 ± 0.1	34.8	34.7	35.4 ± 0.1	35.5	35.3	35.3 ± 0.5	35.9	34.1	35.3 ± 0.2	35.5	35.1
Oxygen	2.4 ± 0.9	3.5	1.6	2.7 ± 1.0	3.9	1.8	4.3 ± 0.2	4.5	4.0	2.7 ± 1.1	4.6	1.5	3.1 ± 1.4	4.4	1.2

Table 6 SIMPER analysis for groups from dendrogram cluster.

Group 1_2	Average	Group 1_3	Average	Group 1_4	Average	Group 1_5	Average
Polychaeta	15.83%	Amphipoda	18.85%	Polychaeta	25.87%	Polychaeta	37.60%
Nematoda	8.44%	Polychaeta	14.01%	Bivalvia	7.86%	Amphipoda	10.85%
Tanaidacea	5.68%	Ophiuroidea	4.85%	Amphipoda	5.98%	Nematoda	4.82%
Sipuncula	4.42%	Decapoda	4.02%	Nematoda	4.77%	Bivalvia	3.49%
Isopoda	4.37%	Bivalvia	3.66%	Sipuncula	4.36%	Gastropoda	2.61%
		Group 2_3	Average	Group 2_4	Average	Group 2_5	Average
		Amphipoda	14.12%	Polychaeta	12.31%	Polychaeta	29.11%
		Polychaeta	4.66%	Bivalvia	6.43%	Amphipoda	8.99%
		Ophiuroidea	3.85%	Nematoda	3.84%	Nematoda	3.26%
		Decapoda	3.13%	Sipuncula	3.49%	Bivalvia	3.13%
		Nematoda	3.09%	Tanaidacea	2.96%	Tanaidacea	1.98%
				Group 3_4	Average	Group 3_5	Average
				Amphipoda	10.17%	Polychaeta	23.60%
				Polychaeta	8.20%	Amphipoda	7.51%
				Bivalvia	5.08%	Nematoda	3.19%
				Ophiuroidea	2.86%	Bivalvia	2.17%
				Nematoda	2.68%	Ophiuroidea	1.96%
						Group 4_5	Average
						Polychaeta	18.87%
						Amphipoda	7.73%
						Bivalvia	4.08%
						Nematoda	3.26%
						Sipuncula	1.87%

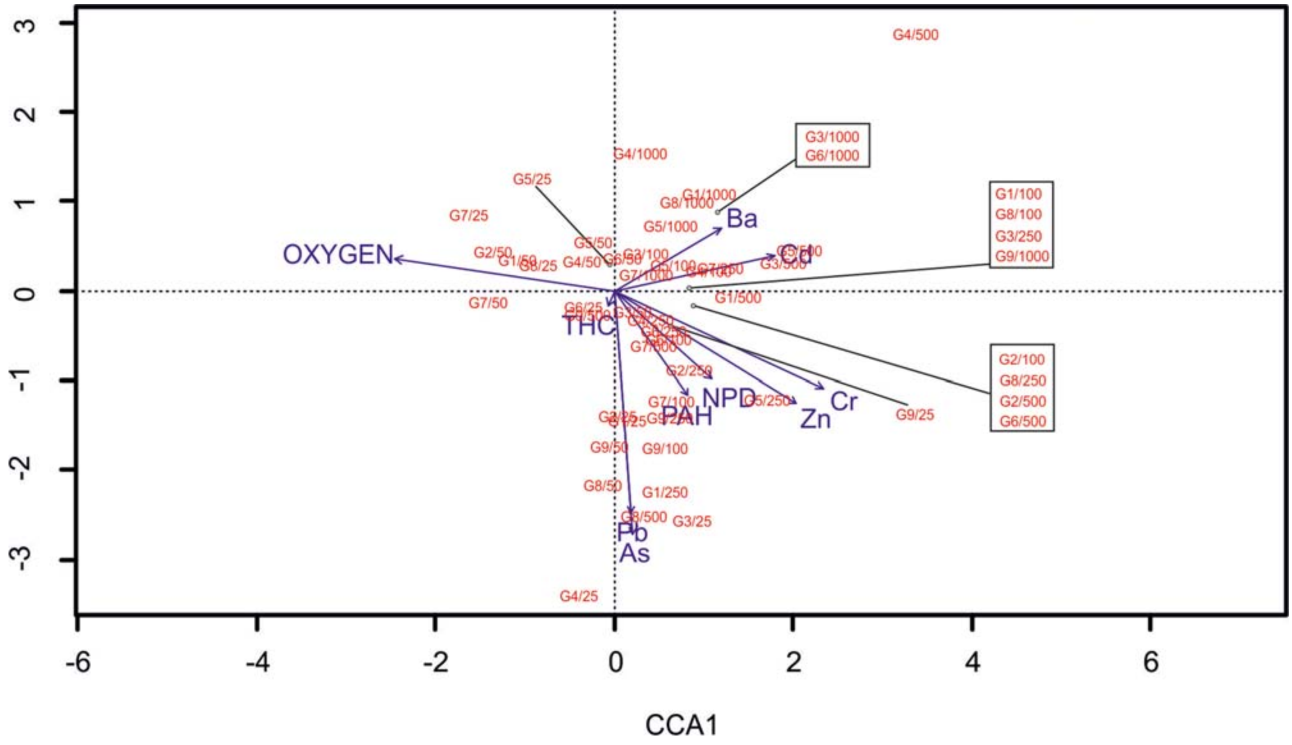

Figure 7 Distribution of stations according to environmental factors (Canonical Correspondence Analysis).

results might therefore be important for the development of sustainable management strategies under the concept of the “Large Marine Ecosystem” (Ukwe et al., 2003). The influence of low pollution levels, visible even in the analysis of higher taxa, might suggest vulnerability of those communities to such disturbance events. Włodarska-Kowalczuk and Kędra

Table 7 VIF and statistical significance of factors used in CCA.

	VIF	Significance
As	7.923847e+00	0.001
Ba	4.448803e+00	0.001
Cd	4.037395e+00	0.001
Cr	9.461655e+00	0.001
Pb	1.112333e+01	0.020
Zn	1.687098e+01	0.013
THC	4.069166e+00	0.012
PAH	1.462323e+01	0.001
NPD	1.419567e+01	0.017
Oxygen	4.417467e+00	0.002

(2007) have demonstrated that even data on generic level might be used as surrogate in the analysis of disturbance processes in benthic marine ecosystems. Nevertheless, further studies should include the analysis of species richness and diversity, especially in the case of the most important indicatory taxa such as amphipods and polychaetes (Olsgard et al., 2003; Ossa-Carratero et al., 2012). The spatial variation of abundance along the coast of Ghana also suggests the need for a closer investigation of the functional analysis of benthic communities based, for example, on the classification into various trophic guilds.

Acknowledgements

The sampling cruise and the environmental data analysis within this programme were funded by the Norwegian Agency for Development Cooperation (NORAD) (Oil for Development Program — OfD) and by the Food and Agriculture Organization of the United Nations (FAO). Krzysztof Pabis and Jacek Sicinski were also supported by the University of Lodz.

References

Akanabi Bamikole, W., Ndubuisi, A., Ochuko, A.P., Olamide Olaronke, O.P., 2009. Macrobenthic fauna of Snake Island area of Lagos lagoon, Nigeria. Res. J. Biol. Sci. 4 (3), 272—276, https://doi.org/rjbsci.2009.272.276.

Aller, J.Y., Aller, R.C., Green, M.A., 2002. Benthic faunal assemblages and carbon supply along the continental shelf/shelf break-slope off Cape Hatteras, North Carolina. Deep-Sea Res. Pt. II 49 (20), 4599—4625, http://dx.doi.org/10.1016/S0967-0645(02)00131-5.

Ayamdoo, N.A., 2016. Protecting the Gulf of Guinea in an oil boom: regulating offshore petroleum pollution in a divided world. J. World Energy Law B. 9 (3), 219—232, http://dx.doi.org/10.1093/jwelb/iww007.

Bakus, G.J., 2007. Quantitative Analysis of Marine Biological Communities. Wiley-Interscience, New Jersey, 434 pp.

Bassindale, R., 1961. On the marine fauna of Ghana. Proc. Zool. Soc. Lond. 137 (4), 481—510, http://dx.doi.org/10.1111/j.1469-7998.1961.tb06086.x.

Blott, S.J., Pye, K., 2001. GRADISTAT: a grain size distribution and statistics package for the analysis of unconsolidated sediments. Earth Surf. Proc. Land. 26 (11), 1237—1248, http://dx.doi.org/10.1002/esp.261.

Brind'Amour, A., Menot, L., Galéron, J., Crassous, P., 2009. Spatial organization of a sedimentary macrobenthic community located on the West African Equatorial margin. Deep-Sea Res. Pt. II 56 (23), 2292—2298, http://dx.doi.org/10.1016/j.dsr2.2009.04.010.

Brown, C.A., Ajao, E.A., 2004. Effects of topographical modification on the composition and abundance of macrofauna in Southern Lagos Lagoon (Ikoyi). West Afr. J. Appl. Ecol. 5 (1), 41—50, http://dx.doi.org/10.4314/wajae.v5i1.45594.

Buchanan, J.B., 1957. The bottom fauna communities across the continental shelf off Accra, Ghana (Gold Coast). Proc. Zool. Soc. Lond. 130 (1), 1—56, http://dx.doi.org/10.1111/j.1096-3642.1958.tb00562.x.

Buchanan, J.B., 1984. Sediment analysis. In: Holme, N.A., McIntyre, A.D. (Eds.), Methods for the Study of Marine Benthos. Blackwell Sci. Publ., Oxford, 41—65.

Carney, R.S., 2005. Zonation of deep biota on continental margins. Oceanogr. Mar. Biol. 43, 211—278, http://dx.doi.org/10.1201/9781420037449.ch6.

Chukwuone, N.A., Ukwe, C.N., Onugu, A., Ibe, C.A., 2009. Valuing the Guinea current large marine ecosystem: estimates of direct output impact of relevant marine activities. Ocean Coast. Manage. 52 (3—4), 189—196, http://dx.doi.org/10.1016/j.ocecoaman.2008.12.008.

Clarke, K.R., 1993. Non-parametric multivariate analyses of changes in community structure. Aust. J. Ecol. 18 (1), 117—143, http://dx.doi.org/10.1111/j.1442-9993.1993.tb00438.x.

Clarke, K.R., Gorley, R.N., 2015. PRIMER v7: User Manual/Tutorial PRIMER-E, Plymouth, 296 pp.

Coleman, N., Gason, A.S.H., Poore, C.B., 1997. High species richness in the shallow marine waters of south-east Australia. Mar. Ecol. Prog. Ser. 154, 17—26, http://dx.doi.org/10.3354/meps154017.

Dell'Anno, A., Pusceddu, A., Corinaldesi, C., Canals, M., Heussner, S., Thomsen, L., Danovaro, R., 2013. Trophic state of benthic deep-sea ecosystems from two different continental margins off Iberia. Biogeosciences 10 (5), 2945—2957, http://dx.doi.org/10.5194/bg-10-2945-2013.

Djagoua, E.V., Kassi, J.B., Mobia, B., Kouadio, J.M., Dro, C., Affian, K., Saley, B., 2011. Ivorian and Ghanaian upwelling comparison: intensity and impact on phytoplankton biomass. AJSIR 5, 740—747, http://dx.doi.org/10.5251/ajsir.2011.2.5.740.747.

Duineveld, G.C.A., Wilde, P.A.W., Berghuis, E.M., Kok, A., 1993. The benthic infauna and benthic respiration off the Banc d'Arguin (Mauretania, Northwest Africa). Hydrobiologia 258, 107—117, http://dx.doi.org/10.1007/978-94-011-1986-3_10.

Edokpayi, C.A., Adenle, T.A., Lawal, M.O., 2010. Notes on the composition, abundance and zonation of benthic invertebrate of an artificial rocky shore, Tarkwa bay, Lagos, Nigeria. NY Sci. J. 3 (9), 63—67.

Edros, L., Zalatnai, M., Morschhauser, T., Bátori, Z., Komoczi, L., 2011. On the terms related to spatial ecological gradients and boundaries. Acta Biol. Szeegediensis 55 (2), 279—287.

Elezz, A.A., Hassan, H.M., Alsaadi, H.A., Easa, A., Al-Meer, S., Elsaid, K., Ghouri, Z.K., Abdala, A., 2018. Validation of total mercury in marine sediment and biological samples, using cold vapour atomic absorption spectrometry. Method. Protocol. 1 (3), art. no. 0031, http://dx.doi.org/10.3390/mps1030031.

Ellis, J.I., Fraser, G., Russell, J., 2012. Discharged drilling waste from oil and gas platforms and its effects on benthic communities. Mar. Ecol. Prog. Ser. 456, 285—302, http://dx.doi.org/10.3354/meps09622.

Ewa-Oboho, I., Oladimeji, O., Emile Asuquo, F., 2008. Effect of dredging on benthic-pelagic production in the mouth of Cross River Estuary (off the Gulf of Guinea), S.E. Nigeria. Indian J. Mar. Sci. 37 (3), 291—297.

Folk, R.L., Ward, W.C., 1957. Brazos River bar [Texas]; a study in the significance of grain size parameters. J. Sediment. Res. 27 (1), 3—26, http://dx.doi.org/10.1306/74D70646-2B21-11D7-8648000102C1865D.

Fox, J., 2016. Applied Regression Analysis and Generalized Linear Models. Sage, Hamilton, 816 pp.

Fox, J., Monette, G., 1992. Generalized collinearity diagnostics. NLM 87 (417), 178—183.

Friedlander, A.M., Ballesteros, E., Fay, M., Sala, E., 2014. Marine communities on oil platforms in Gabon, West Africa: high biodiversity oases in a low biodiversity environment. PLoS ONE 9 (8), art. no. e103709, http://dx.doi.org/10.1371/journal.pone.0103709.

Gaever, S., Olu, K., Derycke, S., Vanreusel, A., 2009. Metazoan meiofaunal communities at cold seeps along the Norwegian margin: influence of habitat heterogeneity and evidence for connection with shallow-water habitats. Deep-Sea Res. Pt. I 56 (5), 772—785, http://dx.doi.org/10.1016/j.dsr.2008.12.015.

Galeron, J., Menot, L., Renau, N., Crassous, P., Khripounoff, A., Treignier, C., Sibuet, M., 2009. Spatial and temporal patterns of benthic macrofaunal communities in the deep continental margin in the Gulf of Guinea. Deep-Sea Res. Pt. II 56 (23), 2299—2312, http://dx.doi.org/10.1016/j.dsr2.2009.04.011.

Guiavarch, E., Pons, A., Creuly, C., Dussap, C.G., 2008. Application of a data reconciliation method to the stoichiometric analysis of *Fibrobacter succinogenes* growth. Appl. Biochem. Biotech. 151 (2—3), 201—210, http://dx.doi.org/10.1107/s12010-008-8172-9.

Iversen, P.E., Green, A.M.V., Lind, M.J., Petersen, M.R.H.P., Bakke, T., Lichtenthaler, R., Klungsøyr, J., Grafert, T., Natvig, H., Ersvik, M., 2011. Guidelines for Offshore Environmental Monitoring on the Norwegian Continental Shelf. Klif Report, Climate and Pollution Agency, Oslo.

Jarvis, I., Jarvis, K.E., 1992. Inductively coupled plasma-atomic emission spectrometry in exploration geochemistry. J. Geochem. Explor. 44 (1—3), 139—200, http://dx.doi.org/10.1016/0375-6742(92)90050-1.

Kouadio, K.N., Diomandé, D., Ouattara, A., Kone, Y.J.M., Gourene, G., 2008. Taxonomic diversity and structure of benthic macroinvertebrates in Aby Lagoon (Ivory Coast, West Africa). Pakistan J. Biol. Sci. 11 (18), 2224—2230, http://dx.doi.org/10.3923/pjbs.2008.2224.2230.

Le Loeuff, P., Cosel, R., 1998. Biodiversity patterns of the marine benthic fauna on the Atlantic coast of tropical Africa in relation to hydroclimatic conditions and paleogeographic events. Acta Oecologica 19 (3), 309—321, http://dx.doi.org/10.1016/S1146-609X(98)80035-0.

Le Loeuff, P., Intés, A., 1999. Macrobenthic communities in the continental shelf of Côte-d'Ivoire. Seasonal and diel cycles in relation to hydroclimate. Acta Oceanologica 22 (5), 529—550, http://dx.doi.org/10.1016/S0399-1784(00)87685-9.

Legendre, P., Legendre, L., 2012. Numerical Ecology. Elsevier, Croydon, 990 pp.

Levin, L.A., 2003. Oxygen minimum zone benthos: adaptation and community response to hypoxia. Oceanogr. Mar. Biol. 41, 1—45.

Levin, L.A., Sibuet, M., 2012. Understanding continental margin biodiversity: a new imperative. Annu. Rev. Mar. Sci. 4, 79—112, http://dx.doi.org/10.1146/anurev-marine-120709-142714.

Levin, L., Whitcraft, C.R., Mendoza, G.F., Gonzalez, J.P., Cowie, G., 2009. Oxygen and organic matter thresholds for benthic faunal activity on the Pakistan margin oxygen minimum zone (700—1100 m). Deep-Sea Res. Pt. II 56 (6—7), 449—471, http://dx.doi.org/10.1016/j.dsr2.2008.05.032.

Lira, M.C., Santos-Magalhaes, N.S., Nicolas, V., Marsaud, V., Silva, M. P., Ponchel, G., Vauthier, C., 2011. Cytotoxicity and cellular uptake of newly synthesized fucoidan-coated nanoparticles. Eur. J. Pharm. Biopharm. 79 (1), 162—170, http://dx.doi.org/10.1016/j.ejpb.2011.02.013.

Longhurst, A.R., 1958. An ecological survey of the west African marine benthos. Fishery Publ. 11, 1—102.

Longhurst, A.R., 1959. Benthos densities off tropical West Africa. J. Conseil Perma. Internat. Explor. Mer 2, 21—28.https://doi.org/10.1038_179542b0.

Main, C.E., Ruhl, H.A., Jones, D.O., Yool, A., Thornton, B., Mayor, D. J., 2015. Hydrocarbon contamination affects deep-sea benthic oxygen uptake and microbial community composition. Deep-Sea Res. Pt. I 100, 79—87, http://dx.doi.org/10.1016/j.dsr.2014.12.008.

McCallum, A.W., Woolley, S., Błażewicz-Paszkowycz, M., Browne, J., Gerken, S., Kloser, R., Poore, G.C.B., Staples, D., Syme, A., Taylor, J., Walker-Smith, G., Williams, A., Wilson, R.S., 2015. Productivity enhances benthic species richness along an oligotrophic Indian Ocean continental margin. Global Ecol. Biogeogr. 24 (4), 462—471, http://dx.doi.org/10.1111/geb.12255.

Menot, L., Crassous, P., Desbruyeres, D., Galéron, J., Khriponoff, A., Sibuet, M., 2009. Colonization patterns along the equatorial West African margin: implications for functioning and diversity maintenance of bathyal and abyssal communities. Deep-Sea Res. Pt. II 53 (23), 2313—2325, http://dx.doi.org/10.1016/j.dsr2.2009.04.012.

Nephin, J., Juniper, S.K., Archambault, P., 2014. Diversity, abundance and community structure of benthic macro- and megafauna on the Beaufort Shelf and Slope. PLoS ONE 9 (7), art. no. e101556, http://dx.doi.org/10.1371/journal.pone.0101556.

Oksanen, J., Blanchet, F.G., Friendly, M., Kindt, R., Legendre, P., McGlinn, D., Minchin, P.R., O'Hara, R.B., Simpson, G.L., Solymos, P., Stevens, M.H.H., Szoecs, E., Wagner, H., 2019. Vegan: Community Ecology Package. R package version 2.5-4, https://CRAN.R-project.org/package=vegan.

Olsgard, F., Brattegard, T., Holthe, T., 2003. Polychaetes as surrogates for marine biodiversity: lower taxonomic resolution and indicator groups. Biodivers. Conserv. 12 (5), 1033—1049, http://dx.doi.org/10.1023/A:102280040.

Olsgard, F., Gray, J.S., 1995. A comprehensive analysis of effects of offshore oil and gas exploration and production on the benthic communities of the Norwegian continental shelf. Mar. Ecol. Prog. Ser. 122, 277—306, http://dx.doi.org/10.3354/meps122277.

OSPAR, 2011. OSPAR Guidelines for Monitoring the Environmental Impact of Offshore Oil and Gas Activities. Reference no. 2004-11.

Ossa-Carratero, J.A., Del-Pilar-Ruso, Y., Gimenez-Casalduero, F., Sanches-Lizaso, J.L., Dauvin, J.C., 2012. Sensitivity of amphipods to sewage pollution. Estuar. Coast Shelf Sci. 96 (1), 129—138, http://dx.doi.org/10.1016/j.ecss.2011.10.020.

Piacenza, S.E., Barner, A.K., Benkwitt, C.E., Boersma, K.S., Cerny-Chipman, E.B., Ingeman, K.E., Kindinger, T.L., Lee, J.D., Lindsley, A.J., Reimer, J.N., Rowe, J.C., Shen, C., Thompson, K.A., Thurman, L.L., Heppell, S.S., 2015. Patterns and variation in benthic biodiversity in a large marine ecosystem. PLoS ONE 10 (8), art. no. e0135135, http://dx.doi.org/10.1371/journal.pone.0135135.

R Core Team, 2013. R: A Language and Environment for Statistical Computing. R Foundation for Statistical Computing, Vienna, Austria, http://www.R-project.org/.

Rex, M.A., Etter, R.J., 2010. Deep-sea Biodiversity; Patterns and Scale. Harvard University Press, Cambridge, Massachusetts, 368 pp.

Rex, M.A., Etter, R.J., Morris, J.S., Crouse, J., McClain, C.R., Johnson, N.A., Stuart, C.T.C.T., Deming, J.W., Thies, R., Avery, R., 2006. Global bathymetric patterns of standing stock and body size in the deep-sea benthos. Mar. Ecol. Prog. Ser. 317, 1—8, http://dx.doi.org/10.3354/meps317001.

Sakko, A.L., 1998. The influence of the Benguela upwelling system on Namibia's marine biodiversity. Biodivers. Conserv. 7 (4), 419—433, http://dx.doi.org/10.1023/A:100886731.

Scheren, P.A., Ibe, A.C., Janssen, F.J., Lemmens, A.M., 2002. Environmental pollution in the Gulf of Guinea — a regional approach. Mar. Pollut. Bull. 44 (7), 633—641, http://dx.doi.org/10.1016/S0025-326X(01)00305-8.

Schneider, W., 1990. Field Guide to the Commercial Marine Resources of the Gulf of Guinea. Food and Agriculture Organization of the United Nations, Rome, 268 pp.

Sibuet, M., Vangriesheim, A., 2009. Deep-sea environment and biodiversity of the West African Equatorial margin. Deep-Sea Res. Pt. II 56 (23), 2156—2168, http://dx.doi.org/10.1016/j.dsr2.2009.04.015.

Solan, M., Aspden, R.J., Paterson, D.M., 2012. Marine Biodiversity and Ecosystem Functioning: Frameworks, Methodologies, and Integration. Oxford Univ. Press, Oxford, 254 pp.

Soltwedel, T., 1997. Meiobenthos distribution pattern in the tropical East Atlantic: indication for fractionated sedimentation of organic matter to the sea floor? Mar. Biol. 129 (4), 747—756, http://dx.doi.org/10.1007/s002270050.

Spalding, M.D., Fox, H.E., Allen, G.R., Davidson, N., Ferdana, Z.A., Finlayson, M., Halpern, B.S., Jorge, A., Lombana, A., Lourie, S. A., Martin, M.D., McManus, E., Molnar, J., Recchia, C.A., Robertson, J., 2007. Marine ecoregions of the World: a bioregionalization of coastal and shelf areas. Bioscience 57 (7), 573—583, http://dx.doi.org/10.1641/B570707.

Ukwe, C.N., Ibe, C.A., Alo, B.I., Yumkella, K.K., 2003. Achieving a paradigm shift in environmental and living resources management in the Gulf of Guinea: the large marine ecosystem approach. Mar. Pollut. Bull. 47 (1—6), 219—225, http://dx.doi.org/10.1016/S0025-326X(02)00473-3.

Ukwe, C.N., Ibe, C.A., Nwilo, P.C., Huidobro, P.A., 2006. Contributing to the WSSD targets on oceans and coasts in West and Central Africa: The Guinea Current Large Marine Ecosystem Project. Int. J. Oceans Oceanogr. 1, 21—44.

UNESCO Intergovernmental Oceanographic Commission, 1982. The Determination of Petroleum Hydrocarbons in Sediments, Manuals and Guides No. 11, Paris, 38 pp.

Warton, D.I., Wright, T.W., Wang, Y., 2012. Distance-based multivariate analyses confound location and dispersion effects. Methods Ecol. Evol. 3 (1), 89—101, http://dx.doi.org/10.1111/j.2041-210X.2011.00127.x.

Wijnsma, G., Wolff, W.J., Meijboom, A., Duvien, P., De Vlas, J., 1999. Species richness and distribution on benthic tidal flat fauna of the Banc d 'Arguin, Mauritania. Oceanol. Acta 22 (2), 233—243, http://dx.doi.org/10.1016/S0399-1784(99)80048-6.

Włodarska-Kowalczuk, M., Kędra, M., 2007. Surrogacy in natural patterns of benthic distribution and diversity: selected taxa versus lower taxonomic resolution. Mar. Ecol. Prog. Ser. 351, 53—63, http://dx.doi.org/10.3354/meps07127.

Włodarska-Kowalczuk, M., Kendall, M.A., Węsławski, J.M., Klages, M., Soltwedel, T., 2004. Depth gradients of benthic standing stock and diversity on the continental margin at a high-latitude ice-free (off Spitsbergen, 79°N). Deep-Sea Res. Pt. I 51 (12), 1903—1914, http://dx.doi.org/10.1016/j.dsr.2004.07.013.

Zapala, M.A., Schork, N.J., 2006. Multivariate regression analysis of distance matrices for testing associations between gene expression patterns and related variables. Proc. Natl. Acad. Sci. U.S.A. 103 (51), 19430—19435, http://dx.doi.org/10.1073/pnas.0609333103.

Zettler, M.L., Bochert, R.F., Pollehne, F., 2009. Macrozoobenthos diversity in an oxygen minimum zone off northern Namibia. Mar. Biol. 156 (9), 1949—1961, http://dx.doi.org/10.1007/s00227-009-1227-9.

Oceanologia (2020) 62, 101—110

Available online at www.sciencedirect.com

ScienceDirect

journal homepage: www.journals.elsevier.com/oceanologia

ORIGINAL RESEARCH ARTICLE

Factors regulating the compositions and distributions of dissolved organic matter in the estuaries of Jiaozhou Bay in North China

Jiaojie Hu[a,b], Li Zou[a,c,*], Jian Wang[b,], Qianqian Ren[c], Bin Xia[d], Ge Yu[a,c]**

[a] *College of Environmental Science and Engineering, Ocean University of China, Qingdao, China*
[b] *SGS-CSTC Standards Technical Services (Qingdao) Co., Ltd., Qingdao, China*
[c] *Key Laboratory of Marine Environmental Science and Ecology, Ocean University of China, Qingdao, China*
[d] *Yellow Sea Fisheries Research Institute, Chinese Academy of Fishery Sciences, Qingdao, China*

Received 18 March 2019; accepted 16 September 2019
Available online 30 September 2019

KEYWORDS
Estuaries in Jiaozhou Bay;
Dissolved organic matter;
CDOM;
Carbohydrates;
Amino acids

Summary Water samples collected from the Jiaozhou Bay every two months between April 2016 and February 2017 were analyzed for dissolved organic carbon (DOC), particulate organic carbon (POC), total dissolved carbohydrates (TCHO), total hydrolyzed amino acids (THAA), and chromophoric dissolved organic matter (CDOM) to explore the biogeochemical processes of dissolved organic matter (DOM) in anthropogenic estuarine and coastal environments. In addition, nutrients, chlorophyll *a* and COD (chemical oxygen demand) in these samples were also analyzed. All parameters exhibited temporal and spatial variations: POC 0.13—22.40 mg/L (average 1.75 mg/L), DOC 0.98—32.75 mg/L (average 5.04 mg/L), COD 0.23—7.58 mg/L (average 1.67 mg/L), TCHO 0.34—14.09 μM (average 3.18 μM), THAA 0.89—8.30 μM (average 4.04 μM), and the absorption coefficient $a(355)$ of CDOM 0.23—16.35 m^{-1} (average 3.09 m^{-1}). The temporal and spatial variations in the concentrations of TCHO, THAA, and DOC implied that the DOM in the study areas had a relatively higher biochemical activity. The canonical correspondence

---

[*] Corresponding author at: College of Environmental Science and Engineering, Ocean University of China, 238# Songling Road, Qingdao, Shandong, 266100, China. Tel.: +86 532 66782260.
[**] Corresponding author at: SGS-CSTC Standards Technical Services, Qingdao Branch, 143# Zhuzhou Road, Qingdao, Shandong, 266101, China. Tel.: +86 532 68999233.
E-mail addresses: zouli@ouc.edu.cn (L. Zou), jian.wang@sgs.com (J. Wang).

Peer review under the responsibility of Institute of Oceanology of the Polish Academy of Sciences.

ELSEVIER Production and hosting by Elsevier

https://doi.org/10.1016/j.oceano.2019.09.002

analysis (CCA) and maximal information coefficient (MIC) revealed that seasonal variations in temperature and the phosphate concentration were the dominant factors regulating the DOM distributions in Jiaozhou Bay, while riverine inputs and *in situ* reproduction mainly controlled the DOM compositions.

1. Introduction

Dissolved organic carbon (DOC) is the largest reducing carbon pool in the ocean. The distributions and compositions of DOC regulate not only the regional primary production (Markager and Vincent, 2000; Wang and Chen, 2018) but also the diagenesis of bioactive elements, such as heavy metals (Chen et al., 2003; Shank et al., 2005), and the activities of marine microorganisms (Jiao et al., 2010). Dissolved amino acids and carbohydrates have been identified as major components of DOM and serve as important nitrogen and carbon sources for phytoplankton (Veuger et al., 2004) and bacteria in the ocean (Liang et al., 2001; Middelboe et al., 1995). These biogenic organic compounds are more labile and primarily represent the DOM characteristics.

DOM in estuaries is derived from terrigenous riverine inputs, *in situ* production, and sediment re-suspension (Castillo et al., 1999; Chen and Bada, 1992; Cheng et al., 2008; Nelson et al., 1998; Rochelle-Newall and Fisher, 2002). Rivers deliver DOM at a flux of 0.20—0.21 Pg C yr^{-1} globally (Battin et al., 2009; Hedges and Keil, 1995). Riverine DOM is relatively stable and resistant to degradation by microorganisms (Hudson et al., 2010; Mantoura and Woodard, 1983). However, mixed DOM derived from anthropogenic materials and local production (such as carbohydrates and amino acids) in estuarine systems is capable of being biochemically utilized (Bronk and Glibert, 1993; Fellman et al., 2010; Stepanauskas et al., 1999). Therefore, riverine DOM might provide significant carbon and nitrogen sources for estuarine microbes and algae (Middelboe et al., 1995). On the other hand, DOM degrades and releases dissolved inorganic carbon (DIC) and inorganic nutrients, leading to environmental problems such as eutrophication in the estuary and coastal areas (Seitzinger and Sanders, 1997). Thus, the sources, compositions, properties, and potential functions of DOM in coastal ecosystems must be discerned.

Jiaozhou Bay is a semi-closed bay located on the west coast of the Yellow Sea in the western Pacific Ocean. From estuaries to central Jiaozhou Bay, DOM concentrations in the waters decrease significantly by 2.6—4.2-fold (Jiang et al., 2007; Kong et al., 2016; Shen et al., 2006; Yang et al., 2010). Thus, the ambient rivers provided a substantial amount of organic carbon to Jiaozhou Bay (Yang et al., 2010). The rapid industrialization and civilization in coastal Qingdao City have exerted substantial effects on the DOM distribution and composition through the discharge of rivers into the bay, which in turn, directly and indirectly, affect the biochemical processes of DOM in the estuaries and Bay (Xi et al., 2018). More than a dozen rivers flow into Jiaozhou Bay, with substantial differences in the natural profiles and backgrounds among these rivers. Haibo River, a small river flowing into east Jiaozhou Bay, represented a major source of DOM in east Jiaozhou Bay, but little DOM accumulated in ambient waters because of strong hydrodynamic and tidal effects (Jiang et al., 2007). Dagu River, the largest river flowing into the northwest bay, carried considerable amounts of humic-like materials into Jiaozhou Bay (Ji et al., 2006). Meanwhile, the variation in the levels of humic-like materials was significantly correlated with the variation in the carbohydrate levels in the estuary of Dagu River (Ji et al., 2006), and a similar correlation was discovered among the levels of carbohydrates, amino acids and nutrients in the bay (Shi, 2015). However, researchers have not clearly determined how these relationships and interactive processes of DOM in the estuaries are impacted by human activities. To date, no studies have been conducted to verify how these rivers control the DOM cycle in Jiaozhou Bay.

Water samples were collected from the bay every two months between Apr. 2016 and Feb. 2017, and DOC, carbohydrate, amino acid and CDOM concentrations in the water samples were analyzed to identify the key factors that regulate DOM variations in the estuaries of Jiaozhou Bay. The specific goals of this study are (1) to describe the variations in the levels of total organic carbon and DOM components, (2) to clarify the characteristics and sources of DOM, (3) to discern the multiple interactions among DOM components and physiochemical factors, and (4) to estimate the impact of relative runoff on DOM transport from each river to the bay.

2. Material and methods

2.1. Sampling sites and methods

Water samples were collected from 10 sites in Jiaozhou Bay every two months from April 2016 to February 2017 (Fig. 1): 2 sites R1 (N36°04′06″, E120°17′73″) and R2 (N36°05′37″, E120°19′41″) at piers and 8 sites in the estuaries. Rivers flowing into the east bay include Haibo (R3, N36°06′73″, E120°19′39″), Licun (R4, N36°09′39″, E120°21′35″), Banqiaofang (R5, N36°11′07″, E120°21′95″), and Loushan (R6, N36°12′32″, E120°21′61″) Rivers, which run through or near Qingdao City. Baisha River (R7, N36°14′55″, E120°18′97″) flows into the north bay and Yang River (R9, N36°07′58″, E120°06′01″) into the west bay, which run through the rural area. The largest river, the Dagu River (R8, N36°10′85″, E120°07′46″), flows into the northeast bay and the Lianwan River (R10, N36°00′26″, E120°11′24″) covers a newly developed area.

Table 1 Methods on physicochemical parameters.

Parameters	Methods	Maximum of relative error [%]	References
COD	Basic potassium permanganate method	1.5	P.R. China National Standard (2007)
SS	Gravimetric method	0.6	P.R. China National Standard (2007)
NO_3^-—N	Cadmium copper reduction method	0.1	Grasshoff et al. (2007)
NO_2^-—N	Diazotization titration method	0.6	Grasshoff et al. (2007)
NH_4^+—N	Indophenol blue spectrophotometric method	0.7	Grasshoff et al. (2007)
PO_4^{3-}—P	Molybdenum blue method	4.3	Grasshoff et al. (2007)
Chl-*a*	Three-color spectrophotometry method	0.3	Jeffrey and Humphrey (1975)

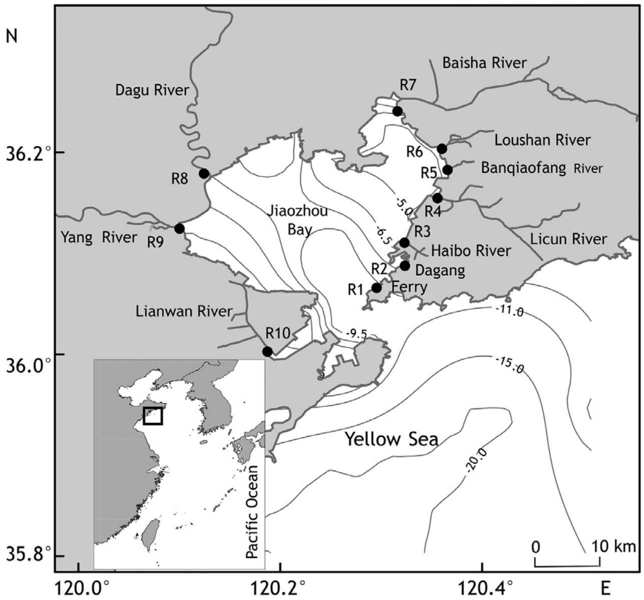

Figure 1 Study area and sampling sites at the estuaries of Jiaozhou Bay.

Samples were collected at a depth of 20 cm under the water surface, because of the shallow depth in the estuaries (< 5 m). Water samples were filtered through pre-treated fibers (Whatman GF/F (Qingdao, Ocean University of China, China), combusted under 450°C for 4 h) and were stored frozen until the analyses of DOC, TCHO, THAA, CDOM, and dissolved nutrient levels. The frozen filters were used to analyze the levels of particulate organic carbon (POC) and chlorophyll *a* (Chl-*a*). Unfiltered water samples were stored in a refrigerator until the chemical oxygen demand (COD) analysis. Temperature (T), salinity (S), pH and the dissolved oxygen (DO) level were monitored simultaneously using a multi-parameter water quality monitor (HQ40d, Hach, Ocean University of China, China).

2.2. Analytical methods

2.2.1. Physicochemical parameters

The levels of COD, Chl-*a*, suspended particle (SS) and nutrients (NO_2^-—N, NO_3^-—N, NH_4^+—N and PO_4^{3-}—P) were measured using the methods listed in Table 1. The dissolved inorganic nitrogen (DIN) concentration is the sum of the NH_4^+—N, NO_2^-—N and NO_3^-—N concentrations. The concentrations of NO_2^-—N, NO_3^-—N, NH_4^+—N and PO_4^{3-}—P were measured using an automatic analyzer (QuAAtro, Salt Analytical GmbH, Ocean University of China, China) (Grasshoff et al., 2007). The maximum relative error is listed in Table 1 and was calculated from the corresponding triplicate measurements.

2.2.2. POC and DOC

The POC concentration was measured in acidified filter samples using an elemental analyzer (PerkinElmer 2400 series-2, UC Davis, US), with a relative error of less than 0.3% in duplicate measurements.

The DOC concentration of water samples was measured using catalytic high temperature oxidation with a total organic carbon analyzer (TOC-L, Shimadzu, Ocean University of China, China). Low carbon water and standard seawater (provided by Hansell Laboratories, University of Miami, USA) were used as the blank and to construct a standard curve for instruments. The relative error was less than 3% for duplicate measurements.

2.2.3. Relative concentrations of CDOM

The absorption spectrum of CDOM was scanned from 190 nm to 800 nm at 1 nm intervals using a UV—Vis spectrophotometer (UV-2550, Shimadzu, Ocean University of China, China) with 1 cm quartz cuvette. Pure water (Milli-Q) was used as blank reference. The absorbance value at every wavelength was calculated by subtracting the absorbance value at 700 nm to deduce the difference in refractivity between seawater and pure water and the baseline drift of scattering induced by fine particles (Castillo et al., 1999). The relative error was less than 4.24% for triplicate measurements, and the photometric accuracy of our instrument was ±0.001 absorbance unit or an equivalent absorption coefficient of 0.23 m^{-1}. The absorption coefficient was calculated using the following equation (Kirk, 1994):

$$a(\lambda) = \frac{1}{L} 2.303 A(\lambda), \tag{1}$$

where $a(\lambda)$ represents the light absorption coefficient of CDOM at wavelength λ (m^{-1}), $A(\lambda)$ represents the corrected absorbance at λ, λ represents the wavelength (nm), and L represents the cuvette length (m). Samples were measured in duplicate.

2.2.4. Carbohydrates

Concentrations of dissolved monosaccharides (MCHO) and total dissolved carbohydrates (TCHO) were measured using

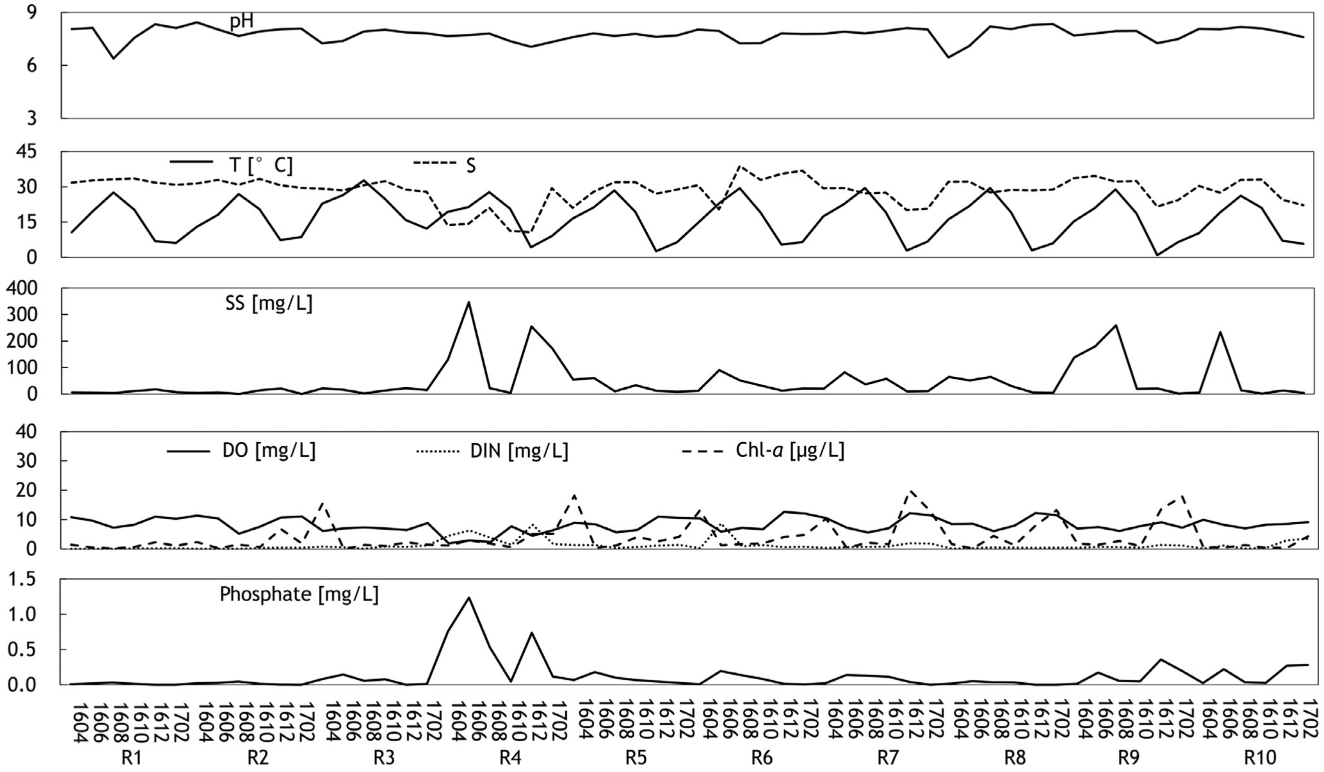

Figure 2 Temporal and spatial variations of temperature (*T*), salinity (*S*), pH, suspended particle (SS), dissolved oxygen (DO), dissolved inorganic nitrogen (DIN), phosphate and chlorophyll *a* (Chl-*a*) at the estuaries of Jiaozhou Bay.

the 2, 4, 6-tripyridyl-s-triazine (TPTZ) method (Myklestad and Børsheim, 2007). The MCHO sample was first heated to 100°C for 10 min, and then reacted with 1 mL of $FeCl_3$ (0.7 mg/L) and 2 mL of TPTZ (2.0 mg/L) to form a violet-colored complex with a maximum absorption at 596 nm (UV-2550, Shimadzu). Pure water (Milli-Q) was used as blank. TCHO was hydrolyzed by 1.2 M H_2SO_4 at 100°C for 2 h, neutralized with NaOH, and then subjected to the steps described for the MCHO measurement. The detection limit was 0.22 μM and the relative error was less than 5.44% for triplicate measurements. Concentrations of polysaccharides (PCHO) were calculated as the difference between TCHO and MCHO concentrations.

2.2.5. Amino acids

Concentrations of dissolved free amino acids (DFAA) were analyzed using liquid chromatography (HPLC) with the modified o-phthaldialdehyde-3-mercaptopropionic acid derivatization method (Kaiser and Benner, 2005). Total hydrolyzed amino acids (THAA) in the water samples were first hydrolyzed with HCl (6.0 M) at 110°C for 22 h in ampule bottles sealed under N_2 to form a hydrolysate. Then, the hydrolysates were evaporated and dissolved in pure water (Milli-Q). The separation of AAs was performed using a ZORBAX Eclipse AAA instrument (3.5 μm, 3.0 × 150 mm). The concentrations of fluorescent derivatives were measured at an excitation wavelength of 330 nm and emission wavelength of 450 nm. Concentrations of dissolved combined amino acids (DCAA) were calculated from the difference between THAA and DFAA concentrations. Standards for 18 amino acids were obtained from Sigma-Aldrich: aspartic acid (Asp), serine (Ser), tryptophan (Trp), glutamic acid (Glu), glycine (Gly), histidine (His), arginine (Arg), threonine (Thr), alanine (Ala), proline (Pro), cysteine (Cys), tyrosine (Tyr), valine (Val, methionine (Met), lysine (Lys), isoleucine (Ile), leucine (Leu) and phenylalanine (Phe). The relative error of the amino acid concentrations was less than 2.80% for duplicate samples.

2.3. Statistical analysis

A canonical correspondence analysis (CCA) was performed using CANOCO 5 to study the relationship between environmental variables (T, S, pH, SS, DO, DIN, PO_4^{3-} and Chl-*a*) and DOM (Braak and Šmilauer, 2012). Potential correlations between DOM and physicochemical parameters were examined by calculating the maximal information coefficient (MIC) using the MINE package in R (Reshef et al., 2011). Then, the matrix of MIC values >0.51 was used to visualize the network associations between physicochemical parameters and DOM using Cytoscape software version 3.3.0 (Shannon et al., 2003).

3. Results and discussion

3.1. Physicochemical parameters in the estuaries of Jiaozhou Bay

The variations in T, S, pH, SS, DO, DIN, PO_4^{3-} and Chl-*a* in the waters of Jiaozhou Bay are shown in Fig. 2. T varied

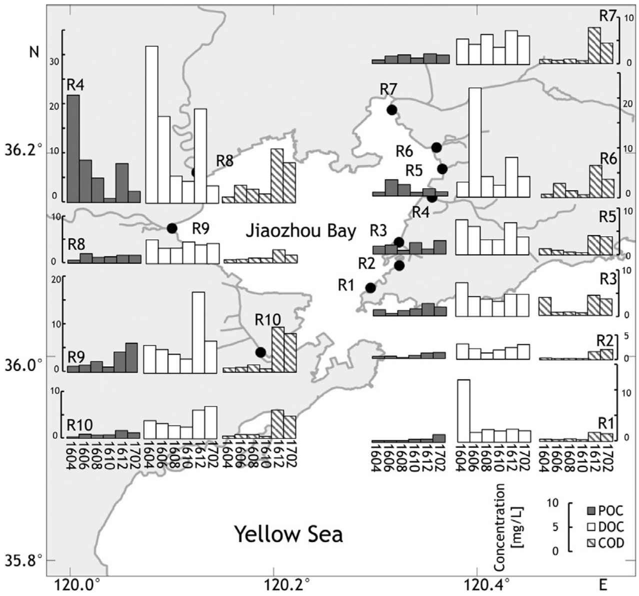

Figure 3 Temporal and spatial variations of POC, DOC and COD at the estuaries of Jiaozhou Bay.

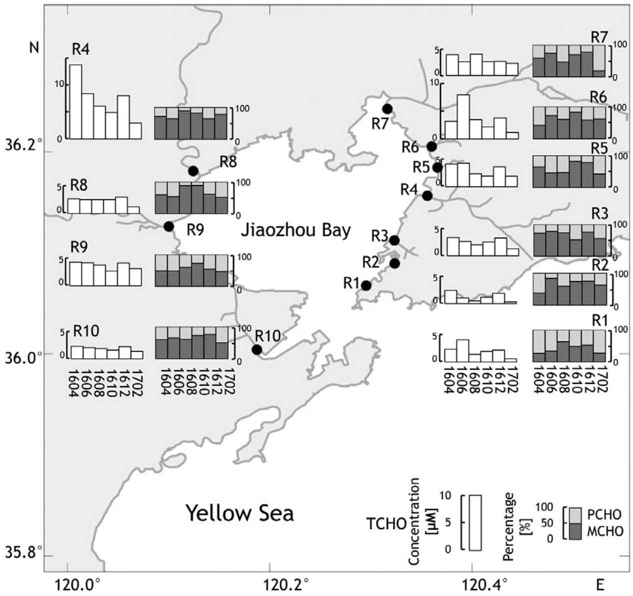

Figure 4 Monosaccharide and polysaccharide concentrations at the estuaries of Jiaozhou Bay.

seasonally, while pH changed little with the season at all sites. With the exception of the Licun River (R4) between April and June, DO concentrations were relatively abundant (greater than 5 mg/L). The SS, DIN, PO_4^{3-}—P and Chl-*a* levels varied spatially and temporally in large ranges. Higher nutrient concentrations were observed in the Licun River (R4), and higher Chl-*a* concentrations were observed in the northwest bay.

3.2. Temporal and spatial variations in POC and DOC concentrations

The concentrations of POC, DOC and COD in the estuaries of Jiaozhou Bay varied spatially and temporally in the range of 0.13—22.40 mg/L (average 1.75 mg/L), 0.98—32.75 mg/L (average 5.04 mg/L), and 0.23—7.58 mg/L (average 1.67 mg/L), respectively (Fig. 3). The DOC concentration accounted for 52.43—97.29% (average 77.00%) of the total organic matter. Higher POC, DOC and COD concentrations were distributed in the northeast bay, consistent with a previous investigation (Zhang et al., 2013). Meanwhile, the DOC concentration was significantly and positively correlated with the POC concentration ($r = 0.8303$, $n = 60$, $P < 0.01$). Except for the obviously high values in the Licun River (R4), higher DOC and POC concentrations were recorded in December and April than in other months. The concentrations of POC and DOC at the Ferry (R1), the Dagang (R2), and the Haibo River (R3) were maintained at similar levels compared with the levels measured 10 years ago (Jiang et al., 2007). The COD concentration is used to indicate the total level of organic matter in many estuary and coastal waters in China (Zhu et al., 2002). This study applied COD as reference parameter, which was significantly and positively correlated with the combined DOC and POC concentrations ($r = 0.8303$, $n = 60$, $P < 0.01$).

3.3. Temporal and spatial variations in DOM components

3.3.1. Carbohydrates

TCHO concentrations in the estuaries of Jiaozhou Bay varied with a range of 0.34—14.09 μM (average 3.18 μM) (Fig. 4). Generally, TCHO concentrations were higher in June and December, but lower in October and February. MCHO concentrations were approximately two-fold higher than the PCHO concentrations, accounting for 23.33—93.95% of the TCHO content (average 64.60%). Moreover, higher MCHO and PCHO concentrations were observed in the Licun River (R4), whereas lower concentrations were observed in the Ferry (R1) and Dagang (R2) Rivers. The TCHO concentration exhibited a similar distribution to the POC and DOC concentrations, as it was higher in the estuaries of northeast bay.

3.3.2. Amino acids

THAA concentrations in the estuaries of Jiaozhou Bay ranged from 0.89—8.30 μM (average 4.04 μM) (Fig. 5). DCAA accounted for 33.72—97.60% of the THAA (average 83.42%), and its concentration was 4 times higher than the DFAA concentration. Similar to the POC, DOC and TCHO concentrations, THAA concentrations at the Licun River (R4) were higher than at other stations, while THAA concentrations at the Ferry (R1) and Dagang (R2) Rivers were lower than at other stations. THAA concentrations varied temporally, with larger ranges observed in April, June and August than in October and December.

3.3.3. CDOM

The absorption coefficient is often used to quantify the relative concentrations of organic matter based on light absorption (Peacock et al., 2013), which exhibits a positive linear correlation with the fluorescence characteristics (Rochelle-Newall and Fisher, 2002; Vignudelli et al., 2004). The relative concentrations of CDOM in coastal waters are

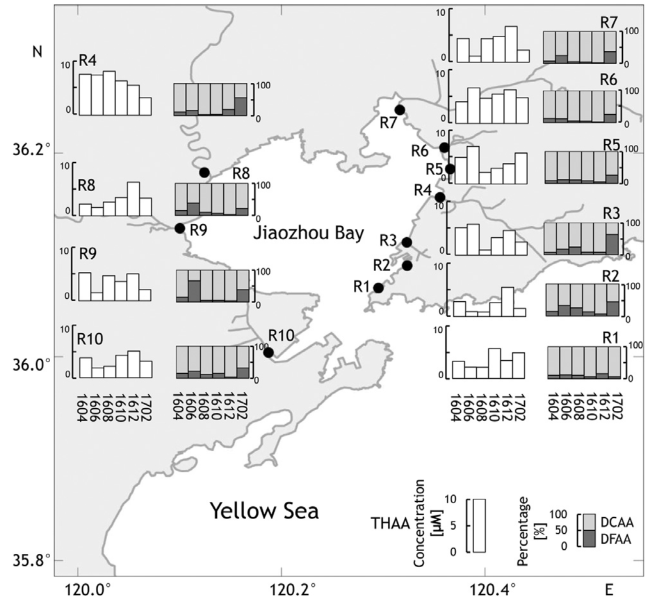

Figure 5 Concentrations of dissolved free (DFAA) and associated (DCAA) amino acids at the estuaries of Jiaozhou Bay.

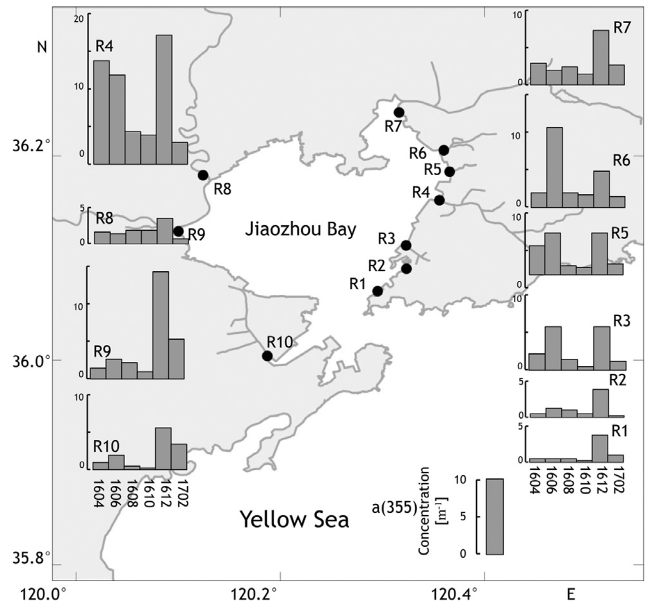

Figure 6 Relative concentrations of CDOM ($a(355)$) at the estuaries of Jiaozhou Bay.

indicated by the absorption coefficient at a wavelength of 355 nm ($a(355)$) (Green and Blough, 1994). The relative concentrations of CDOM in the estuaries of Jiaozhou Bay ranged from 0.23—16.35 m^{-1} (average 3.09 m^{-1}) (Fig. 6). Spatially, higher concentrations were observed in the Licun River (R4), while lower concentrations were observed in the Ferry (R1) and Dagang (R2) Rivers. Temporally, higher concentrations were observed in December, while lower concentrations were recorded in August and October. This finding might correlate with the dilution caused by local precipitation (Ren et al., 2018). Although the relative concentrations of CDOM in estuaries varied temporally and spatially, they were all

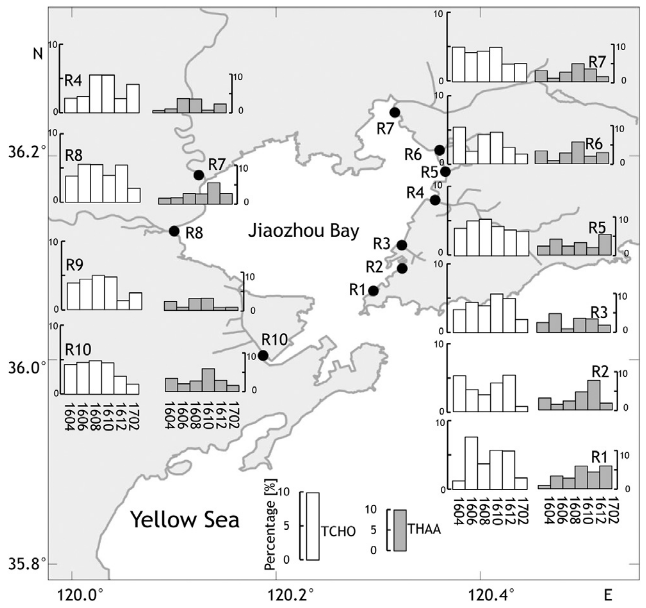

Figure 7 Percentages of carbohydrates and amino acids to DOC at the estuaries of Jiaozhou Bay.

comparable to the relative concentrations of CDOM in the Liaohe estuary and reed wetland of Liaohe (Li et al., 2009; Zhang et al., 2016). The relative concentrations of CDOM in Haibo River (R3) measured in the present study are comparable with previous results (Jiang et al., 2007).

3.4. Contributors to the standing stock of DOM

The percentages of TCHO and THAA in DOC (TCHO-C% and THAA-C%) reflected the levels of activity and degradation of DOM components, and they were associated with labile organic matter, such as fresh plankton DOM (Davis et al., 2009). In general, higher TCHO-C% and THAA-C% indicate higher bioactivity (Davis et al., 2009). TCHO-C% and THAA-C% in the estuaries of Jiaozhou Bay ranged from 5.17—31.21% (average 15.87%) and 1.51—10.77% (average 4.05%), respectively (Fig. 7). The temporal variations were larger than the spatial variations. Specifically, TCHO-C% was higher (approximately 2 times) in August and October than in February. THAA-C% was higher in October, followed by December, which was approximately 2 times higher than the average values recorded in other months. The seasonal variations indicated that DOM was more active in summer and autumn than in winter in the estuaries of Jiaozhou Bay. Both the absolute DOC concentrations and relative bioactivity of DOM in the estuaries of Jiaozhou Bay were higher than in the estuaries and bays of the Adriatic Sea, Galveston Bay and Delaware estuary, which are also significantly impacted by human activities (Hung et al., 2001; Pettine et al., 2001; Witter and Luther, 2001; Yang et al., 2010).

The estuarine DOM originated from both riverine inputs and *in situ* primary production. Researchers have postulated that the humic-like materials are mainly derived from terrestrial input (Castillo et al., 1999), while Chl-*a* usually indicates in *situ* primary production, and glycine (Gly) traces the bacterial activities (Davis et al., 2009). The analysis of the linear relationship (Table 2) revealed significant posi-

Table 2 Correlation between concentrations of TCHO and THAA and relative contents of some organic matters.

	Humus-like	Protein-like	Glycine [Gly]	Chl-*a*
TCHO	0.790[a]	0.793[a]	0.628[a]	0.022
THAA	0.578[a]	0.525[a]	0.795[a]	0.160

[a] Showed significant correlation. ($p < 0.01$, $n=60$, 2-tailed).

tive correlations between TCHO and THAA concentrations and the fluorescence intensities of humic-like materials, microbial protein-like materials (Ren et al., 2018), and Gly (simultaneous results), but no significant relationship was observed with Chl-*a* levels. Thus, riverine organic matter and bacterial degradation products primarily contribute to the standing stocks of TCHO and THAA. However, the insignificant relationships between TCHO/THAA and Chl-*a* indicated that primary production had little contribution to the standing stocks of TCHO and THAA. In previous studies, PCHO was mainly derived from the extracellular release by phytoplankton (Biersmith and Benner, 1998), and TCHO was positively correlated with phytoplankton growth and primary production (Kerhervé et al., 2002). The higher concentrations of Chl-*a* in the study area, ranging from 0.17 to 23.63 μg/L (averaging at 4.04 μg/L), inferred vigorous local phytoplankton productivity. Marine bacterial production activities preferentially use newly produced organic carbon (Bronk and Glibert, 1993). Therefore, we speculated that DOM produced through primary production in the study area was preferentially used by bacteria, and only a small amount was retained in the standing stock of DOM in the estuaries, leading to the insignificant relationships between TCHO and THAA with Chl-*a* in the study areas.

3.5. Factors regulating the DOM distributions

A canonical correspondence analysis (CCA) was used to discern the influences of environmental factors, including physical (T, S, pH and SS), chemical (DO, DIN and PO_4^{3-}) and biological (Chl-*a*) factors, on the OM (POC, DOC, TCHO, THAA and CDOM) distributions in the study estuaries. Correlation coefficients were higher between DOM characteristics and the first two axes (CCA1 and CCA2) of environmental factors (0.855 and 0.713) (Fig. 8), suggesting that close interactions existed between DOM characteristics and environmental factors. At the same time, the correlation coefficients of the first and second axes were as low as 0.0034 among DOM parameters, and even close to zero among the environmental factors, suggesting few interactions existed among the DOM parameters and separate environmental factors. The contributions of the first and second axes accounted for 78.4%. Thus, the CCA results were reliable to reveal the effects of environmental factors on DOM distributions.

As indicated by the correlation between the first axis (CCA1) and environmental factors, the DOM composition is influenced by T, PO_4^{3-}, DO, SS, pH, DIN, Chl-*a* and S in order of higher to lower significance. According to the correlation between the second axis (CCA2) and environmental factors, the DOM composition is influenced by DIN, DO, S, Chl-*a*, PO_4^{3-}, SS and pH in order of higher to lower significance. The CCA results shown in Fig. 8 suggest important effects of T and the PO_4^{3-} concentration in April, June, August and October, DIN and PO_4^{3-} concentrations in December, and the DIN concentration in February. In general, T and PO_4^{3-} concentrations were the primary factors affecting the spatial and temporal distributions of DOM in the Jiaozhou Bay, followed by DO and SS concentrations. DO and Chl-*a* concentrations were also key factors controlling the spatial and temporal distributions of amino acids and carbohydrates. Moreover, S, DIN and PO_4^{3-} concentrations were the factors that effectively regulated the spatial and temporal distributions of POC, DOC and classified DOM components.

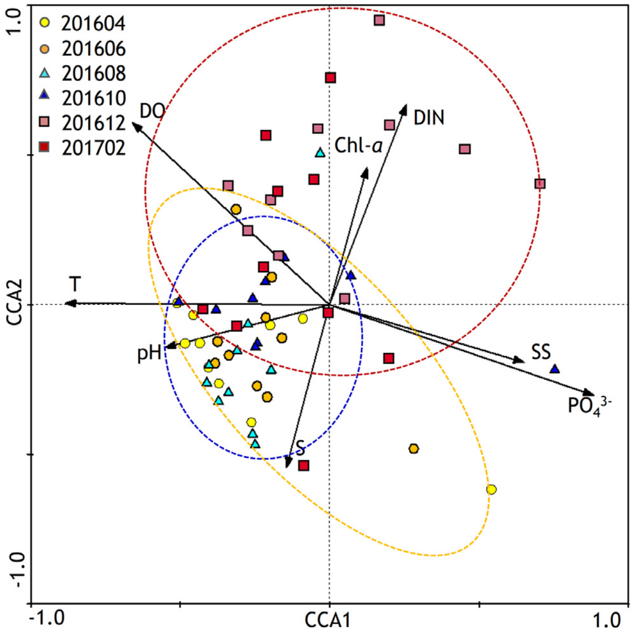

Figure 8 CCA analysis between DOM and environmental factors at the estuaries of Jiaozhou Bay. (DOM composition is represented by POC, DOC, TCHO, THAA and CDOM, while environmental factors are represented by T, pH, DO, S, Chl-*a*, SS, DIN and PO_4^{3-}. The length and direction of arrow line represent the importance of factor and relationship to DOM composition. The dots in one dash circle represent the similar group of DOM composition.)

T not only represents a direct factor regulating the degradation rate of organic matter but also controls biological metabolism by regulating biological activity (Hudson et al., 2010; Mantoura and Woodard, 1983). As a primary factor, T exhibited significant temporal variations with seasons in the study area. The important functions of S (negative correlation), DIN and PO_4^{3-} (positive correlation) in regulating DOM implied that the riverine materials were the major sources of DOM in Jiaozhou Bay. The results from the CCA analysis are consistent with the findings described in Section 3.4 and Table 2. Namely, DO and Chl-*a* are the key factors controlling the spatial and temporal distributions of amino acids and carbohydrates. We inferred that the *in situ* primary production generated a certain amount of DOM, which contained greater concentrations of the active components amino acids and carbohydrates.

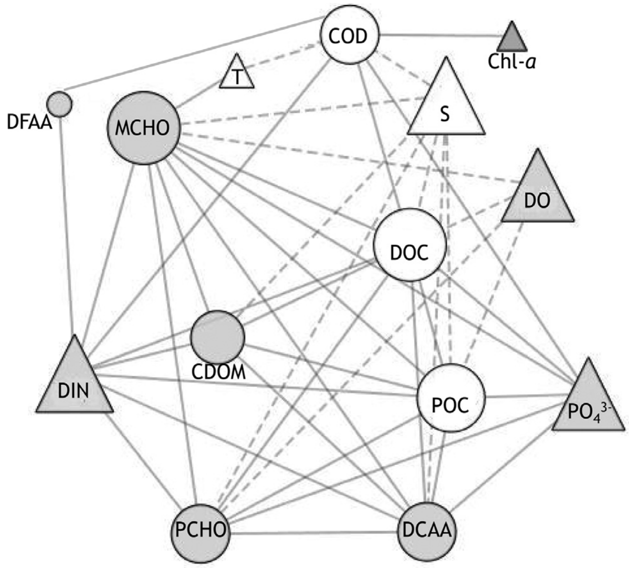

Figure 9 Maximal information coefficient (MIC) analysis of DOM components and physicochemical factors at the estuaries of Jiaozhou Bay. (The triangle is the environmental parameter, the circle is the dissolved organic parameter; solid line represents the positive correlation, dotted line represents negative correlation, and there is no line connecting between the parameters without correlation or with non-significant correlation; the size of the circle is proportional to the influence of each factor in the water environment.)

3.6. The impacts of physicochemical factors on DOM components

The maximal information coefficient (MIC) was applied to clarify the interactions among OM components (POC, DOC, MCHO, TCHO, DFAA, DCAA and CDOM) and environmental factors (T, S, DO, DIN, PO_4^{3-} and Chl-*a*). Based on the results (Fig. 9), DOC and MCHO concentrations had the most weight and they were representative characteristics of the local DOM. S was the most important physicochemical factor and was negatively correlated with the levels of DOC, MCHO and other DOM components. Based on the MIC, we concluded that riverine discharge dominated the existing DOM components in the studied estuaries. Although T was a primary factor contributing to the spatial and temporal distributions of DOM, it exerted a small effect on MCHO and COD concentrations. Thus, T exerted minor effects on the compositions and properties of DOM. According to the results of the statistical analysis, Chl-*a* had a small effect on COD and did not directly affect other DOM components. Therefore, the primary products of phytoplankton had little contribution to the existing DOM compositions, which was also supported by the CCA results. Nutrients (DIN and PO_4^{3-}) had higher weights and were positively correlated with DOM components, and DO also had a higher weight but was negatively correlated with DOM components. Thus, we speculated that DO played an important role in oxidizing DOM components in the studied estuaries and was simultaneously responsible for the release of nutrients. CDOM had a lower weight among the DOM components, and was not significantly correlated with physiochemical factors. Therefore, CDOM was derived from the similar sources or mutual transformation with other components of DOM, but was less impacted by physicochemical factors and was maintained at relatively stable levels.

Based on the CCA and MIC results, T, S, DO, DIN, PO_4^{3-} and Chl-*a* principally regulate the DOM distributions and composition. Then, numerical equations between these 5 parameters and DOM composition were established using a multiple regression analysis to further address the potential contribution of every principal parameter to the DOM concentration. The equations are listed below:

$$\mathrm{POC} = -0.118\mathrm{T} - 0.075\mathrm{S} - 0.567\mathrm{DO} - 0.222\mathrm{DIN} + 7.506\mathrm{PO}_4^{3-} - 0.001\mathrm{Chl} - a + 9.855, \tag{2}$$

$$\mathrm{DOC} = -0.088\mathrm{T} - 0.040\mathrm{S} - 0.248\mathrm{DO} + 1.438\mathrm{DIN} + 8.002\mathrm{PO}_4^{3-} + 0.048\mathrm{Chl} - a + 6.783, \tag{3}$$

$$\mathrm{CDOM} = -0.119\mathrm{T} - 0.167\mathrm{S} - 0.242\mathrm{DO} + 0.164\mathrm{DIN} + 4.125\mathrm{PO}_4^{3-} + 0.038\mathrm{Chl} - a + 10.966, \tag{4}$$

$$\mathrm{TCHO} = 0.018\mathrm{T} - 0.068\mathrm{S} - 0.138\mathrm{DO} + 0.351\mathrm{DIN} + 3.258\mathrm{PO}_4^{3-} + 0.022\mathrm{Chl} - a + 5.007, \tag{5}$$

$$\mathrm{THAA} = -0.010\mathrm{T} - 0.029\mathrm{S} + 0.033\mathrm{DO} + 0.325\mathrm{DIN} + 1.488\mathrm{PO}_4^{3-} + 0.031\mathrm{Chl} - a + 4.077. \tag{6}$$

PO_4^{3-} ranks first in increasing the DOM concentration for every unit increase in its concentration. This finding is consistent with the relative absence of PO_4^{3-} in Jiaozhou Bay, as well as most estuaries in China (Gong et al., 2015). DIN ranks second and plays an important role in regulating the DOM concentration, but exerted an obviously weaker effect than PO_4^{3-} for every unit increase. As the primary limiting element, any increase in the PO_4^{3-} concentration would stimulate the primary productivity in the bay. This finding was confirmed by the positive relationship between PO_4^{3-} and Chl-*a* concentrations, as well as the positive relationship between Chl-*a* and DOM concentrations. However, the lower correlation coefficient between Chl-*a* and DOM concentrations suggested that primary production had a lower contribution to the standing pool of DOM. This result is consistent with the contribution of the Chl-*a* concentration to the DOM standing stock described in Section 3.4. DO has a similar contribution to DIN, and presents a negative correlation with the concentrations of DOM components, except THAA. DO is largely produced via primary productivity in oceans and is also consumed as an oxidant during the degradation of organic matter. Both of these processes are intricately linked with DOM production and elimination. The relationship between DO and DOM concentrations implies that degradation rather than primary production has a greater contribution to DOM components in the studied estuaries. T and S rank at lower levels in terms of contributions to the DOM concentration for every unit increase. However, this result does not contradict the important roles of T and S in determining the DOM composition and distribution identified using the CCA and MIC analyses described above. When the units of every parameter are considered, T and S ranged from 6.01—21.95°C and 10.68—33.50, which exhibited much wider variations than the absolute concentrations of PO_4^{3-} and DIN throughout the year. Thus, T and S play key roles in determining the DOM composition and distribution when the wide variations of T and S are considered in the studied areas.

4. Conclusions

Jiaozhou Bay is a typical semi-closed bay at the edge of the western Pacific Ocean and is significantly regulated by anthropogenic activities. An investigation of data from one year showed that the concentrations of POC, DOC and COD in the study area were relatively higher than in comparable estuaries and bays, ranging from 0.13—22.40 mg/L (average 1.75 mg/L), 0.98—32.75 mg/L (average 5.04 mg/L), and 0.23—7.58 mg/L (average 1.67 mg/L), respectively. In addition to the significant positive relationship between DOC and POC concentrations, higher concentrations of these components were observed in December and April temporally, and in Licun River spatially. TCHO and THAA concentrations did not exhibit the same patterns as the POC and DOC concentrations, because higher concentrations were observed in summer and autumn but lower concentrations were recorded in winter. Meanwhile, wider temporal variations in TCHO and THAA concentrations were observed than in the spatial variations. Furthermore, the variations in TCHO-C% and THAA-C%, including both absolute and relative high concentrations, implied that DOM with higher bioactivity was observed in the study area, particularly in the period between summer and autumn.

According to the CCA and MIC results, the variations in T controlled the spatial and temporal distributions of DOM in the estuaries of Jiaozhou Bay, while the materials derived from rivers and bacteria dominated the existing DOM compositions. Phytoplankton contributed many of the bioactive organic components, such as amino acids and carbohydrates, but they accounted for a minor fraction of the existing DOM. MCHO and THAA were typical characteristic components, reflecting variations and processes of DOM in the estuaries of Jiaozhou Bay. The relative contributions of POC, DOC and CDOM displayed similar patterns in the Jiaozhou Bay estuaries, while TCHO and THAA concentrations varied due to their higher bioactivities.

Acknowledgments

This study is supported by the National Key Research and Development Program of China (No. 2018YFC1407601) and Natural Science Foundation of China (No. 41831280). Thanks for the support by the Qingdao Dairy Compound Detection Expert Workstation, hosted by SGS-CSTC Standards Technical Services (Qingdao) Co., Ltd.

References

Battin, T.J., Kaplan, L.A., Findlay, S., Hopkinson, C.S., Marti, E., Packman, A.I., 2009. Biophysical controls on organic carbon fluxes in fluvial networks. Nature Geosci. 1 (8), 95—100.

Biersmith, A., Benner, R., 1998. Carbohydrates in phytoplankton and freshly produced dissolved organic matter. Mar. Chem. 63 (1—2), 131—144.

Braak, C.J.F.T., Šmilauer, P., 2012. Canoco Reference Manual and User's Guide: Software for Ordination, Version 5.0. Ithaca, 20—71.

Bronk, D.A., Glibert, P.M., 1993. Application of a ^{15}N tracer method to the study of dissolved organic nitrogen uptake during spring and summer in Chesapeake Bay. Mar. Biol. 115 (3), 501—508.

Castillo, C.E., Coble, P.G., Morell, J.M., José, M.L., Corredor, J.E., 1999. Analysis of the optical properties of the Orinoco River plume by absorption and fluorescence spectroscopy. Mar. Chem. 66 (1), 35—51.

Chen, R.F., Bada, J.L., 1992. The fluorescence of dissolved organic matter in seawater. Mar. Chem. 37 (3—4), 191—221.

Chen, W., Westerhoff, P., Leenheer, J.A., Booksh, K., 2003. Fluorescence excitation—emission matrix regional integration to quantify spectra for dissolved organic matter. Environ. Sci. Technol. 37 (24), 5701—5710.

Cheng, Y.Y., Guo, W.D., Hu, M.H., 2008. Fluorescence characteristics of dissolved organic matter released from estuarine sediments during resuspension. Geochimica 37 (1), 51—58.

Davis, J., Kaiser, K., Benner, R., 2009. Amino acid and amino sugar yields and compositions as indicators of dissolved organic matter diagenesis. Org. Geochem. 40 (3), 343—352.

Fellman, J.B., Spencer, R.G.M., Hernes, P.J., Edwards, R.T., Amore, D.V.D., 2010. The impact of glacier runoff on the biodegradability and biochemical composition of terrigenous dissolved organic matter in near-shore marine ecosystems. Mar. Chem. 121 (1), 112—122.

Gong, Y., Yu, Z.G., Yao, Q.Z., Chen, H.T., Mi, T.Z., Tan, J.Q., 2015. Seasonal variation and sources of dissolved nutrients in the Yellow River, China. Int. J. Environ. Res. Publ. Health 12 (8), 9603—9622.

Grasshoff, K., Kremling, K., Ehrhardt, M., 2007. Methods of Seawater Analysis, 3rd edn., Weiheim, 159—228.

Green, S.A., Blough, N.V., 1994. Optical absorption and fluorescence properties of chromophoric dissolved organic matter in natural waters. Limnol. Oceanogr. 39 (8), 1903—1916.

Hedges, J.I., Keil, R.G., 1995. Sedimentary organic matter preservation: an assessment and speculative synthesis. Mar. Chem. 49 (2—3), 123—126.

Hudson, N., Baker, A., Reynolds, D., 2010. Fluorescence analysis of dissolved organic matter in natural, waste and polluted waters — a review. River Res. Appl. 23 (6), 631—649.

Hung, C.C., Tang, D.G., Warnken, K.W., Santschi, P.H., 2001. Distributions of carbohydrates, including uronic acids, in estuarine waters of Galveston Bay. Mar. Chem. 73, 305—318.

Jeffrey, S.W., Humphrey, G.F., 1975. New spectrophotometric equations for determining chlorophylls *a*, b, c1 and c2 in higher plants, algae and natural phytoplankton. Biochem. Physiol. Pflanzen 167 (2), 191—194.

Ji, N.Y., Zhao, W.H., Wang, J.T., Miao, H., 2006. Change of humic-like fluorescence characteristics of dissolved organic matter from Dagu River to Jiaozhou Bay. Environ. Sci. 27 (6), 1073—1077.

Jiang, F.H., Yang, H.H., Li, X.C., Wang, X.R., Wang, X.L., Yin, Y.F., 2007. Excitation-emission-matrix spectral property of dissolved organic matter in seawater of Jiaozhou Bay, China. Spectrosc. Spect. Anal. 27 (9), 1765—1769.

Jiao, N., Herndl, G.J., Hansell, D.A., Benner, R., Azam, F., 2010. Microbial production of recalcitrant dissolved organic matter: long-term carbon storage in the global ocean. Nat. Rev. Microbiol. 8 (8), 593—599.

Kaiser, K., Benner, R., 2005. Erratum: hydrolysis-induced racemization of amino acids. Limnol. Oceanogr. Meth. 3 (8), 318—325.

Kerhervé, P., Buscail, R., Gadel, F., Francois, G., Léon, S., 2002. Neutral monosaccharides in surface sediments of the northwestern Mediterranean sea. Org. Geochem. 33 (4), 421—435.

Kirk, J.T.O., 1994. Light and Photosynthesis in Aquatic Ecosystems. Cambridge, 20—50.

Kong, X., Zhang, P., Yang, N.N., Liang, S.K., 2016. Potential bioavailability of dissolved organic nitrogen in the discharge outlets of sewage treatment plants around the Jiaozhou Bay. Environ. Sci. 37 (3), 854—861.

Li, L., Liang, S.K., Shi, X.Y., Shi, X.L., 2009. Contaminative conditions analysis of main rivers flowing into Jiaozhou Bay in 2007. Environ. Sci. Manage. 34 (6), 23—28.

Liang, X.B., Wang, G.J., Huang, R.G., Wu, Y.Y., 2001. Dynamic study of protein and amino acids in lake sediments. Acta Miner. Sin. 21 (1), 59—63.

Mantoura, R.F.C., Woodward, E.M.S., 1983. Conservative behavior of riverine dissolved organic carbon in the Severn Estuary: chemical and geochemical implications. Geochim. Cosmochim. Acta 47 (7), 1293—1309.

Markager, S., Vincent, W.F., 2000. Spectral light attenuation and the absorption of UV and blue light in natural waters. Limnol. Oceanogr. 45 (3), 642—650.

Middelboe, M., Borch, N.H., Kirchman, D.L., 1995. Bacterial utilization of dissolved free amino acids, dissolved combined amino acids and ammonium in the Delaware Bay Estuary: effects of carbon and nitrogen limitation. Mar. Ecol. Prog. Ser. 128 (1—3), 109—120.

Myklestad, S.M., Børsheim, K.Y., 2007. Dynamics of carbohydrates in the Norwegian Sea inferred from monthly profiles collected during 3 years at 66°N, 2°E. Mar. Chem. 107 (4), 475—485.

Nelson, N.B., Siegel, D.A., Michaels, A.F., 1998. Seasonal dynamics of colored dissolved material in the Sargasso Sea. Deep Sea Res. PT I 45 (6), 931—957.

P.R. China national standard, 2007. The Specification For Marine Monitoring. Beijing, 95—102.

Peacock, M., Burden, A., Cooper, M., 2013. Quantifying dissolved organic carbon concentrations in upland catchments using phenolic proxy measurements. J. Hydrol. 477, 251—260.

Pettine, M., Capri, S., Manganelli, M., Patrolecco, L., Puddu, A., Zoppini, A., 2001. The dynamics of DOM in the Northern Adriatic Sea. Estuar. Coast. Shelf Sci. 52 (4), 471—489.

Ren, Q.Q., Zou, L., Yu, G., Li, L., 2018. Optical absorption properties of CDOM at the estuaries of Jiaozhou Bay. J. Res. Environ. Sci. 31 (8), 1407—1416.

Reshef, D.N., Reshef, Y.A., Finucane, H.K., Grossman, S.R., McVean, G., Turnbaugh, P.J., Lander, E.S., Mitzenmacher, M., Sabeti, P.C., 2011. Detecting novel associations in large data sets. Science 334 (6062), 1518—1524.

Rochelle-Newall, E.J., Fisher, T.R., 2002. Chromophoric dissolved organic matter and dissolved organic carbon in Chesapeake Bay. Mar. Chem. 77 (1), 23—41.

Seitzinger, S., Sanders, R., 1997. Contribution of dissolved organic nitrogen from rivers to estuarine eutrophication. Mar. Ecol. Prog. Ser. 159, 1—12.

Shank, G.C., Zepp, R.G., Whitehead, R.F., Moran, M.A., 2005. Variations in the spectral properties of freshwater and estuarine CDOM caused by partitioning onto river and estuarine sediments. Estuar. Coast. Shelf Sci. 65 (1—2), 289—301.

Shannon, P., Markiel, A., Ozier, O., Baliga, N.S., Wang, J.T., Ramage, D., Amin, N., Schwikowski, B., Ideker, T., 2003. Cytoscape: A Software Environment for Integrated Models of Biomolecular Interaction Networks. California, 2498—2504.

Shen, Z., Liu, Q., Yu, L.W., Yun, Y., 2006. Nutrient structure of seawater and ecological responses in Jiaozhou Bay, China. Estuar. Coast. Shelf Sci. 69 (1), 299—307.

Shi, D., 2015. Spatial and Temporal Distribution of Dissolved Carbohydrates in the East Shelf Seas of China. Qingdao, 12—23.

Stepanauskas, R., Leonardson, L., Tranvik, L.J., 1999. Bioavailability of wetland-derived DON to freshwater and marine bacterioplankton. Limnol. Oceanogr. 44 (6), 1477—1485.

Veuger, B., Middelburg, J.J., Boschker, H.T.S., Nieuwenhuize, J., Rijswijk, P.V., 2004. Microbial uptake of dissolved organic and inorganic nitrogen in Randers fjOrd. Estuar. Coast. Shelf Sci. 61 (3), 507—515.

Vignudelli, S., Santinelli, C., Murru, E., Nannicini, L., Seritti, A., 2004. Distributions of dissolved organic carbon (DOC) and chromophoric dissolved organic matter (CDOM) in coastal waters of the northern Tyrrhenian Sea (Italy). Estuar. Coast. Shelf Sci. 60 (1), 133—149.

Wang, M., Chen, Y., 2018. Generation and characterization of DOM in wastewater treatment processes. Chemosphere 201, 96—109.

Witter, A.E., Luther, G.W., 2001. Spectrophotometric measurement of seawater carbohydrate concentrations in neritic and oceanic waters from the U.S. Middle Atlantic Bight and the Delaware estuary. Mar. Chem. 77 (2), 143—156.

Xi, M., Zi, Y., Wang, Q., Wang, S., Cui, G., Kong, F., 2018. Assessment of the concentration, structure, and source of soil dissolved organic matter in the coastal wetlands of Jiaozhou Bay, China. Phys. Chem. Earth 103, 35—44.

Yang, G.P., Zhang, Y.P., Lu, X.L., Ding, H.B., 2010. Distributions and seasonal variations of dissolved carbohydrates in the Jiaozhou Bay, China. Estuar. Coast. Shelf Sci. 88 (1), 12—20.

Zhang, P.Y., Yang, G.P., Chen, Y., Leng, W.S., Ji, C.X., 2016. Temporal and spatial variations of particulate and dissolved amino acids in the East China Sea. Mar. Chem. 186, 133—144.

Zhang, Y.P., Yang, G.P., Lu, X.L., Ding, H.B., Zhang, H.H., 2013. Distributions of dissolved monosaccharides and polysaccharides in the surface microlayer and surface water of the Jiaozhou Bay and its adjacent area. Contin. Shelf Res. 63, 85—93.

Zhu, S., Zheng, X., Li, D., 2002. Ozonation of naphthalene sulfonic acids in aqueous solutions. Part I: elimination of COD, TOC and increase of their biodegradability. Water Res. 36 (5), 1237—1243.

Oceanologia (2020) 62, 111—115

Available online at www.sciencedirect.com

ScienceDirect

journal homepage: www.journals.elsevier.com/oceanologia/

SHORT COMMUNICATION

A new record of the invasive blue crab (*Callinectes sapidus* Rathbun, 1896) and his parasite from the Baltic basin

Przemysław Czerniejewski, Natalia Kasowska, Angelika Linowska*, Agnieszka Rybczyk

Faculty of Food Sciences and Fisheries, West Pomeranian University of Technology, Szczecin, Poland

Received 19 February 2019; accepted 27 June 2019
Available online 12 July 2019

KEYWORDS
Blue crab;
Callinectes sapidus;
Alien species;
Spread;
Poland;
Parasite;
Trichodina sp.

Summary A specimen of the invasive *Callinectes sapidus* was recently found in the catchment basin of the Baltic Sea (Lake Dąbie, Poland). The discovery is significant because it indicates a widening of the crab's biogeographic range in northern Europe and confirms its expansion along European estuaries. The captured juvenile specimen from Lake Dąbie (estuary of the Oder River) had a carapace width (CW) of 125.58 mm, carapace length (CL) of 53.23 mm, and weight (w) of 100.19 g. This is the first record of this species in this part of the Baltic Sea catchment basin, following the discovery of a female caught in a plaice net northeast of Copenhagen (1951) and an adult male caught off Skagen, Northern Jutland, between the Kattegat and the Skagerrak (2007).

Marine non-indigenous species (NIS) pose a serious threat to the aquatic environment of coastal areas due to their adverse impact on native species, eco-system biodiversity, and habitats (Ojaveer et al., 2016). In recent decades, most introductions of invasive species have been related to increased human activity, specifically sea transport, aquaculture, and tourism (Murray et al., 2011).

In European waters at least 87 NIS have been characterized (Katsanevakis et al., 2014), including a significant number of crustaceans. One is *Callinectes sapidus* (blue crab), originating from the western Atlantic Coast (Millikin and

---

* Corresponding author at: Department of Hydrobiology, Ichthyology and Biotechnology of Breeding, Faculty of Food Sciences and Fisheries, West Pomeranian University of Technology, ul. Kazimierza Królewicza 4, 71-550 Szczecin, Poland. Fax: +48 914496693.

E-mail address: angelika.linowska@zut.edu.pl (A. Linowska).
Peer review under the responsibility of Institute of Oceanology of the Polish Academy of Sciences.

Production and hosting by Elsevier

https://doi.org/10.1016/j.oceano.2019.06.004

Williams, 1984) and currently found distributed throughout European waters (Mancinelli et al., 2017), especially in the eastern Mediterranean (e.g. Adriatic and Aegean Seas) (Beqiraj and Kashta, 2010; Dulcic and Dragicevic, 2010; Sumer et al., 2013).

Although considered an invasive species in the Mediterranean (Katsanevakis et al., 2014), the negative effects of *C. sapidus* on native benthic communities and ecosystems are not well studied. This crustacean is characterized by high fertility and aggressive behavior, facilitating colonization of new waters (Millikin and Williams, 1984). Nonetheless, discovery of *C. sapidus* in the Baltic Sea catchment basin comes as a surprise, as over the last 50 years it has been reported only a handful of times in northern and central European waters.

In Europe this species has been noted since 1900 when it appeared on the French Atlantic coast. In the northern European waters *C. sapidus* was first observed in the Netherlands in 1932 (Wolff, 2005). Then, in 1981, it was first observed in Belgian waters (ICES WGITMO, 2007). On the German North Sea coast, *C. sapidus* was caught in 1964, 1965, 1990, 1998, 2007, and 2008 (Nehring and Meer, 2010; Nehring, 2011). Moreover, in Denmark, a single specimen was recorded in Øresund in 1951, and the next one near Skagen in 2007 (Tendat and Flintegaard, 2007). Those sites have been the furthest north-easterly locations of *C. sapidus* occurrence in Europe to date.

In this study, we report a novel occurrence of *C. sapidus* in the Baltic basin and discuss its morphometry and parasites.

The blue crab (*C. sapidus*) specimen was caught on 11 October 2018 during commercial fishing in the western part of Lake Dąbie, at the mouth of the Duńczyca Canal (coordinates: 53°25.566′N 014°36.979′E; 53°25.981′N 014°37.513′E) (Baltic Sea Basin) (Fig. 1). The specimen was photographed (Fig. 2) and sex was determined on the basis of external and internal structures (Millikin and Williams, 1984). Morphometric measurements (CW — carapace width including lateral spines, CL — carapace length, CH — carapace height) were performed (electronic caliper MEGA 150 mm 20513). Total body weight (W) and weight of hepatopancreas (WH) were also determined (laboratory balance RADWAG AS 160.R2).

On the basis of the obtained data, the condition of the crab was evaluated using the Fulton coefficient ($K = 100W/CW^3$,

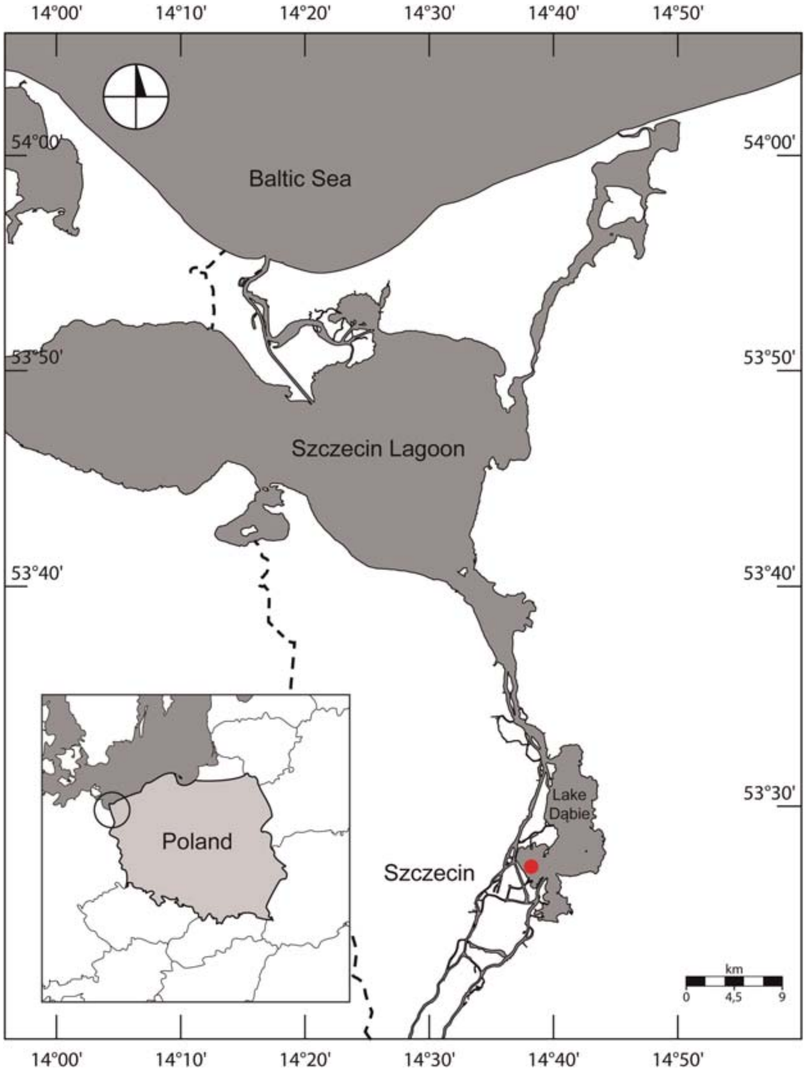

Figure 1 The site where the studied specimen of *Callinectes sapidus* (blue crab) was caught.

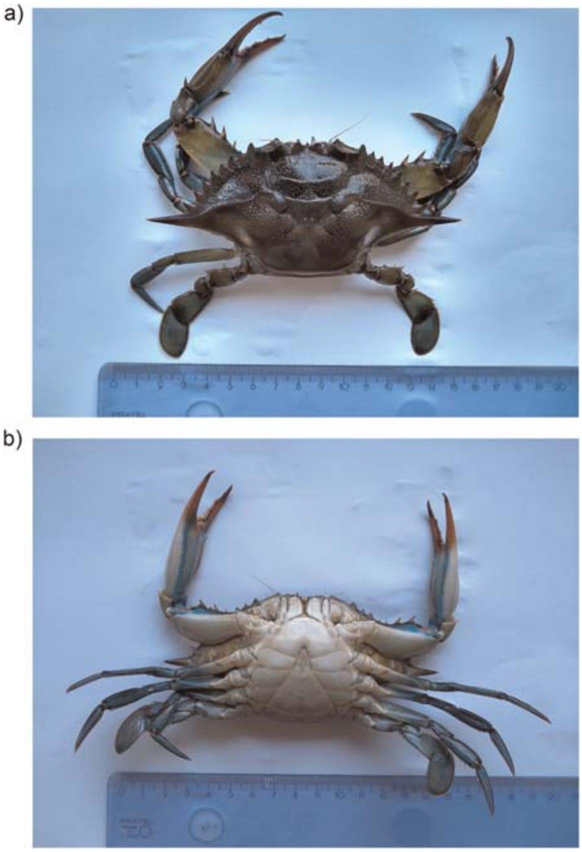

Figure 2 (a) Dorsal and (b) ventral view of the *Callinectes sapidus* juvenile female caught in Lake Dąbie.

where W is the crab weight [g] and CW is the carapace weight [cm]) (Sumer et al., 2013) and hepatosomatic index (HSI = WH × 100/W, where WH is the weight of hepatopancreas [g] and W is the crab wet weight [g]) (Cilenti et al., 2015).

Later, the crab was visually inspected to detect macroscopic lesions and visible external parasites. Heart, gonads, hepatopancreas, stomach, gut, and gills were prepared and examined for the presence of internal parasites (Goedknegt et al., 2017). Crabs gills were placed on a Petri dish and observed under a stereomicroscope (Zeiss Stemi DV4). In addition, microscopic preparations were made by collecting material from setae on claws and legs, from joint depressions of the legs, and from gills, which were inspected under transient light with the Olympus BX50 microscope equipped with an AxioVision camera with ZEN 2 core v.2.5 software.

The crab was characterized by a wide carapace (CW = 125.58 mm, CL = 53.23 mm, and CH = 26.31 mm) with a light blue dorsal surface (Fig. 2). The caught individual weighed 100.19 g.

The found female was identified as a juvenile based on the shape of its abdomen and internal organs (Millikin and Williams, 1984), even though the width of its carapace exceeded 125 mm. Immature females have a triangular abdomen with most segments indistinguishably fused but at the terminal maturation molt all segments become free (see Williams, 1974).

The Fulton coefficient provides important information about the 'well-being' of a species and can indicate aspects such as recent feeding conditions and the degree of adjustment to the environment. In the studied specimen calculated coefficient (K) value was 5.06, and hepatosomatic index (HSI) was 4.06. The Fulton coefficient indicated that the caught specimen was in good condition. The coefficient was higher than in the crab coming from the warmer waters of the Beymelek Lagoon — $K = 4.60$ (Sumer et al., 2013). The juvenile female from Lake Dąbie also had a better condition than adult females from Lesina ($K = 3.28$) and Verano ($K = 3.86$) lagoons (Cilenti et al., 2015).

Detailed parasitological analysis did not reveal the presence of internal parasites, including muscle parasites. Microscopic observation of material from joint depressions revealed the presence of the parasitic protozoan *Trichodina* sp. (Oligohymenophorea: Mobilida) (Fig. 3). It is difficult to

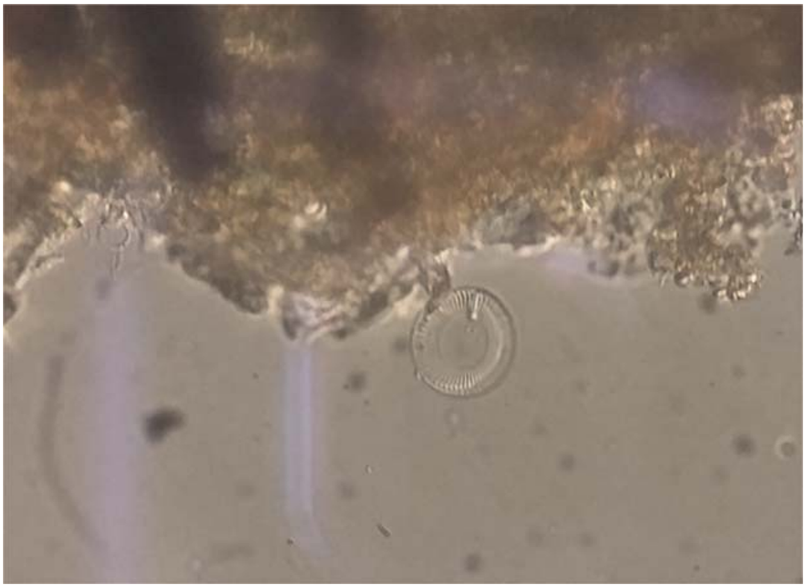

Figure 3 *Trichodina* sp. from the joint of the blue crab (*Callinectes sapidus*).

say that *Trichodina* sp. in this localization on the host is an epibiont or parasite, but it has been described as a parasite on another crab species — *Callinectes amnicola* (Enkamen et al., 2013). Although protozoa of the genus *Trichodina* have not previously been recorded on *C. sapidus* in European waters, they are common parasites of gills and body surfaces of fish in Western Pomerania (Mrozińska-Gogol, 2008). Due to the blue crab's migratory lifestyle, it could act as a vector spreading this parasite in the reservoir and thus could contribute to its transmission to fish, especially because *Trichodina* sp. proliferates exponentially and in favorable conditions a single specimen can reproduce very quickly by division and start a new invasion.

Establishing the presence of a new parasite for *C. sapidus* is particularly interesting because the parasitic fauna of this species residing in Europe is poorly understood. Messick and Sindermann (1992) identified 6 taxa of parasites recognized as crab pathogens in its native environment. Some of them, such as *Hematodinium perezi* (Protozoa), are also recorded in blue crabs found in Europe (Pagliara and Mancinelli, 2018). The change of the environment from marine to freshwater (and vice versa) acts as a specific disinfection treatment and there are few pathogens able to survive a change in salinity. This can explain the lack of other external parasites of the studied *C. sapidus*.

C. sapidus is a euryhaline and eurythermal species that inhabits estuaries and shallow coastal lagoons (Beqiraj and Kashta, 2010). Adult males prefer more brackish water (20—25 ppt) as evidenced by their discovery in the waters of the Rivers Elbe and Weser (1—23 ppt) (Grabemann et al., 1983), while adult females dominate in waters with higher salinity (>30 ppt). According to Costlow (1967), juveniles are more tolerant to variations in salinity and temperature than adults, and so it follows that the low salinity in Lake Dąbie is not prohibitive to immature individuals of this species. *C. sapidus* larvae require salinities above 22 ppt to survive, hence the low salinity in the estuary waters of the Oder and the Baltic Sea prohibits reproduction.

Ballast tanks of marine vessels are the most likely source bringing this species into European waters (Nehring, 2011) as in its native habitats *C. sapidus* occurs in large numbers close to major shipping lanes. *C. sapidus* exhibits an ability to adapt rapidly to new conditions and therefore, is a highly expansive species (Gennaio et al., 2006; Nehring et al., 2008). Successful competition for space and resources, supported by the large reinforced exoskeleton, strength, and eating habits of this crab, are of key importance in their fight for domination in trophic networks (Millikin and Williams, 1984). As a result, blue crabs may compete with other crab species, increasing mortality and affecting the distribution and dynamics of native crabs (Mancinelli et al., 2017). So far, however, there has been no evidence to indicate a negative impact on biodiversity, e.g. direct predation, displacement, or inhibition of other invertebrates, such as native crabs or other crustaceans (Katsanevakis et al., 2014).

It seems that the presence of the *C. sapidus* specimen in the waters of the Baltic Sea was not a result of invasion but an accidental and isolated case. Nevertheless, its appearance in a non-native habitat and good condition indicate that this species could successfully colonize waters of the western Baltic.

References

Beqiraj, S., Kashta, L., 2010. The establishment of blue crab *Callinectes sapidus* Rathbun, 1896 in the Lagoon of Patok, Albania (south-east Adriatic Sea). Aquat. Invasions 5 (2), 219—221, http://dx.doi.org/10.3391/ai.2010.5.2.16.

Cilenti, L., Pazienza, G., Scirocco, T., Fabbrocini, A., D'Adamo, R., 2015. First record of ovigerous *Callinectes sapidus* (Rathbun, 1896) in the Gargano Lagoons (south-west Adriatic Sea). Bioinvasions Rec. 4 (4), 281—287, http://dx.doi.org/10.3391/bir.2015.4.4.09.

Costlow Jr., D.J., 1967. The effect of salinity and temperature on survival and metamorphosis of megalops of the blue crab *Callinectes sapidus*. Helgoländ. Wiss. Meeresun. 15 (1—4), 84—97, http://dx.doi.org/10.1007/BF01618611.

Dulcic, J., Dragicevic, B., 2010. New record of the blue crab, *Callinectes sapidus* Rathbun, 1896, (Decapoda: Brachyura) in The Adriatic Sea. Ann. Ser. Hist. Nat. 20 (1), 23—28.http://zdjp.si/wp-content/uploads/2015/12/lipej.pdf.

Enkamen, A.P., Eyo, V.O., Ekpo, I.E., Bassey, B.O., 2013. Parasites of blue crab (*Callinectes amnicola*) in the Cross River Estuary, Nigeria. Int. J. Fish. Aquat. Stud. 1 (1), 18—21.

Gennaio, R., Scordella, G., Pastore, M., 2006. Occurrence of blue crab *Callinectes sapidus* (Rathbun, 1986) (Crustacea, Brachyura), in the Ugento ponds area (Lecce, Italy). Thalassia Salentina 29, 29—39.

Goedknegt, M.A., Havermans, J., Waser, A.M., Luttikhuizen, P.C., Velilla, E., Camphuysen, K.C.J., van der Meer, J., Thieltges, D.T., 2017. Cross-species comparison of parasite richness, prevalence, and intensity in a native compared to two invasive brachyuran crabs. Aquat. Invasions 12 (2), 201—212, http://dx.doi.org/10.3391/ai.2017.12.2.08.

Grabemann, I., Krause, G., Siedler, G., 1983. Langzeitige Änderungen des Salzgehaltes der Unterweser. Dtsch. Hydrogr. Z. 36 (2), 61—77, http://dx.doi.org/10.1007/BF02313285.

Katsanevakis, S., Wallentinus, I., Zenetos, A., Leppakoski, E., Çinar, M.E., Ozturk, B., Grabowski, M., Golani, D., Cardoso, A.C., 2014. Impacts of marine invasive alien species on ecosystem services and biodiversity: a pan-European review. Aquat. Invasions 9 (4), 391—423, http://dx.doi.org/10.3391/ai.2014.9.4.01.

Mancinelli, G., Chainho, P., Cilenti, L., Falco, S., Kapiris, K., Katselis, G., Ribeiro, F., 2017. The Atlantic blue crab *Callinectes sapidus* in southern European coastal waters: distribution, impact and prospective invasion management strategies. Mar. Pollut. Bull. 119 (1), 5—11, http://dx.doi.org/10.1016/j.marpolbul.2017.02.050.

Messick, G.A., Sindermann, C.J., 1992. Synopsis of Principal Diseases of the Blue Crab, *Callinectes sapidus*. Nat. Mar. Fisheries Serv., Oxford Lab., 25 pp.

Millikin, M.R., Williams, A.B., 1984. Synopsis of biological data on the blue crab, *Callinectes sapidus* Rathbun. NOAA Tech. Rep. NMFS 1 (4), 39 pp.

Mrozińska-Gogol, J., 2008. A check-list of parasites of percid fishes (Actinopterygii: Percidae) from the estuaries of the Polish coastal zone. Helminthologia 45 (4), 196—203, http://dx.doi.org/10.2478/s11687-008-0039-7.

Murray, C.C., Pakhomov, E.A., Therriault, T.W., 2011. Recreational boating: a large unregulated vector transporting marine invasive species. Divers. Distrib. 17 (6), 1161—1172, http://dx.doi.org/10.1111/j.1472-4642.2011.00798.x.

Nehring, S., 2011. Invasion history and success of the American blue crab *Callinectes sapidus* Rathbun, 1896 in European and adjacent waters. In: Galil, B., Clark, P., Carlton, J. (Eds.), In the Wrong Place — Alien Marine Crustaceans: Distribution, Biology and Impacts. Invading Nature — Springer Series in Invasion Ecology, vol. 6. Springer, Dordrecht, 607—624, http://dx.doi.org/10.1007/978-94-007-0591-3_21.

Nehring, S., Meer, U., 2010. First record of a fertilized female blue crab, *Callinectes sapidus* Rathbun, 1896 (Crustacea: Decapoda: Brachyura), from the German Wadden Sea and subsequent secondary prevention measures. Aquat. Invasions 5 (2), 215—218, http://dx.doi.org/10.3391/ai.2010.5.2.15.

Nehring, S., Speckels, G., Albersmeyer, J., 2008. The American blue crab *Callinectes sapidus* Rathbun on the German North Sea coast: status quo and further perspectives. Senck. Marit. 38, 39—44, http://dx.doi.org/10.1007/BF03043867.

Ojaveer, H., Olenin, S., Narščius, A., Florin, A.B., Ezhova, E., Gollasch, S., Jensen, K.R., Lehtiniemi, M., Minchin, D., Normant-Saremba, M., Strake, S., 2016. Dynamics of biological invasions and pathways over time: a case study of a temperate coastal sea. Biol. Invasions 19 (3), 799—813, http://dx.doi.org/10.1007/s10530-016-1316-x.

Pagliara, P., Mancinelli, G., 2018. Parasites affect hemocyte functionality in the hemolymph of the invasive Atlantic blue crab *Callinectes sapidus* from a coastal habitat of the Salento Peninsula (SE Italy). Medit. Mar. Sci. 19 (1), 193—200, http://dx.doi.org/10.12681/mms.13886.

Sumer, C., Teksam, I., Karatas, H., Menderes Aydin, C., 2013. Growth and reproduction biology of the blue crab, *Callinectes sapidus* Rathbun, 1896, in the Beymelek Lagoon (southwestern coast of Turkey). Turk. J. Fish. Aquat. Sci. 13 (4), 675—684.

Tendat, O.S., Flintegaard, H., 2007. Et fund af en sjaelden krabbe i danske farvande: den bla svommekrabbe, *Callinectes sapidus*. Flora Fauna Arhus 113, 53—56.

WGITMO, I.C.E.S., Report of the Working Group on, 2007.In: Introductions and Transfers of Marine Organisms (WGITMO). 21—23 March 2007, ICES CM 2007/ACME:05. Dubrovnik, Croatia, 160 pp.

Williams, A.B., 1974. The swimming crabs of the genus *Callinectes* (Decapoda: Portunidae). Fish. Bull. 72 (3), 685—798.

Wolff, W.J., 2005. Non-indigenous marine and estuarine species in the Netherlands. Zool. Med. Leiden 79 (1), 1—116.